



IntechOpen

Coastal Environment,
Disaster, and Infrastructure
A Case Study of China's Coastline

Edited by X. San Liang and Yuanzhi Zhang



COASTAL ENVIRONMENT, DISASTER, AND INFRASTRUCTURE - A CASE STUDY OF CHINA'S COASTLINE

Edited by **X. San Liang** and **Yuanzhi Zhang**

Coastal Environment, Disaster, and Infrastructure - A Case Study of China's Coastline

<http://dx.doi.org/10.5772/intechopen.79950>

Edited by X. San Liang and Yuanzhi Zhang

Contributors

X. San Liang, Jianyu Hu, Jianrong Zhu, Hui Wu, Weibing Guan, Ying Xu, Yuanzhi Zhang, Xiaochun Wang

© The Editor(s) and the Author(s) 2018

The rights of the editor(s) and the author(s) have been asserted in accordance with the Copyright, Designs and Patents Act 1988. All rights to the book as a whole are reserved by INTECHOPEN LIMITED. The book as a whole (compilation) cannot be reproduced, distributed or used for commercial or non-commercial purposes without INTECHOPEN LIMITED's written permission. Enquiries concerning the use of the book should be directed to INTECHOPEN LIMITED rights and permissions department (permissions@intechopen.com). Violations are liable to prosecution under the governing Copyright Law.



Individual chapters of this publication are distributed under the terms of the Creative Commons Attribution 3.0 Unported License which permits commercial use, distribution and reproduction of the individual chapters, provided the original author(s) and source publication are appropriately acknowledged. If so indicated, certain images may not be included under the Creative Commons license. In such cases users will need to obtain permission from the license holder to reproduce the material. More details and guidelines concerning content reuse and adaptation can be found at <http://www.intechopen.com/copyright-policy.html>.

Notice

Statements and opinions expressed in the chapters are those of the individual contributors and not necessarily those of the editors or publisher. No responsibility is accepted for the accuracy of information contained in the published chapters. The publisher assumes no responsibility for any damage or injury to persons or property arising out of the use of any materials, instructions, methods or ideas contained in the book.

First published in London, United Kingdom, 2018 by IntechOpen

eBook (PDF) Published by IntechOpen, 2019

IntechOpen is the global imprint of INTECHOPEN LIMITED, registered in England and Wales, registration number:

11086078, The Shard, 25th floor, 32 London Bridge Street

London, SE19SG – United Kingdom

Printed in Croatia

British Library Cataloguing-in-Publication Data

A catalogue record for this book is available from the British Library

Additional hard and PDF copies can be obtained from orders@intechopen.com

Coastal Environment, Disaster, and Infrastructure - A Case Study of China's Coastline

Edited by X. San Liang and Yuanzhi Zhang

p. cm.

Print ISBN 978-1-78984-393-4

Online ISBN 978-1-78984-394-1

eBook (PDF) ISBN 978-1-83881-841-8

We are IntechOpen, the world's leading publisher of Open Access books Built by scientists, for scientists

3,800+

Open access books available

116,000+

International authors and editors

120M+

Downloads

151

Countries delivered to

Our authors are among the
Top 1%

most cited scientists

12.2%

Contributors from top 500 universities



WEB OF SCIENCE™

Selection of our books indexed in the Book Citation Index
in Web of Science™ Core Collection (BKCI)

Interested in publishing with us?
Contact book.department@intechopen.com

Numbers displayed above are based on latest data collected.
For more information visit www.intechopen.com



Meet the editors



X. San Liang received his Ph.D. from Harvard University, MA, USA. He has worked at China's State Oceanic Administration, Harvard University, New York University/Courant Institute, Massachusetts Institute of Technology, Central University of Finance and Economics/China Institute for Advanced Study, etc., and was a team leader of the Ninth Chinese National Antarctic Research Expedition. Presently he is Jiangsu Chair Professor at Nanjing Institute of Meteorology, China. He is interested in a variety of fields such as, not exclusively, atmosphere-ocean-climate science, nonlinear dynamical systems, turbulence, hydrodynamic stability, multiscale modeling, predictability, information flow, uncertainty estimation, causality analysis, etc. His contributions include those in multiscale interaction analysis, and causal inference in time series and dynamic events, the latter being a fundamental problem of scientific research.



Dr. Yuanzhi Zhang is a Research Fellow and Professor of urban remote sensing and coastal zone environments at the Chinese University of Hong Kong and Nanjing University of Information Science and Technology in China. Dr. Zhang received Doctor of Science degree in Technology from Helsinki University of Technology (now Aalto University) in Finland. Dr. Zhang is the author and co-author of more than 100 peer-reviewed journal articles and 10 books or book chapters. He received the First-Rank Award of the Guangdong Provincial Prize of Science and Technology, China, in 2013 and the Second-Rank Award, ARCA (Actions for Raising Critical Awareness) Prize at the International Symposium "Environment 2010: Situation and Perspectives for the European Union", Porto, Portugal, in 2003.

Contents

Preface XIII

Section 1 Ocean Upwelling 1

Chapter 1 **Coastal Upwelling Off the China Coasts 3**
Jianyu Hu, X. San Liang and Hongyang Lin

Chapter 2 **The Yellow Sea Surface Cold Patches in Warm Seasons 27**
X. San Liang, Minghai Huang, Hui Wu and Yihe Wang

Section 2 Estuarine Processes 47

Chapter 3 **Saltwater Intrusion in the Changjiang Estuary 49**
Jianrong Zhu, Hui Wu, Lu Li and Cheng Qiu

Chapter 4 **Dynamics of the Changjiang River Plume 75**
Hui Wu, Tianning Wu, Jian Shen and Jianrong Zhu

Section 3 Coastal Pollution 101

Chapter 5 **Marine Ecological Disasters and Their Physical Controlling Mechanisms in Jiangsu Coastal Area 103**
Min Bao, Weibing Guan, Zhenyi Cao, Qi Chen and Yun Yang

Chapter 6 **Nuclear Pollution in the East China Sea from the Fukushima Disaster 123**
X. San Liang and Yineng Rong

- Section 4 Climate Change and Impact (Sea Level Rise) 141**
- Chapter 7 **Long-Term Sea Level Variability in the Yellow Sea and East China Sea 143**
Ying Xu, Mingsen Lin and Quanan Zheng
- Chapter 8 **The Slow Coastal-Trapped Waves off Subei Bank in the Yellow Sea and Their Climatic Change in the Past Decades 159**
X. San Liang
- Section 5 Meteorology and Atmospheric Physics (Precipitation, Soil Moisture, Typhoon) 179**
- Chapter 9 **Analysis for Soil Moisture in Jiangsu Province, China, Using GLDAS Data 181**
Jingze Cai, Yuanzhi Zhang, Yu Li, Tingchen Jiang, X. San Liang, Xia Lu and Jin Yeu Tsou
- Chapter 10 **Analysis for the Effect of Sea Surface Temperature (SST) on the Coastal Environments of Jiangsu Province, China 193**
Chenxu Ji, Yuanzhi Zhang, Kapo Wong, Yu Li, Tingchen Jiang, Xiangsan Liang and Xia Lu
- Chapter 11 **The Cyclogenesis and Decay of Typhoon Damrey 203**
X. San Liang and Lan Wang
- Section 6 Urbanization and Its Impacts 227**
- Chapter 12 **Analysis of Urban Impervious Surface in Coastal Cities: A Case Study in Lianyungang, China 229**
Tingchen Jiang, Yuxi Liu, Kapo Wong, Yuanzhi Zhang, Yu Li and X. San Liang
- Chapter 13 **Evaluating Urban Heat Island Effects in Rapidly Developing Coastal Cities 241**
Siqiang Wang, Meng Xiang, Yanan He, JinYeu Tsou, Yuanzhi Zhang, X. San Liang and Xia Lu
- Section 7 Methodology Development 257**
- Chapter 14 **Evaluation of Ocean Forecasting in the East China Sea 259**
Xiaochun Wang, Yingjun Zou and Xianqiang He

Chapter 15	Validation and Application of SMAP SSS Observation in Chinese Coastal Seas 273
	Qiong Wu, Xiaochun Wang, Xianqiang He and Wenhao Liang

Preface

Home to a large proportion of the world's population, coastal regions and their deteriorating environments are of great concern. The reason for this deterioration is complex. Naturally involved processes may include physical, chemical, biological, and geological factors, on scales ranging from microscopic to global (e.g., sea level rise). Compounding the problem is human activity, which exerts its effect on the environment both directly and indirectly, resulting in polluted coastal waters and economic loss (such as the damaged fishing industry). This book provides a selected collection of scholarly papers in interdisciplinary fields related to coastal environmental change, coastal disasters, and coastal infrastructure due to global warming, with a focus on the coasts of the rapidly developing country China, where the coastal environmental problem is particularly acute.

Coastal problems are notoriously interdisciplinary. What makes this book distinctly different from others is that it intends to bring together disciplines such as oceanography, ecology, geography, meteorology, climate science, etc., and make a comprehensive account of the interdisciplinary subjects. With contributions from over 30 authors, the book focuses on the following diverse fields: coastal upwelling, estuarine processes, coastal pollution, sea level rise and other climate change phenomena, meteorological and atmospheric problems, urbanization and its impacts, and coastal infrastructure, from theoretical study and phenomenological description, to methodological development. The following is a brief description of the contents:

- Almost all the major fishing grounds in the world's oceans are related to upwelling, an important mechanism that brings upward cooler and nutrient-rich water, resulting in high primary productivity and hence fishery production. The first two chapters are dedicated to the study of upwelling along China's coasts. Their generating mechanisms and possible responses to global warming are discussed.
- Chapters 3 and 4 deal with processes found in a typical estuary, the Changjiang/Yangtze estuary. Presented are the dynamics of the Changjiang River plume and the mechanism of salt water intrusion. Particularly, in Chapter 3, salt water intrusion variations resulting from two huge projects in China, namely, the "Three Gorges Dam" and "South to North Water Diversion" projects, and their impacts on the major international city, Shanghai, are examined.
- In coastal research, ecological disaster is of particular concern. One of the blooming phenomena is red tide, in which certain phytoplankton, protozoa, or bacteria are explosively proliferating or are highly aggregated and cause discoloration of the water. Chapter 5 is dedicated to this topic. Today, another form of pollution, nuclear pollution, has been of increasing concern, after the disastrous Fukushima nuclear leak on March 11, 2011. The impact of this accident on the East China coast is discussed in Chapter 6.
- In the following chapter, sea level rise in the Yellow Sea and East China Sea is examined; it is found that the rising rate is slower than the globally averaged rate, implying the idiosyncrasy of two marginal seas in a changing globe. But it seems that the slow wave modes are connected with the strongest interannual global signal, i.e., the El Niño-Southern Oscillation (Chapter 8). Also presented in this chapter is a self-contained introduction to

coastal-trapped waves, a class of subinertial signals that play a pivotal role in coastal air/sea interactions but are essentially missing in the heated debate on coastal problems.

- Meteorological resource and disaster is another issue in coastal research. In Chapters 9 and 10, the relation of precipitation to soil moisture and sea surface temperature is studied. It should be noted that the former is a well-known unresolved problem; in Chapter 9 some observations are presented, with the environment in Jiangsu, China, as an example. Chapter 11 examines the cyclogenesis of a tropical storm; a continuing challenge in dynamic meteorology.
- Urbanization is a hot topic in a fast developing country like China. This is of particular concern in coastal regions, with the ever-growing population. In Chapter 12, urbanization is studied by analyzing urban impervious surfaces. Theories and methods are first introduced, and applications are presented with Lianyungang, Jiangsu, as an example. An extensively studied problem in urbanization is the urban heat island effect; Chapter 13 shows a case study using satellite observations.
- In response to the growing needs of coastal research, methodological development is important. Chapter 14 introduces a method of evaluating the accuracy of ocean forecasts. Application to East China Sea forecasting could contribute to the design and implementation of the next generation of Chinese ocean forecasting systems. In Chapter 15, for the first time, sea surface salinity (SSS) observations from the Soil Moisture Active Passive mission are used to investigate seasonal variability of SSS along China's coasts.

Given the wide diversity of topics, this book is expected to provide a relatively comprehensive reference to coastal researchers, graduate students, as well as policymakers and coastal resource managers.

As the editors we would like to express our sincere appreciation to all the authors for their valuable contributions. During the submissions, Yang Yang and Qing Lu handled all the communications. They, together with Ying Wang and Yunlong Shi, edited the manuscripts to meet the guidelines before submission. We feel deeply thankful to them. Special thanks are due to the managing editor, Ms. Viktorija Zgela, and the technical staff; without their hard work, we could not have been successful. This monograph is supported by the Provincial Government of Jiangsu, China, through the 2015 Innovation Program for Research and Entrepreneurship Teams.

X. San Liang

School of Marine Sciences
Nanjing University of Information Science and Technology
Nanjing, China

School of Atmospheric Sciences
Nanjing University of Information Science and Technology
Nanjing, China

Yuanzhi Zhang

School of Marine Sciences
Nanjing University of Information Science and Technology
Nanjing, China

Ocean Upwelling

Coastal Upwelling Off the China Coasts

Jianyu Hu, X. San Liang and Hongyang Lin

Additional information is available at the end of the chapter

<http://dx.doi.org/10.5772/intechopen.80738>

Abstract

Upwelling is an important oceanographic phenomenon that brings cooler and nutrient-rich water upward to the surface, facilitating the growth of phytoplankton and other primary producers, which results in high levels of primary productivity and hence fishery production. This chapter presents a review of recent studies on six major upwelling regions along the China coasts, with a focus on the eastern and southeastern coasts of mainland China, based on in situ measurements, satellite observations and numerical simulations. These upwelling regions result primarily from the summer monsoon winds, though other mechanisms, such as river discharge, baroclinicity, topography, tides, and the presence of mean current, may also be in play. In this review, their impacts on local biogeochemical processes are briefly summarized. Also discussed are their possible responses to the globally changing climate.

Keywords: coastal upwelling, off the China coasts, characteristics, mechanism, impact

1. Introduction

Upwelling is an important oceanographic phenomenon that refers to an upward movement of seawater, with a typical speed of order 10^{-6} – 10^{-4} m/s. Accompanied by the upwelling process, the subsurface/deep cooler, and normally nutrient-rich, water rises toward the ocean surface, leading to a background with high biological productivity that is beneficial for the growth of phytoplankton and other primary producers. Therefore, good fishing grounds are commonly found in the vicinity of upwelling regions. From the dynamical point of view, major mechanisms for the generation of the coastal upwelling include the alongshore wind and wind stress curl, although other factors (e.g., tides, topography, and river discharge) also play considerable roles depending on the regions under investigation [1].

The coastal upwelling of cold and nutrient-rich waters off the China coasts is significant not only for the regional fishing industry, but also for the global carbon cycle and thus for the Earth's climate. Therefore, the coastal upwelling becomes a research hotspot of coastal oceanography in China, which has attracted great attention for recent decades. For example, Miao and Hu [2] analyzed the characteristics of wind-driven coastal upwelling off the southeastern China coast using coastal upwelling index (CUI) data, which are calculated online the Pacific Fisheries Environmental Laboratory (PFEL) website (http://www.pfel.noaa.gov/products/las/docs/global_upwell.html) using the method of Bakun [3]. It is indicated that there exist wind-driven coastal upwelling regions in summer off the eastern Hainan Island and the Leizhou Peninsula, and along the coast from Shantou to Zhejiang (**Figure 1**). The wind-driven coastal upwelling off the eastern Hainan Island is stronger than that in other regions, and the upwelling is stronger from June to August compared to other months. Wind-driven coastal upwelling off Zhejiang appears earlier than that off the eastern Hainan Island. The wind-driven coastal upwelling experiences different variation periods along the central and southern Fujian coast, Guangdong coast, eastern Hainan Island coast, northern Fujian coast and Zhejiang coast.

Hu and Wang [1] reviewed the progress of upwelling studies in the China seas since 2000 and summarized 12 major upwelling regions in the China seas, including the South China Sea (SCS), the Taiwan Strait (TWS), the East China Sea (ECS), the Yellow Sea, and the Bohai Sea (**Figure 2**). Half of these upwelling regions are located along the southeastern coast of mainland China, that is, the upwelling off the Yangtze River Estuary, the upwelling along Zhejiang coast, the upwelling regions along the northwestern and southwestern coasts of Taiwan Strait, the upwelling along the eastern Guangdong coast, and the upwelling around

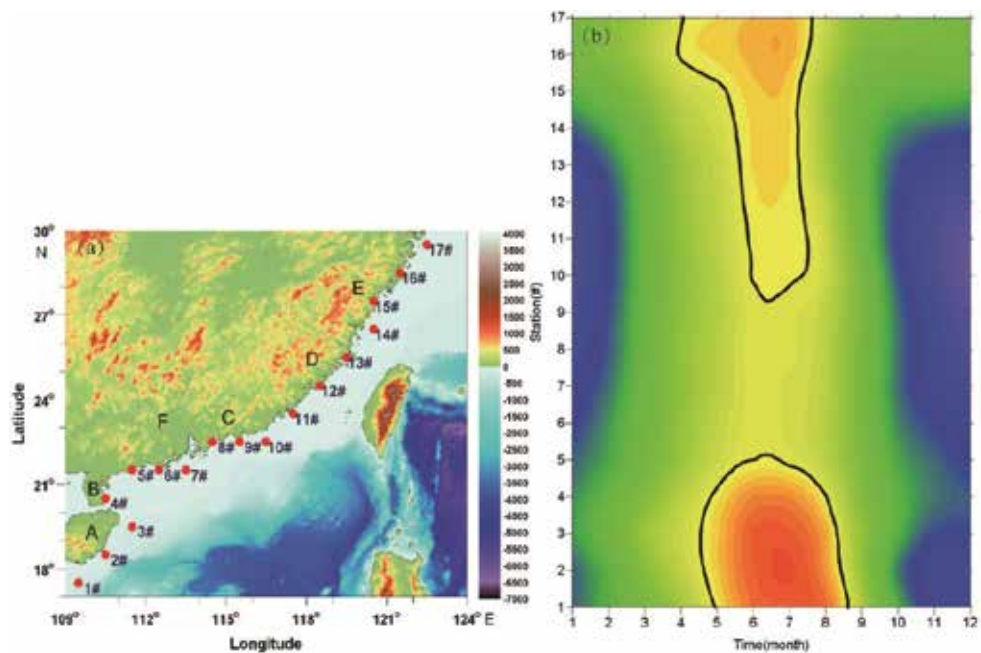


Figure 1. Monthly mean coastal upwelling index (b) off the southeastern China coast (the station locations for calculating the coastal upwelling index are shown in panel (a)). Redrawn from Miao and Hu [2].

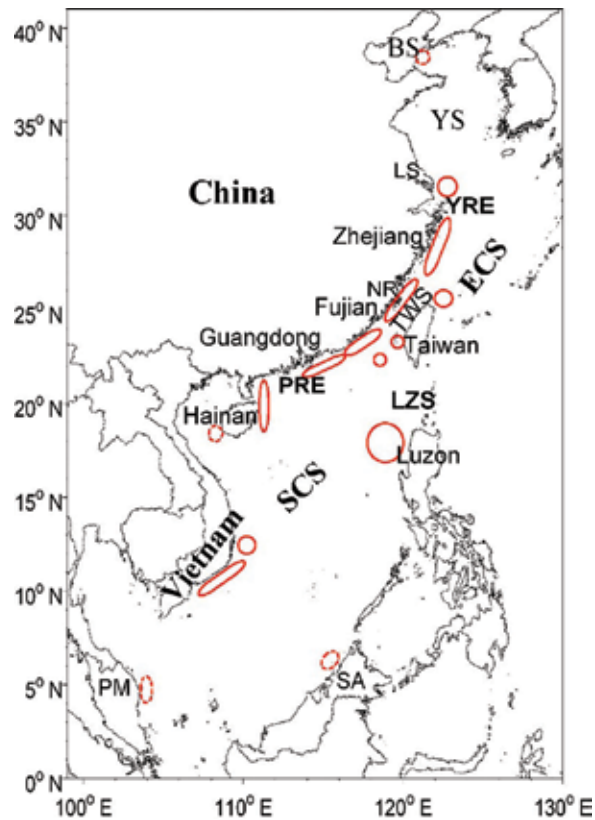


Figure 2. Map of major upwelling regions in the China seas, including the South China Sea (SCS), the Taiwan Strait (TWS), the East China Sea (ECS), the Yellow Sea (YS), and the Bohai Sea (BS). In this figure, the Yangtze River Estuary and the Pearl River Estuary are indicated by YRE and PRE, respectively. PM stands for the Peninsular Malaysia; LZS for Luzon Strait; and LS, NR, and SA for Lüsi, Nanri, and Sabah, respectively. The red ellipses or circles schematically mark locations of the major upwelling regions in the China seas. The ellipses or circles in dashed lines are upwelling regions that are sometimes mentioned. Cited from Hu and Wang [1].

the eastern Hainan Island. It is concluded that these coastal upwellings are principally wind-driven, and are hence strongly related to the seasonal variability of monsoon winds.

In this chapter, we describe six major coastal upwelling regions off the southeastern coast of mainland China and discuss the influence factors for these coastal upwelling regions.

2. Major characteristics of coastal upwelling off the southeastern coast of mainland China

2.1. Upwelling in the northern continental shelf of the South China Sea

Published about 15 years ago, Wu and Li [4] and Li et al. [5] overviewed studies of upwelling in the SCS over four decades among 1964–2003, focusing primarily on the spatiotemporal variability of upwelling in the continental shelf of the northern SCS. They pointed out that

in summer upwelling occurs over almost the entire continental shelf of the northern SCS. **Figure 3** presents the locations of some upwelling regions, investigated by several representative studies [6–10]. Most of these upwellings have been demonstrated to be induced by the prevailing southwesterly monsoon. Since then, much progress on the coastal upwelling study has been intensively made in the northern SCS using cruise observations, satellite observations, and numerical modelling.

2.1.1. Cruise observations

Over the past two decades, a number of hydrography-oriented cruises have been conducted in the continental shelf of the northern SCS. These data further evidenced the upwelling and its variability. Using underway measurements of sea surface temperature and salinity collected during July–August 2000, Zhuang et al. [11] observed an evident upwelling-related, low-temperature, and high-salinity area along the coast between Dongshan and Huilai (see locations in **Figure 2** or **3**). Based on the hydrological data from a cruise during July–August 2002, Xu et al. [12] analyzed the upwelled cold water along the eastern coast of Guangdong, and found that cold cores were distributed near the Daya Bay and the Huilai coast. Upwellings off the Pearl River (also called the Zhujiang River) Estuary were examined during different monsoon periods in July 2000 by Zeng et al. [13], and in May 2001 and November 2002 by Zhu et al. [14], respectively. Zhang et al. [15] investigated hydrological (including upwelling) characteristics off the Pearl River Estuary using data from two cruises in summer and winter 2006. Cai et al. [16] and Wan et al. [17] analyzed the characteristics of upwelling in the eastern Guangdong and southern Fujian coastal waters using the comprehensive cruise data; their results illustrated the coastal upwelling between Shantou and Dongshan undergoing an alternating strong-weak-strong stage during July–August 2006. Based on the conductivity-temperature-depth (CTD) data from the summer cruises of 2001,

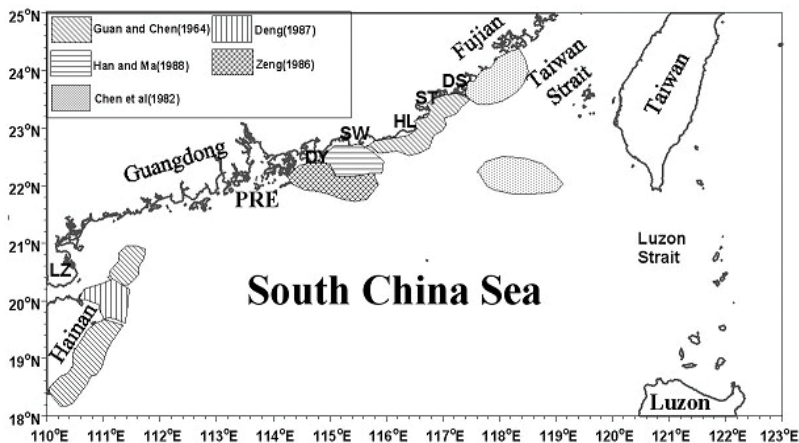


Figure 3. Reported upwelling regions in the continental shelf of the northern SCS. Redrawn from Wu and Li [4]. It summarizes the research included in [6–10]. PRE stands for the Pearl River Estuary; LZ for the Leizhou Peninsula; DS, ST, HL, SW, and DY for Dongshan, Shantou, Huilai, Shanwei, and the Daya Bay, respectively.

2002, 2006, and 2009, Xu et al. [18] revealed the interannual variation in the spatial structure and intensity of upwelling in the eastern Guangdong and southern Fujian coastal seas. The abovementioned cruise data confirmed that the summertime coastal upwelling is conspicuous along the coasts of eastern Guangdong and southern Fujian, with the former occurring earlier and stronger than the latter.

2.1.2. Satellite observations

Using satellite remote sensing data, combined with shipboard measurements conducted in July 2000, Zhuang et al. [19] analyzed upwelling phenomena off the Fujian and Guangdong coasts. Qiao and Lü [20] applied satellite sea surface temperature (SST) and chlorophyll-a (Chl-a) data from different sources to summarize some basic characteristics of the coastal upwelling in the SCS. Applying the Quick Scatterometer (QuikSCAT) wind data, Wang et al. [21] examined relative roles of Ekman transport and Ekman pumping in driving summer upwelling. These results indicated that the coastal upwelling often occurs in the coastal area around the eastern Hainan Island and in the waters along eastern Guangdong and southern Fujian coasts in summer, which may be resulted from multiple dynamic factors such as wind forcing, tidal mixing, and the interactions between local circulation and topography. However, the coastal upwelling in the eastern Guangdong is primarily driven by Ekman transport.

2.1.3. Numerical modelling

Several numerical models have been applied to study the upwelling and its mechanism in the northern SCS since 2000. For example, Chai et al. [22] simulated several upwelling regions in the SCS using the Princeton Ocean Model (POM), and explained their mechanisms. Jing et al. [23, 24] studied the summer upwelling system in the northern continental shelf of the SCS using a three-dimensional (3D) baroclinic nonlinear model. Zhang and Jiang [25] studied the mechanism of cross-shelf transport of the cold bottom water (upwelling water) on the coastal shelf off Shanwei using the Regional Ocean Modeling System (ROMS). These model results showed that the summertime upwelling is a common phenomenon during June–September east of the Hainan Island and the Leizhou Peninsula, and in the coastal areas from Shantou to Nanri. Both southwesterly wind and wind stress curl are responsible for generating the coastal upwelling east of Hainan, while the wind-driven cross-shelf Ekman transport is a significant dynamic factor to the coastal upwelling off the eastern Guangdong and southern Fujian coasts.

2.1.4. Intensive studies

The upwelling off the eastern coast of Hainan Island is strong in summer, which has attracted a lot of intensive studies for recent years [26]. Specifically, Chai et al. [27] simulated the upwelling using the POM; Su and Pohlmann [28] applied a 3D high-resolution model to study the upwelling mechanism; Li et al. [29] investigated the spatial structure and variation of the summertime upwelling in the waters east and northeast of Hainan Island during 2000–2007 by using a nested high-resolution POM forced by QuikSCAT winds; Wang et al. [21] estimated

the mean Ekman transport and Ekman pumping in the coastal waters east and southeast of the Hainan Island; Lin et al. [30, 31] compared the upwelling patterns in the eastern and northeastern Hainan Island using a combination of cruise observations, reanalysis data and satellite data, and studied the mechanism for the upwelling off the northeastern coast of Hainan Island with a numerical model. These results suggested that the coastal upwelling off the eastern coast of Hainan Island usually exists from April to September, with the strongest intensity in summer; the upwelling is mainly induced by summer monsoon wind. By contrast, Jing et al. [24] proposed that the Ekman pumping associated with the local wind stress curl is a key factor modulating the generation of the coastal upwelling off eastern Hainan Island and eastern Leizhou Peninsula. Based on the cruise data in summer 2006, together with the QuikSCAT winds, Xu et al. [32] pointed out that the coastal upwelling regions are merged below 10 m layer in the waters off eastern Hainan and western Guangdong, and that the coastal upwelling off eastern Hainan Island is intermittent and modulated by the alongshore wind while that off the western Guangdong is mainly induced by the wind stress curl.

On upwelling variability, Liu et al. [33] studied the variability of summer coastal upwelling in the northern SCS during the last 100 years. Jing et al. [34] identified that the coastal upwelling in the northern SCS was closely linked to the modulation of El Niño events; they found that during the summer of 1998 (a La Niño year), the coastal upwelling was greatly strengthened associated with an abnormally intensive alongshore wind stress blowing over the region. Su et al. [35] studied the variation of coastal upwelling off the eastern Hainan coast over 50 years of 1960–2006 using an “SST upwelling index”. By using an SST record (AD 1876–1996) derived from coral *Porites* Sr/Ca, Liu et al. [36] revealed that upwelling in the northern SCS underwent a distinct multidecadal variability, which was proved to be caused by the Asian summer monsoon with an abrupt shift in 1930 from a relatively warm to cold condition, and then back to the warm condition after 1960. These results showed a general intensifying of coastal upwelling off eastern Hainan Island subject to prominent interannual and decadal variations; the intensifying trend was also consistent with the global warming in the twentieth century.

2.2. Coastal upwelling in the Taiwan Strait and its adjacent sea areas

Xiao et al. [37] and Hu et al. [38] collected many papers and comprehensively reviewed the upwelling studies in the TWS mostly before 2000, and also proposed suggestions for upcoming investigators. The reviews showed that the main coastal upwelling regions (**Figure 4**) in the western TWS are located near Dongshan and Pingtan. Over the past two decades, some progress has been made in studying the TWS upwelling, especially on its variability, mechanism and responses to the El Niño-Southern Oscillation (ENSO), and local environmental variation.

2.2.1. Variability of the coastal upwelling in the western TWS

Strong coastal upwelling usually appears in the western TWS during the summer southwesterly monsoon period, which has been confirmed by a number of hydrological and satellite

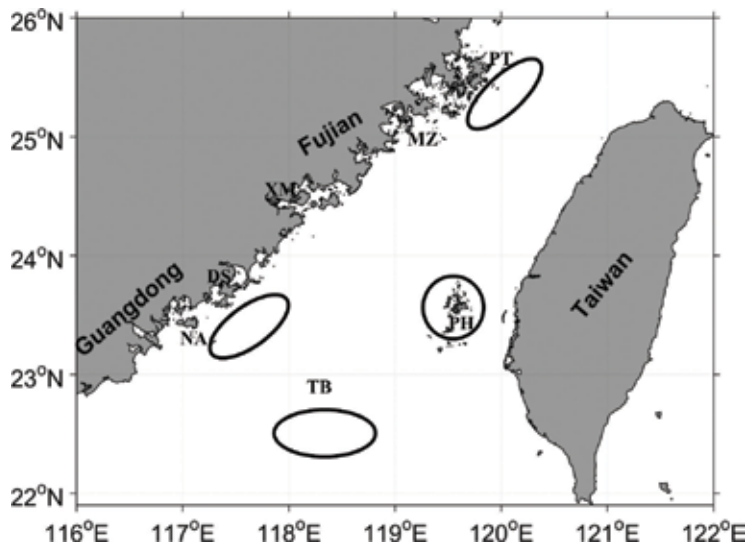


Figure 4. Schematic map of main upwelling regions in the TWS. Redrawn from Hu et al. [38]. DS: Dongshan; MZ: the Meizhou Island; NA: Nan-ao; PH: the Penghu Islands; PT: Pingtan; TB: the Taiwan Bank; XM: Xiamen. Four ellipses and circle schematically indicate the locations of four upwelling regions.

observations in the last decades (e.g., [39–45]). These studies showed that the intensity of coastal upwelling is affected by many factors, such as the northward or northeastward current, southwesterly monsoon, and bottom topography. Recently, more attention has been paid to the variability of the coastal upwelling in the western TWS. Three examples are given next.

Hong et al. [46] studied the interannual variability of summer coastal upwelling in the TWS using a long time series of SST data from 1985 to 2005. It is shown that in some years, the coastal waters near Pingtan or Dongshan had clear upwelling signatures at the sea surface with a negative temperature anomaly and positive salinity anomaly. The alongshore wind stress was demonstrated to be responsible for such interannual variations.

Hu et al. [47] studied the variable hydrographical structure in the southwestern TWS using measurements from four summer cruises in 2004–2007, and revealed that the coastal upwelling near Dongshan occurred with different scales, locations, and intensities. Evident coastal upwelling was seen in the southwestern TWS during each July of 2005 and 2007, and was largely associated with local wind condition as confirmed by numerical modeling results.

Zhang et al. [48] investigated the evolution of a coastal upwelling event in the southern TWS using intensive cruise data and satellite data in summer 2004; the upwelling-related surface cold water was observed near Dongshan in early July, which then reduced its size by half with a decreased Chl-a concentration after half a month, and eventually vanished by the end of July.

2.2.2. TWS upwelling and its responses to ENSO and local environmental variation

As reviewed by Hong and Wang [49], Shang et al. [50], and Hong et al. [51], the TWS upwelling exhibits clear connections to the ENSO, global climate change, and local environmental variation.

Hu et al. [52] showed that two upwelling-related low temperature (high salinity) regions in the western TWS have clear interannual and intermonthly variability in summer. Combining SST and Chl-a data, Shang et al. [53–55] proposed that the ENSO events can potentially have significant impacts on the upwelling in the TWS. Tang et al. [56] revealed interannual variation of two upwelling zones (one near Dongshan) in the southern TWS. These studies indicated that the coastal upwelling in the western TWS has evident connections to the ENSO events. The local wind is much weaker in the TWS during the 1997 El Niño year than that during the 1998 La Niña year [57], suggesting that the ENSO event can affect the wind pattern over the TWS and thus modulate the surface ocean currents, SST, and coastal upwelling in an interannual scale. Hong et al. [46] further revealed that, for the entire western TWS, the summer coastal upwelling was strong in 1987, 1993, and 1998 (**Figure 5**), during which periods three peaks of the SST Empirical Orthogonal Function Mode 1 (EOF_1) time series matched well, with a time lag of 3 months, with those of the multivariate ENSO index (MEI).

By comparing remote sensing SST with in situ chemical and biological data collected since 1985, Hong et al. [58] obtained evidence of upwelling variation in response to interannual environmental variability in the TWS. According to these observations, the coastal upwelling was weakened in summer of 1997, resulting in an apparent anomaly in nutrient distribution, phytoplankton and zooplankton abundances, and community structure. Hong et al. [51] further summarized the hydrographical features with an emphasis on upwelling, which is the key driver of biogeochemical processes and ecosystem dynamics in the TWS. Hydrographic and satellite data revealed evident teleconnections between the TWS upwelling and the ENSO variability. Besides, Wang et al. [59] estimated the physical (i.e., coastal upwelling) and biological

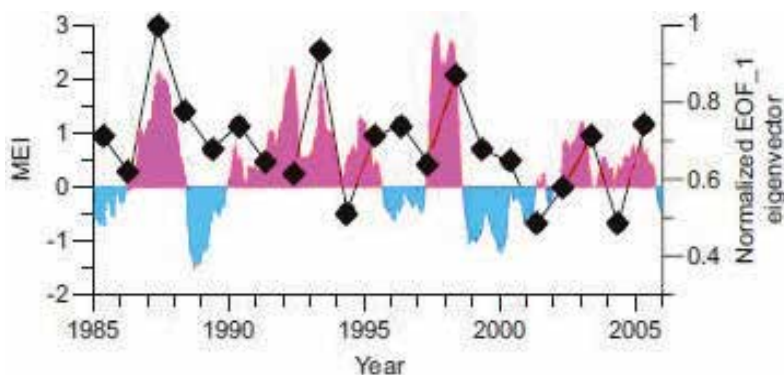


Figure 5. Variation of the eigenvector of SST EOF Mode 1 (EOF_1) in the TWS (black dots) and monthly multivariate ENSO index (MEI; shaded areas) 3 months ahead of the SST EOF_1 eigenvector during 1985–2005. The SST EOF_1 eigenvector is normalized by its maximum for the period 1985–2005. Redrawn from Hong et al. [46].

effects on the nutrient transport in the TWS during summer through a coupled physical-biological numerical ocean model. These studies concluded that the TWS upwelling has a profound impact on biogeochemical processes, biological productivity, and ecosystem structure.

2.2.3. Further understanding of mechanism for the coastal upwelling in the TWS

Several numerical models, such as a 3D nonlinear baroclinic shallow water model [60–62], the Coupled Hydrodynamical-Ecological Model for Regional and Shelf Seas (COHERENS; [63]) model [64], and a 3D nonlinear Estuarine, Coastal and Ocean Modeling System with Sediment (ECOMSED) model [65], have been used to study the mechanism of upwelling along the coasts of Fujian and Zhejiang in summer and winter. These numerical modeling results indicated that the wind stress, the Taiwan Warm Current, tidal nonlinear effect, and bottom topography are the main mechanisms for the upwelling in the coastal waters of Fujian and Zhejiang in both winter and summer. Specifically, the southwesterly or southerly wind induces the coastal upwelling in summer.

Furthermore, Jiang et al. [66] investigated the mechanisms of coastal upwelling in the southern TWS using a nested circulation model based on the POM. It is indicated that the upslope current over a distinctly widened shelf transports the cold water toward the shore in the lower layer, while the southwesterly monsoon wind drives the cold water away from the shore in the surface layer, thus generating the upwelling along the southwestern coast of the TWS.

2.3. Coastal upwelling in the East China Sea

The studies of coastal upwelling in the ECS have been conducted using hydrographic measurements, satellite observations, and numerical modelling. For recent decades, much progress of the upwelling study has been made particularly in the quick developments of numerical modelling technology and remote sensing approach.

2.3.1. Hydrographic measurements

Zhao et al. [67] reported an upwelling north of the Yangtze River (or the Changjiang River) Estuary, covering an area of roughly 1° by 1° centered at ($31^\circ 30'N$, $122^\circ 40'E$). Several cruise measurements, such as the China-Korea joint investigation in the Yellow Sea and its adjacent sea area [68] and the marine flux investigation in the ECS in July 1998 [69], confirmed the existence of this upwelling in the Yangtze River Estuary. Zhu et al. [70] analyzed the hydrological characteristics in the outer Yangtze River Estuary and showed that the upwelling usually occurs near the first turning point of the Yangtze River Diluted Water. Zhu et al. [71] conducted comprehensive observations in August 2000 and indicated that the coastal upwelling appears along the Zhejiang coast, in the west of the submarine river valley and along the Lüsü coast. Lü et al. [72] presented signals of low-temperature and high-salinity upwelling water in the Yangtze River Estuary using three sections of temperature and salinity distributions (**Figure 6**) obtained from a cruise in August 2000. There is evidence that in the Yangtze River Estuary the subsurface high-salinity water can rise toward the 5–10 m layer from beneath.

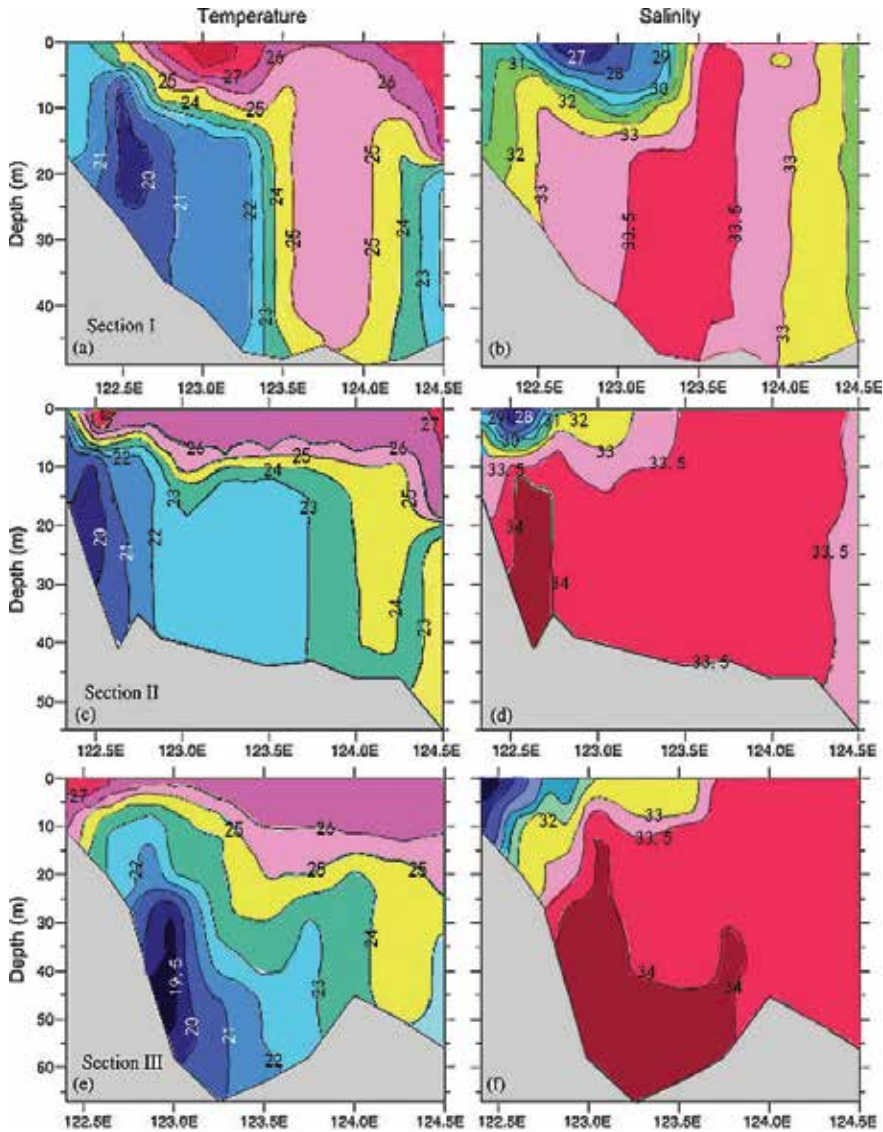


Figure 6. Vertical distributions of temperature ($^{\circ}\text{C}$; left panels) and salinity (right panels) along Section 32.0°N (top), Section 31.5°N (middle), and Section 31.0°N in the Yangtze River Estuary. Redrawn from Lü et al. [72].

2.3.2. Satellite observations

Hu and Zhao [73] studied the long-term variation of coastal upwelling off northeastern Zhejiang in summer using SST (1987–2005), Chl-a (2002–2006), and wind (1992–2006) datasets; their results showed that the upwelling, with high Chl-a concentration, has seasonal, annual, and interannual variations. Hu and Zhao [74] investigated the short-term variation of upwelling in the Zhejiang coastal areas during May–October 2004 and indicated that the upwelling has a close relation to the along-shore wind variation. Lou et al. [75] depicted the evolution of the upwelling along Zhejiang coast, which appears in June, peaks

Authors	Model	Features
Li and Zhao [78]	POM	Upwelling phenomena in the Yangtze River Estuary.
Zhao et al. [79]	POM	Upwelling mechanism in the Yangtze River Estuary.
Zhu [77]	3D numerical model	Baroclinic (barotropic) effect is the main factor for inducing upwelling in the north (south) of submarine river valley off the Yangtze River Estuary.
Bai and Wang [80]	POM	Upwelling occurs around 10 km away from the coastline in the Yangtze River Estuary.
Liu et al. [81]	3D baroclinic ocean model	Seasonal variation of the vertical circulation in the ECS.
Liu et al. [82]	3D baroclinic ocean model	Temperature and salinity features are associated with upwelling or downwelling.
Zhu et al. [83]	ECOM-si model (ECOM with semi implicit scheme)	Upwelling is mainly the baroclinic effect induced by mixing between the fresh water from the Yangtze River and the saline water offshore.
Qiao et al. [84]	MASNUM	Owing to a strong density gradient, the baroclinic pressure gradient force is large near the frontal zone, which elicits an upwelling branch along the topographic slope.
Lü et al. [72]	MASNUM	Upwelling is induced as a branch of the secondary circulation. Topography, Yangtze River discharge, and the Taiwan Warm Current all affect the upwelling.
Jing et al. [85]	ECOMSED model	Upwelling occurs along the coasts of Zhejiang and Fujian throughout the year, which is strong in summer and relatively weak in winter.
Lü et al. [86]	MASNUM	Tides (barotropic and baroclinic processes) are key to the upwelling off the Yangtze River Estuary.
Bai et al. [87]	ECOMSED model	Upwelling is mainly induced by the Ekman effect and affected by the Taiwan Warm Current and continental slope rising.
Yang et al. [88]	ROMS	A branch current bifurcates from the subsurface of the Kuroshio northeast of Taiwan, upwells northwestward, then turns to northeast around (27.5°N, 122°E), and finally reaches 31°N off the Yangtze River mouth.
Cao et al. [76]	ROMS	Wind primarily influences the short-term evolution of upwelling, while the topographic variation determines the upwelling center off the Yangtze River Estuary.
Liu and Gan [89]	3D high-resolution numerical model	Intensified upwelling is formed by a strengthened shoreward transport downstream of the promontory coastline.
Yang et al. [90]	ROMS coupled with phosphate model	The transported phosphate-rich water is further upwelled to the surface due to the upwelling just off the Zhejiang coast.

Note: MASNUM is a model established by the Laboratory of MARine Sciences and NUMerical Modeling, the State Oceanic Administration, China.

Table 1. Numerical models used in studying the upwelling in the ECS.

in July and August, and then diminishes until disappears in late September. The mean SST in the upwelling region is about 25-28°C in summer, with a temperature difference of approximately 2-4°C from the ambient nonupwelling waters. Cao et al. [76] investigated the

summertime upwelling off the Yangtze River Estuary using satellite data and proposed that along-shore wind stress and wind stress curl play similar important roles on the upwelling evolution.

2.3.3. Numerical modeling

Numerical models have been developed or applied for studying the characteristics of coastal upwelling and its dynamics in the ECS (**Table 1**). These simulations suggested that the coastal upwelling usually appears off the Yangtze River Estuary and along the Zhejiang coast, mostly in summer. The continental slope, wind speed, and the angle between the wind direction and the coastline control the coastal upwelling intensity. Topography, Yangtze River discharge, the Taiwan Warm Current, and the branch current bifurcating from the subsurface of the Kuroshio all affect the upwelling. In addition, baroclinic (barotropic) effect is the main factor for inducing upwelling in the north (south) of submarine river valley off the Yangtze River Estuary [77]. However, in the coastal waters near the Zhoushan Islands (located off the northeastern coast of Zhejiang), wind forcing may sometimes exert negative influences on the generation of coastal upwelling by weakening the intrusion of the Taiwan Warm Current onto the continental shelf [72].

3. Discussion

3.1. Influence of topography on upwelling

As mentioned above, the influence of topography on the generation and modulation of coastal upwelling has been observed in the ECS, TWS, and the northern SCS; so it is worthy of being separately discussed here as an important upwelling-related factor. A 3D modelling study by Gan et al. [91] revealed that the widened shelf off Shantou plays an important role in intensifying the local upwelling. The strongest advection occurs over the converging isobaths near Shanwei, i.e., the head of the widened shelf (**Figure 7**) where a negative pressure gradient also exists at the lee of the coastal cape over the inner shelf and locally amplifies shoreward motion. In addition, Chen [92] discussed the effects of cape and canyon on wind-driven coastal upwelling in the western TWS, suggesting that the positive vertical velocity is produced by changes in the relative vorticity downstream of the cape or canyon, which becomes a dominant upwelling mechanism there. Topography also exerts influences on upwelling by steering bottom currents upward. Upwelling can even be intensified by a strengthened shoreward transport downstream of a promontory coastline [89]. Recently, Wang et al. [93] investigated relative contributions of the local wind and topography to the coastal upwelling intensity in the northern SCS in the case when the upwelling-favorable wind retreats, using a high-resolution version of the POM. It is indicated that the topographically induced upwelling is comparable with the wind-driven upwelling at surface; while at bottom, topography has a stronger contribution than the local wind in controlling the upwelling intensity in the inner shelf of the northern SCS [93].

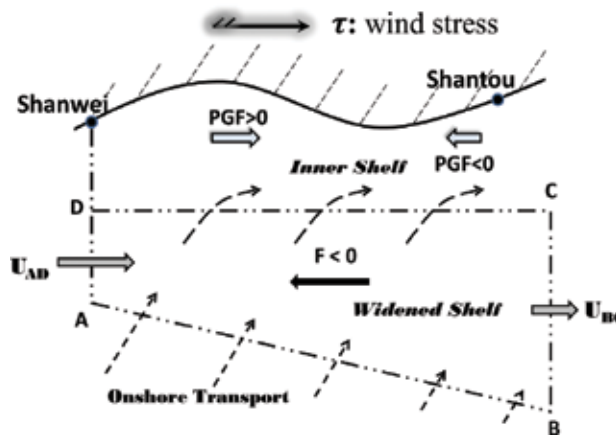


Figure 7. Schematic picture showing the wind-driven upwelling processes and forcing mechanism over the middle and inner shelves of a widened shelf. Redrawn from Gan et al. [91]. PGF denotes pressure gradient force; U_{AD} and U_{BC} are mean velocities normal to the two streamlines AD and BC, respectively. The line AD is at the head of the widened shelf (near Shanwei) and BC, downstream of it (near Shantou).

3.2. Influence of river on upwelling

For the upwelling near the Pearl River Estuary, the interaction between upwelling and river plume should be considered [94–96]. The enhanced stratification due to the presence of plume thins the surface frictional layer and strengthens the cross-shelf circulation in the upper water column. As a result, the surface Ekman current and the compensating flow beneath the plume are amplified, while the shoaling of the deeper dense water minimally changes in the upwelling region. The pressure gradient generated between the buoyant plume and the ambient sea water accelerates the wind-driven current along the inshore edge of the plume, but retards it along the offshore edge [95]. The buoyancy in the plume considerably modulates the alongshore and cross-shelf upwelling circulation in the upper water column [95], and that the upwelling initially occurs to the east of the Pearl River Estuary, intensifies eastward, and reaches its maximum near Shantou [96]. For the upwelling off the Yangtze River Estuary area, upwelling is associated with a strong salt-induced horizontal density gradient. The plume fronts separate the diluted and saline water, and this density structure elicits upwelling as a branch of the density-driven secondary circulation [72].

3.3. Influence of circulation on upwelling

The density (or salinity) front, which separates the inshore low-salinity coastal water from the offshore Taiwan Warm Current Water, is one of the primary inducing factors for the upwelling along the western coast of ECS. Using a numerical model, Yang et al. [88] revealed that the upwelling off the Zhejiang coast comes from the subsurface water of the Kuroshio northeast of Taiwan in summer (**Figure 8**). The phosphate-rich upwelling water off the coast of Zhejiang is mainly originated from the deep sea water in a special area (122.1°E–122.5°E, 130 m–300 m deep) northeast of Taiwan, as the nearshore Kuroshio branch current continuously transports the phosphate-rich deep sea water to the bottom area off the coast of Zhejiang [90].

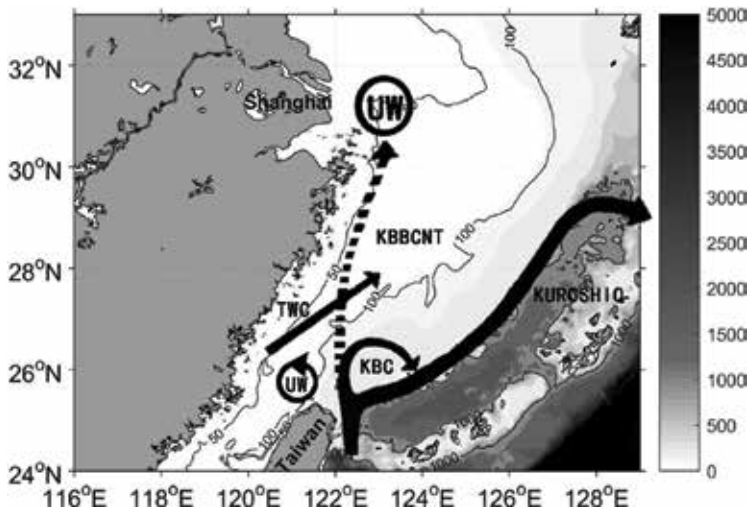


Figure 8. Summer ocean circulation pattern in the ECS. The solid thin lines represent the isobaths of 50, 100, and 1000 m. The bold dashed line represents the possible ocean current of the Kuroshio Bottom Branch Current to the northeast of Taiwan (KBBCNT). The bold solid lines show the Kuroshio, the Kuroshio Branch Current (KBC), and the Taiwan Warm Current (TWC), and UW denotes upwelling. Redrawn from Yang et al. [88].

As for the northern SCS, Wang et al. [97] investigated the subsurface upwelling signals off the coasts of Fujian and Guangdong provinces in summer 2000, using a combination of hydrographical, tide-gauge and mooring data, satellite observations, and numerical circulation model output. It is suggested that the subsurface upwelling is closely related to the coastal sea level fluctuation and is evidently modulated by both local wind-forcing and large-scale SCS circulation.

3.4. Influence of tide on upwelling

Lü et al. [98] studied the summertime upwelling off the western coast of Hainan Island using satellite SST data and numerical modeling. The presence of the tidal mixing front [99] was believed to play a profound role in stimulating the upwelling near the southwestern coast of Hainan Island. This upwelling was also evidenced by comprehensive cruise data collected in the summer of 2006 [100]. On the other hand, the southwesterly monsoon induces downwelling that competes with the front-induced upwelling off the western coast of Hainan Island.

In the TWS and the ECS, Hong et al. [101] also indicated that tidal mixing plays important roles in enhancing the upwelling in the TWS. In addition, tides contribute to the upwelling generation because tidal mixing facilitates the expansion of the Yangtze River Diluted Water, and strong tidal mixing results in considerable horizontal density gradient across a tidal front and thus induces upwelling [72, 86].

Internal tides may also affect the upwelling intensity [102, 103]. These studies used satellite multisensor data such as the moderate resolution imaging spectroradiometer (MODIS) SST, QuikSCAT ocean surface winds, and sea surface dynamic height, and suggested that

the interaction between upwelling and internal tides enhances the uplifting of lower-layer water; thus, the summertime upwelling pattern and intensity tend to be altered on the shelf off Guangdong.

4. Summary

There are six major coastal upwelling regions off the southeastern coast of mainland China, as shown in **Figure 2**. The main features of these coastal upwelling regions are summarized below.

In the northern SCS, coastal upwelling regions are distributed primarily off the eastern coast of Hainan Island and off the coasts of eastern Guangdong. The southwesterly monsoonal winds are the most prominent factor controlling the upwelling generation. Besides the along-shore wind stress, wind stress curl, distinct topographic features, frontal eddies, and local circulations are among the mechanisms for the coastal upwelling in the northern SCS.

In the TWS, two main coastal upwelling regions are identified, i.e., along the southwestern and northwestern coasts of the TWS. The former appears between Xiamen and Shantou, while the latter occurs from the east of Pingtan to Meizhou. Both upwellings are regarded as wind-driven, which occur during the southwesterly monsoon period with a relatively strong intensity in July. In addition, the bottom topography and the ascending of the northward current also affect the upwelling. With respect to the time-varying features, the coastal upwelling in the western TWS shows short-term variations caused by winds, and has evident responses to ENSO or local environmental variations.

In the ECS, coastal upwellings are observed in the Yangtze River Estuary and along the coast off Zhejiang. The alongshore wind, topography, tides, and local circulation are among the significant factors in determining the generation of coastal upwellings.

Upwelling in the coastal waters of China seas is complex, in terms of the spatial distribution, time-varying characteristics, generation mechanisms, and factors affecting its evolution and dynamics. It covers a wide range of temporal variability, including interannual and multidecadal timescales associated with the ENSO events and global climate change, as well as shorter timescales associated with fluctuations caused by winds or internal tides. Consequently, observations based solely on limited cruise measurements would not be able to provide in-depth knowledge of the upwelling dynamics or its associated biogeochemical processes. A number of dedicated offshore surveys covering all seasons have been conducted in the China seas over 2005–2011, aiming with a constant goal of collecting more hydrographic data as well as biogeochemical parameters. A much better understanding of the main characteristics and dynamics of upwelling in the China seas has been gained, based on these in situ measurements, multisources of satellite remote sensing data and outputs from global/regional ocean circulation models (some with biogeochemical modules) [104, 105]. Nevertheless, there are still certain issues related to coastal upwelling, which remain to be addressed in the near future, for example, the possible changes of upwelling under global climate change, the influences of submesoscale processes on the upper-ocean upwelling, etc.

Acknowledgements

This work is jointly supported by the National Basic Research Program of China (2015CB954004) and the National Natural Science Foundation of China (41776027, 41606009 and U1405233).

Author details

Jiayu Hu^{1*}, X. San Liang² and Hongyang Lin¹

*Address all correspondence to: hujy@xmu.edu.cn

1 State Key Laboratory of Marine Environmental Science, College of Ocean and Earth Sciences, Xiamen University, Xiamen, China

2 School of Marine Sciences, Nanjing University of Information Science and Technology, Nanjing, China

References

- [1] Hu JY, Wang XH. Progress on upwelling studies in the China seas. *Reviews of Geophysics*. 2016;**54**(3):653-673
- [2] Miao X, Hu JY. Analysis on characteristics of wind-driven coastal upwelling off the southeastern China coast using coastal upwelling index. *Marine Science Bulletin*. 2011; **30**(3):258-265 (in Chinese with English abstract)
- [3] Bakun A. Coastal upwelling indices, west coast of North America, 1946-71. U.S. Dept. of Commerce, NOAA Tech. Rep, 1973, NMFS SSRF-671
- [4] Wu RS, Li L. Summarization of study on upwelling system in the South China Sea. *Journal of Oceanography in Taiwan Strait*. 2003;**22**(2):269-276 (in Chinese with English abstract)
- [5] Li L et al. Upwelling in the South China Sea. In: Su JL, Yuan YL, editors. *Hydrography near the China Seas*. Beijing: China Ocean Press; 2005. p. 272-278 (in Chinese)
- [6] Guan BX, Chen SJ. The current systems in the near-sea area of China Seas. Qingdao: Technical Report, Institute of Oceanology, Chinese Academy of Sciences; 1964. 85pp (in Chinese)
- [7] Chen JQ et al. A study on upwelling in Minnan-Taiwan Shoal fishing ground. *Taiwan Strait*. 1982;**1**(2):5-13 (in Chinese with English abstract)
- [8] Zeng LM. A preliminary analysis of indicators of offshore upwelling off eastern Guangdong. *Tropic Oceanology*. 1986;**5**:68-73 (in Chinese with English abstract)
- [9] Deng S. Analysis on upwelling in the south of Qizhou Islands. Technical Report, South China Sea Branch of State Oceanic Administration; 1987 (in Chinese)

- [10] Han WY, Ma KM. A study of coastal upwelling off eastern Guangdong. *Acta Oceanologica Sinica*. 1988;**10**(1):52-59 (in Chinese with English abstract)
- [11] Zhuang W et al. An analysis on surface temperature and salinity from southern Taiwan Strait to Zhujiang River estuary during July-August, 2000. *Journal of Tropical Oceanography*. 2003;**22**(4):68-76 (in Chinese with English abstract)
- [12] Xu JD et al. Hydrology features in outer sea of eastern Guangdong in summer 2002. *Journal of Oceanography in Taiwan Strait*. 2003;**22**(2):218-228 (in Chinese with English abstract)
- [13] Zeng GN et al. Analysis of hydrologic section off Zhujiang River estuary in northern South China Sea during various southwest monsoon phases. *Journal of Tropical Oceanography*. 2005;**25**(3):10-17 (in Chinese with English abstract)
- [14] Zhu J et al. Analysis on sectional characteristics of temperature and salinity off the Zhujiang River estuary—during the cruises of May 2001 and November 2002. *Journal of Xiamen University (Natural Science)*. 2005;**44**(5):680-683 (in Chinese with English abstract)
- [15] Zhang Y et al. Analysis on hydrological characteristics off the Pearl River Estuary in summer and winter of 2006. *Journal of Tropical Oceanography*. 2011;**30**(1):20-28 (in Chinese with English abstract)
- [16] Cai SZ et al. Characteristics of upwelling in eastern Guangdong and southern Fujian coastal waters during 2006 summer. *Journal of Oceanography in Taiwan Strait*. 2011;**30**(4):489-497 (in Chinese with English abstract)
- [17] Wan XF et al. Seasonal variation features of the hydrodynamic environment in the western Taiwan Strait. *Journal of Applied Oceanography*. 2013;**32**(2):156-163 (in Chinese with English abstract)
- [18] Xu JD et al. Observational study on summertime upwelling in coastal seas between eastern Guangdong and southern Fujian. *Journal of Tropical Oceanography*. 2014;**33**(2):1-9 (in Chinese with English abstract)
- [19] Zhuang W et al. Coastal upwelling off eastern Fujian-Guangdong detected by remote sensing. *Chinese Journal of Atmospheric Sciences*. 2005;**29**(3):438-444 (in Chinese with English abstract)
- [20] Qiao FL, Lü XG. Coastal upwelling in the South China Sea. In: Liu AK, Ho CR, Liu CT, editors. *Satellite Remote Sensing of South China Sea*. Taiwan: Tingmao Publish Company; 2008. p. 135-158
- [21] Wang DK et al. Role of Ekman transport versus Ekman pumping in driving summer upwelling in the South China Sea. *Journal of Ocean University of China*. 2013;**12**(3):355-365
- [22] Chai F et al. Formation and distribution of upwelling and downwelling in the South China Sea. In: Xue HJ et al, editors. *Oceanography in China*, Vol. 13. Beijing: Ocean Press; 2001. p. 117-128 (in Chinese with English abstract)

- [23] Jing ZY et al. Numerical study on summer upwelling over northern continental shelf of South China Sea. *Journal of Tropical Oceanography*. 2008;**27**(3):1-8 (in Chinese with English abstract)
- [24] Jing ZY et al. Numerical study on the summer upwelling system in the northern continental shelf of the South China Sea. *Continental Shelf Research*. 2009;**29**(2):467-478
- [25] Zhang YY, Jiang YW. The mechanism of cold water cross-shelf transport in the continental shelf off Shanwei. *Journal of Xiamen University (Natural Science)*. 2012;**51**(4):746-752 (in Chinese with English abstract)
- [26] Xie LL et al. Overview of studies on Qiongdong upwelling. *Journal of Tropical Oceanography*. 2012;**31**(4):35-41 (in Chinese with English abstract)
- [27] Chai F et al. Upwelling east of Hainan Island. In : Hue HJ et al, editors. *Oceanography in China*. Vol. 13. Beijing: Ocean Press; 2001. p. 129-137 (in Chinese with English abstract)
- [28] Su J, Pohlmann T. Wind and topography influence on an upwelling system at the eastern Hainan coast. *Journal of Geophysical Research-Oceans*. 2009;**114**(C6):C06017
- [29] Li YN et al. Numerical simulation of the structure and variation of upwelling off the east coast of Hainan Island using QuikSCAT winds. *Chinese Journal of Oceanology and Limnology*. 2012;**30**(6):1068-1081
- [30] Lin PG et al. Observation of summertime upwelling off the eastern and northeastern coasts of Hainan Island, China. *Ocean Dynamics*. 2016;**66**(3):387-399
- [31] Lin PG et al. Dynamics of wind-driven upwelling off the northeastern coast of Hainan Island. *Journal of Geophysical Research-Oceans*. 2016;**121**:1160-1173
- [32] Xu JD et al. Study on coastal upwelling in eastern Hainan Island and western Guangdong in summer, 2006. *Acta Oceanologica Sinica*. 2013;**35**(4):11-18 (in Chinese with English abstract)
- [33] Liu Y et al. Variation of summer coastal upwelling at northern South China Sea during the last 100 years. *Geochimica*. 2009;**38**(4):317-322 (in Chinese with English abstract)
- [34] Jing ZY et al. Upwelling in the continental shelf of northern South China Sea associated with 1997-1998 El Niño. *Journal of Geophysical Research-Oceans*. 2011;**116**(C2):C02033
- [35] Su J et al. A western boundary upwelling system response to recent climate variation (1960-2006). *Continental Shelf Research*. 2013;**57**(SI):3-9
- [36] Liu Y et al. Recent 121-year variability of western boundary upwelling in the northern South China Sea. *Geophysical Research Letters*. 2013;**40**(12):3180-3183
- [37] Xiao H et al. Summarization of studies on hydrographic characteristics in Taiwan Strait. *Journal of Oceanography in Taiwan Strait*. 2002;**21**(1):126-138 (in Chinese with English abstract)

- [38] Hu JY et al. A review of research on the upwelling in the Taiwan Strait. *Bulletin Marine Science*. 2003;**73**(3):605-628
- [39] Hu JY et al. Analysis on sea surface temperature and salinity in the Taiwan Strait during August 1998. *Tropic Oceanology*. 2000;**19**:15-22 (in Chinese with English abstract)
- [40] Tang DL et al. Upwelling in the Taiwan Strait during the summer monsoon detected by satellite and shipboard measurements. *Remote Sensing of Environment*. 2002;**83**(3):457-471
- [41] Chen H et al. Underway measurement of sea surface temperature and salinity in the Taiwan Straits in August, 1999. *Marine Science Bulletin*. 2002;**4**:11-18
- [42] Chen ZZ et al. Observation of upwelling and diluted water in southern Taiwan Strait during July, 2005. *Journal of Tropical Oceanography*. 2008;**27**(4):19-22 (in Chinese with English abstract)
- [43] Chen XH et al. Densely underway measurement of surface temperature and salinity in Xiamen-Quanzhou near-shore area. *Advances in Earth Science*. 2009;**24**(6):629-635 (in Chinese with English abstract)
- [44] Lin PG et al. Variation characteristics of upwelling in Taiwan Strait and its relationship with wind in summer 2011. *Journal of Oceanography in Taiwan Strait*. 2012;**31**(3): 307-316 (in Chinese with English abstract)
- [45] Zhu J et al. On summer stratification and tidal mixing in the Taiwan Strait. *Frontiers of Earth Science*. 2013;**7**(2):141-150
- [46] Hong HS et al. Interannual variability of summer coastal upwelling in the Taiwan Strait. *Continental Shelf Research*. 2009;**29**:479-484
- [47] Hu JY et al. Variable temperature, salinity and water mass structures in the southwestern Taiwan Strait in summer. *Continental Shelf Research*. 2011;**31**:S13-S23
- [48] Zhang CY et al. Evolution of a coastal upwelling event during summer 2004 in the southern Taiwan Strait. *Acta Oceanologia Sinica*. 2011;**30**(1):1-6
- [49] Hong HS, Wang DZ. Studies on biogeochemical process of biogenic elements in the Taiwan Strait. *Journal of Xiamen University (Natural Science)*. 2001;**40**(2):535-544 (in Chinese with English abstract)
- [50] Shang SL et al. An overview of the marine ecosystem response to climate-ocean variability. *Journal of Marine Sciences*. 2005;**23**(3):14-22 (in Chinese with English abstract)
- [51] Hong HS et al. An overview of physical and biogeochemical processes and ecosystem dynamics in the Taiwan Strait. *Continental Shelf Research*. 2011;**31**:S3-S12
- [52] Hu JY et al. Hydrographic and satellite observations of summertime upwelling in the Taiwan Strait: A preliminary description. *Terrestrial Atmospheric and Oceanic Sciences*. 2001;**12**(2):415-430

- [53] Shang SL et al. Upwelling induced variability of Chlorophyll in the Taiwan Strait as observed by SeaWiFS and AVHRR. In: RJ Frouin et al., editors. Proceedings of SPIE Vol. 4892 Ocean Remote Sensing and Applications. Bellingham, WA: SPIE; 2003
- [54] Shang SL et al. Short-term variability of chlorophyll associated with upwelling events in the Taiwan Strait during the southwest monsoon of 1998. *Deep-Sea Research II*. 2004; **51**(10-11):1113-1127
- [55] Shang SL et al. Hydrographic and biological changes in the Taiwan Strait during the 1997-1998 El Nino winter. *Geophysical Research Letters*. 2005;**32**):L11601
- [56] Tang DL et al. Long-time observation of annual variation of Taiwan Strait upwelling in summer season. *Advances in Space Research*. 2004;**33**(3):307-312
- [57] Kuo N-J, Ho C-R. ENSO effect on the sea surface wind and sea surface temperature in the Taiwan Strait. *Geophysical Research Letters*. 2004;**31**(13):L13309
- [58] Hong HS et al. Evidence of ecosystem response to the interannual environmental variability in the Taiwan Strait. *Acta Oceanologia Sinica*. 2005;**27**(2):63-69 (in Chinese with English abstract)
- [59] Wang J et al. Summer nitrogenous nutrient transport and its fate in the Taiwan Strait: A coupled physical-biological modeling approach. *Journal of Geophysical Research-Oceans*. 2013;**118**(9):4184-4200
- [60] Pan YP, Sha WY. Numerical study on winter coastal upwelling off Fujian and Zhejiang coast. *Oceanologia et Limnologia Sinica*. 2004;**35**(3):193-201 (in Chinese with English abstract)
- [61] Pan YP, Sha WY. Numerical study on the summer coastal upwelling off Fujian and Zhejiang. *Marine Science Bulletin*. 2004;**23**(3):1-11 (in Chinese with English abstract)
- [62] Pan YP, Sha WY. Numerical study on the coastal upwelling off Fujian and Zhejiang. *Marine Forecasts*. 2004;**21**(2):86-95 (in Chinese with English abstract)
- [63] Luyten PJ et al. COHERENS—A coupled hydrodynamical-ecological model for regional and shelf seas: User documentation. Management Unit of the Mathematical Models of the North Sea. 1999:1-914
- [64] Zeng GN. Application of COHERENS model on environmental dynamics of the Taiwan Strait. Ph.D thesis of Xiamen University, Xiamen; 2006. 154pp (in Chinese with English abstract)
- [65] Jing ZY et al. Numerical study on the coastal upwelling and its seasonal variation along Fujian and Zhejiang coast. *Journal of Hohai University*. 2007;**35**(4):464-470 (in Chinese with English abstract)
- [66] Jiang YW et al. Characteristics and mechanisms of the upwelling in the southern Taiwan Strait: A three-dimensional numerical model study. *Journal of Oceanography*. 2011; **67**:699-708

- [67] Zhao BR et al. Characteristics of the ecological environment in upwelling area adjacent to the Changjiang River estuary. *Oceanologia et Limnologia Sinica*. 2001;**32**(3):327-333 (in Chinese with English abstract)
- [68] Zou EM et al. An analysis of summer hydrographic features and circulation in the southern Yellow Sea and the northern East China Sea. *Oceanologia et Limnologia Sinica*. 2001;**32**(3):340-348 (in Chinese with English abstract)
- [69] Bai H et al. Light transmission in summer and its relation to sediment transportation in the East China Sea. *Marine Sciences*. 2002;**26**(5):45-48 (in Chinese with English abstract)
- [70] Zhu DD et al. Hydrologic distribution characteristics of HAB frequent occurrence area in the outer Changjiang River estuary. *Chinese Journal of Applied Ecology*. 2003;**14**(7): 1131-1134 (in Chinese with English abstract)
- [71] Zhu JR et al. Observation of the diluted water and plume front off the Changjiang River estuary during August 2000. *Oceanologia et Limnologia Sinica*. 2003;**34**(3):249-255 (in Chinese with English abstract)
- [72] Lü XG et al. Upwelling off Yangtze River estuary in summer. *Journal of Geophysical Research-Oceans*. 2006;**111**:C11S08
- [73] Hu MN, Zhao CF. Long-time observation of upwelling in the Zhoushan Islands and adjacent seas during the summer season. *Periodical of Ocean University of China*. 2007;**S1**: 235-240 (in Chinese with English abstract)
- [74] Hu MN, Zhao CF. Upwelling in Zhejiang coastal areas during summer detected by satellite observations. *Journal of Remote Sensing*. 2008;**12**(2):297-304 (in Chinese with English abstract)
- [75] Lou XL et al. Satellite observation of the Zhejiang coastal upwelling in the East China Sea during 2007-2009. *Proceedings of SPIE*. 2011:8175
- [76] Cao GP et al. Mechanism of upwelling evolvement in the Yangtze River Estuary adjacent waters in summer, 2007. *Marine Sciences*. 2013;**37**(1):102-112 (in Chinese with English abstract)
- [77] Zhu JR. Dynamic mechanism of the upwelling on the west side of the submerged river valley off the Changjiang mouth in summertime. *Chinese Science Bulletin*. 2003;**48**(24): 2754-2758
- [78] Li HF, Zhao BR. Simulation of the three-dimensional circulation of the East China Sea in summer. *Studia Marina Sinica*. 2003;**45**:48-63 (in Chinese with English abstract)
- [79] Zhao BR et al. Numerical simulation of upwelling in the Changjiang River mouth area. *Studia Marina Sinica*. 2003;**45**:64-76 (in Chinese with English abstract)
- [80] Bai XZ, Wang F. Numerical study on the mechanism of the expansion of the Changjiang River diluted water in summer. *Oceanologia et Limnologia Sinica*. 2003;**34**(6):593-603 (in Chinese with English abstract)

- [81] Liu XQ et al. Dynamic process of vertical circulation and temperature- salinity structure in coastal area of East China Sea, I. Basic characteristics of the circulation. *Oceanologia et Limnologia Sinica*. 2004;**35**(5):393-403 (in Chinese with English abstract)
- [82] Liu XQ et al. Dynamic process of vertical circulation and temperature- salinity structure in coastal area of East China Sea, II. Temperature and salinity structure. *Oceanologia et Limnologia Sinica*. 2004;**35**(6):497-506 (in Chinese with English abstract)
- [83] Zhu JR et al. Observation and modeling analysis of dynamic mechanism of the upwelling at Lüsi. *Journal of East China Normal University*. 2004;**2**:87-91 (in Chinese with English abstract)
- [84] Qiao FL et al. Coastal upwelling in the East China Sea in winter. *Journal of Geophysical Research-Oceans*. 2006;**111**(C11):C11S06
- [85] Jing ZY et al. Numerical study on the coastal upwelling and its seasonal variation in the East China Sea. *Journal of Coastal Research*. 2007;**50**:555-563
- [86] Lü XG et al. Tidally induced upwelling off Yangtze River estuary and in Zhejiang coastal waters in summer. *Science in China (Series D): Earth Sciences*. 2007;**50**(3):462-473
- [87] Bai T et al. Numerical study of upwelling of the Changjiang River Estuary and its adjacent sea area in summer. *Marine Sciences*. 2009;**33**(11):65-72 (in Chinese with English abstract)
- [88] Yang DZ et al. Numerical study of the ocean circulation on the East China Sea shelf and a Kuroshio bottom branch northeast of Taiwan in summer. *Journal of Geophysical Research-Oceans*. 2011;**116**(C5):C05015
- [89] Liu ZQ, Gan JP. Modeling study of variable upwelling circulation in the East China Sea: Response to a coastal promontory. *Journal of Physical Oceanography*. 2013;**44**:1078-1094
- [90] Yang DZ et al. Numerical study on the origins and the forcing mechanism of the phosphate in upwelling areas off the coast of Zhejiang Province, China in summer. *Journal of Marine Systems*. 2013;**123**:1-18
- [91] Gan JP et al. Intensified upwelling over a widened shelf in the northeastern South China Sea. *Journal of Geophysical Research-Oceans*. 2009;**114**(C9):C09019
- [92] Chen ZY. Coastal upwelling study: Observation, dynamic analysis and modelling. Ph.D thesis of Xiamen University, Xiamen; 2013. 145 pp. (in English with Chinese abstract)
- [93] Wang DX et al. Relative contributions of local wind and topography to the coastal upwelling in the northern South China Sea. *Journal of Geophysical Research-Oceans*. 2014;**119**(C4):2550-2567
- [94] Wong LA et al. A model study of the circulation in the Pearl River Estuary (PRE) and its adjacent coastal waters: 1. Simulations and comparison with observations. *Journal of Geophysical Research-Oceans*. 2003;**108**(C5):3156
- [95] Gan JP et al. Interaction of a river plume with coastal upwelling in the northeastern South China Sea. *Continental Shelf Research*. 2009;**29**(4):728-740

- [96] Shu YQ et al. The 4-D structure of upwelling and Pearl River plume in the northern South China Sea during summer 2008 revealed by a data assimilation model. *Ocean Modelling*. 2011;**36**(3-4):228-241
- [97] Wang DX et al. Coastal upwelling in summer 2000 in the northeastern South China Sea. *Journal of Geophysical Research-Oceans*. 2012;**117**:C04009
- [98] Lü XG et al. Upwelling off the west coast of Hainan Island in summer: Its detection and mechanisms. *Geophysical Research Letters*. 2008;**35**(2):L02604
- [99] Hu JY et al. Tidal front around the Hainan Island, northwest of the South China Sea. *Journal of Geophysical Research-Oceans*. 2003;**108**(C11):3342
- [100] Sun ZY et al. Horizontal distribution of temperature and salinity in eastern Beibu Gulf in summer 2006. In: Hu JY, Yang SY, editors. *A Collection of Research Papers on Marine Science in the Beibu Gulf (Vol. 1)*. Beijing: China Ocean Press; 2008. p. 73-78 (in Chinese with English abstract)
- [101] Hong HS et al. Source water of two-pronged northward flow in the southern Taiwan Strait in summer. *Journal of Oceanography*. 2011;**67**(4):385-393
- [102] Gu YZ et al. Remote sensing observation and numerical modeling of an upwelling jet in Guangdong coastal water. *Journal of Geophysical Research-Oceans*. 2012;**117**:C08019
- [103] Pan AJ et al. A preliminary study of the internal tide in the summertime upwelling regime off the Guangdong shelf edge in 2002 and its local feedback. *Journal of Oceanography in Taiwan Strait*. 2012;**31**(2):151-159 (in Chinese with English abstract)
- [104] Qiao FL. *Regional Oceanography of the China Seas: Physical Oceanography*. Beijing: Ocean Press; 2012. 300 pp (in Chinese)
- [105] Xiong XJ et al. *China Coastal Ocean: Physical Oceanography and Marine Meteorology*. Beijing: Ocean Press; 2012. 280 pp (in Chinese)

The Yellow Sea Surface Cold Patches in Warm Seasons

X. San Liang, Minghai Huang, Hui Wu and
Yihe Wang

Additional information is available at the end of the chapter

<http://dx.doi.org/10.5772/intechopen.80732>

Abstract

An important hydrographic phenomenon in the Yellow Sea is the surface cold patches (SCP) in warm seasons, among which the most conspicuous are the Shandong SCP, Subei SCP, and Mokpo SCP. Previous studies based on monthly mean fields propose that these patches result from the collaboration of tidal mixing and tidal induced upwelling. While this is true for patches like the Shandong SCP, the monthly mean tidal mixing and upwelling alone cannot explain all their formations. In this study, through a detailed analysis of their patterns over a spring-neap tidal cycle, it is found that the Subei and Mokpo SCPs show distinct spring-neap variations. During the neap tide phase, strong stratification is established, and hence the cold patches in these two areas may be greatly weakened or even suppressed, while during the spring tide phase, the surface temperature reaches its minimum. That is to say, for these two SCPs, besides the well-accepted mechanisms, the effect of spring-neap tidal variation must be taken into account.

Keywords: Yellow Sea, upwelling, tidal mixing, surface cold patches

1. Introduction

The Yellow Sea is the northern part of the East China Sea, a western Pacific marginal shallow sea surrounded by China and Korea (**Figure 1**). Approximately, it has a meridional extension of 960 km, a zonal extension of 700 km, and an average depth of 44 m, with a maximum of 100 m in the central trough. Its sea bottom and shores are full of sand and silt carried by the Yellow River (Huanghe) and other rivers. These deposits, together with the sand storms from the Gobi Desert, turn the surface of the water golden yellow, making it one of the four seas named after color—the others being the Black Sea between Eastern Europe and Western Asia, the Red Sea near Gulfs of Aden and Suez, and the White Sea on the northwest coast of Russia.

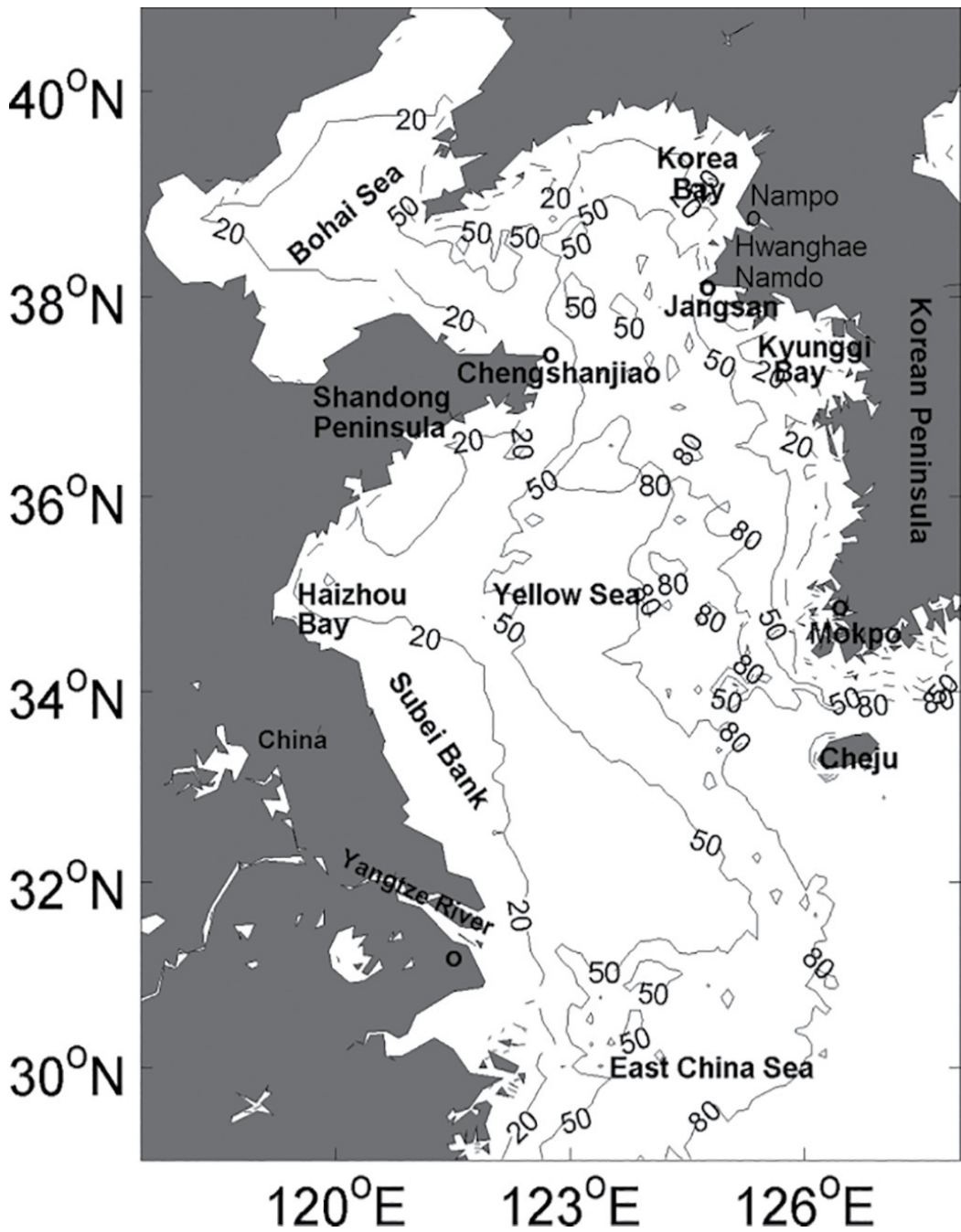


Figure 1. Bathymetry of the study area (contour interval: 30 m).

It has long been observed that cold water masses prevail in warm seasons in the deep or bottom layers of the central Yellow Sea. These are the Yellow Sea Cold Water Mass (YSCWM), a conspicuous phenomenon which has attracted wide attention from physical oceanographers

ever since 1921 [1]. YSCWM is induced by bottom topography and summer atmospheric conditions. It has a double-cell circulation. It is believed to have a double-cell circulation. The detailed circulation, however, is still controversial. Proposed so far are three structures: (1) above the thermocline, it is an anticyclonic horizontal circulation with downwelling at the center and upwelling around; below the thermocline the circulation is the opposite [2]; (2) the double cell is formed by convection, with upwelling at the center through the whole water column and downwelling near the coast [3]. But the convection is limited within a thin shell, outside which the water is almost motionless in the vertical direction; and (3) based on the observations and numerical modeling, Su and Huang [4] found a structure similar to (1), but with totally opposite flow directions. That is to say, it is a cyclonic flow above and an anticyclonic flow below, with the accordingly vertical circulations. All these, however, are yet to be verified with more observations.

Around the YSCWM, we often observe cold centers at the sea surface (e.g., [5, 6]), in contrast to the ambient high SST in boreal summer. These are the surface cold patches (SCPs). For the SCPs off Mokpo, Korea, their generation has been ascribed to tidal mixing (e.g., [7]). But details are yet to be revealed. Recently, Lu et al. [8] reported that tidal mixing and tide-induced upwelling may collaborate to lead to the formation of the SCPs. By observation, the patches sit along the slope of the Yellow Sea trough, where intensified tidal mixing occurs. The abrupt change of bathymetry tends to increase the velocity shear and hence enhance the vertical mixing, while the enhanced mixing will change the horizontal density distribution, leading to a secondary upwelling. This is further substantiated by the observation that the SCP sites agree with the occurrences of maximal tidal currents, which result in extensive tidal mixing and, by the above argument, strong upwelling (cf. Figure 12 in [8]).

The generating mechanism via tidal mixing implies that there must be a good correspondence [8, 9] between the SCP locations and the Simpson-Hunter index [10],

$$SH = \log (H/|U^3|), \quad (1)$$

(where H and U are, respectively, the water depth and the amplitude of the tidal velocity), which describes, for the summer shelf seas, the influence of surface buoyancy input and tidal mixing in controlling the water column structure. By the SH distribution, there are three conspicuous fronts in the Yellow Sea; they are, in a clockwise order, Subei Bank Front (SBF), Shandong Peninsula Front (SPF), and Mokpo Front (MKF) [11]. Correspondingly, three most conspicuous SCPs are identified. Through comparative experiments, it is found that the SCPs off Shandong and Mokpo are mainly induced, respectively, through tidal mixing and tide-induced upwelling, while the Subei SCP is generated through a combination of the two mechanisms. In a word, tidal mixing and tide-induced upwelling are the two key factors in the formation of the SCPs.

The above analyses are with the monthly mean maps of the summer sea surface temperature (SST). However, by observation, the SCPs actually do not last throughout the summer; they sometimes disappear. A monthly mean analysis may exclude some possible mechanism(s) in arriving at the mean fields. In fact, we do see such an example in Chesapeake Bay, where the spring-neap tidal cycles are found to exert effects on the turbulent mixing, stratification, and residual circulation [12]. For the Yellow Sea (and the surrounding seas like Bohai Sea and East

Sea), satellite ocean color observations have also shown distinct difference of ocean optical and biogeochemical properties over a spring-neap tidal cycle (Shi et al., 2011); the fresh water flux (FWF) from the Changjiang diluted water is found to contain spring-neap signals, too (it is usually maximized during the spring tide) [13, 14]; and, more importantly, there has been evidence that the spring-neap cycles may potentially affect the YSCWM in fall [15]. However, there has been rare attention to the influence of the spring-neap cycle on the generation and evolution of the SCPs. The study as of today is Huang et al. [16], which will be briefly summarized here. In the following, we first give a brief description of the seasonal evolution of the SCPs (Section 2) and then set up a three-dimensional (3D) model to test the hypothesis (Section 3). Section 4 provides a validation of the results. Based on the model results, Section 5 gives a detailed analysis of the effects of the spring-neap tidal cycles on the SCPs. This article is summarized in Section 6.

2. The observed seasonal SCP evolution

Figure 2 shows the seasonal evolution of the Yellow Sea SCPs with the multi-year Moderate Resolution Imaging Spectroradiometer (MODIS) SST data (2003–2016). As can be seen, the

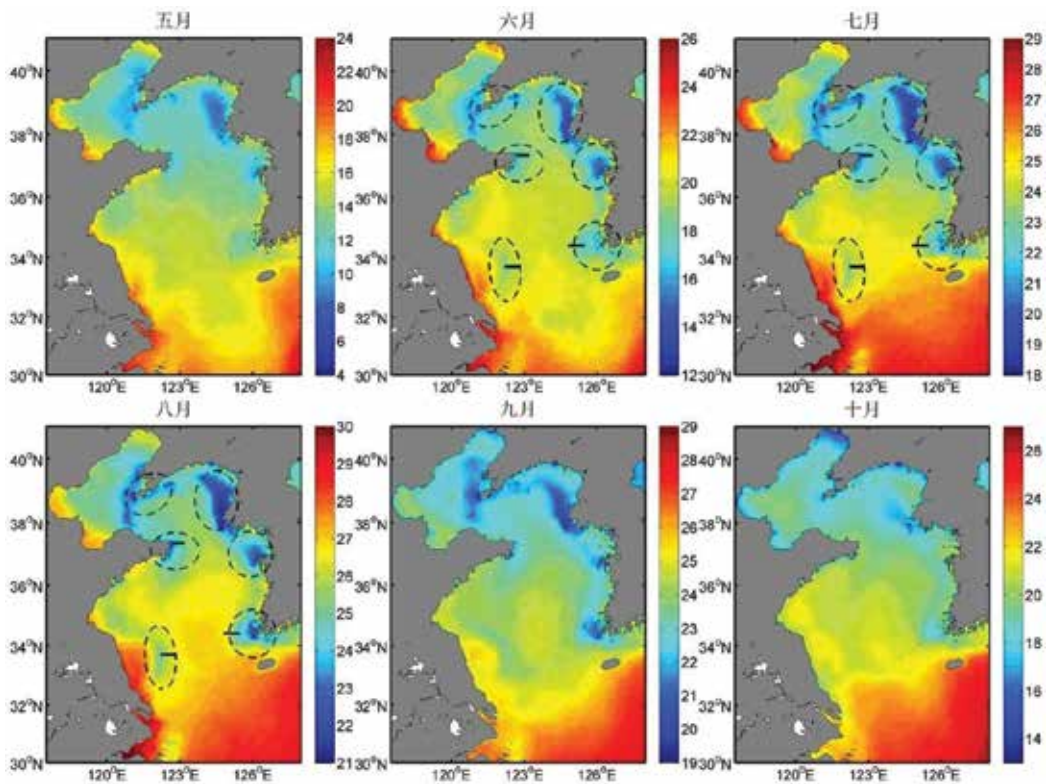


Figure 2. Monthly SST (in °C) climatology (2003–2016) based on MODIS-Aqua and -Terra measurements from May to October. The SCPs are marked by dashed ellipses during summer time and the three lines are shown in the June map.

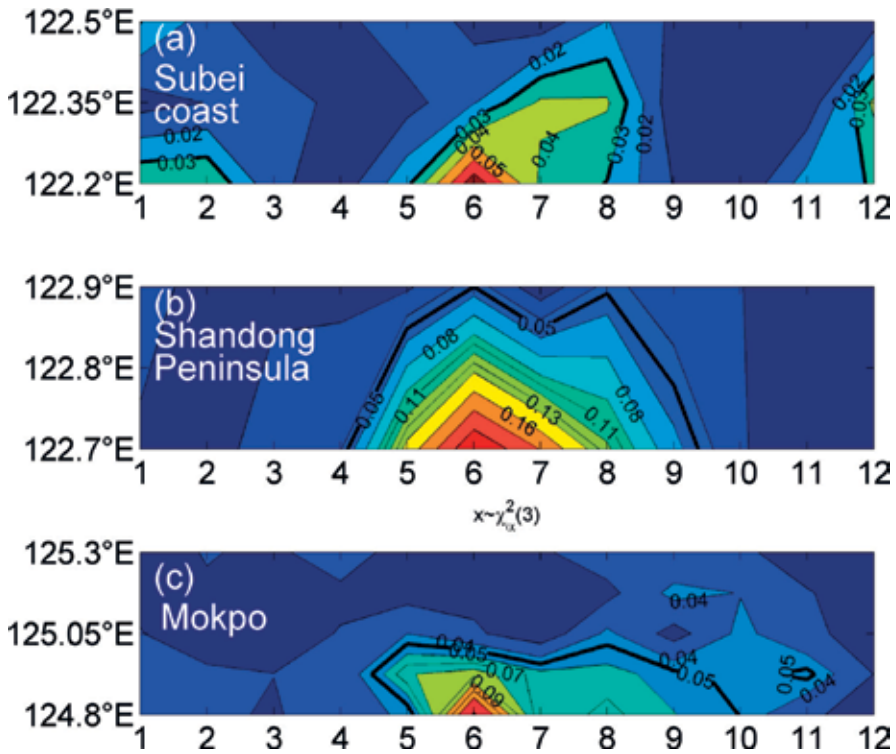


Figure 3. Annual cycles of the $|S_T|$ (from MODIS) off (a) Subei coast (122.2°E–122.5°E, 33.7°N), (b) Shandong Peninsula (122.7°E–122.9°E, 37.35°N), and (c) Mokpo (124.8°E–125.3°E, 34.4°N). Units are K/km.

SCPs usually appear in spring and decay in fall and become pronounced in summer. For a better illustration, we follow Ma et al. [17] and compute the zonal temperature gradient $S_T = \frac{\partial T}{\partial x}$ and display in **Figure 3** $|S_T|$ for the segments off Subei coast, Shandong Peninsula, and Mokpo (the three lines are marked in **Figure 2**). The annual cycles of $|S_T|$ are obvious. Defining the 0.03°C/km isoline as the boundary of the SCP off Subei coast, we then see that the SCP first emerges in May, flourishes in summer, and disappears in late August. Likewise, by defining the 0.05°C/km contour as the boundary, we can have the evolution of the Shandong SCP (**Figure 3b**), which is by observation stronger than its Subei counterpart. It forms in late April, and lasts through late September, with its maximum in June and July. The Mokpo SCP can also be demarcated by the isoline of 0.05°C/km. It is found to emerge in May, lasting through October until it completely disappears.

3. Model setup

We adopt the ECOM-si model developed at *East China Normal University* [14] to achieve our goal. The model domain encompasses the entire East China Sea (including Yellow Sea, Bohai

Sea, and East Sea) and parts of the Pacific Ocean and the Japan Sea, with an open boundary roughly parallel to the Ryukyu Islands. This model has a resolution varying from several hundred meters near the Changjiang River mouth to 2–3 km in the open ocean. Vertically there are 20 terrain-following sigma levels. Besides, a wet/dry scheme is included with a critical depth of 0.25 m. Wu et al. [18] found that the inclusion of inter-tidal flats is very important in simulating the Changjiang plume.

The open boundary conditions include specified shelf and tidal currents. The former is extracted from the daily Hybrid Coordinate Ocean Model (HYCOM) data with a horizontal resolution of $1/12^\circ$, the latter is specified with harmonic constants as determined by Wu et al. [13]. The boundary and initial conditions of salinity and temperature are extracted from the daily HYCOM and Simple Ocean Data Assimilation (SODA) datasets, respectively, and the surface fluxes (heat and momentum fluxes) are derived from the European Centre for Medium-Range Weather Forecasts (ECMWF) dataset (with a time resolution of 6 hours). For more details, see Wu et al. [13, 14].

The integration begins on January 1, 2008. After 1 year's spin-up, the model reaches a statistical equilibrium. In the following, the hourly outputs for the summer time (July–August) from 2009 to 2013 will be used.

4. Validation

4.1. Temperature

Our focus is the summertime SCPs, so we look only at simulation for July and August. Data used for validation span an extended multi-year period from 2009 to 2013.

We first compare the model results with historical in situ observations. **Figure 4** shows such a comparison between the cruise data from Korean Oceanographic Data Center (KODC) and

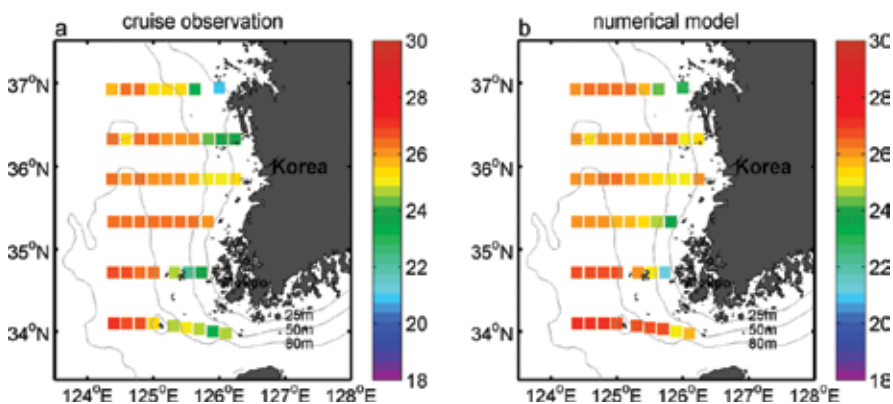


Figure 4. (a) KODC hydrographic mean SST in summer time from 2010 to 2013 (22 Aug 2010–27 Aug 2010; 1 Jul 2011–5 Jul 2011; 10 Aug 2012–18 Aug 2012; 13 Aug 2013–20 Aug 2013). (b) As (a), but for modeled SST. Contours denote the bathymetry of the Yellow Sea (contour interval: 25 m).

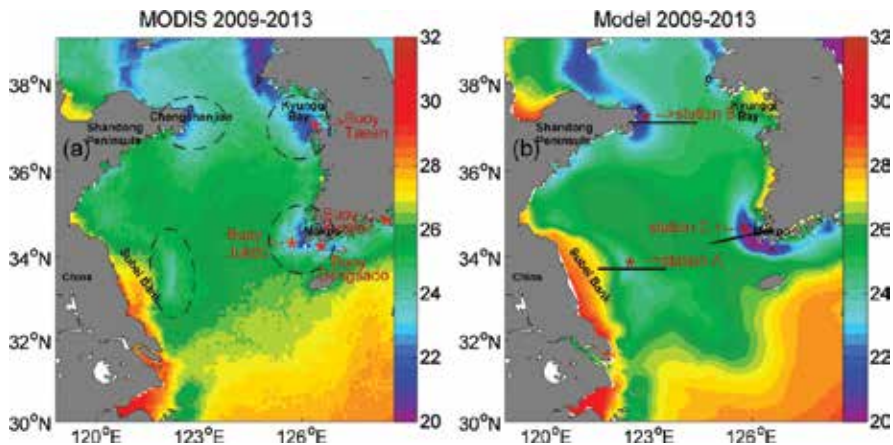


Figure 5. Distribution of the monthly mean SST ($^{\circ}\text{C}$) from July to August for 2009–2013 from (a) MODIS and (b) model result. The SCPs are marked by dashed ellipses.

National Fishers Research and Development Institute (NFRDI). From it, we see that the simulation has produced satisfactory results comparable with the cruise observations, with an error tolerance within 2°C .

A comparison of the model results with the MODIS also shows good agreement. **Figure 5a** and **b** are the observed (MODIS) and modeled monthly mean SST from July to August, respectively. Generally, the latter agrees well with the former, although the modeled SST off Subei coast is warmer than the MODIS SST by $1\text{--}2^{\circ}\text{C}$. From both distributions, four SCPs are evident; they are located off Subei Bank, off Chengshanjiao (Cheng Shan Point in the east of Shandong), in Kyunggi Bay, and off Mokpo. Their intensities are also in good agreement, except for that of the two along the Korean coast. Nonetheless, the simulated Mokpo SCP is still satisfactory, though it is too strong by comparison. The problem is with the Byunggi Bay SCP, which is not well reproduced in the model. This is because (1) the model does not have enough resolution around the bay (data unavailable), and (2) the Han River discharge into the Bay is not included (also due to a lack of data). We have tested with some artificial runoff but it seems that the SCP simulation in the bay is essentially not affected, so the poor bathymetry resolution in the eastern part of the Yellow Sea may be blamed. But, anyhow, our focus will be the SCPs off Subei, Shandong, and Mokpo, which will not be influenced by the unsatisfactory simulation of the SST around the Kyunggi Bay.

4.2. Tides

Tides are pivotal to the SCP formation; their successful simulation is the key to this study. **Figure 6** shows the modeled cotidal charts for the four major constituents M2, S2, K1, O1, N2, and P1. From the semidiurnal tides (M2 and S2), we particularly see two amphidromic points in the Yellow Sea (located off Chengshanjiao and Haizhou Bay). These, among other features, agree well with satellite observations and previous model results such as Fang et al. [19], Lu et al. [8], Ren et al. [11], to name a few. Our model simulation is hence validated.

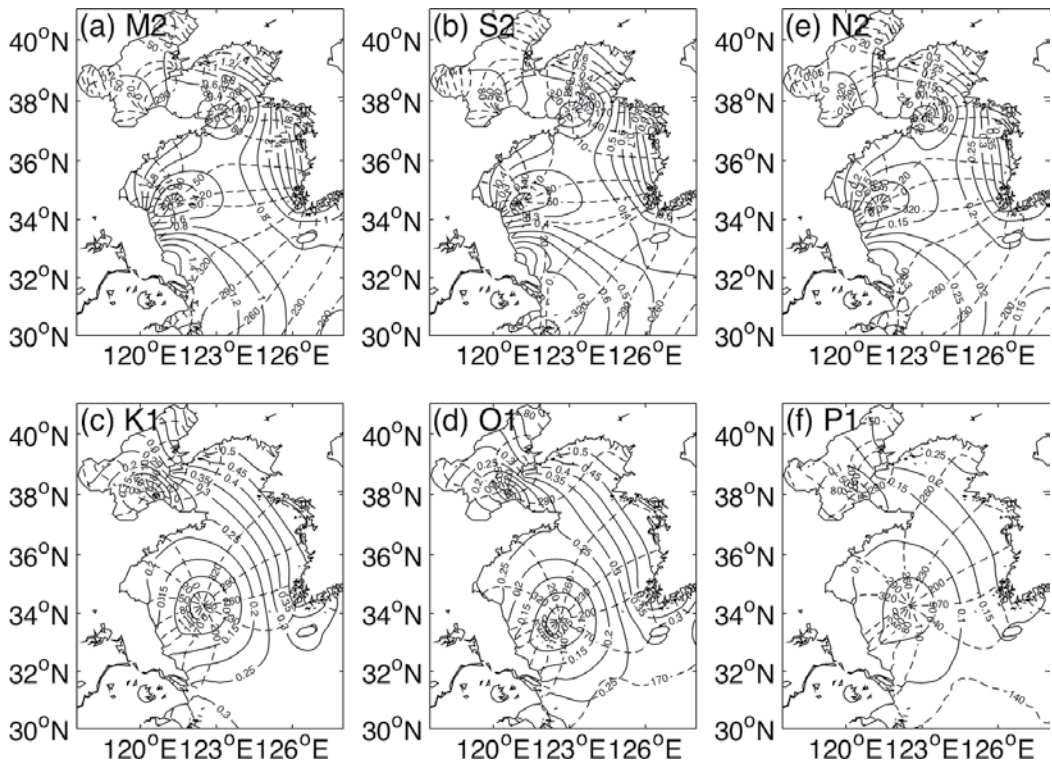


Figure 6. Simulated cotidal charts for (a) M2, (b) S2, (c) K1, (d) O1, (e) N2, and (f) P1 tidal constituents. Dashed and solid lines denote phase lag (degree; referred to Beijing standard time (UTC+8)) and amplitude (cm), respectively.

5. The tidal cycles of the Yellow Sea SCPs

First, look at the evolution of the Subei SCP. For this purpose, a point east of the Subei Bank or Subei Shoal is chosen to plot the time series of the modeled temperature. This is the station A (122.3°E, 33.7°N), as marked in **Figure 5b**. **Figure 7** displays the 3-m temperature (blue) at it from July to August for the 5 years 2009–2013. They are then band-pass filtered with a Butterworth filter to retain only the features between 7 and 21 days and re-plotted in red. Clearly, the spring-neap cycle exists in all the 5 years' band-passed signals—the near surface water is coldest (warmest) during the spring (neap) tidal phases. For the vertical distribution at the station, the cycle is also obvious. **Figure 8** displays the 2012 sequence of the profiles of temperature, vertical velocity, vertical diffusivity, horizontal speed, and the reconstructed tidal current magnitude and surface elevation, from which the spring-neap variations are clearly seen.

The variations of the above oceanic fields provide a possible explanation for the corresponding SCP cycle. During the spring tidal phases, the strong tidal mixing brings up the deep cold water, while the upwelling supplies cold water from the subsurface layer. During the neap tidal phases, the tidal mixing is minimized, and the upwelling in the upper layer is weak. The deep cold water cannot be brought to the surface and, accordingly, the SCP is suppressed. For

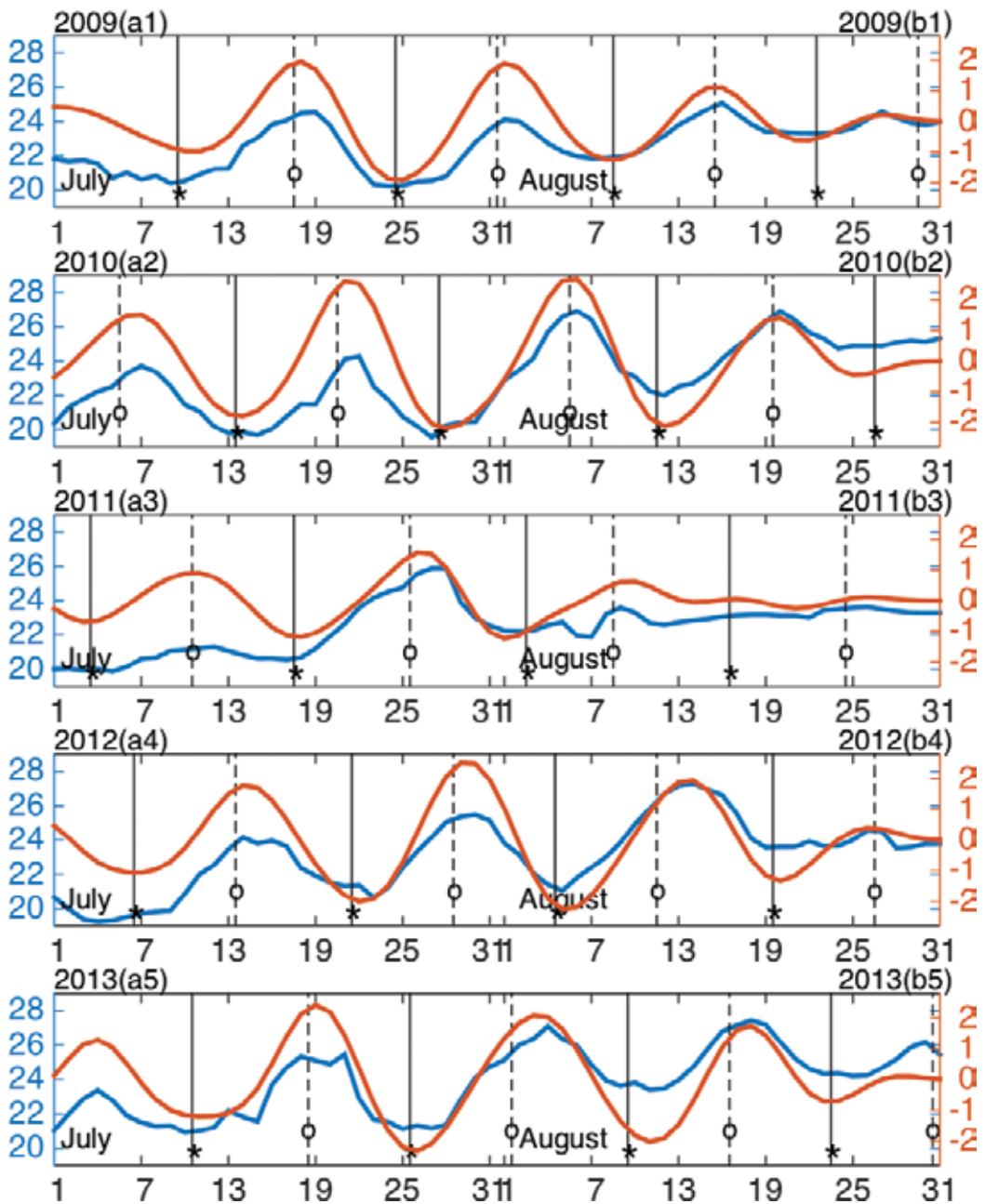


Figure 7. Time series of modeled temperature ($^{\circ}\text{C}$) at station A from July to August for 2009–2013. Blue: Raw time series; red: band-pass (7–21 days) filtered time series. The asterisk indicates the time of spring tide, while the circle marks that of neap tide.

example, on July 13 (Day 13) and August 12 (Day 43), a strong stratification is established in the absence of mixing and convection; the upper layer water becomes warmer, and hence the SCP fades away.

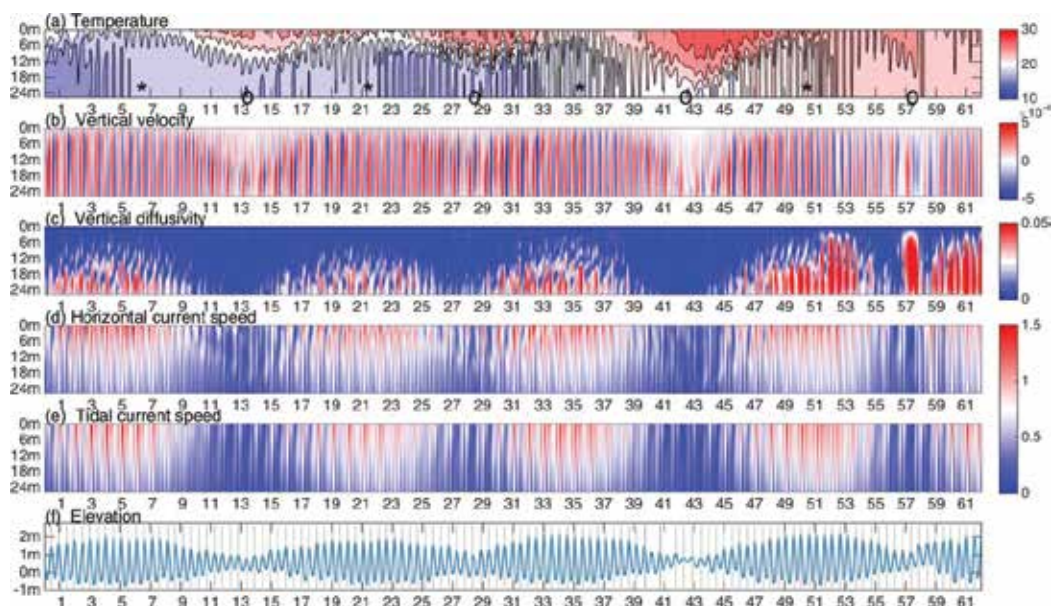


Figure 8. Time-depth distribution of the modeled and reconstructed data at station A (**Figure 5b**) from July to August 2012. The rows from top to bottom are (a) temperature ($^{\circ}\text{C}$), (b) vertical velocity (ms^{-1}), (c) vertical diffusivity ($\text{m}^2 \text{s}^{-1}$), (d) horizontal current (ms^{-1}), (e) reconstructed tidal current velocity (ms^{-1}), and (f) surface elevation (m). The asterisk indicates the time of spring tide, while the circle denotes that of neap tide.

The SCP has a vertical structure which also experiences a variation over the spring-neap tidal cycle. **Figure 9** shows a sequence of the temperature on the cross-section along the latitude 33.7°N , from 121.5°E to 123.5°E in August 2012. From the figure, we see that, on August 4, 2 days after the new moon, the SCP reaches its maximum strength, with the 23°C isotherm line outcropping to the surface. On August 11, just 2 days after the first quarter moon, the outcropping isoline is 26°C , which, however, is completely suppressed during August 12–16. The spring-tide SCP temperature may differ from the neap-tide SCP temperature by as large as 3°C . Obviously, tides along cannot account for all the SCP formation; the effect of the spring-neap tidal variation cannot be ignored.

To contrast the spring tidal temperature from the neap tidal temperature, we, respectively, take the means of the temperatures on the spring tide days (defined as 2 days after new or full moon) and neap tide days (2 days after quarter moon) in summer for all the 5 years during 2009–2013. The mean temperatures are shown in **Figure 10a** and **b**; also shown is their difference (**Figure 10c**). The large difference in both structure and magnitude implies that the previous analysis simply based on the monthly mean fields cannot tell the whole story. Particularly, the large difference in temperature, as shown in **Figure 10c**, happens to take place in the region where the SCP forms, corresponding well to the spring-neap variation. Therefore, for the region off Subei Bank, we may safely say that the formation of the summertime SCP is mainly induced during the spring phase because of the pronounced tidal effect. In the days of

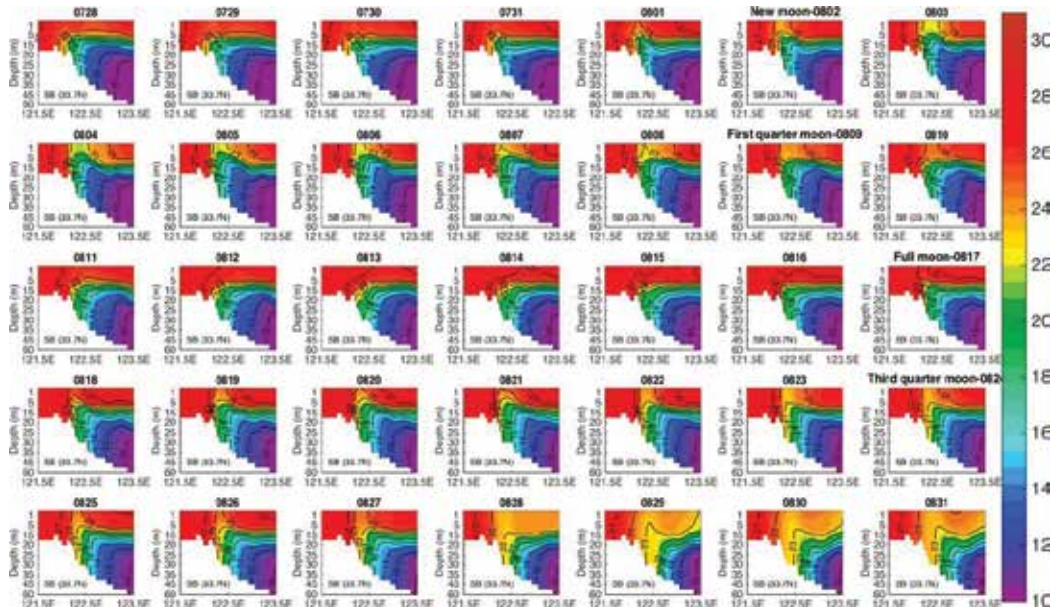


Figure 9. Temperature profiles along 33.7°N from August 1 to August 31. The 22–26°C isolines (with a 1°C interval) are contoured.

neap tides, such as August 14–16, 2012, with the establishment of strong stratification, the weak tidal effect cannot have the deep cold water brought up to the surface, and the SCP may completely be suppressed.

Another conspicuous SCP along the China coast is the one off Shandong Peninsula. Following the same procedure as above, we pick a representative point or “station” B at (122.7°E, 37.1°N), as marked in **Figure 5b**, for the analysis. Shown in **Figure 11** are the original and band-pass filtered temperature series at the point. Compared with that of **Figure 7**, the spring-neap variation at B is much weaker; its maximal magnitude is less than 1°C (~2°C in **Figure 7**). The evolutions of the vertical structures of the fields at B are also distinctly different from those at A, as drawn in **Figure 12**. This is particularly true for the vertical velocity (**Figure 12b**), which is not only weaker than its counterpart at A (off Subei Bank) but also tends to be homogenized over the spring-neap cycle and vertical diffusivity (**Figure 12c**), which implies that the here tidal mixing is strong during the spring phases, and hence the water column tends to be more homogeneously distributed in the vertical direction. It has been reported that tidal mixing plays the dominant role in inducing the Shandong Front [8, 11]. Our results are in agreement with this.

Following what we did in **Figure 10**, we draw the mean temperature profile along the latitude 37.1°N off the tip of Shandong peninsular (marked in **Figure 5b**) for both the spring and neap tidal phases (**Figure 13a** and **b**). What makes a remarkable difference from that in **Figure 10** is the insignificant difference between **Figure 13a** and **b**. In fact, the spring and neap profiles here look quite similar (the difference is shown in **Figure 13c**), in sharp contrast to those off the

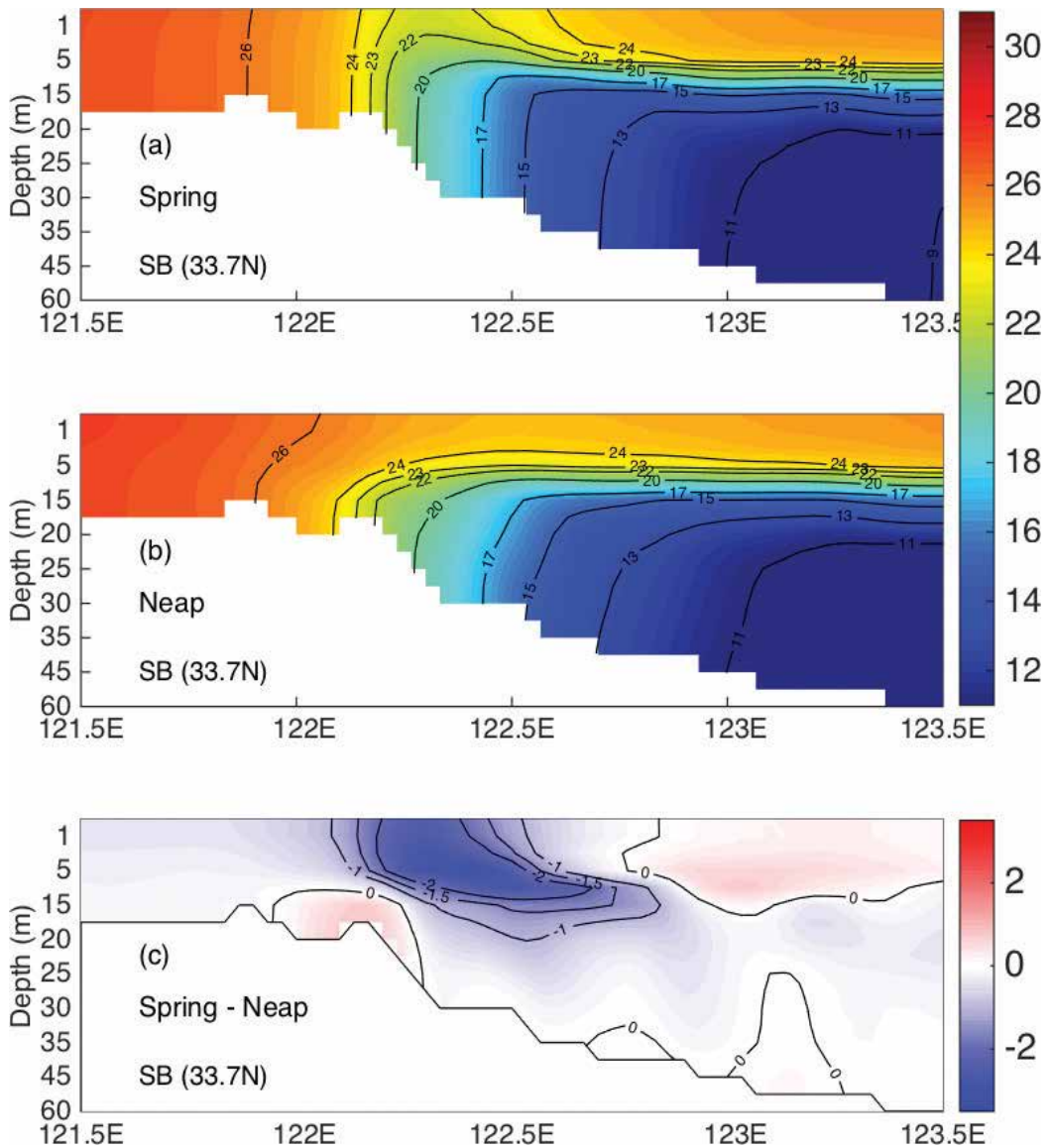


Figure 10. Section profiles of the (a) spring mean, (b) neap mean, and (c) their difference (spring minus neap) temperature along the 33.7°N, from 121.5°E to 123.5°E off the Subei coast.

Subei Bank. By this observation, the previous studies on SCPs using the monthly mean temperature data may be appropriate only for the cold patch off Shandong.

Previously, Ren et al. [11] suggested that tidal mixing is the key to the formation of the Shandong Front, while off Subei Bank, the Subei Front results from collaboration of both tidal

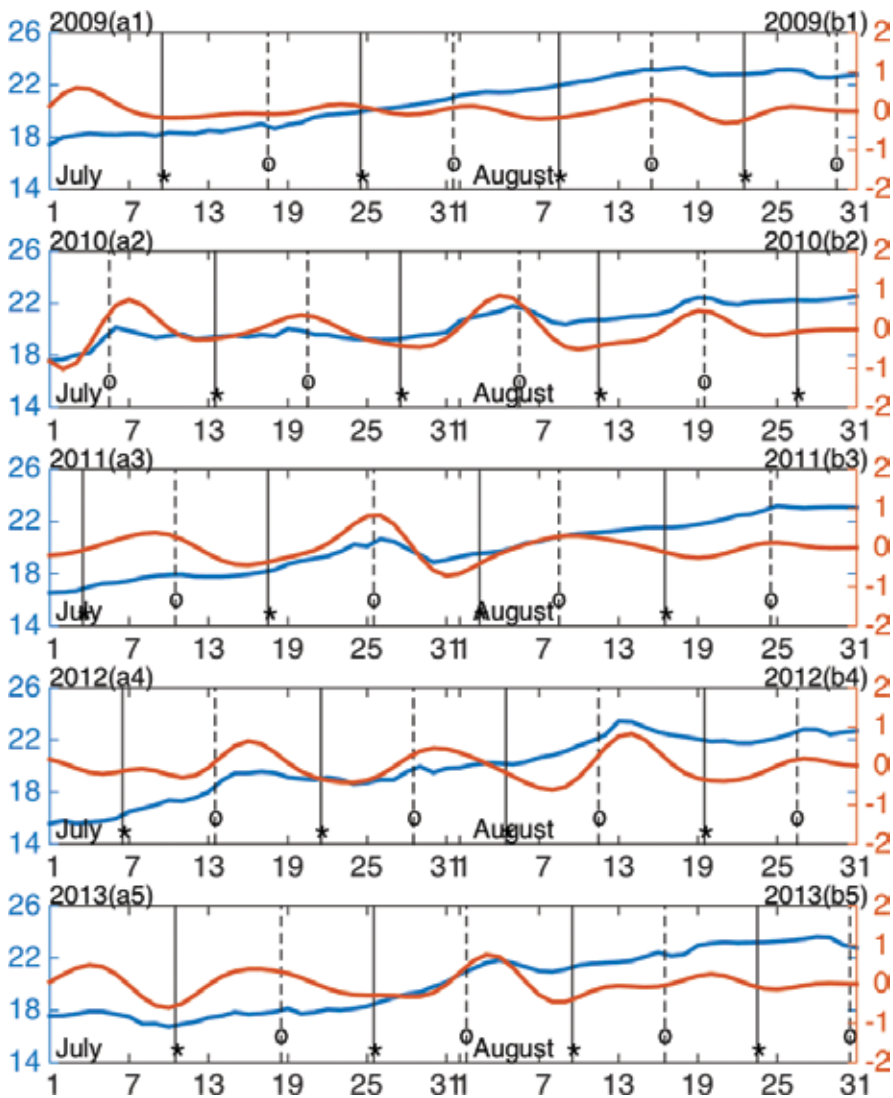


Figure 11. As Figure 7, but for station B.

induced upwelling and tidal mixing. The different generating mechanisms may be reflected in the temperature distribution, and hence we see different temperature variations over the spring-neap cycle at the two stations A and B.

The third SCP in the Yellow Sea, the SCP off Mokpo southwest of Korean Peninsula, is somehow different from both its counterparts in the western Yellow Sea. Again, we choose a representative point C at 125.6°E , 34.7°N (cf. Figure 5b), and analyze the temperature series at it (Figure 14). Similar to station A (off Subei coast), the series at this station also shows

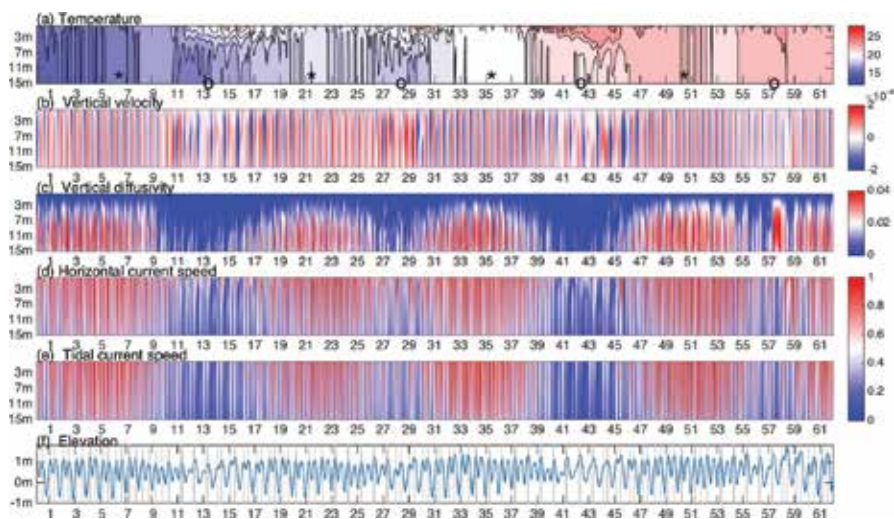


Figure 12. As Figure 8, but for station B.

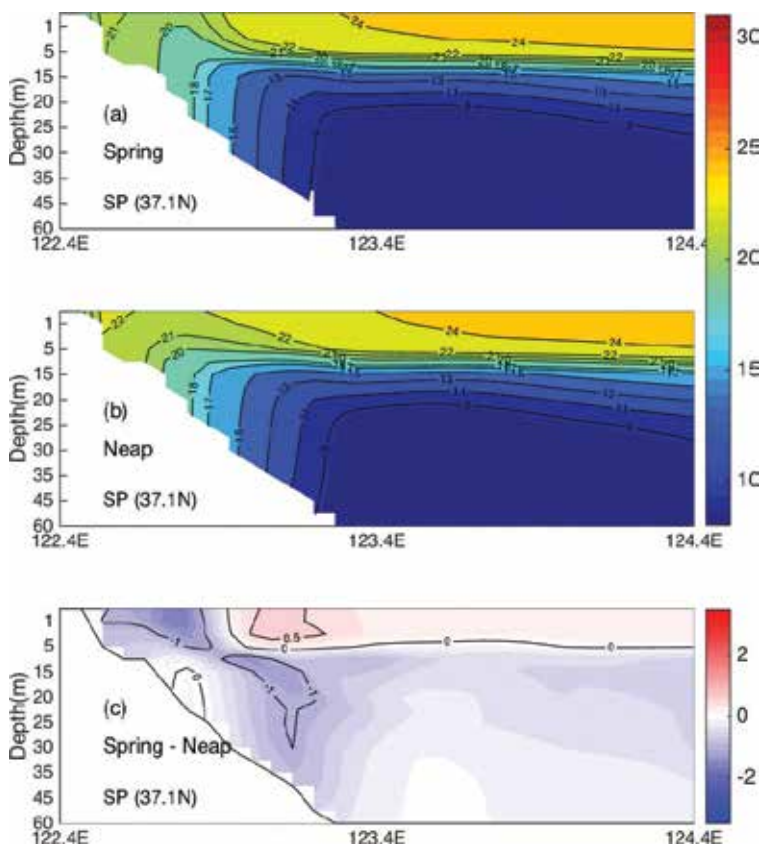


Figure 13. As Figure 10, but for the profiles off Shandong Peninsula.

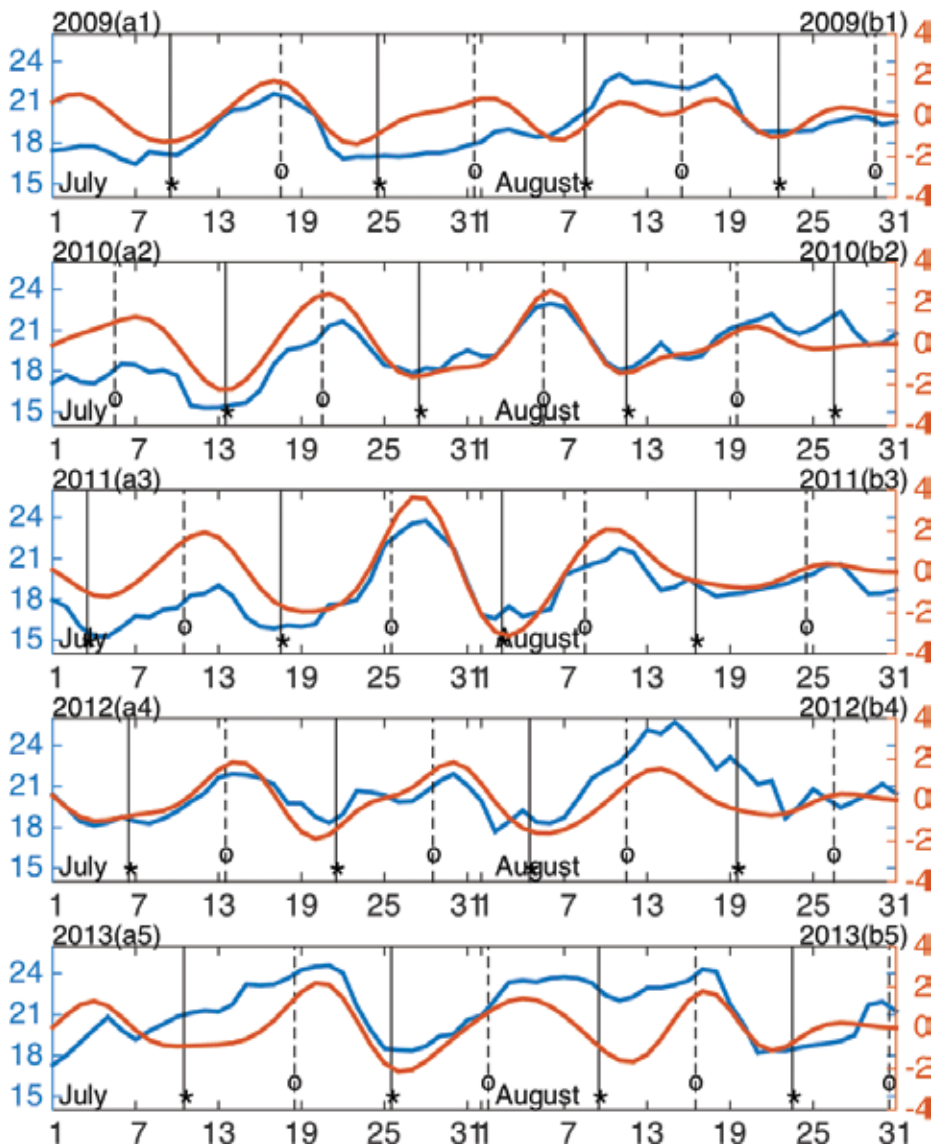


Figure 14. As Figure 7, but for station C.

significant spring-neap variations. From Figure 15, both upwelling and tidal mixing are conspicuous on the spring-neap cycle. During the spring tidal phases, strong upwelling and strong tidal mixing lead to the generation of the SCP, while during the neap tidal phases, the SCP fades away as both the vertical velocity and vertical diffusivity become greatly weakened.

As we did for Figure 10, the cross-section temperature distribution along the latitude $\sim 34.5^{\circ}\text{N}$ off the tip of Mokpo (marked in Figure 5b) is displayed in Figure 16. Here, the outcropped isoline on the spring profile is about 19°C , while on the neap profile, it is around 21°C . The

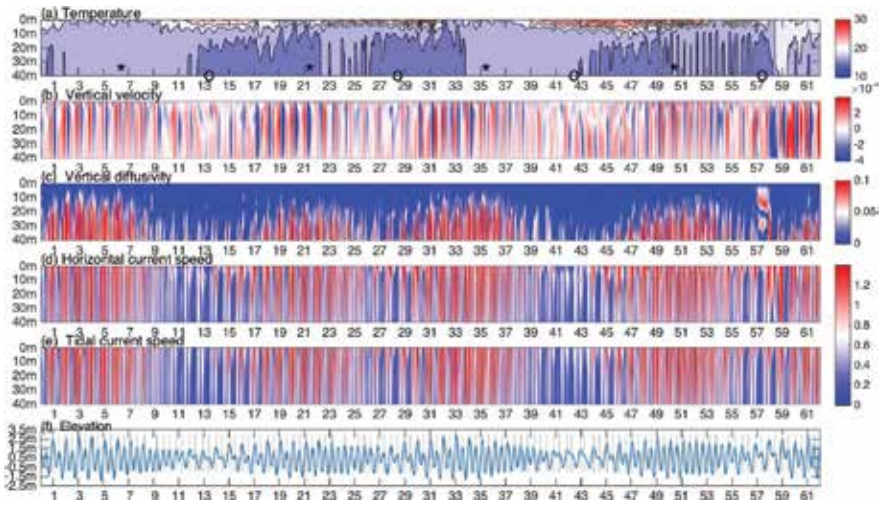


Figure 15. As Figure 8, but for station C.

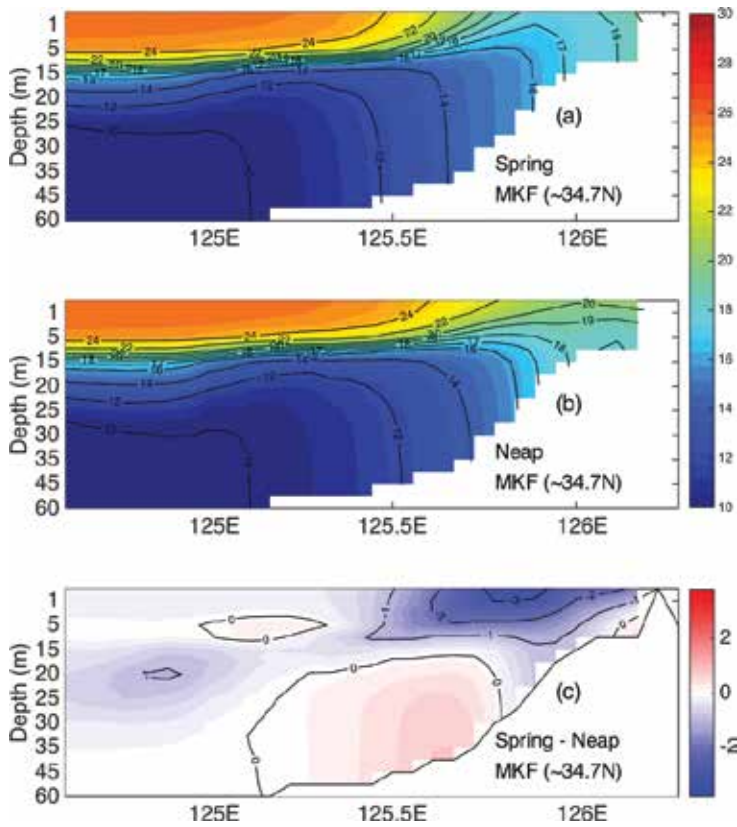


Figure 16. As Figure 10, but for the profile off Mokpo.

spring-neap difference (**Figure 16c**) shows a pattern just like that of **Figure 10c**, with a minimum trapped in the near-surface below the SCP and vanishing values elsewhere.

6. Concluding remarks

The long observed SCPs along the China and Korea coasts are a conspicuous hydrographic phenomenon in Yellow Sea. They generally form in spring, grow in summer, and decay in fall, though the precise time may differ case by case. Using a 3D numerical model, in this study, we have investigated how the spring-neap tidal cycle influences the formations and evolutions of these SCPs in July and August.

The temperature variation over a spring-neap tidal cycle separated from the nonstationary background shows that the lowest temperature occurs during spring tidal days (defined as 2 days after new moon or full moon), and the highest occurs during neap tidal days (2 days after quarter moon). This spring-neap variation is consistent with the previous ocean color observation by, say, Shi et al. [20], who showed that the ocean color in Yellow Sea varies on a period largely equivalent to a spring-neap tidal cycle, with the largest (smallest) turbid water coverage 2–3 days behind the new/full (quarter) moon. This variation is the most conspicuous for the SCPs off Subei Bank and off Mokpo, while for the Shandong SCP, it is not significant, suggesting that the underlying generating mechanism could be different. Indeed, the time-depth distributions of temperature, vertical velocity, and vertical diffusivity off Subei Bank show that the mixing is weak, and vertical velocity is small in the neap tidal phase, and, as a result, strong stratification is established, suppressing the upwelling and subsequently the SCP; on the other hand, the SCP is enhanced in the spring phase, thanks to the strong upwelling and tidal mixing which bring the deep cold water upward through the thermocline to the surface. The Mokpo SCP bears a similar variable scenario. The Shandong SCP, however, does not show significant variation over a spring-neap cycle. Its formation is mainly through tidal mixing, in contrast to the Subei SCP and Mokpo SCP. But here the tidal mixing alone makes a relatively homogeneous temperature distribution in the vertical direction. This prevents the influence of the spring-neap cycle from taking effect on the vertical movement of deep water, yielding an insignificant spring-neap variation. The composite analysis of the MODIS SST data and buoy observations also support these observations.

Acknowledgements

The hydrography and buoy data are from the Korean Oceanographic Data Center (KODC; http://kodc.nifs.go.kr/page?id=kr_index) and National Marine Data and Information Service (NMDIS; <http://www.cmoc-china.cn/>). The MODIS data are available at (<https://modis.gsfc.nasa.gov/>), and the phases of the moon are provided by NASA (<https://eclipse.gsfc.nasa.gov/lunar.html>). The surface fluxes are from ECMWF (<http://apps.ecmwf.int/datasets/>). This study was partially supported by the 2015 Innovation Program for Research and Entrepreneurship Teams, Jiangsu, China.

Author details

X. San Liang^{1,2*}, Minghai Huang¹, Hui Wu³ and Yihe Wang³

*Address all correspondence to: x.san.liang@gmail.com

1 School of Marine Sciences, Nanjing University of Information Science and Technology, Nanjing, China

2 School of Atmospheric Sciences, Nanjing University of Information Science and Technology, Nanjing, China

3 State Key Laboratory of Estuarine and Coastal Research, East China Normal University, Shanghai, PR China

References

- [1] Uda M. The results of simultaneous oceanographical investigations in the Japan Sea and its adjacent waters in May and June 1932. *Journal of the Imperial Fishery Experimental Stations (In Japanese)*. 1934;(5):57-190
- [2] Feng M, Hu D, Li Y. A theoretical solution for the thermohaline circulation in the Southern Yellow Sea. *Chinese Journal of Oceanology and Limnology*. 1992;**10**(4):289-300
- [3] Li H, Yuan Y. On the formation and maintenance mechanisms of the cold water mass of the Yellow Sea. *Chinese Journal of Oceanology and Limnology*. 1992;**10**(2):97-106
- [4] Su J, Huang D. On the current field associated with the Yellow Sea cold water mass. *Chinese Journal of Oceanology and Limnology*. 1995;(S1):1-7
- [5] Seung Y-H, Chung J-H, Park Y-C. Oceanographic studies related to the tidal front in the mid-Yellow Sea off Korea: Physical aspect. *Journal of the Oceanological Society of Korea*. 1990;**25**:84-95
- [6] Zou EM, Guo BH, Tang YX, Lee JH, Lie HJ. An analysis of summer hydrographic features and circulation in the Southern Yellow Sea and the Northern East China Sea. *Oceanologia et Limnologia Sinica*. 2001;**32**(3):340-348
- [7] Lie HJ. Summertime hydrographic features in the Southeastern Hwanghae. *Progress in Oceanography*. 1986;**17**(17):229-242
- [8] Lü X, Qiao F, Xia C, Wang G, Yuan Y. Upwelling and surface cold patches in the yellow sea in summer: Effects of tidal mixing on the vertical circulation. *Continental Shelf Research*. 2010;**30**(6):620-632
- [9] Zhao B. A preliminary study of continental shelf fronts in the western part of southern Huanghai sea and circulation structure in the front region of the Huanghai cold water

- mass (HCWM). *Oceanologia et Limnologia Sinica*. 1987 (in Chinese, with English Abstr); **18**:217-226
- [10] Simpson JH, Hunter JR. Fronts in the Irish Sea. *Nature*. 1974;**250**(5465):404-406
- [11] Ren S, Xie J, Jiang Z. The roles of different mechanisms related to the tide-induced fronts in the Yellow Sea in summer. *Advances in Atmospheric Sciences*. 2014;**31**(5):1079-1089
- [12] Li M, Zhong L. Flood–ebb and spring–neap variations of mixing, stratification and circulation in Chesapeake Bay. *Continental Shelf Research*. 2007;**29**(1):4-14
- [13] Wu H, Zhu J, Shen J, Wang H. Tidal modulation on the Changjiang River plume in summer. *Journal of Geophysical Research – Atmospheres*. 2011;**116**(C8):192-197
- [14] Wu H, Shen J, Zhu J, Zhang J, Li L. Characteristics of the Changjiang plume and its extension along the Jiangsu coast. *Continental Shelf Research*. 2014;**76**(2):108-123
- [15] Li J, Li G, Xu J, Dong P, Qiao L, Liu S, et al. Seasonal evolution of the Yellow Sea cold water mass and its interactions with ambient hydrodynamic system. *Journal of Geophysical Research, Oceans*. 2016;**121**:6779-6792
- [16] Huang M, Liang XS, Wu H, Wang Y. Different generating mechanisms for the summer surface cold patches in the Yellow Sea. *Atmosphere-Ocean*. 2017:1-13. DOI: 10.1080/07055900.2017.1371580
- [17] Ma J, Qiao F, Xia C. Tidal effects on temperature front in the Yellow Sea. *Chinese Journal of Oceanology and Limnology*. 2004;**22**(3):314-321
- [18] Wu H, Zhu J. Advection scheme with 3rd high-order spatial interpolation at the middle temporal level and its application to saltwater intrusion in the Changjiang estuary. *Ocean Modelling*. 2010;**33**(1–2):33-51
- [19] Fang G, Wang Y, Wei Z, Choi BH, Wang X, Wang J. Empirical cotidal charts of the bohai, yellow, and east china seas from 10 years of topex/poseidon altimetry. *Journal of Geophysical Research – Atmospheres*. 2004;**109**(C11):227-251
- [20] Shi W, Wang M, Jiang L. Spring–neap tidal effects on satellite ocean color observations in the Bohai Sea, Yellow Sea, and East China Sea. *Journal of Geophysical Research – Atmospheres*. 2011;**116**(C12032). DOI: 10.1029/2011JC007234

Estuarine Processes

Saltwater Intrusion in the Changjiang Estuary

Jianrong Zhu, Hui Wu, Lu Li and Cheng Qiu

Additional information is available at the end of the chapter

<http://dx.doi.org/10.5772/intechopen.80903>

Abstract

Saltwater intrusion in the Changjiang Estuary and the impacts of river discharge, tide, wind, sea level rise, river basin, and major estuary projects on saltwater intrusion are studied in this chapter. There is a net landward flow in the NB (North Branch) when river discharge is low during spring tide, resulting in a type of saltwater intrusion known as the SSO (saltwater-spilling-over from the NB into the SB (South Branch)), which is the most striking characteristic of saltwater intrusion in the estuary. A three-dimension numerical model with HSIMT-TVD advection scheme was developed to study the hydrodynamic processes and saltwater intrusion in the Changjiang Estuary. Saltwater intrusion in the estuary is controlled mainly by river discharge and tide, but is also influenced by wind, sea level rise, river basin, and estuary projects. Saltwater intrusion is enhanced when river discharge decreases. There is more time for the reservoir to take freshwater from the river when river discharge is larger. The fortnightly spring tide generates greater saltwater intrusion than the neap tide. The saltwater intrusion in the SP (South Passage) is stronger than that in the NP (North Passage), and the intrusion in the NP is stronger than that in the NC (North Channel). The northerly wind produces southward currents along the Subei coast as well as the landward Ekman transport, which enhances the saltwater intrusion in the NC and NB and weakens the saltwater intrusion in the NP and SP. Saltwater intrusion becomes stronger as the sea level rises and is much stronger when river discharge is much small. The DWP (Deep Waterway Project) alleviates the saltwater intrusion in the NC and the lower reaches of the NP and enhances the saltwater intrusion in the SP and in the upper reaches of the NP. The Three Gorges Dam (TGD) increases river discharge in winter, which weakens saltwater intrusion, and is favorable for reducing the burden of freshwater supplement in the highly populated estuarine region. The Water Diversion South to the North Project (WDP) decreases river discharge, enhances saltwater intrusion, and is unfavorable for freshwater supply in the estuary.

Keywords: Changjiang Estuary, saltwater intrusion, dynamic process, numerical model, freshwater resource

1. Introduction

The Changjiang, also known as the Yangtze River, is one of the largest rivers in the world. The Changjiang Estuary has a 90-km-wide river mouth, which is characterized by multiple bifurcations (**Figure 1**). First, the estuary is divided by Chongming Island into the South Branch (SB) and North Branch (NB). The SB and its lower reaches form the main channel of the Changjiang and discharge most of the river discharge, while the NB is heavily silted. Second, the lower SB is bifurcated into the South Channel (SC) and North Channel (NC) by Changxing Island and Hengsha Island. Finally, the SC is bifurcated into the South Passage (SP) and North Passage (NP) by Jiuduansha Island [1]. The Changjiang Estuary is unique among well-studied estuaries, has an extremely dynamic hydrological environment due to runoff, tide, wind, mixing, topography, and continental shelf current outside the river mouth, which are the main dynamic control factors on hydrodynamic processes in the estuary [2–4].

Saltwater intrusion in the Changjiang Estuary is controlled mainly by the river discharge and tide [2, 5–8], but is also influenced by wind [4], topography [9], river watershed and estuary projects [10–12], and sea level rise [13]. The natural evolution and artificial reclamation of the intertidal zone from the 1950s to the 2000s have severely narrowed the upper reaches of the NB [14]. As a consequence, the upper reaches of the NB have become almost orthogonal to the SB, while the lower reaches have become funnel shaped. The evolution of river regime of the NB helps to prevent runoff from entering the NB, especially during the dry season; meanwhile, it makes the tidal range larger in the NB than in the SB. Strong tidal forcing in the NB induces significant subtidal circulation, resulting in a net landward flow when river discharge is low during spring tide [1]. This residual transport forms a type of saltwater intrusion known as the saltwater-spilling-over (SSO) from the NB into the SB, which is the most striking characteristic of saltwater intrusion in the estuary. During spring tide, the water level rises considerably in the upper reaches of the NB due to its funnel shape, leading to a massive amount of saline water spilling over the shoals into the SB [1]. The saline water that spilled into the SB is then transported downstream forced by runoff and arrives in the middle reaches of the SB during

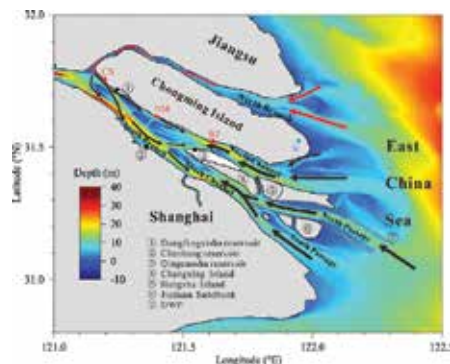


Figure 1. Map of the Changjiang Estuary and the pathways of saltwater intrusion (arrows). Key geographic locations and hydrologic stations are marked. The red dots indicate the locations of Baozhen (BZ) and Chongxi (CX) hydrologic stations. The black dots indicate the locations of water intakes of the reservoirs. W is the location of the weather station at the Chongming eastern shoal. DWP stands for the deep waterway project.

the subsequent neap tide. This process impacts the water intakes of the Dongfengxisha, Chenhang, and Qingcaosha reservoirs and threatens the freshwater supply to Shanghai, a megacity in China.

The Changjiang Estuary has been the most important freshwater resource for Shanghai. The huge QCSR (Qingcaosha reservoir) was built in 2010 along northwestern Changxing Island, supplying more than 70% of the freshwater for the 13 million people in Shanghai. The QCSR takes the water from the Changjiang when the salinity is lower than 0.45 (the salinity standard of drinking water), but it suspends its operation when the saltwater intrusion influences the water intake. In order to understand the dynamic processes and mechanism of saltwater intrusion in the Changjiang Estuary, we studied the impacts of tide, river discharge, wind, sea level rise, river basin, and major estuary projects on saltwater intrusion, which not only has important scientific significance, but also has great application meaning for safety of freshwater resource in Shanghai.

Estuarine saltwater intrusion is a common phenomenon, which can produce estuarine circulation [15] and change stratification [16], thereby influencing sediment transport, producing peak estuarine turbidity [17], and degrading the safety of freshwater intake of estuarine reservoirs.

In this chapter, we analyze and simulate the saltwater intrusion in the Changjiang Estuary. In Section 2, we describe the numerical model used to simulate the saltwater intrusion in the estuary. In Section 3, we first simulate the saltwater intrusion in a climatological state under various dynamic factors, and then analyze the impacts of river discharge, tide, wind, sea level rise, river watershed, and artificial estuary projects on the saltwater intrusion by numerical experiments. In Section 4, a summary is provided.

2. Numerical model

ECOM-si was developed based on the Princeton Ocean Model (POM; [18, 19]) with several improvements [20] to address the demand for numerical simulations of water body bounded by complicated coastlines. This model incorporates the Mellor-Yamada level-2.5 turbulent closure scheme to provide a time and space dependent parameterization of vertical turbulent mixing [21–23]. This model was further developed by Wu and Zhu [24] using the third HSIMT-TVD scheme for the advection term in the mass transport equation. This scheme is flux-based, with third order accuracy in space, second order accuracy in time, and no numerical oscillation.

Under the assumption of incompressibility, Boussinesq and hydrostatic approximations, and using the horizontal nonorthogonal curvilinear and vertical stretched sigma coordinate system, the governing equations of ocean circulation and water mass (consisting of momentum, continuity, temperature, salinity, and density equations) are as follows [25]:

$$\begin{aligned} \frac{\partial D J u_1}{\partial t} + \frac{\partial D J \hat{U} u_1}{\partial \xi} + \frac{\partial D J \hat{V} u_1}{\partial \eta} + \frac{\partial J \omega u_1}{\partial \sigma} - D h_2 \hat{V} \left[v_1 \frac{\partial}{\partial \xi} \left(\frac{J}{h_1} \right) - u_1 \frac{\partial}{\partial \eta} \left(\frac{J}{h_2} \right) + J f \right] - D h_2 u_1 v_1 \frac{\partial}{\partial \xi} \left(\frac{h_3}{h_1 h_2} \right) \\ = -h_2 g D \frac{\partial \zeta}{\partial \xi} + \frac{g h_2 D}{\rho_0} \frac{\partial D}{\partial \xi} \int_{\sigma}^0 \frac{\partial \rho}{\partial \sigma} d\sigma - \frac{g h_2 D^2}{\rho_0} \frac{\partial}{\partial \xi} \int_{\sigma}^0 \rho d\sigma + \frac{1}{D} \frac{\partial}{\partial \sigma} \left(K_m \frac{\partial J u_1}{\partial \sigma} \right) + D J F_x \end{aligned} \quad (1)$$

$$\begin{aligned} & \frac{\partial DJv_1}{\partial t} + \frac{\partial DJ\hat{U}v_1}{\partial \xi} + \frac{\partial DJ\hat{V}v_1}{\partial \eta} + \frac{\partial J\omega v_1}{\partial \sigma} + Dh_1\hat{U} \left[v_1 \frac{\partial}{\partial \xi} \left(\frac{J}{h_1} \right) - u_1 \frac{\partial}{\partial \eta} \left(\frac{J}{h_2} \right) + Jf \right] - Dh_1u_1v_1 \frac{\partial}{\partial \eta} \left(\frac{h_3}{h_1h_2} \right) \\ & = -h_1gD \frac{\partial \zeta}{\partial \eta} + \frac{gh_1D}{\rho_o} \frac{\partial D}{\partial \eta} \int_{\sigma}^0 \frac{\partial \rho}{\partial \sigma} d\sigma - \frac{gh_1D^2}{\rho_o} \frac{\partial}{\partial \eta} \int_{\sigma}^0 \rho d\sigma + \frac{1}{D} \frac{\partial}{\partial \sigma} \left(K_m \frac{\partial v_1}{\partial \sigma} \right) + DJF_y \end{aligned} \quad (2)$$

$$\frac{\partial \zeta}{\partial t} + \frac{1}{J} \left[\frac{\partial}{\partial \xi} (DJ\hat{U}) + \frac{\partial}{\partial \eta} (DJ\hat{V}) \right] + \frac{\partial \omega}{\partial \sigma} = 0 \quad (3)$$

$$\frac{\partial JD\theta}{\partial t} + \frac{\partial JD\hat{U}\theta}{\partial \xi} + \frac{\partial JD\hat{V}\theta}{\partial \eta} + \frac{\partial J\omega\theta}{\partial \sigma} = \frac{1}{D} \frac{\partial}{\partial \sigma} \left(K_h \frac{\partial J\theta}{\partial \sigma} \right) + DJF_{\theta} \quad (4)$$

$$\frac{\partial JDs}{\partial t} + \frac{\partial JD\hat{U}s}{\partial \xi} + \frac{\partial JD\hat{V}s}{\partial \eta} + \frac{\partial J\omega s}{\partial \sigma} = \frac{1}{D} \frac{\partial}{\partial \sigma} \left(K_h \frac{\partial Js}{\partial \sigma} \right) + DJF_s \quad (5)$$

$$\rho_{total} = \rho_{total}(\theta, s) \quad (6)$$

where,

$$\omega = w - \sigma \left(\hat{U} \frac{\partial D}{\partial \xi} + \hat{V} \frac{\partial D}{\partial \eta} \right) - \left[(1 + \sigma) \frac{\partial \zeta}{\partial t} + \hat{U} \frac{\partial \zeta}{\partial \xi} + \hat{V} \frac{\partial \zeta}{\partial \eta} \right] \quad (7)$$

In the above equations, the new coordinate (ξ , η , and σ) is defined as: $\xi = \xi(x, y)$, $\eta = \eta(x, y)$, $\sigma = \frac{z-\zeta}{H+\zeta}$.

The vertical coordinate σ varies from -1 at $z = -H$ to 0 at $z = \zeta$, where, x , y and z are the east, north, and vertical axes of the Cartesian coordinate, respectively; ζ is the sea surface elevation; and H is the total water depth. The ξ and η components of velocity (defined as u_1 , v_1) can be expressed in the forms of $u_1 = \frac{h_2}{J} (x_{\xi}u + y_{\xi}v)$, $v_1 = \frac{h_1}{J} (x_{\eta}u + y_{\eta}v)$ [25], in which, u and v are the x and y velocity components, $\xi_x = \frac{y_{\eta}}{J}$, $\xi_y = -\frac{x_{\eta}}{J}$, $\eta_x = -\frac{y_{\xi}}{J}$, $\eta_y = \frac{x_{\xi}}{J}$, where J is the Jacobin function in the form of $J = x_{\xi}y_{\eta} - x_{\eta}y_{\xi}$, and the subscripts (ξ and η) indicate derivatives. The metric factors h_1 and h_2 of the coordinate transformation are defined as $h_1 = \sqrt{x_{\xi}^2 + y_{\xi}^2}$, $h_2 = \sqrt{x_{\eta}^2 + y_{\eta}^2}$, $\hat{U} = \frac{1}{J} (h_2u_1 - \frac{h_3}{h_1}v_1)$, $\hat{V} = \frac{1}{J} (h_1v_1 - \frac{h_3}{h_2}u_1)$, in which, $h_3 = y_{\xi}y_{\eta} + x_{\xi}x_{\eta}$, where θ is the water temperature, s is the salinity, f is the Coriolis parameter, g is the gravitational acceleration, K_m is the vertical eddy viscosity coefficient, and K_h is the thermal vertical eddy friction coefficient. F_u , F_v , F_{θ} , and F_s represent the two horizontal momentum terms, thermal term, and salt diffusion term, respectively. ρ and ρ_o are the perturbation and reference density, which satisfy $\rho_{total} = \rho + \rho_o$. F_u , F_v , F_{θ} , and F_s are calculated by using Smagorinsky's [26] formula in which horizontal diffusion is directly proportional to the product of horizontal grid sizes. K_m and K_h are calculated using the modified Mellor-Yamada level-2.5 turbulent closure scheme [20–22].

The surface and bottom boundary conditions for the momentum and heat equations are given by:

$$\frac{\rho_0 K_m}{D} \left(\frac{\partial u_1}{\partial \sigma}, \frac{\partial v_1}{\partial \sigma} \right) = (\tau_{0\xi}, \tau_{0\eta}); \quad \frac{\rho_0 K_H}{D} \left(\frac{\partial \theta}{\partial \sigma} \right) = Q_{net}; \quad \frac{\rho_0 K_H}{D} \left(\frac{\partial s}{\partial \sigma} \right) = s(\hat{P} - \hat{E}); \quad \omega = 0, \text{ at } \sigma = 0,$$

$$\frac{\rho_0 K_m}{D} \left(\frac{\partial u_1}{\partial \theta}, \frac{\partial v_1}{\partial \theta} \right) = (\tau_{b\xi}, \tau_{b\eta}); \quad \frac{\partial \theta}{\partial \sigma} = 0; \quad \frac{\partial s}{\partial \sigma} = 0; \quad \omega = 0, \text{ at } \sigma = -1$$

where $(\tau_{0\xi}, \tau_{0\eta})$ and $(\tau_{b\xi}, \tau_{b\eta}) = C_d \sqrt{U^2 + V^2} (U^2 + V^2)$ are the ξ and η components of surface wind and bottom stresses; Q_{net} is the net surface heat flux; \hat{P} is the precipitation flux; and \hat{E} is the evaporation flux. The surface wind stress was calculated based on the neutral steady state drag coefficient developed by Large and Pond [27]. The drag coefficient C_d at the bottom is determined by matching a logarithmic bottom layer to the model at a height z_{ab} above the bottom, that is, $C_d = \max \left[k^2 / \ln \left(\frac{z_{ab}}{z_0} \right)^2, 0.0025 \right]$.

where $k = 0.4$ is the Karman's constant and z_0 is the bottom roughness parameter [25].

Eqs. (1)–(7) are solved prognostically as initial value problems of oceanic motion. The initial velocity takes the form $u_1 = v_1 = 0$ and the water elevation is also set to $\zeta = 0$. The initial temperature and salinity are specified using observational data.

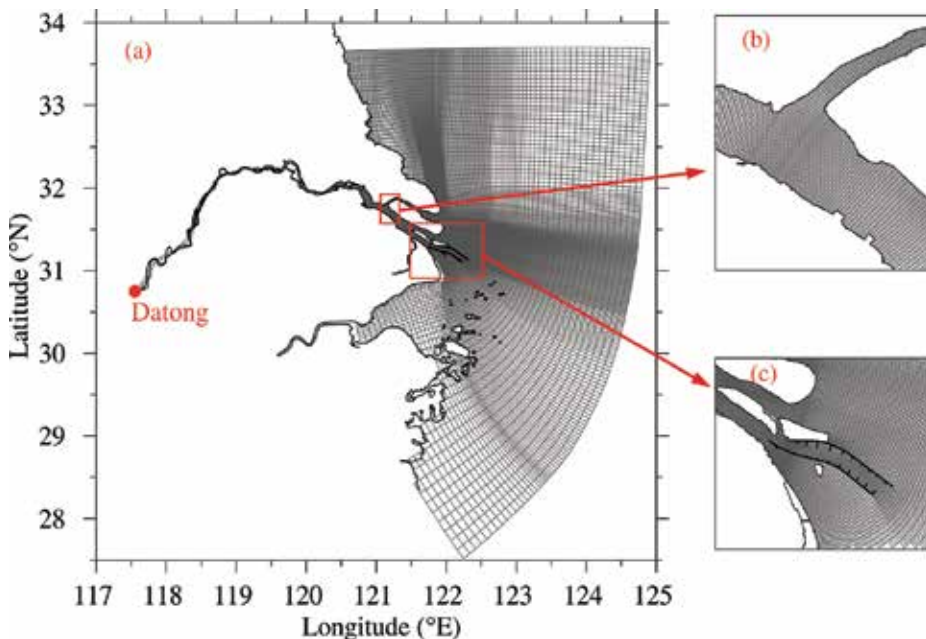


Figure 2. The numerical model mesh (a), an enlarged view of the model mesh around the bifurcation of the NB and the SB (b), and an enlarged view of the model mesh in the NP (c).

The model domain covered the entire Changjiang Estuary, Hangzhou Bay, and adjacent seas from 117.5°E to 125°E and from 27.5°N to 33.7°N (**Figure 2a**). The model was composed of 307×224 cells horizontally and 10 uniform σ levels vertically. The horizontal mesh was designed to fit the coastline, with high-resolution grids near the Changjiang mouth, especially near the bifurcation of the SB and NB (**Figure 2b**), and near the NP where a deep waterway was maintained for navigation (**Figure 2c**). A lower-resolution grid was used in open water. The grid resolution ranged from 300 to 600 m in proximity to the river mouth and was 15 km near open water. A wet/dry scheme was included to characterize the intertidal zone due to tidal excursion, and the critical depth was set to 0.2 m.

Derived from the NaoTide dataset (<http://www.miz.nao.ac.jp/>), the open sea boundary included 16 astronomical constituents: M_2 , S_2 , N_2 , K_2 , K_1 , O_1 , P_1 , Q_1 , MU_2 , NU_2 , T_2 , L_2 , $2N_2$, J_1 , M_1 , and OO_1 . The river boundary in the model was specified by the measured daily river discharge at the location of Datong Hydrographic Station, which is 630 km upstream from the river mouth. Wind field used to calculate the sea surface momentum was simulated by the WRF (Weather Research Forecast) Model, or from the observed data of weather station at the Chongming eastern shoal.

The velocities and elevation were initially set to zero. The initial salinity distribution was derived from the Ocean Atlas in the Huanghai Sea and East China Sea (Hydrology) (Editorial Board for Marine Atlas [28]) outside the Changjiang mouth and from observed data inside the river mouth in recent years. Because salinity dominates the density variability in the Changjiang Estuary, water temperature was set to a constant value of 10°C in the model. We have been applying the model in the Changjiang Estuary to study the hydrodynamic processes and saltwater intrusion and have done a lot of work on model validation. The numerical model has been validated many times using data in the Changjiang Estuary, and the results suggest that the model can successfully simulate the hydrodynamic processes and saltwater intrusion in the estuary. A detailed description of the model validation can be found in Wu and Zhu [24], Li et al. [4], and in Qiu and Zhu [12].

3. Dynamic mechanism of saltwater intrusion

The saltwater intrusion in the Changjiang Estuary is controlled mainly by the runoff and tide, but is also influenced by wind, topography, sea level rise, and various projects in the river watersheds and estuary. Using the numerical model described above, we first simulated the saltwater intrusion considering various dynamic factors in a climatological state and then analyzed the impacts of various dynamic factors on the saltwater intrusion using sensitivity experiments.

3.1. Simulation of saltwater intrusion

We considered the monthly mean river discharge and wind in winter to simulate the climatological saltwater intrusion. The river discharge was set at 11,800 m³/s, which was the mean value measured at Datong Station in January and February from 1950 to 2015. The surface

wind was set to a northerly wind with a constant speed of 5 m/s, which is roughly the mean wind condition in the estuary in winter. The model was run for 60 days from January 1 to March 1, and the analysis was carried out on the outputs of the last spring-neap tidal cycle, or 15 days for salinity spatial distribution, and of the last two spring-neap tidal cycles, or 30 days for temporal variation of salinity at the water intakes of the reservoirs.

To describe the subtidal movement of water in the Changjiang Estuary, we filtered out the tidal current to obtain the residual current during spring and neap tides. In this study, six semidiurnal tidal cycles were used as an averaging time window to remove the semidiurnal and diurnal tidal signals.

The residual water current in the Changjiang Estuary is influenced by several dynamic factors, including runoff, tide, wind, and density gradient. Abundant water discharge drives the residual current to flow seaward, and most is diverted into the SB because of the nearly orthogonal bifurcated channel (**Figure 3**). During spring tide, the surface residual current in the upper reaches of the NB is landward, whereas the residual current is seaward in the middle and lower reaches (**Figure 3a**). Compared to that in the NB, the surface residual current in the SB is much larger. The surface residual currents in the NC, NP, and SP all flow seaward [12].

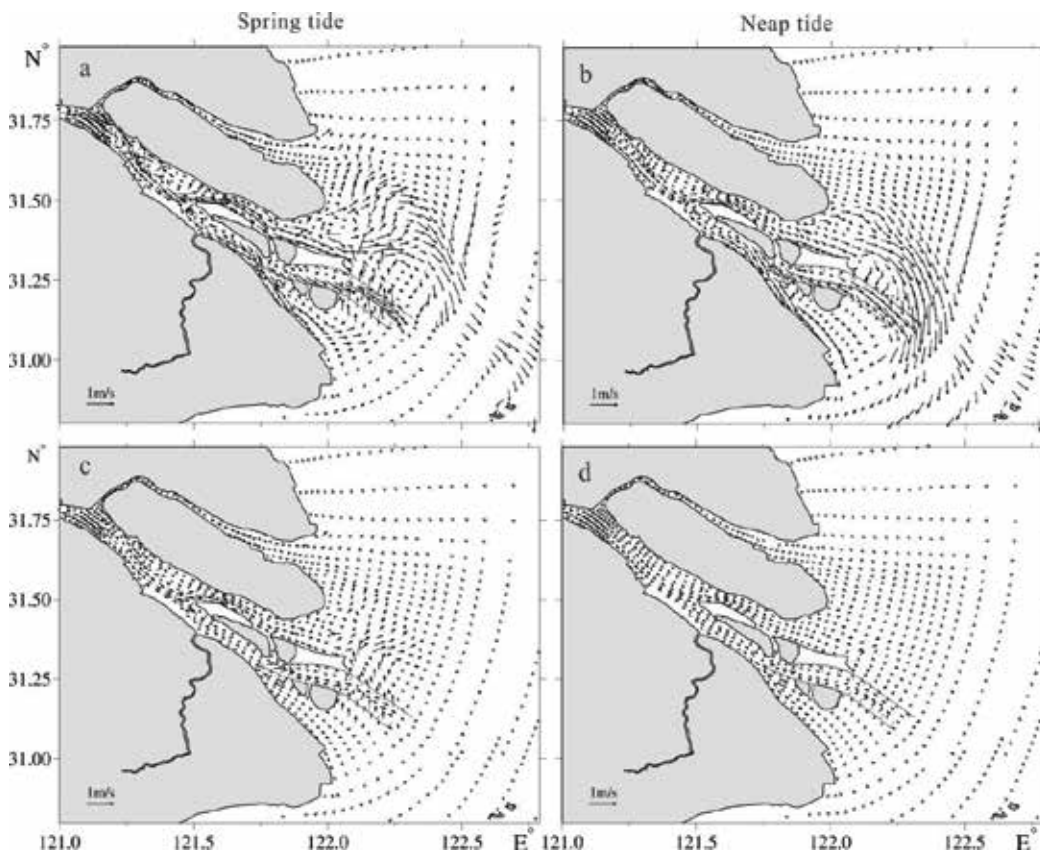


Figure 3. Distribution of residual currents during spring tide (left panel) and neap tide (right panel) under the river discharge of 11,800 m³/s. (a and b) Surface layer; (c and d) bottom layer.

Moreover, the water overflows across the DWP (Deep Waterway Project) from the SP into the NP and even into the NC, and this acts as one-way transport because the water can cross the dike during flood tide and cannot return to the SP due to the lower elevation during ebb tide. In the bottom layer, the pattern of the residual current is similar with that in the surface layer, but the current is much weaker due to the bottom friction (**Figure 3c**).

During neap tide, the residual current in the surface layer of the upper reaches of the NB is seaward, that is, the net water transport is from the SB into the NB (**Figure 3b**), just opposite of the situation in spring tide. The residual current on the east side of Chongming Island flows eastward and then flows southeastward under the force of northerly wind, rather than flowing northeastward in spring tide, because the wind can easily change the weaker tidal current in neap tide. The overflow across the DWP vanishes in neap tide due to the smaller tidal range. In the bottom layer, the residual currents in neap tide in the SP, middle and lower reaches of the NP, and in the sandbar of the NC are all landward flow because the vertical mixing becomes weaker, which results in stronger landward baroclinic pressure force (**Figure 3d**).

The NB is totally occupied by high-saline water, and the isohaline 5 is close to the bifurcation of the NB and SB. There exist salinity fronts in the upper reaches of the NB, sandbar areas of the NC, NP, and SP (**Figure 4**). At flood slack during spring tide, the saltwater spills over from the NB into the SB, resulting in the water mass with salinity greater than 0.45 appearing in the upper reaches of the SB (**Figure 4a**). As suggested by Wu and Zhu [29], the SSO is mainly caused by the Lagrangian residual and tidal pumping. There exists fresh water in the SB. Around the river mouth, high-salinity water intrudes, and salinity differs among the channels. The distance that isohaline 15 moves upstream in the SP is pronounced compared to that in the NP and is pronounced in the NP compared to that in the NC. The saltwater intrusion in the SP is stronger than that in the NP and is stronger in the NP than that in the NC. In the bottom layer, due to the gravity force, the salinity in the sandbar areas of the NC, NP, and SP is higher

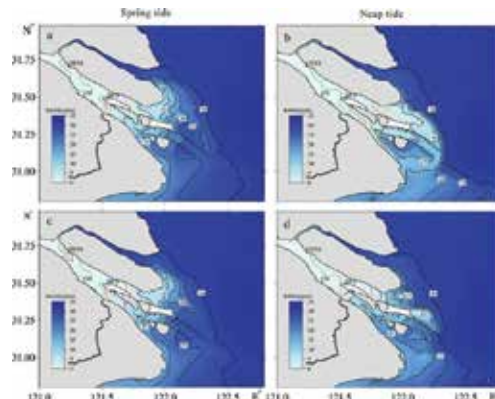


Figure 4. Distribution of salinity at flood slack during spring tide (left panel) and neap tide (right panel) under the river discharge of $11,800 \text{ m}^3/\text{s}$. (a and b) Surface layer; (c and d) bottom layer. The green isohalines are 0.45; the red isohalines 1.00; the orange isohalines 2.00; and the black isohalines begin at 5.00 with an interval of 5.00. The reference site of flood slack is Baozhen hydrologic station (red dot, labeled in **Figure 1**), similarly hereinafter.

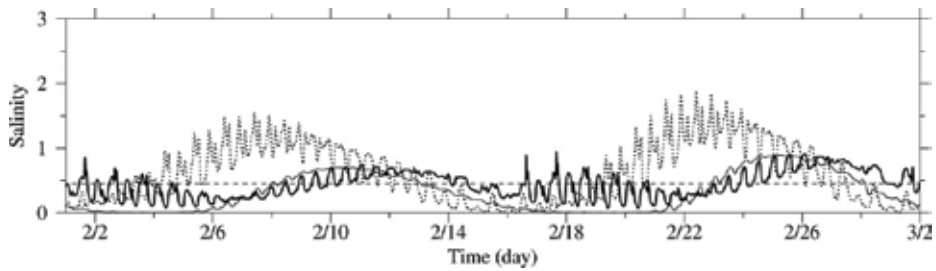


Figure 5. Temporal variation of salinity at the water intakes of the reservoirs under the river discharge of $11,800 \text{ m}^3/\text{s}$. Dashed curve: Dongfengxisha reservoir; thin curve: Chenhang reservoir; and thick curve: Qingcaosha reservoir. The horizontal dashed line is the salinity of 0.45, which is the salinity standard of drinking water, similarly hereinafter.

than that in the surface layer (**Figure 4c**). In other water areas, the salinity in the bottom layer is almost the same as that in the surface layer, due to strong vertical mixing in spring tide.

At flood slack during neap tide, the salinity at the upper reaches of the NB becomes lower, and the isohalines extend downstream due to the lower tidal range (**Figure 4b**). There is no SSO; the saline water induced by the SSO in spring tide moves downstream under the runoff force in the SB. Consistent with the change of residual current, the northward extension of the diluted water on the east side of Chongming Island, which appears in spring tide, vanishes, and the distance of eastward freshwater transport in the NC is pronounced. Compared with the saltwater intrusion in the NC, NP, and SP during spring tide, the intrusion becomes weaker in the surface layer due to weaker tide, but becomes stronger in the bottom layer due to weaker vertical mixing and stronger landward baroclinic pressure force and stratification in neap tide.

At present, approximately 70% freshwater supply in Shanghai is taken from the water resources in the Changjiang Estuary. The saltwater intrusion in winter threatens the freshwater safety of the city. There are three reservoirs in the estuary, that is, the QCSR, Chenhang Reservoir, and Dongfengxisha Reservoir (locations marked in **Figure 1**). During saltwater intrusion, the salinity is higher than 0.45 (the salinity standard of drinking water) at water intakes, and the reservoirs can no longer take water from the Changjiang Estuary. Under the river discharge of $11,800 \text{ m}^3/\text{s}$ during a period of spring-neap tide in February, approximately two-thirds of the time water is taken from the Chenhang Reservoir; approximately half the time, from the Dongfengxisha Reservoir; and more than half the time, from the QCSR (**Figure 5**). Therefore, it is not a problem for the reservoirs in the Changjiang Estuary to receive fresh water from the river to meet the supply demand of drinking water under the climatological mean value of river discharge.

3.2. Impact of river discharge

River discharge is one of the most important dynamic factors determining estuarine saltwater intrusion. The measured river discharge at Datong Station, which accounts for 94.7% of the total river basin discharge, is the upper tidal limit in dry season and is generally used as an

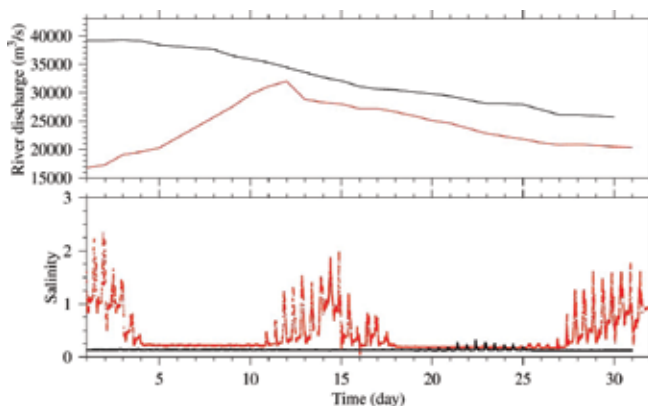


Figure 6. Temporal variation of observed salinity at Chongxi hydrologic station. Red line: March 2009; black line: September 2009.

upper boundary of the estuary in modeling. The river discharge has seasonal variation, which increases from January to July, and then decreases from July to December. The monthly mean river discharge has the minimum of $11,500 \text{ m}^3/\text{s}$ in January and reaches the maximum of $49,800 \text{ m}^3/\text{s}$ in July (Changjiang Water Resources Commission, based on the data from 1950 to 2016). The river discharge has interannual variation with higher or lower values in some winters. In this subsection, we analyze the impact of river discharge on the saltwater intrusion based on the measured data and numerical experiments.

The Chongxi Hydrologic Station is located southwest of Chongming Island (red dot in **Figure 1**). The measured salinity shows that the saltwater intrusion was stronger during spring tide, with salinity higher than 1.0 in March 2009 when the river discharge at Datong Station was lower, and the intrusion was very weak in the whole month of September in 2009 when the river discharge at Datong Station was higher (**Figure 6**). Therefore, seasonal variation of river discharge has significant influence on the saltwater intrusion in the estuary.

Salinity at the Chongxi Hydrologic Station was higher during spring tide when the river discharge at Datong Station was lower in April 2009 and was also higher during the first 5 days in April 2010 when the river discharge was close to that in April 2009. In contrast, salinity was much lower, and there was no saltwater intrusion from 6 to 30 in April 2010 when the river discharge was distinctly higher (**Figure 7**). These observational results indicate that annual variation of the river discharge has evident impact on the saltwater intrusion in the estuary.

Besides the numerical experiment with the climatological value of river discharge in January and February, we performed two more experiments with a higher river discharge of $14,000 \text{ m}^3/\text{s}$ and a lower river discharge of $8000 \text{ m}^3/\text{s}$ to compare their impacts on the saltwater intrusion. Under the river discharge of $14,000 \text{ m}^3/\text{s}$, the salinity in the upper reaches of the NB is obviously decreased (**Figure 8**); there is no saline water with salinity greater than 0.45 in the SB, that is, no SSO occurs. At flood slack during spring and neap tides, there is fresh water in both surface and bottom layers at the three water intakes of the reservoirs. Compared with the results under the river discharge of $11,800 \text{ m}^3/\text{s}$, the isohalines near the river mouth under the

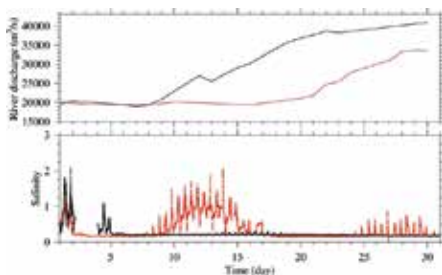


Figure 7. Temporal variation of observed salinity at Chongxi hydrologic station. Red line: April 2009; black line: April 2010.

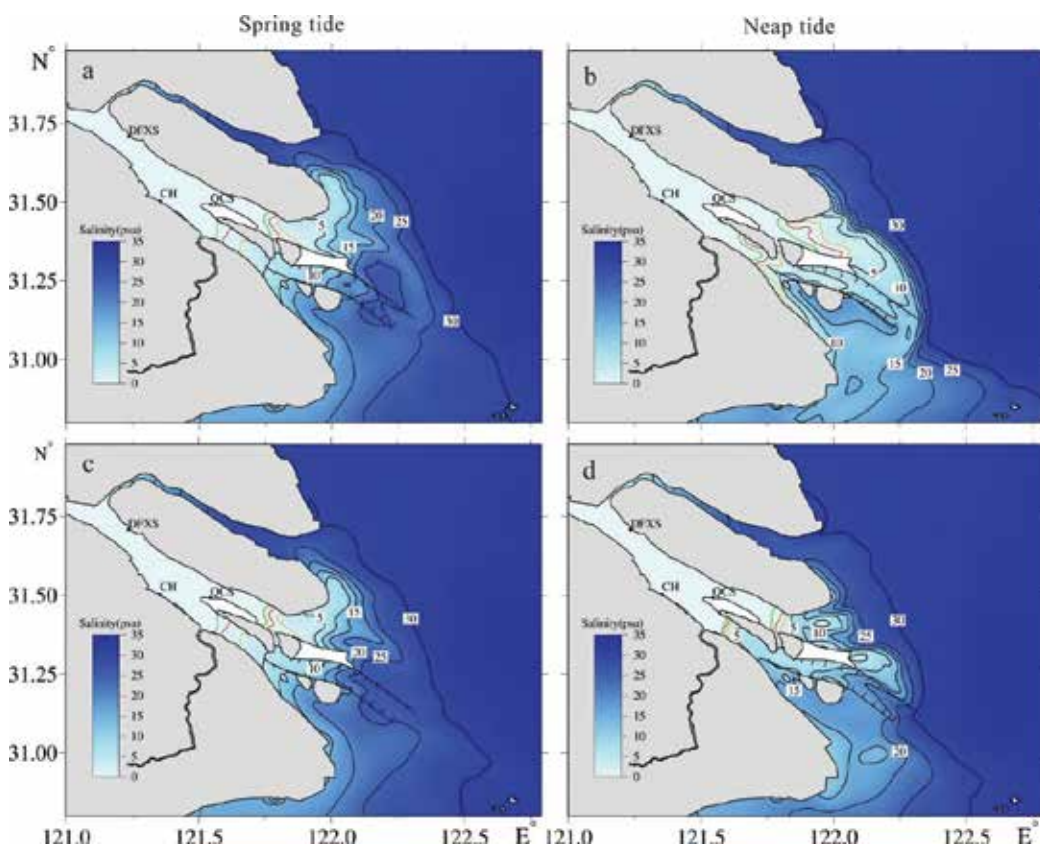


Figure 8. Distribution of salinity at flood slack during spring tide (left panel) and neap tide (right panel) under the river discharge of 14,000 m³/s. (a and b) Surface layer; (c and d): bottom layer.

river discharge of 14,000 m³/s move downstream distinctly, indicating that the saltwater intrusion is weakened due to larger river discharge. In spring tide, more diluted water is transported from the NC into the NB (**Figure 8a** and **c**). Compared with the locations of the isohalines in spring tide, the isohalines of 0.45 in the NC and SC move downstream in neap

tide (**Figure 8b** and **d**), meaning that the saltwater intrusion in neap tide is weaker than that in spring tide.

Under a larger river discharge of $14,000 \text{ m}^3/\text{s}$, the salinity during a period of spring-neap tides in February at the water intakes of the Qingcaosha and Chenhang reservoirs is lower than 0.45 at any time, that is, there is no saltwater intrusion influencing the water intakes of the two reservoirs (**Figure 9**). Approximately, two-thirds of the time the salinity at the water intake of the Dongfengxisha Reservoir is lower than 0.45. Therefore, there is sufficient time for the reservoirs to take fresh water from the river when the river discharge is larger.

Under the lower river discharge of $8000 \text{ m}^3/\text{s}$, the salinity in the upper reaches of the NB is obviously increased (**Figure 10**). There is saline water with salinity greater than 1.0 in the SB, that is, SSO becomes stronger. At flood slack during spring and neap tides, there is no fresh water in both surface and bottom layers at the three water intakes of the reservoirs. Compared with results under the river discharge of $11,800 \text{ m}^3/\text{s}$, the isohalines near the river mouth move upstream clearly, indicating that the saltwater intrusion is enhanced due to the lower river discharge. Compared with the locations of the isohalines in spring tide, the isohaline 5 in the NC and the SC moves downstream in neap tide, meaning that the saltwater intrusion in neap tide is weaker than that in spring tide. Salinity is higher than 20 in most areas of the SP, that is, the saltwater intrusion there is very strong.

Under the lower river discharge of $8000 \text{ m}^3/\text{s}$ during a period of spring-neap tides in February, fresh water can be taken from the river approximately one-thirds of the time for the Dongfengxisha Reservoir, half the time for the Chenhang Reservoir, and shorter time for the QCSR (**Figure 11**). Therefore, there is less time for the reservoirs to take fresh water from the river when the river discharge is lower.

Based on the analyses of observed data and numerical experiments, we can conclude that the effect of river discharge on the saltwater intrusion in the Changjiang Estuary is significant. When the river discharge decreases, SSO and saltwater intrusion are enhanced in each channel.

3.3. Impact of tide

The tides in the estuary exhibit semidiurnal, diurnal and fortnightly spring-neap signals [5, 25]. The tide is medium with mean tidal range of 2.66 m at the mouth, and is the most energetic

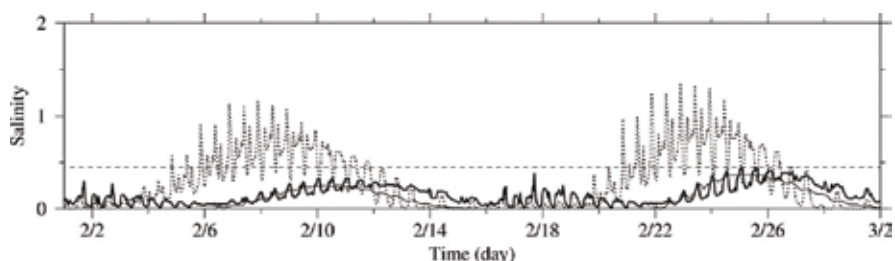


Figure 9. Temporal variation of salinity at the water intakes of the reservoirs under the river discharge of $14,000 \text{ m}^3/\text{s}$. Dashed curve: Dongfengxisha reservoir; thin curve: Chenhang reservoir; and thick curve: Qingcaosha reservoir.

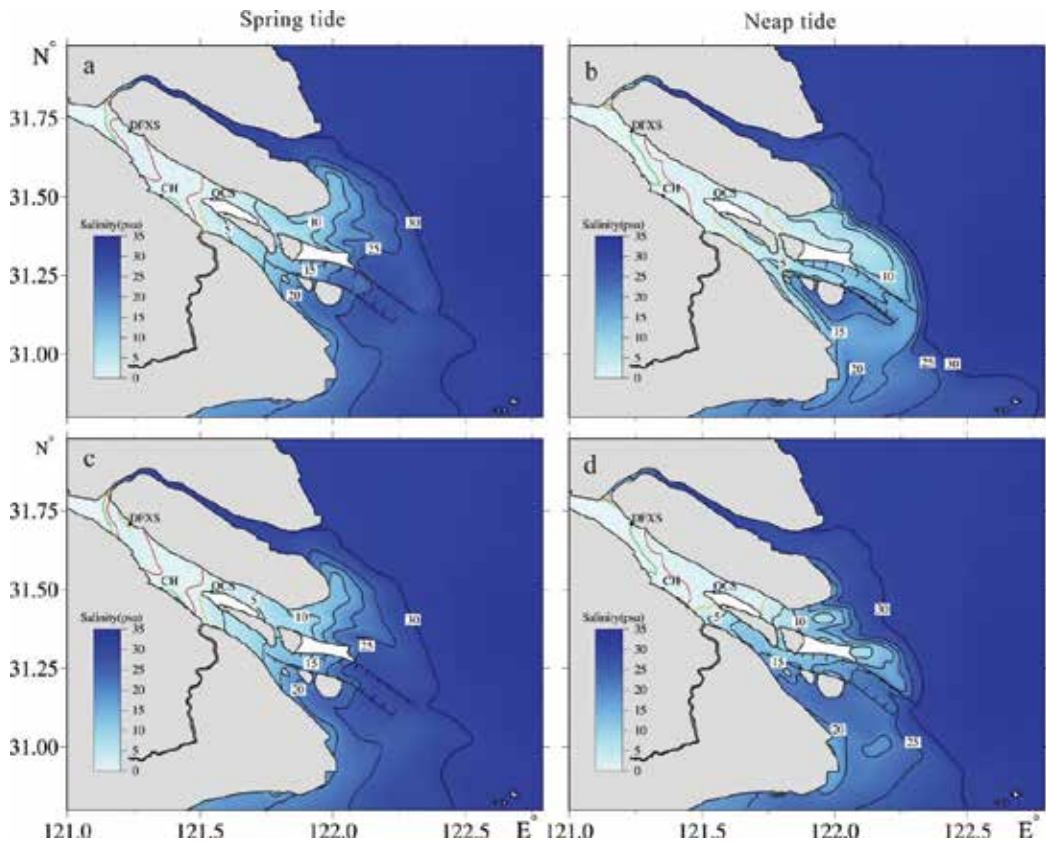


Figure 10. Distribution of salinity at flood slack during spring tide (left panel) and neap tide (right panel) under the river discharge of 8000 m³/s. (a and b) Surface layer; (c and d) bottom layer.

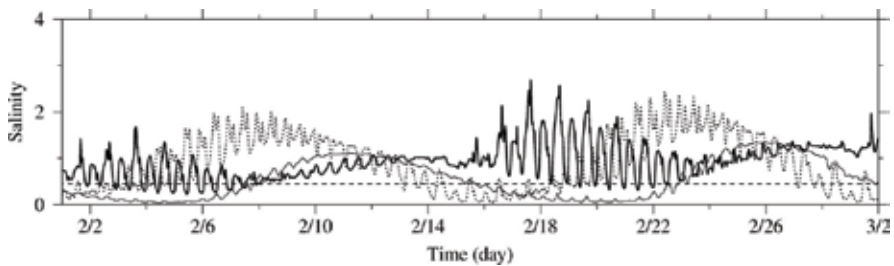


Figure 11. Temporal variation of salinity at the water intakes of the reservoirs under the river discharge of 8000 m³/s. Dashed curve: Dongfengxisha reservoir; thin curve: Chenhong reservoir; and thick curve: Qingcaosha reservoir.

source of water movement in the Changjiang Estuary. On the intertidal timescales, the semidiurnal tide drives saltwater into the estuary during flood tide and out of the estuary during ebb tide. The fortnightly spring tide generates a greater saltwater intrusion than the neap tide does. The saltwater intrusion is also enhanced by the seasonal variability of tides, with the maximum tidal range in March [8, 25].

The results of numerical experiments in Subsections 3.2 and 3.3 clearly show that the saltwater intrusion in spring tide is stronger than that in neap tide. In this subsection, we further analyze the impact of tide on saltwater intrusion based on the observed data. We conducted an observation in the SP in January 2010 and selected one measured site located in the upper reaches of the SP to illustrate the variation of currents and salinity with tides (**Figure 12**). The observed data show that the current was a rectilinear current inside the river mouth rather than a rotational current as that outside the river mouth. The current speed was larger in the spring tide than in the neap tide. The current speed in the surface layer was larger than that in the bottom layer due to the bottom friction. The current duration in ebb current was longer than that in flood current. The salinity in the surface layer was higher than that in the bottom layer. The semidiurnal and fortnightly variations of salinity were evident, which were certainly caused by tides.

The observed salinity at the Chongxi Hydrological Station in January 2010 also distinctly shows semidiurnal and fortnightly variations with tides (**Figure 13**). Therefore, tides are one of the important dynamic factors determining the saltwater intrusion in the estuary.

3.4. Impact of wind

Wind over the Changjiang Estuary is primarily the monsoon, which is weak southerly in summer and strong northerly in winter. Li et al. [4] studied the impact of wind on the saltwater intrusion in the Changjiang Estuary. The observation at the Chongxi Hydrologic Station indicated the salinity increased abnormally during strong northerly wind. It was confirmed

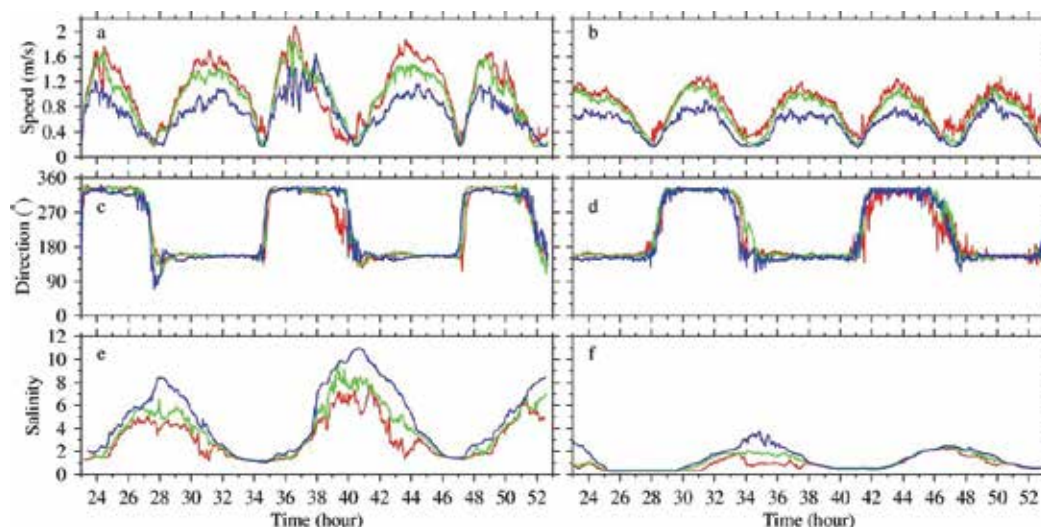


Figure 12. Temporal variations of observed current speed (upper), current direction (middle), and salinity (lower) at the upper reaches of the SP during spring tide (left panel, from 23:00 on January 18 to 5:00 on January 20, 2010) and the neap tide (right panel, from 23:00 on January 25 to 5:00 on January 27, 2010). Red line: surface layer; green line: middle layer; and purple line: bottom layer.

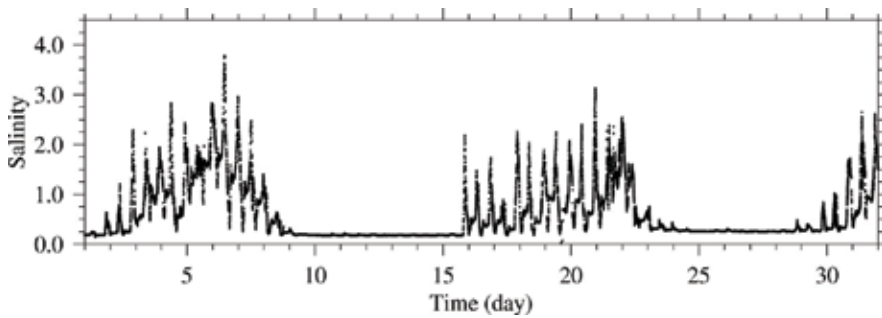


Figure 13. Temporal variation of observed salinity at Chongxi hydrological station in January 2010.

that the abnormal increments of salinity at the Chongxi Hydrologic Station during the neap and moderate tides were caused by strong northerly wind.

Numerical experiments were carried out to study the effects of different wind speeds and directions on wind-driven currents and saltwater intrusion. In the control experiment, the river boundary was specified using a discharge of $11,000 \text{ m}^3/\text{s}$, which was roughly the monthly averaged value in January and February; wind was set to the northerly wind of 5 m/s , which represented the general wind condition in January and February. Two additional numerical experiments were run without wind (Experiment A) or with stronger northerly wind of 10 m/s (Experiment B), to represent weaker and stronger wind stress cases. In addition, two more experiments with a northeasterly wind of 5 m/s (Experiment C) and a northwesterly wind of 5 m/s (Experiment D) were conducted to explore the effect of wind direction on the saltwater intrusion.

When driven by the northerly wind of 5 m/s , southward currents along the Subei Coast formed and landward Ekman transport appeared due to the Coriolis force (**Figure 14a**). In the lower reaches of the NB, the wind-driven circulation was landward on the north side and seaward on the south side to ensure the mass conservation. In the SC and NC, a significant horizontal circulation is formed, which flowed landward in the NC and seaward in the SC. In the SP and NP, this circulation was seaward. Such patterns of wind-driven circulation can increase the flood current and decrease the ebb/net water current in the NC, thereby restricting the extension of the fresher water there and weakening the saltwater intrusion in the SC, SP, and NP. In addition, the wind-induced circulation in the upper and middle reaches of the NB flowed into the SB and discharged seaward in the upper reaches of the SB [4].

The difference of depth-averaged salinity between Experiment A (no wind) and the control experiment during spring tide is shown in **Figure 15a**. In Experiment A, because there is no wind-driven southward current along the coast and the landward Ekman water transports, the salinity in the mouth of the NB was significantly decreased by 3–10, and decreased by 1 off the SP and NP. In addition, without considering the wind-driven circulation, the saltwater intrusion in the upper reaches of the NB was weakened with salinity decreasing by 1–5, and the intensity of SSO was abated, which caused a slight decrease of salinity in the SB. Without the effects of wind-driven circulation in the SC and NC, the saltwater intrusion in the NC was

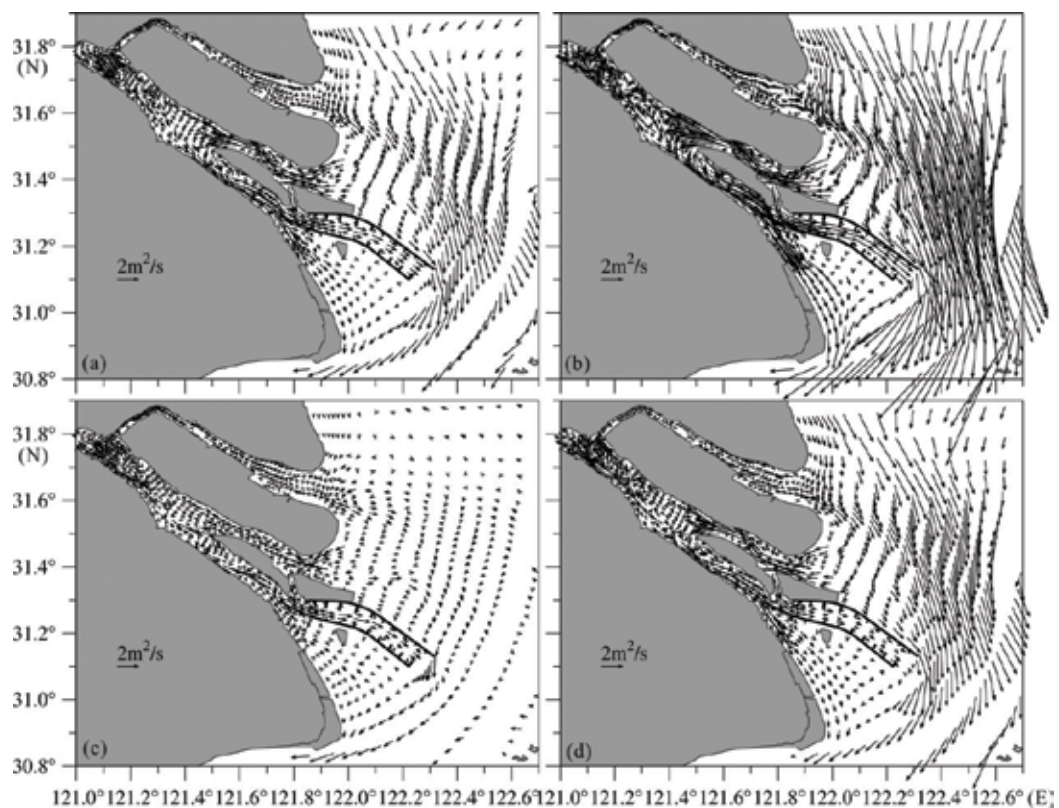


Figure 14. Pure wind-driven net unit width water flux under the northerly wind of 5 m/s (a), the northerly wind of 10 m/s (b), the northeasterly wind of 5 m/s (c), and northwesterly wind of 5 m/s (d).

weakened with salinity decreasing by 0.2–1.0, whereas that in the SC, SP, and NP was enhanced with salinity increasing by 1–3. During neap tide, there was larger variation of salinity in the mouth of the NB, the eastern of the Chongming Island and the SP compared to that during spring tide (not shown) [4].

The wind-driven current was enhanced greatly by the northerly wind of 10 m/s, but the current pattern remained the same as that in the control experiment (**Figure 14b**). Under the interaction of river discharge and tide, when including the northerly wind of 10 m/s (Experiment B), the wind driven circulation during the spring tide off the Changjiang Estuary brought more seawater to the mouth, and the salinity off the NB increased by 1–5 compared to the control experiment. The salinity in the upper reaches of the NB increased by 5 and thereby enhanced the SSO, which further increased the salinity with a range of 1–2 in the SB. The salinity in the east of Chongming Island increased by more than 20, and the saltwater intrusion was pronounced in the NC with salinity increase of 5–20. The salinity in the SC increased by ~1, which was due to the stronger SSO. The saltwater intrusion in the SP and NP were weakened, and the salinity decreased by a maximum value of 5 in the SP. During neap tide (not shown), the difference of salinity in the NC and SP was more significant compared to that during spring tide, whereas it was almost the same in the rest of the study area [4].

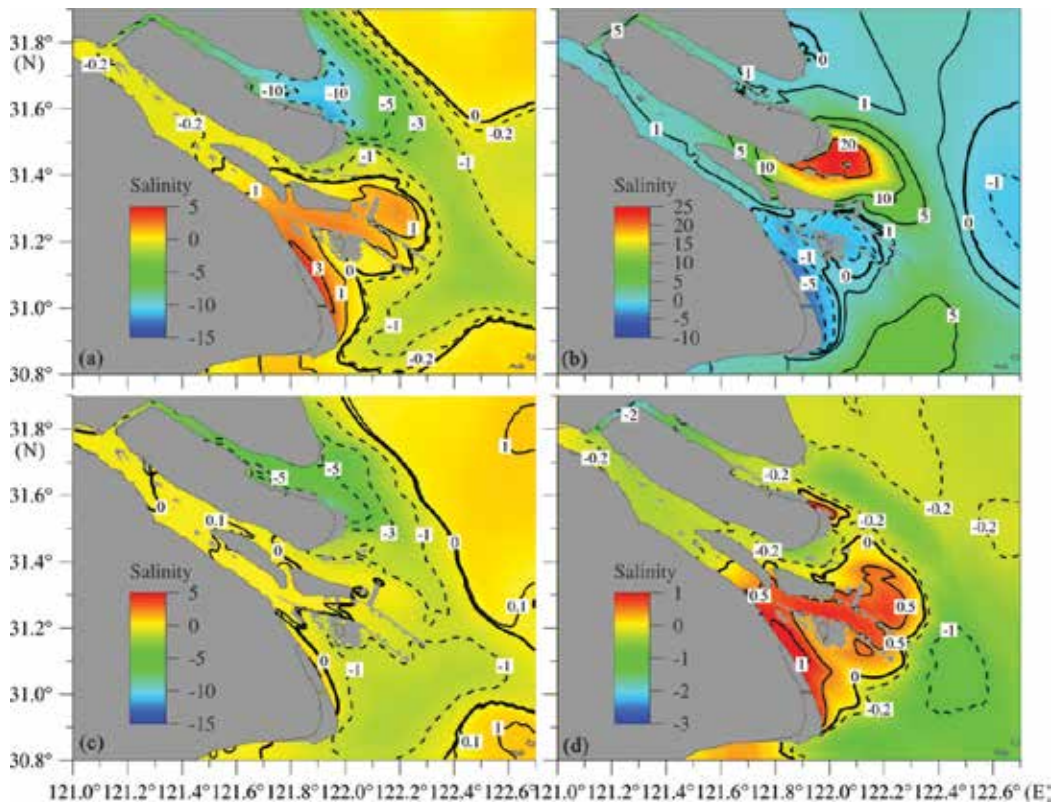


Figure 15. Salinity difference distribution of depth-averaged salinity in experiment a (a), experiment B (b), experiment C (c), and experiment D (d) with respect to depth-averaged salinity in the control experiment during spring tide. Zero contour is bold, solid contours denote positive values, and dashed ones denote negative values.

When driven by the northeasterly wind of 5 m/s, the wind-driven circulation in the lower reaches of the NB as well as that in the SC and NC was significantly weakened (**Figure 14c**). Under the interaction of river discharge and tide, when including the northeasterly wind of 5 m/s (Experiment C), a weaker saltwater intrusion in the NB was detected during the spring tide (**Figure 15c**), compared to the control experiment, and their difference was more than 5 at the mouth and decreased gradually to 1 in the upper reaches. The salinity at the mouth of the NC decreased by 1–3, while it decreased by ~1 in the middle and lower reaches of the NP and SP, and in the areas off the SP and NP. In addition, the salinity in most areas of the SB, the upper reaches of NC, the SC, and the upper reaches of the NP is similar to that in the control experiment. In Experiment C, the relatively weak circulation in the NC led to fresher water there exchanging with the high-saline water off the NB and further decreased the salinity in the NB with strong tide [4].

When driven by the northwesterly wind of 5 m/s, the features of wind-driven circulation in the SC and NC are similar to those under the northerly wind of 5 m/s. Along the southeast-ward channel in the middle and lower reaches of the NB, the seaward water transport driven by local wind stress is greater than that induced by landward Ekman transport, and the wind-driven

circulation was from the SB to the NB (**Figure 14d**) to ensure the continuity of water mass [4]. Under the interaction of river discharge and tide, when including the northwesterly wind of 5 m/s (Experiment D), the salinity in the middle and lower reaches of the NB decreased by 0.2 during spring tide (**Figure 15d**), while it decreased by 2 in the upper reaches. The local effects of the northwesterly wind in the middle and lower reaches of the NB restrict flood tidal currents, and thereby weaken the saltwater intrusion in this channel. The salinity decreased by 0.2 in the middle and upper reaches of the SB and in the upper reaches of NC, while it increased by 0.5 in the mouth of the NC, SP, and NP [4].

3.5. Impact of sea level rise

Global sea level rise has been of great concern by governments and societies with its impacts on saltwater intrusion and material transports in estuaries, which threaten freshwater habitats and drinking water supplies. Sea level rise deepens water depth and changes currents and saltwater intrusion in estuaries. Qiu and Zhu [13] simulated the variations of saltwater intrusion according to different sea level rise scenarios in a typical year and a dry year. Three sea level rise scenarios were considered. Scenario 1: 2.90 mm/a, total sea level rise around 0.290 m in future 100 years; Scenario 2: 4.83 mm/a, total sea level rise around 0.483 m in future 100 years; and Scenario 3: 10.00 mm/a, total sea level rise around 1.000 m in future 100 years. The river discharge record from 1990 to 2013 at Datong Station showed that a severe drought occurred in January 1999, with an average discharge of 9480 m³/s, while the discharge is 13,463 m³/s in the same month of 2012, which was a typical year. The saltwater intrusion generally occurs from the mid-December and keeps on influencing the Changjiang Estuary until the following March. The river discharge reduces to its minimal value in January, during which the saltwater can intrude farther upstream and the saltwater intrusion becomes the most serious in the whole year. Thus, the period of model simulation was set from October to the following May to present the whole process of saltwater intrusion and focus on the monthly mean salinity during January. The river discharges from 1998 to 1999 (dry year) and from 2011 to 2012 (typical year) were used [13].

To evaluate the influence of sea level rise on the saltwater intrusion in the Changjiang Estuary, both present-day sea level and future scenarios with sea level rise were used in the simulations. In the base case, the model results for the dry year and typical year were simulated by using the present-day sea level. In each sea level rise scenario, the increased sea level was added to the mean sea level used in the base case. We named the cases as Experiment S1, S2, and S3 to indicate the situations after sea level rising by 0.290, 0.483 and 1.00 m, respectively [13]. All other set-ups in these cases were identical to the base case.

In a dry year, the saltwater near the river mouth intrudes more landward than that in a typical year, and the distance that isohaline 1 moves upstream in the upper NC and the SC is distinctly farther (**Figure 16a** and **b**). The NB is generally occupied by saline water in both dry and typical years, while the SSO is pronounced in a dry year due to the lower river discharge [13].

Figure 16C–H shows pronounced variation, that is, salt content increases obviously as sea level rises in both dry year and typical year. Due to the difference of river discharge, the change

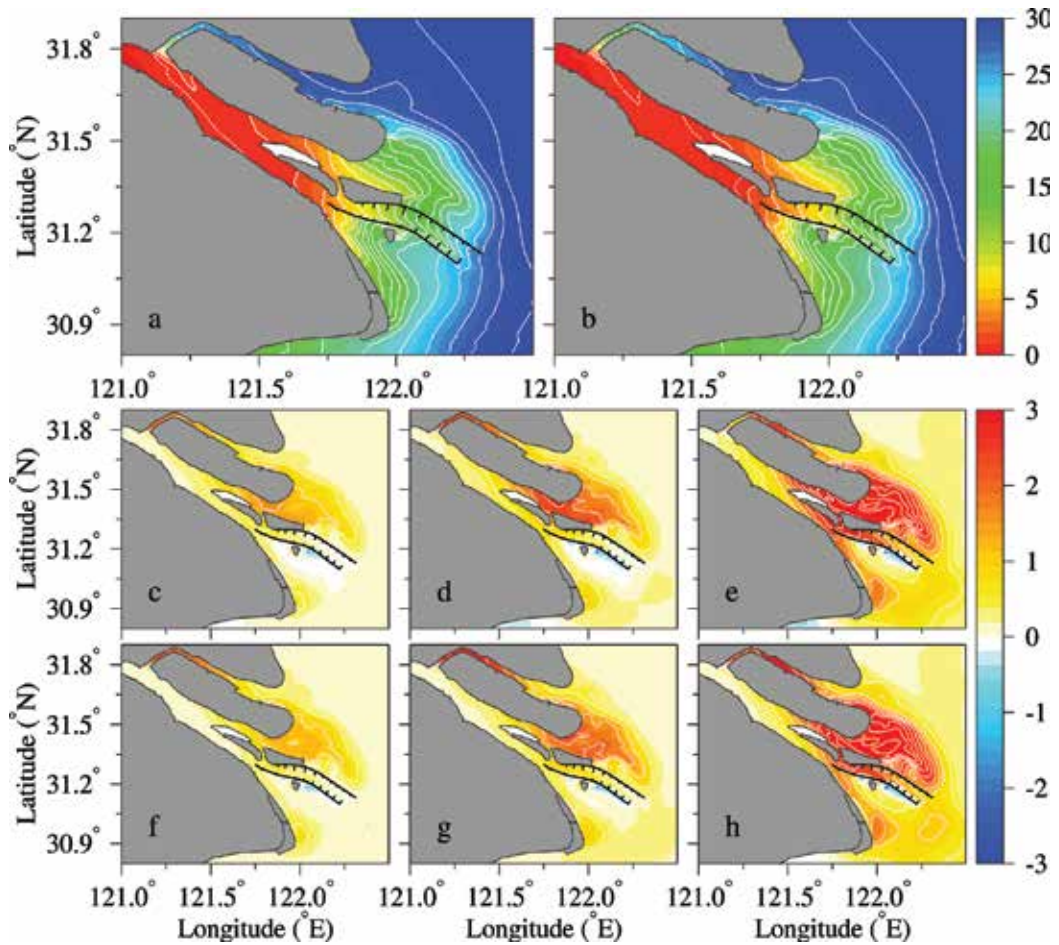


Figure 16. Distributions of depth-averaged salinity in the base case in dry year (a) and typical year (b), respectively. White lines indicate the salinity isohalines from 1 to 31 with an increment of 2, and the dashed lines indicate the isohaline of 0.5. (c-h) Distributions of depth-averaged salinity difference in numerical experiments S1, S2, and S3 with respect to the base case during January in dry year (c, d, e) and typical year (f, g, h), respectively. White lines indicate the salinity difference isohalines with an interval of 0.50. All the results are monthly mean in January in the corresponding year [13].

of saltwater intrusion has an interannual variation, namely, the salinity increase in the NC, NP, and SP is larger in a dry year than that in a typical year as sea level rises. However, because the salt content in the NB is higher in a dry year than in a typical year in the base case (**Figure 16a** and **b**), salinity increase is lower in a dry year in all sea level rise scenarios. Wu et al. [2] showed a relationship between runoff and semi-monthly water flux in the upper NB, which suggests that the SSO may impact the SB more severely under a lower river discharge. The SSO, together with the enhanced saltwater intrusion from the NC, increases the salt content in the upper SB in both dry and typical years with rising sea level (**Figure 16C-H**). Under the lower river discharge, the salinity increase in a dry year is more pronounced in the upper SB as sea level rises, and the enhanced SSO is one of the important factors for this

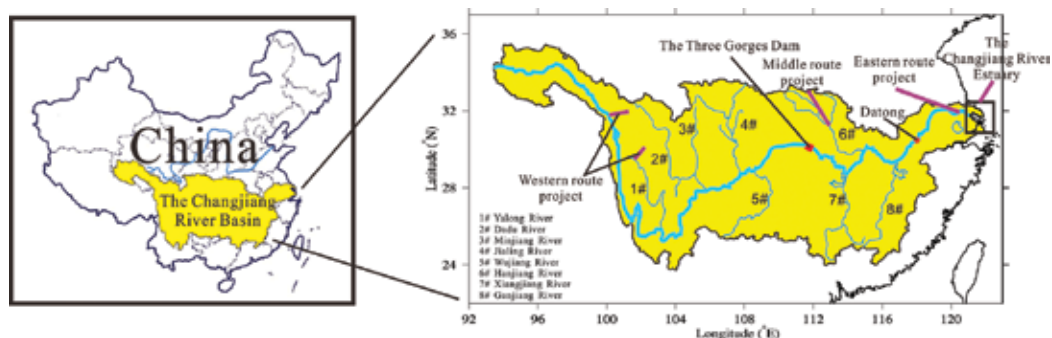


Figure 17. Sketch of the Changjiang Basin and the locations of the Three Gorges Project and Water Diversion South to the North Project.

increase [13]. Then, the increased SSO will move downstream under runoff and impact the lower reaches.

3.6. Impact of major projects in the river basin and estuary

There have been many man-made projects in the river basin and estuary. In this subsection, we consider the impacts of one major project in the estuary and two major projects in the river basin on the saltwater intrusion. The three projects are the DWP in the estuary (labeled in **Figure 1**), the Three Gorges Dam (TGD), and the Water Diversion South to the North Project (WDP) (**Figure 17**).

Zhu et al. [10] analyzed the impact of the DWP on the saltwater intrusion in the Changjiang Estuary. In the NC, the saltwater intrusion was alleviated distinctly after the DWP, because the dykes of the project blocked off the southward drift of the brackish water plume under the northerly monsoon and the Coriolis force. The saltwater intrusion in the project area was intensified at the upper section and alleviated at the lower section. In the SP, the saltwater intrusion was intensified as the background salinity increased and the river discharge decreased. The DWP had an obvious impact on the saltwater intrusion in the Changjiang Estuary [10].

The TGD is the largest water conservancy project in the world. It significantly regulates the discharge of the Changjiang on a seasonal scale [10]. It stores water in autumn and releases it during the following dry season. Qiu and Zhu [12] used the numerical model to simulate the seasonal saltwater intrusion around the Changjiang Estuary under the scenarios with and without the TGD regulation. The seaward residual water transport was augmented during the dry season after the TGD began operating, which means that more fresh water was discharged into the sea, resulting in a weaker saltwater intrusion in each channel. During spring tide (**Figure 18a**), the salinity generally decreased in the estuary. The net water flux increased in the NB and diluted the high-salinity water in its upper reaches [12]. This led to a decline in the salt flux that spilled over into the SB. Around the river mouth, the salinity in the NP and SP generally decreased to about 1. In the NC, the salinity also decreased. During neap tide (not shown), the salinity difference reached -2.5 in the upper

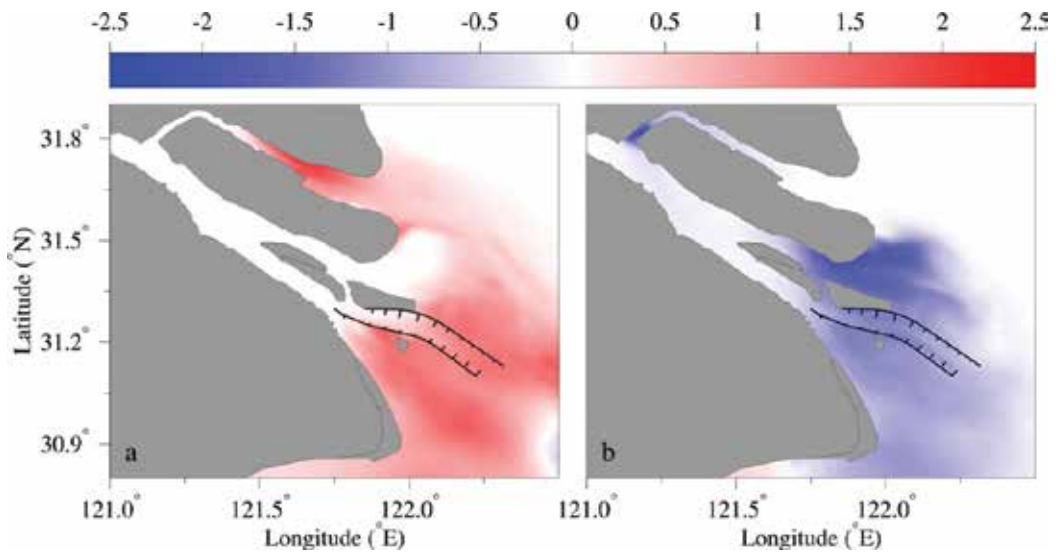


Figure 18. Tidally averaged surface salinity difference between after and before the project during spring tide. (a) TGR; (b) eastern WDP. A positive value means salinity increase after the projects and the negative value indicates salinity decrease after the projects.

NB that was mainly caused by the seaward movement of the salinity front. The value of salinity difference was about 1 in the SP and NP, and it decreased slightly in the NC. These results showed that as the TGD supplemented river discharge during the dry season, the saltwater intrusion was suppressed. They also showed that the operation of the TGD was favorable for reducing the burden of freshwater supplement in the highly populated estuarine region.

The WDP is a strategic project to ease the shortage of water resources in northern China. China has been enduring floods in the south and droughts in the north. The water resources will be reallocated by the WDP through the inter-basin water transfer to mitigate the shortage of water resources in northern China. The WDP has three water transfer plans, namely, the Western Route Project, Middle Route Project, and Eastern Route Project. The Eastern Route Project draws water from Yangzhou, which is in the lower reaches of the Changjiang, and conveys the drawn water to northern China through the Grand Canal and the parallel rivers. Two numerical experiments before and after the eastern WDP were set up with the monthly mean river discharge of 11,200 m³/s in January, and 10,400 m³/s (reduced by 800 m³/s due to the third phase eastern WDP), respectively. The eastern WDP caused a decrease of river discharge, resulting in an enhancement of the saltwater intrusion, especially around the sand bars at the river mouth where the salinity experienced a notable increase. This project enhanced the SSO and increased the net seaward salt flux in the SB. During spring tide (**Figure 18b**), the salinity in the upper SB was mainly affected by the SSO, while that around the sand bars at the river mouth where the salinity fronts existed was mainly impacted by the seawater intrusion. During neap tide (not shown), the saltwater intrusion was weaker due to weaker tides. Accordingly, the SSO was much weaker and had a weaker effect on the salinity in the upper

SB. After the eastern WDP, the enhancement of the saltwater intrusion during neap tide was weaker in the NC and greater in the SP and the NP, compared to that during spring tide.

4. Summary

The Changjiang is one of the largest rivers in the world, with three bifurcations and four outlets into the sea. Its discharge exhibits pronounced seasonal variation, with the lowest monthly mean value of $11,200 \text{ m}^3 \text{ s}^{-1}$ in January and the highest of $49,700 \text{ m}^3 \text{ s}^{-1}$ in July. The tide has semidiurnal, diurnal, and fortnightly spring-neap signals with a moderate tidal range. Winds are controlled primarily by the monsoon, which brings weaker southerly wind in summer and stronger northerly wind in winter. There is a net landward flow in the NB when river discharge is low during spring tide, resulting in a type of saltwater intrusion known as the SSO, which is the most striking characteristic of saltwater intrusion in the estuary.

A three-dimensional numerical model was developed to study the hydrodynamic processes and saltwater intrusion in the Changjiang Estuary. A third-order spatial interpolation at a moderate temporal resolution coupled with a TVD limiter (HSIMT-TVD) advection scheme was used in this model to solve the transport equation and prevent numerical oscillations. The model was validated many times in the Changjiang Estuary, and the results suggested that the model can successfully simulate the hydrodynamic processes and saltwater intrusion in the estuary.

With combined effect of river discharge, tide, wind, and baroclinic force induced by the density gradient, the simulated winter residual currents during spring tide in the SB, SC, NC, and NP flow seaward mainly due to the runoff and have a higher magnitude in these channels than over the tidal flats. In the sandbar areas between the SP and NP, water is transported northward across the tidal flats. The residual current over the tidal flat east of Chongming Island is northward. In the NB, the residual current is weaker, and there is a net water transport toward the SB.

The saltwater intrusion in the Changjiang Estuary is controlled mainly by river discharge and tide, but is also influenced by wind, sea level rise, river basin, and estuary projects. The saltwater intrusion is enhanced when river discharge decreases. There is sufficient time for the reservoirs to take fresh water from the river when river discharge is large. On the intertidal timescale, the semidiurnal tide drives saltwater into the estuary during flood tide and out of the estuary during ebb tide. The fortnightly spring tide generates a greater saltwater intrusion than during neap tide. The model reproduced the phenomenon of SSO. The saltwater intrusion in the SP is stronger than that in the NP, and the intrusion in the NP is stronger than that in the NC.

Considering wind, sea level rise, and major projects in the river basin and estuary, we simulated and analyzed their impacts on the saltwater intrusion in the Changjiang Estuary. The northerly wind produced southward currents along the Subei Coast as well as the landward Ekman transport, which brought seawater into the Changjiang Estuary. A significant horizontal wind-driven circulation was formed in the SC and NC, which flowed landward in the NC

and seaward in the SC, SP, and NP. The saltwater intrusion was enhanced by the landward circulation, while it was weakened by the seaward circulation. With increasing northerly wind speed, the saltwater intrusion was enhanced in the NB and NC, while it was weakened in the SC, SP, and NP. When driven by the northeasterly wind, the wind-driven circulation in the SC and NC was significantly decreased, and the saltwater intrusion was weakened in the NB and NC compared to the same speed of northerly wind. In the upper reaches of the NB, the water was directly dragged by the local wind, causing an increment of water spilling over the flats from the NB into the SB. However, the SSO was weakened during spring tide, because the fresher water extended from the NC into the NB was more pronounced. When driven by the northwesterly wind, the patterns of the wind-driven circulation in the SC and NC were almost the same as those driven by the northerly wind of the same speed. In the middle and lower reaches of the NB, the water was directly dragged by the local wind, causing a weakened saltwater intrusion there, which decreased the salinity in the upper reaches of the NB and weakened the SSO. The saltwater intrusion was slightly weakened in the upper reaches of the SB and NC and was enhanced in the mouth of the NC, SP, and NP. The influence of wind stress was more pronounced during neap tide than during spring tide. The river discharge and tide mainly determined the features of the saltwater intrusion in the Changjiang Estuary, though the wind also played a key role.

The saltwater intrusion becomes stronger as sea level rises and is much stronger when river discharge is much smaller. The SSO, together with the enhanced saltwater intrusion from the NC, increases the salt content in the upper SB with the rising sea level. Under a lower river discharge, the salinity increase in dry year is more pronounced in the upper SB as the sea level rises, and the enhanced SSO is one of the important factors for such increase.

The impact of the DWP is that the saltwater intrusion was alleviated distinctly in the NC because the dykes of the project blocked off the southward drift of the brackish water plume under the northerly monsoon and the Coriolis force. The saltwater intrusion in the NP was intensified at the upper section and alleviated at the lower section. In the SP, the saltwater intrusion was intensified as the background salinity increased and the river discharge decreased. The TGD increased river discharge in winter and weakened the saltwater intrusion. The operation of the TGD is favorable for reducing the burden of freshwater supplement in the highly populated estuarine region. The WDP decreased river discharge, enhanced the saltwater intrusion, especially around the sand bars at the river mouth where the salinity experienced a notable increase, and was unfavorable for freshwater supply in the estuary.

Author details

Jianrong Zhu*, Hui Wu, Lu Li and Cheng Qiu

*Address all correspondence to: jrzh@sklec.ecnu.edu.cn

State Key Laboratory of Estuarine and Coastal Research, East China Normal University, Shanghai, China

References

- [1] Lyu H, Zhu J. Impact of the bottom drag coefficient on saltwater intrusion in the extremely shallow estuary. *Journal of Hydrology*. 2018;**557**:838-850
- [2] Wu H, Zhu J, Chen B, Chen Y. Quantitative relationship of runoff and tide to saltwater spilling over from the north branch in the Changjiang estuary: A numerical study. *Estuarine, Coastal and Shelf Science*. 2006;**69**(1):125-132
- [3] Xiang Y, Zhu J, Wu H. The impact of the shelf circulations on the saltwater intrusion in the Changjiang estuary in winter. *Progress in Natural Science*. 2009;**19**(2):192-202. (in Chinese)
- [4] Li L, Zhu J, Wu H. Impacts of wind stress on saltwater intrusion in the Yangtze estuary. *Science China Earth Sciences*. 2012;**55**(7):1178-1192
- [5] Shen HT, Mao ZC, Zhu J. *Saltwater Intrusion in the Changjiang Estuary*. Beijing: China Ocean Press; 2003. (in Chinese)
- [6] Li L, Zhu J, Wu H, Wang B. A numerical study on water diversion ratio of the Changjiang (Yangtze) estuary in dry season. *Chinese Journal of Oceanology and Limnology*. 2010;**28**(3):700-712
- [7] Zhu J, Wu H, Li L, Wang B. Saltwater intrusion in the Changjiang estuary in the extremely drought hydrological year 2006. *Journal of East China Normal University (Natural Science)*. 2010;**4**(1):1-6. (in Chinese)
- [8] Qiu C, Zhu J, Gu Y. Impact of seasonal tide variation on saltwater intrusion in the Changjiang River estuary. *Chinese Journal of Oceanology and Limnology*. 2012;**30**(2): 342-351
- [9] Li L, Zhu J, Wu H, Guo Z. Lateral saltwater intrusion in the north channel of the Changjiang estuary. *Estuaries and Coasts*. 2014;**37**(1):36-55
- [10] Zhu J, Ding P, Zhang L, Wu H, Cao H. Influence of the deep waterway project on the Changjiang estuary. In: *The Environment in Asia Pacific Harbours*. Netherlands: Springer; 2006. pp. 79-92
- [11] Xu K, Zhu J, Gu Y. Impact of the eastern water diversion from the south to the north project on the saltwater intrusion in the Changjiang estuary in China. *Acta Oceanologica Sinica*. 2012;**31**(3):47-58
- [12] Qiu C, Zhu J-R. Influence of seasonal runoff regulation by the three gorges reservoir on saltwater intrusion in the Changjiang River estuary. *Continental Shelf Research*. 2013;**71**(6):16-26
- [13] Qiu C, Zhu J. Assessing the influence of sea level rise on salt transport processes and estuarine circulation in the Changjiang River estuary. *Journal of Coastal Research*. 2015;**31**: 661-670

- [14] Zhu J, Bao D. The effects of river regime changes in the Changjiang estuary on hydrodynamics and salinity intrusion in the past 60 years I. River regime changes. *Acta Oceanologica Sinica*. 2016;**38**(12):11-22. (in Chinese)
- [15] Pritchard DW. The dynamic structure of a coastal plain estuary. *Journal of Marine Research*. 1956;**15**(1):33-42
- [16] Simpson JH, Brown J, Matthews J, Allen G. Tidal straining, density currents, and stirring in the control of estuarine stratification. *Estuaries*. 1990;**13**(2):125-132
- [17] Geyer WR. The importance of suppression of turbulence by stratification on the estuarine turbidity maximum. *Estuaries*. 1993;**16**(1):113-125
- [18] Blumberg AF, Mellor GL. A description of a three-dimensional coastal ocean circulation model. In: *Three-Dimens Coast Ocean Models*. 1987. pp. 1-16
- [19] Blumberg AF. A primer for ECOM-si. In: *Tech Rep HydroQual*. 1994. p. 66
- [20] Chen C, Zhu J, Ralph E, Green SA, Budd JW, Zhang FY. Prognostic modeling studies of the Keweenaw current in Lake Superior. Part I: Formation and evolution. *Journal of Physical Oceanography*. 2001;**31**(2):379-395
- [21] Mellor GL, Yamada T. A hierarchy of turbulence closure models for planetary boundary layers. *Journal of the Atmospheric Sciences*. 1974;**31**(7):1791-1806
- [22] Mellor GL, Yamada T. Development of a turbulence closure model for geophysical fluid problems. *Reviews of Geophysics*. 1982;**20**(4):851-875
- [23] Galperin B, Kantha LH, Hassid S, Rosati A. A quasi-equilibrium turbulent energy model for geophysical flows. *Journal of the Atmospheric Sciences*. 1988;**45**(1):55-62
- [24] Wu H, Zhu J. Advection scheme with 3rd high-order spatial interpolation at the middle temporal level and its application to saltwater intrusion in the Changjiang estuary. *Ocean Model*. 2010;**33**(1):33-51
- [25] Zhu J, Wu H, Li L. Hydrodynamics of the Changjiang estuary and adjacent seas. In: *Ecological Continuum from the Changjiang (Yangtze River) Watersheds to the East China Sea Continental Margin*. Cham: Springer; 2015. pp. 19-45. (Estuaries of the World)
- [26] Smagorinsky J. General circulation experiments with the primitive equations. *Monthly Weather Review*. 1963;**91**(3):99-164
- [27] Large WG, Pond S. Open ocean momentum flux measurements in moderate to strong winds. *Journal of Physical Oceanography*. 1981;**11**(3):324-336
- [28] Editorial Board for Marine Atlas. *Ocean Atlas in Huanghai Sea and East China Sea (Hydrology)*. Beijing: China Ocean Press; 1992
- [29] Wu H, Zhu J. Analysis of the transport mechanism of the saltwater spilling over from the north branch in the Changjiang estuary in China. *Acta Oceanologica Sinica*. 2007;**29**(1): 17-25. (in Chinese)

Dynamics of the Changjiang River Plume

Hui Wu, Tianning Wu, Jian Shen and Jianrong Zhu

Additional information is available at the end of the chapter

<http://dx.doi.org/10.5772/intechopen.80734>

Abstract

The extension of the Changjiang River plume is one of the fundamental processes in the Yellow and East China Seas, which is responsible not only for the physical properties of seawater but also for the numerous physical, biogeochemical, and sedimentary processes in this region. The studies of the Changjiang River plume dated back to 1960s, followed by generations, and are still attracting numerous focuses nowadays. Here in this chapter, we will review the past studies on the Changjiang River plume and present some latest studies on this massive river plume. The latest research progresses on the Changjiang River plume are mainly related to the tidal modulation mechanisms. It is found that the tide shifts the Changjiang River plume to the northeast outside the river mouth, bifurcates the plume at the head of submarine canyon, and arrests the unreal up-shelf plume intrusion that occurred frequently in previous model studies. It is also found that the tidal residual current transports part of the Changjiang River plume to the Subei Coastal Water. These tidal modulation effects can answer the questions on the dynamics of Changjiang River plume that puzzled the research community for decades.

Keywords: river plume dynamics, tide, up-shelf extension, numerical simulation, Changjiang River Estuary

1. Introduction

The Changjiang River, 6300 km long, drainage basin of 1.8 million km² and annual discharge of 9.32×10^{11} m³, is the largest river entering the western Pacific Ocean. It empties 51% freshwater, 23% sediments, 66% nitrogen, and 84% phosphorus of the total riverine fluxes in China, respectively [38, 44, 53] (**Figure 1**). Consequently, the Changjiang River Estuary (CRE) is one major fishery ground of China, but the excess nutrients and pollution inputs also have caused severe eutrophication, harmful algal blooms (HAB), and hypoxia [25, 42, 45, 64].

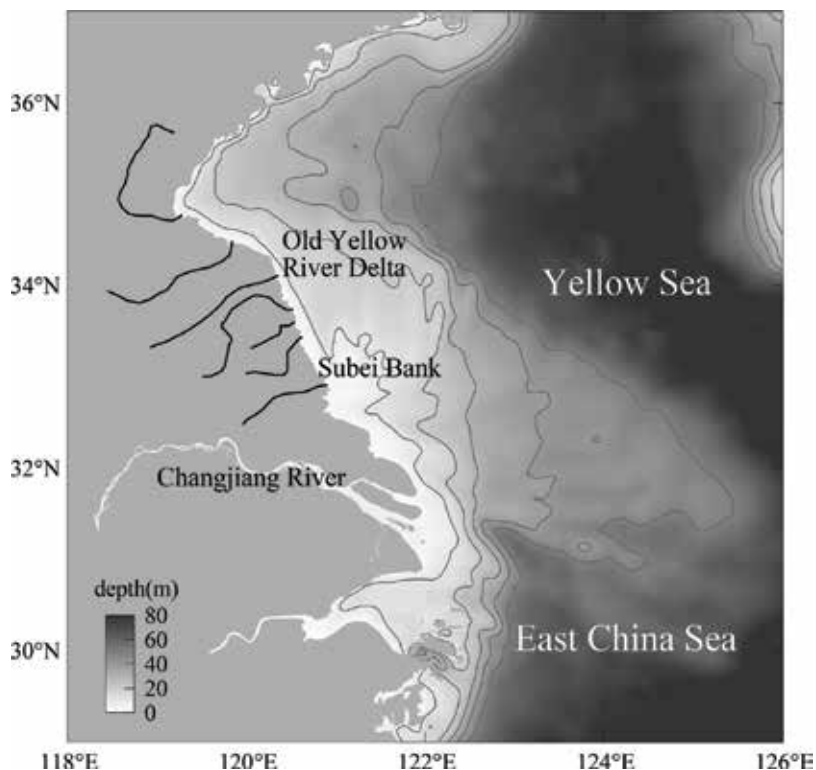


Figure 1. Topography of the Changjiang River Estuary and Subei Coastal Water.

North of the CRE is the most turbid coastal water in the East Asian marginal seas, that is, the Subei Coastal Water (SCW), which receives the Old Yellow River discharge in 1128–1855 [11, 58]. The SCW is well known for its unique radial tidal ridge system [15, 28] and frequent macroalgal blooms [29]. The extension of the Changjiang River plume substantially controls the distributions of sediments and nutrients in the Yellow and East China Seas (YECS) and determines the physical properties of water mass such as salinity and stratification, therefore is responsible for the occurrence of HABs and hypoxia. It also significantly influences the water mass composition in the SCW, as indicated by some recent studies (e.g., [50]). The CRE-SCW represents a rare type of coastal water body, which is coinfluenced by huge river discharges, energetic tides, strong shelf circulations, and the seasonal monsoon. Therefore, the behavior of the Changjiang River plume is complicated, which has attracted numerous research efforts in the past 60 years.

2. A research history voyage on the Changjiang River plume

Prof. Hanli Mao and his colleagues made the earliest study on the Changjiang River plume [30]. By analyzing the hydrological data obtained in the vicinity of the Changjiang River Estuary, they found that the Changjiang River plume extends southward along the Zhejiang

and Fujian Coast in winter season but northeastward toward the Jeju Island in summer season (**Figure 2**). Such a bi-directional plume extension was confirmed later by numerous studies, such as Beardsley [4] and Zhao et al. [60], among many others. The northeastward plume extension in summer is an iconic hydrodynamic feature in the Yellow and East China Seas, which directly causes the harmful algal blooming and hypoxia off the Changjiang River Estuary, by fueling the nutrients and forming the stratification [25, 64]. This offshore plume branch finally reaches the vicinity of the Jeju Island and further enters the Japan/East Sea through the Tsushima-Korea Strait [6, 21].

It has become a major oceanographic research topic to find the dynamic mechanisms responsible for the northeastward extension of the summertime Changjiang River plume. The wind direction in summer is southerly, which could favor an offshore extension under the surface Ekman transport. However, the observed northeastward plume extensions were not always

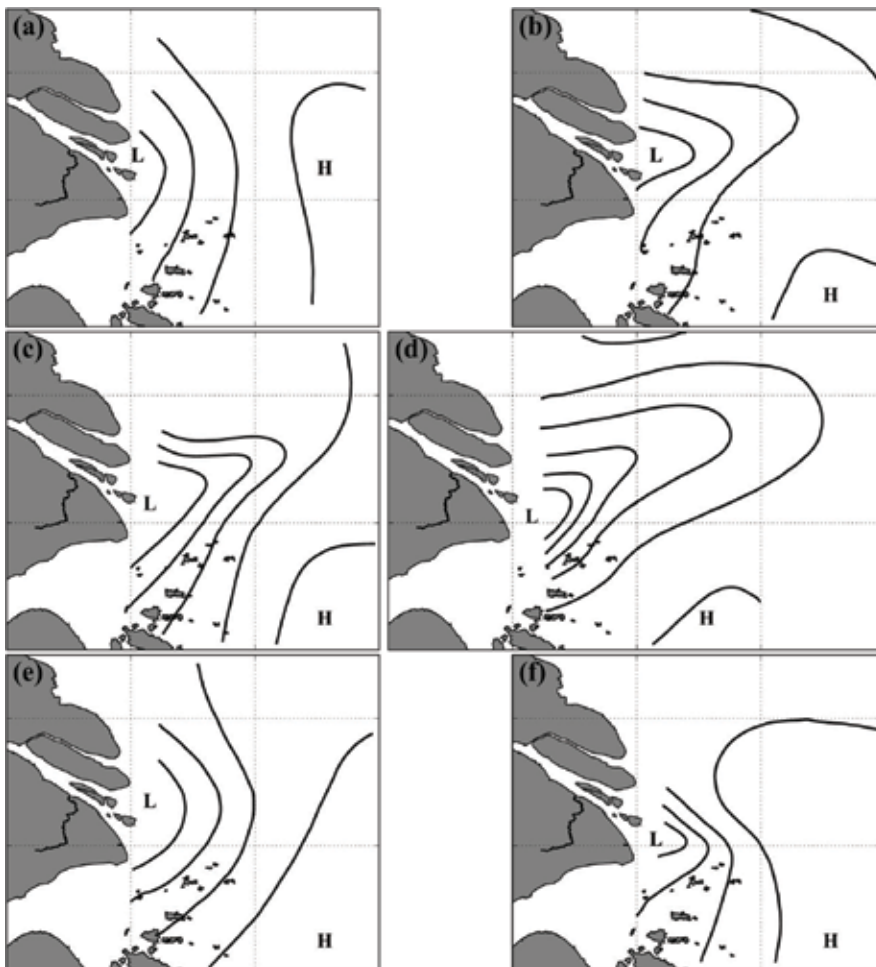


Figure 2. Distribution of the Changjiang River plume in April (a), May (b), June (c), July (d), August (e), and September (f). “L” means low salinity water; “H” means high salinity water. Replotted from Mao et al. [30].

associated with an upwelling-favorable southerly wind [60]. Some theoretical studies indicated that the magnitude of wind-driven current is too small to change the plume extension direction [23, 30]. In summer, the mean wind speed is $<3 \text{ m s}^{-1}$ and is generally weak, except during the typhoon weather. These studies suggested that a large Changjiang River runoff could be a prerequisite and proposed a "critical discharge" ($\sim 40,000 \text{ m}^3 \text{ s}^{-1}$), beyond which the northeastward extension should occur [3, 23, 30]. However, in many years with large runoff, the northeastward extension was actually absent; whereas, in some other years with low runoff, it was still observed [36, 57, 60]. Some studies speculated that the northward-flowing Taiwan warm current played a role in the northeastward plume extension, through the barotropic [60] or baroclinic [35] effects.

Since 1990s, with the growing computer power and the advances of numerical methods, researchers began to use three-dimensional numerical models to study the extension of Changjiang River plume. Zhu et al. [62, 63] developed the first three-dimension, baroclinic, and terrain-following coordinate numerical model focusing on the Changjiang River plume. With this tool, they highlighted that (1) the increasing runoff does not necessarily result in enhanced northeastward plume extension; (2) the Taiwan warm current flows along the bathymetry, which does not interact with the Changjiang River Plume; (3) the circulation induced by the Yellow Sea Cold Water Mass (YSCWM) is important for the summertime Changjiang River plume extension; and (4) the southerly wind in summer favors the northeastward plume extension. The YSCWM is in the bottom layers of the central Yellow Sea, due to the seasonal variation of sea surface heat flux [19, 59]. The rapid warming in spring and summer produces a strong thermocline in the Yellow Sea, which reduces the vertical mixing and keeps the bottom water temperature lower than 8°C in summer season. However, the YSCWM is often located in the Yellow Sea Trough that is distant from the Changjiang River Estuary, and hence its role in regulating the Changjiang River plume is debatable. Also using a numerical model, Chang and Isobe [6] suggested that the wind and the "Taiwan-Tsushima Warm Current System" greatly controls the summertime plume extension.

Interestingly, it seems that these model results were inconsistent with the previous observational studies, which indicated that the observed Changjiang River plume could shift northeastward even without favorable winds (e.g., [23, 30, 60]). Moreover, the modeled Changjiang River plume often confusingly extended northward (NOT northeastward!) along the Jiangsu Coast, distinct from the observations. For example, in Chang and Isobe [6], the modeled Changjiang River plume even reached the northern tip of the Shandong Peninsula. The unreal northward plume extension is opposite to the Coriolis effect, which is often termed as "up-shelf intrusion." Up-shelf plume intrusion occurs frequently in river plume intrusions [8, 9, 12, 16, 17, 22, 55], which was believed to be an artifact of numerical simulation. Many studies set an artificial down-shelf background current, solely to prevent the up-shelf intrusion (e.g., [9, 54]). Zhu et al. [62] set a strong southward-flowing Subei Coastal Current to prevent northward plume propagation. However, the existence of southward-flowing Subei Coastal Current in summer is highly debatable. Liu et al. [29] observed that under the southerly summer monsoon, the movement of Subei Coastal Water was actually northward. The Subei Coastal Current set in Zhu et al. [62] actually served as the background current. Some researchers thought that the modeled up-shelf plume intrusion is a realistic phenomenon

(e.g., [31]), and they raised the Changjiang River plume as an example. Unfortunately, they probably confused the observed northeastward offshore extension with the modeled northward up-shelf intrusion, which are substantially different.

One overlooked dynamic factor in these previous studies is the tide, which is very energetic in the Yellow and East China Sea. As indicated by the dominant tide constituent, M_2 , the Changjiang River Estuary is influenced by two distinct tide systems: the progressive tide in the East China Sea and the rotating tide in the Yellow Sea (**Figure 3**). Tide wave from the Northwest Pacific propagates nearly parallel to the Ryukyu Islands, entering the East China

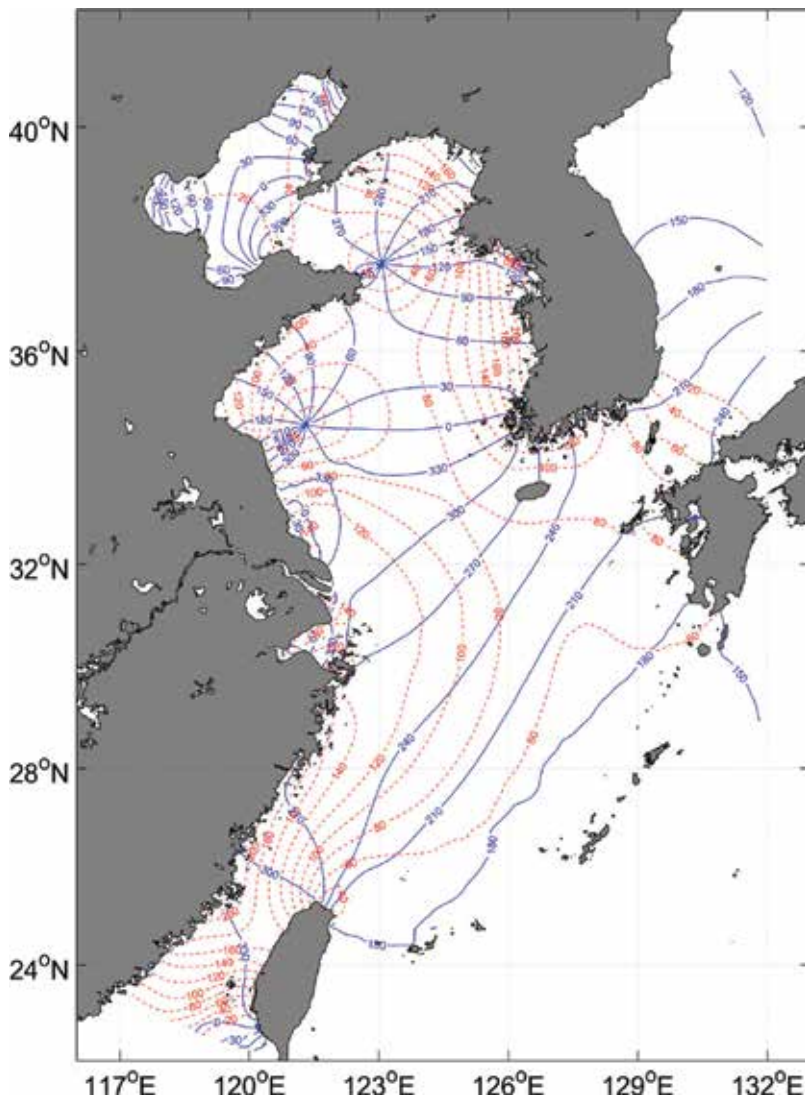


Figure 3. Co-tide map of the M_2 tide constituent. The blue solid lines are the co-phase lines with an interval of 30° , and the red dashed lines are the co-amplitude lines with an interval of 20 cm.

Sea and marching northwestward to the Changjiang Estuary. Off the river mouth, the co-phase lines become denser due to the shallowness of topography, which reduces the tidal wave speed. Annually averaged tidal range at the Changjiang River mouth is 2.67 m, and the maximum tidal range reaches 4.62 m. Gao et al. [14] highlighted the significant intra-tidal variability of the Changjiang River plume near the river mouth. Sampling at different tidal phases can result in a distinct salinity distribution. Moon et al. [34] found that the spring-neap variation of the tidal mixing can detach the diluted water from the Changjiang River plume at the slope region of the Changjiang Bank. Rong and Li [37] and Li and Rong [26] found that the tidal forcing intensifies the down-shelf transport of Changjiang diluted water, since the tidal forcing arrested the frontal instabilities, and therefore more buoyant water was moved to the down-shelf. Here in this chapter, we will show that the tidal forcing is actually responsible for many unexplained phenomena of the Changjiang River plume.

3. Numerical model

The numerical model used was developed by Wu et al. [49]. The hydrodynamic kernel of our model is the ECOM-si [5] with a robust HSIMT-TVD advection scheme developed by Wu and Zhu [47] to solve the transport equations. The model used the modified Mellor and Yamada level 2.5 turbulent closure model [13, 32] for vertical mixing and τ scheme of Smagorinsky [40] for horizontal mixing. A wet/dry scheme was included with a minimum depth of 0.25 m. The model domain covered the entire East China Sea, Yellow Sea, Bohai Sea, and parts of the Pacific Ocean and the Japan Sea. The model grid mesh spanned 272×285 cell indices in the horizontal. Off the river mouth, the model mesh was about $2 \text{ km} \times 3 \text{ km}$ (in two directions). Twenty σ layers were used in the vertical with refined upper layer thicknesses. For a typical depth of 60 m off the Changjiang River mouth, the upper 10 m of the water column had eight layers. The open boundary was driven by the shelf currents and the tide currents. Surface heat flux was included in the model by the monthly data from NCEP (National Centers for Environmental Prediction). A bulk formula suggested by Ahsan and Blumberg [1] was used to calculate the atmospheric radiation (long-wave radiation), the evaporation heat flux, and the sensible heat flux.

4. Model validation

4.1. Validation of monthly mean salinity field

Model performance was evaluated with the monthly mean salinity documented by the Editorial Board for Marine Atlas [2]. In this numerical experiment, the model was driven with the climatological monthly runoff (based on historic observations by the Changjiang Water Resource Commission) and wind (from NCEP/CFSR) as well as 11 harmonic tidal current constituents. The model spun up for one year and the results of the second year were analyzed. The comparisons between the modeled monthly mean salinity and the Atlas' data in four selected months are shown in **Figure 4**. The modeled 30-psu isohalines (thick white lines)

were compared with those from the Editorial Board for Marine Atlas [2] (dashed red lines), which showed that the model performance were reliable.

4.2. Validation of cruising survey

The model was further validated with the in-situ data of surface salinity and temperature obtained in July 19–28, 2016. The model was driven by the daily runoff (observed by the Changjiang Water Resource Commission), 6-hourly wind, and 11 harmonic tidal current constituents.

Model results at the sampling locations and time of each observation were plotted for comparison (Figure 5). In the survey period, the Changjiang River plume featured a typical north-eastward summertime extension, covering a large area outside the river mouth (Figure 5a).

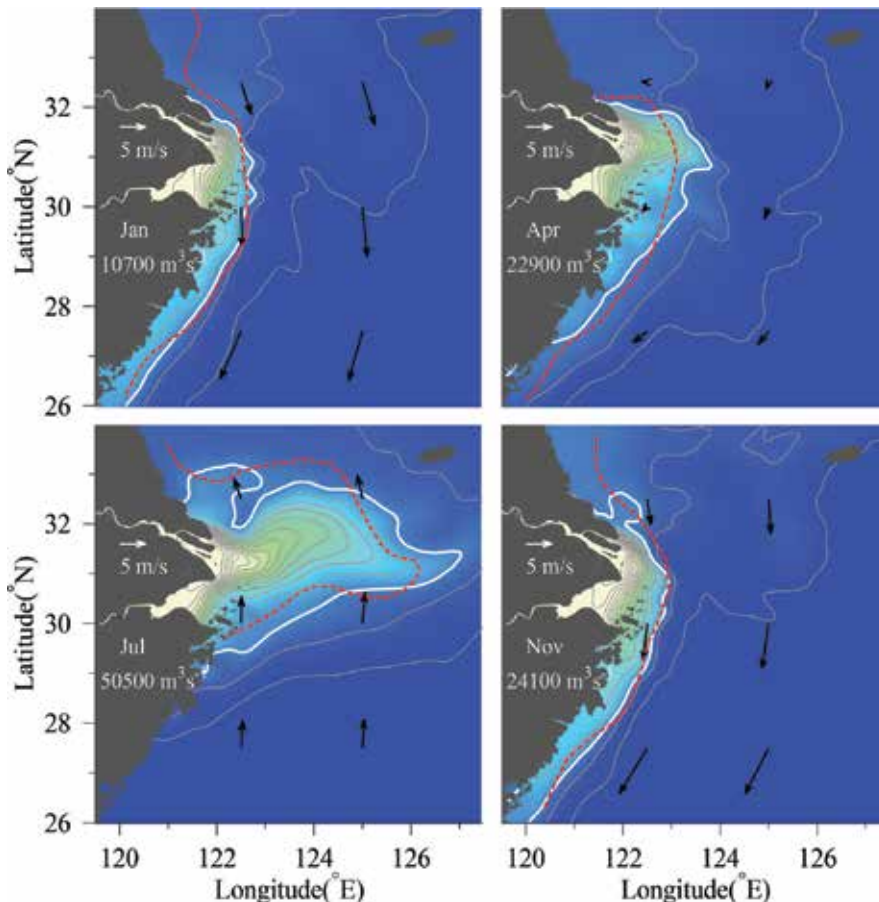


Figure 4. Sea surface salinity resulting from the climatological run in four selected months. The arrows are the monthly climatological wind. Monthly Changjiang River discharges are labeled. The contour interval of surface salinity is 2 psu, and the 30-psu contour is highlighted with thick white line. Dashed red line shows the 30-psu isohaline digitized from Editorial Board for Marine Atlas [2].

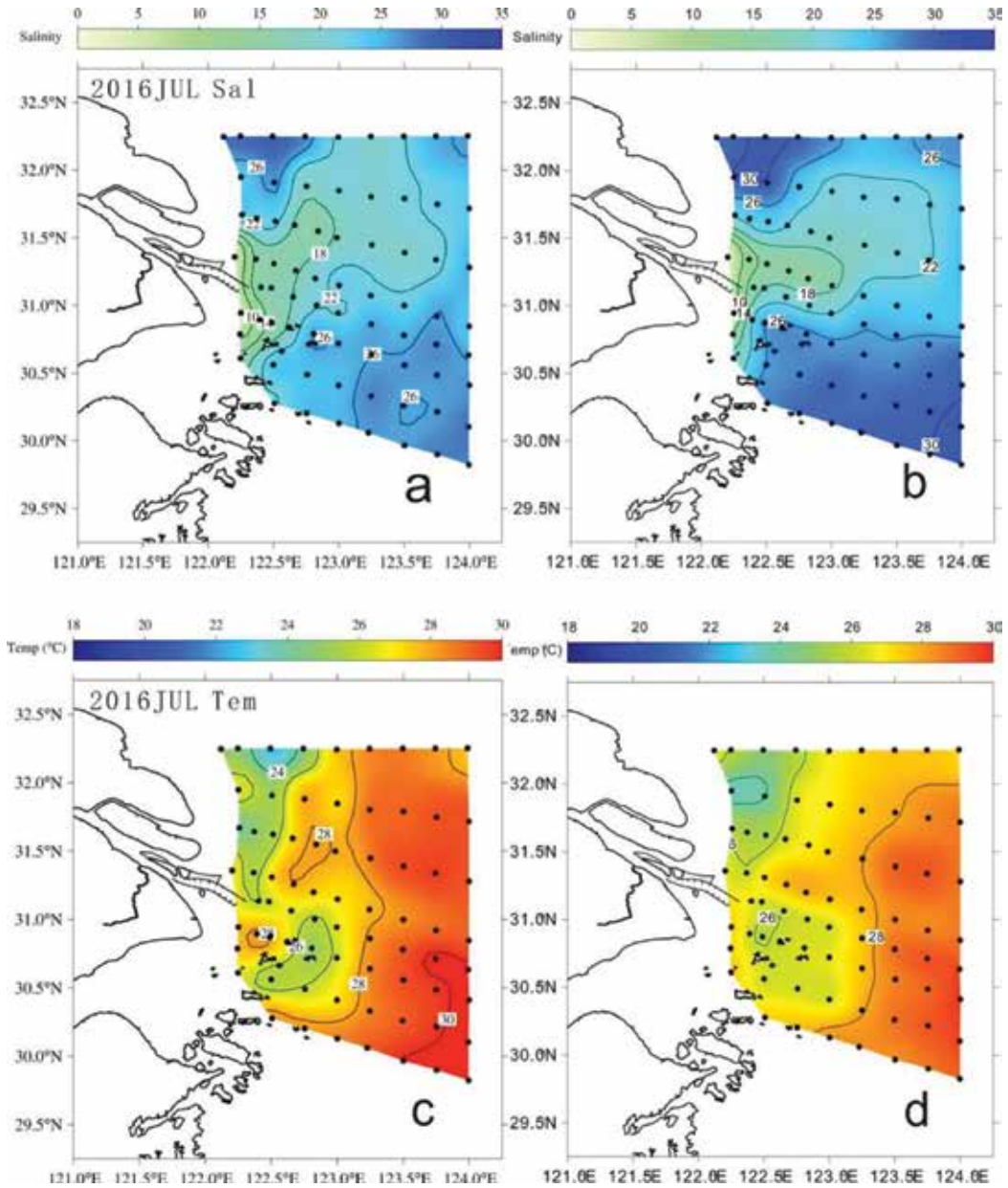


Figure 5. Comparisons between the observed ((a) and (c), dots signify the sampling stations) and the modeled ((b) and (d)) surface salinity ((a) and (b)), and temperature ((c) and (d)) distributions during July 2016.

Outside the river mouth, the sea surface temperature was generally high, but there were also some cold water patches near the river mouth, produced by strong tidal mixing that brings the bottom cold water to the sea surface. Overall, the model reproduced these features fairly well.

5. Suppression of up-shelf plume intrusion by tide

We used the validated numerical model to explore the tidal modulation mechanism on the Changjiang River plume [49]. Two numerical experiments were set up (Exp1 and Exp2). External forcings such as the wind and shelf currents were excluded for the moment, with only the runoff and tide retained.

5.1. Changjiang River plume without the tide

Previous nontidal simulations on the Changjiang river plume often gave an unreal massive up-shelf extension along the Jiangsu Coast (e.g., [6]). Our simulation (Exp1) reproduced this feature with tidal forcing excluded as previous studies. A large portion of the Changjiang diluted water spreads along the Jiangsu Coast after leaving the river mouth (**Figure 6A**), and the downstream current occurred only at the offshore edge of the plume. A train of wave was detected as well at the plume front, which was caused by baroclinic

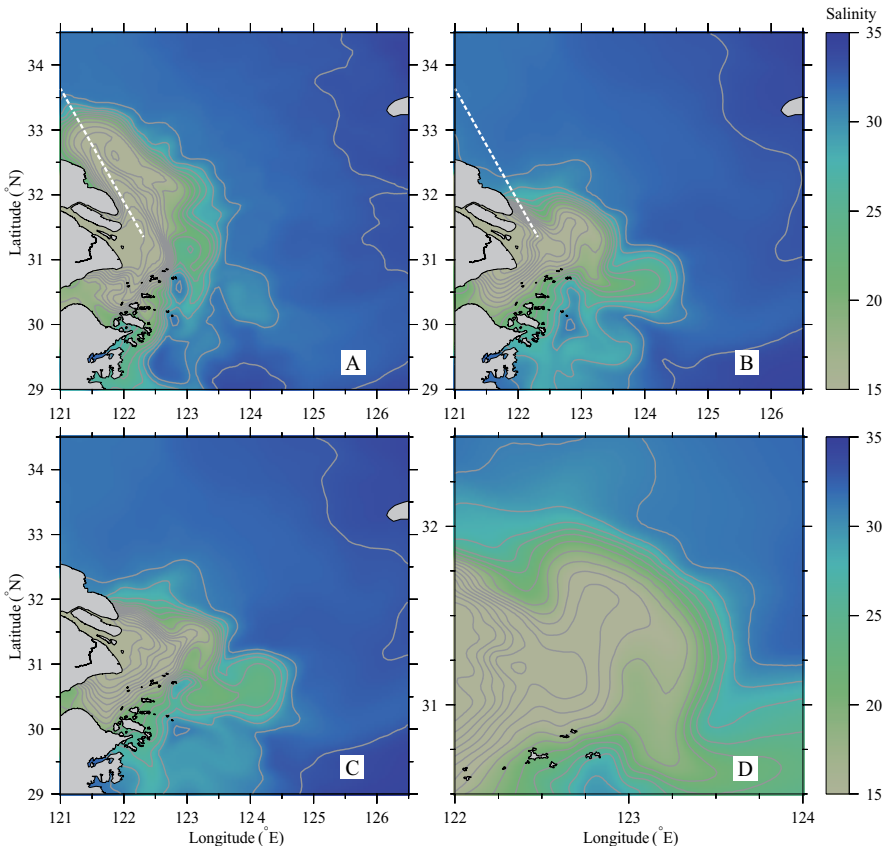


Figure 6. (A) Modeled surface salinity with river discharge only. (B) Tidal-averaged surface salinity during spring tide from the simulation with river discharge and tide. (C) Same as B but during the neap tide. (D) A zoom-in view of B.

instability [10]. Without the tidal forcing, the Changjiang River plume featured an expected anticyclonic bulge-like rotation [7, 54], but was elongated dramatically and extended to the upstream.

Similar up-shelf plume extension occurred frequently in previous numerical simulations for other realistic or idealized river plumes with settings similar to Exp1 (i.e., without tide, wind, nor ambient currents) [8, 9, 12, 16, 17, 22, 55]. Although many researchers believed that such an upstream plume extension is a model artifact, Matano and Palma [31] argued that such a characteristic is associated with the geostrophic adjustment the buoyant discharge, which creates an onshore baroclinic gradient force that drives a proportion of the discharge in the upstream direction. The plume extension from Exp1 is thus not surprising, and similar simulation results can be found in several other numerical studies of the Changjiang River plume in which the tide was excluded.

5.2. Influence of the tide in arresting the upstream extension

A common problem of Exp1 and previous simulations is the absence of tidal forcing. Massive up-shelf extension vanishes when the tidal forcing was added in Exp2 (**Figure 6B**). Instead of generating any downstream background current, the tide can produce an upstream residual current along the Jiangsu Coast due to its nonlinear interaction with the shallow topography, as is reported by Wu et al. [48]. Hence, it is not the down-shelf current that arrests the upstream extension of Changjiang River plume.

The actual mechanism is the tidal mixing. It is well known that the East China Sea and Yellow Sea have a meso- to macroscale tide system (**Figure 3**). Tidal range exceeds 4 m in spring tide around the Changjiang River Estuary. Moreover, the bathymetry is shallow around the river mouth. Hence, due to the strong tide and shallowness, tidal mixing is very strong around the Changjiang River Estuary. To address this point, we can look at the sectional profiles of salinity and turbulent viscosity along the Jiangsu Coastal with and without the tidal forcing (**Figure 7**). Without the tidal forcing, high stratification occurs near the surface (**Figure 7A**) since the turbulent viscosity was small (**Figure 7C**). With the tidal forcing included, the water column became well mixed (**Figure 7B**) since strong turbulent mixing occurred in the middle and lower layers (**Figure 7D**). A strong along-coastal baroclinic gradient was thereby formed at the northern side of the Changjiang River mouth, which drove a cross-coastal flow and prevented the upstream extension of the plume. It should be emphasized again that tidal mixing was not considered in previous model studies that produced the up-shelf plume extension. Because the tide exists at most regions of the world, this may give an additional explanation as to why most river plumes turn to the downstream direction besides the Coriolis forcing.

5.3. Tide-forced plume patterns

Besides arresting the upstream plume extension, the tidal forcing also modulated the Changjiang River plume in other remarkable ways. During the spring tide, the Changjiang River plume turned to the downstream at first inside the 30-m isobath, rotated

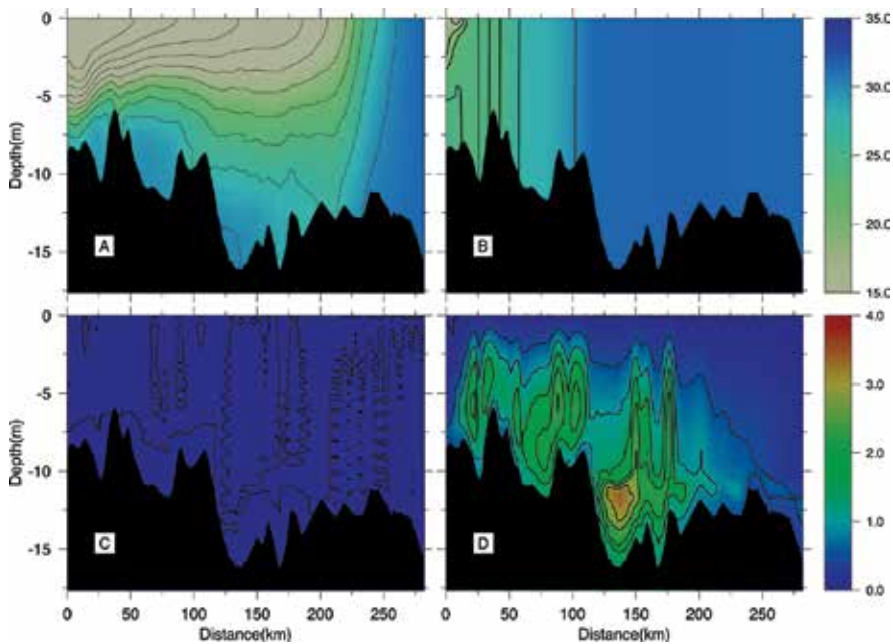


Figure 7. Sectional salinity (upper panels) and vertical turbulent viscosity (lower panels) (unit: $10^{-2} \text{ m}^2 \text{ s}^{-1}$) from Exp1 (left panels) and Exp2 (right panels). For section position, see **Figure 6**.

northeastward at approximate 122.5°E , and then rotated anti-cyclonically to the downstream (**Figure 6B**, a zoom-in view was shown in **Figure 6D**). A significant bulge occurred around the head of submarine canyon. However, such a bulge was weakened during the neap tide (**Figure 6C**), which implied that strength of the tide probably impacted on the bulge. The detail mechanisms responsible for this spring-neap variation of plume bulge are still unclear.

Interestingly, because of the rotation of the bulge, a northeastward freshwater tongue occurred near 122.5°E (during the spring tide, **Figure 6D**) or 123°E (during the neap tide, **Figure 6C**). Comparing with the nontidal simulation results, it seems that the tidal forcing is responsible for the northeastward turning of the Changjiang River plume, at least in the near field. Hence, it is understandable that why this turning can occur under various wind and runoff conditions, as was pointed out by previous studies.

5.4. Tidal modulation on river plume under the wind and shelf currents

Superimposing the southerly wind of 4 m s^{-1} and shelf currents, both model runs with (Exp3) and without tide (Exp4) showed a northeastward extension of the Changjiang River plume (**Figure 8**), but significant difference can also be found. Without tide, the plume also extended northward strongly due to the up-shelf plume intrusion (**Figure 8A**). Mao et al. [30] used the 26-psu isohaline as the exterior edge of the main body of Changjiang diluted water and the 32-psu isohaline as the extending edge of diluted water. Here, we use the 16-psu isohaline

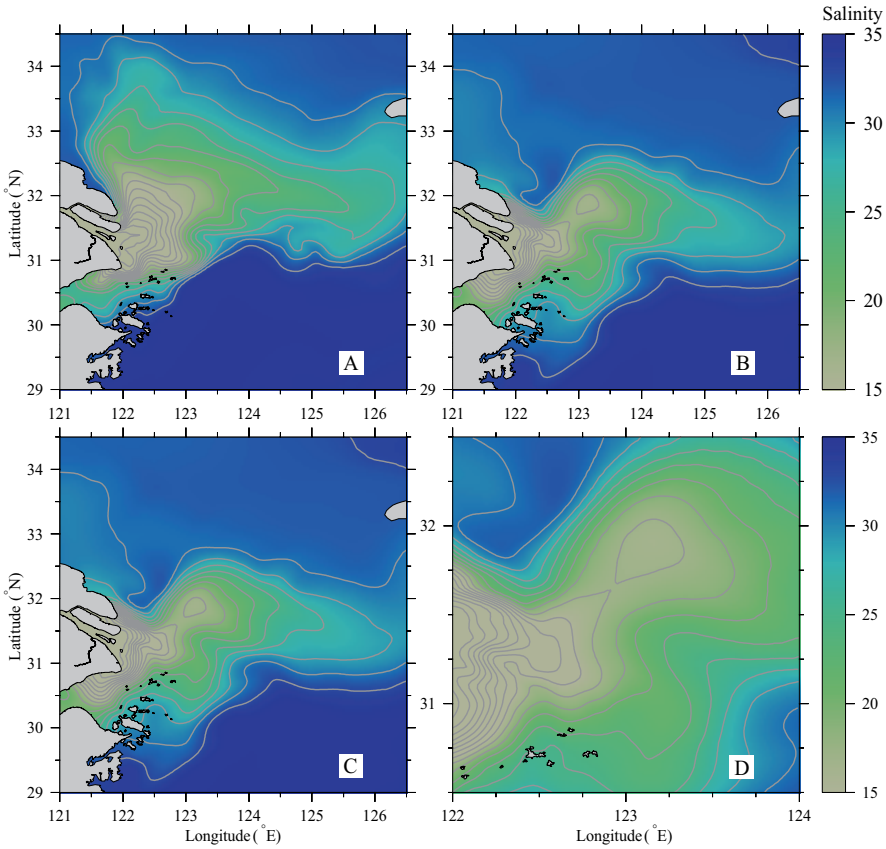


Figure 8. Surface salinity and current from Exp3 (A), tidal-averaged surface salinity during the spring tide (B) and the neap tide (C) from Exp4. (D) A zoom-in view of B.

additionally as the edge of freshwater. Defining A_s and V_s as the area and volume with salinity less than s (outside the Changjiang River mouth), respectively, the areas and volumes outside the 10-m isobath are shown in **Table 1**. A_{32} and V_{32} do not show significant differences with or without tide, while A_{26} and V_{26} are distinct. With the tidal forcing, the area and volume of the main body of diluted water are only about 60 and 70%, respectively, of the nontidal case. This is expected because the tide enhances vertical mixing and increases the surface salinity. Almost no differences can be found between spring and neap tides for A_{26} and V_{26} but significant differences appeared for those with salinity less than 16 psu. During spring tide, A_{16} and V_{16} were only 42 and 61%, respectively, of their values during neap tide. The biggest A_{16} but the smallest V_{16} under the nontidal case indicates that the plume was very thin without tide. These results also indicate that, in the near-field, the plume is highly varied during the spring-neap cycle, while, in the far field, it is less influenced.

South to the Changjiang River mouth, the ambient current is northward because of both the southerly wind and Taiwan warm current (**Figure 8**). Most of the Changjiang diluted

	S < 16		S < 26		S < 32	
	Area (km ²)	Volume (km ³)	Area (km ²)	Volume (km ³)	Area (km ²)	Volume (km ³)
Without tide	10,589	25	61,843	295	483,469	9428
Spring tide	4193	26	38,542	213	469,514	9903
Neap tide	9872	42	38,503	213	477,769	10,048

Table 1. Plume areas and volumes (with salinity less than 16, 26, and 32) during the spring and neap tides outside the isobath 10 m.

water spreads northeastward during both spring tide (**Figure 8A**) and neap tide (**Figure 8B**). During spring tide, the near-field plume is almost the same as that without external forcing (**Figure 6B**). The recirculating plume bulge vanished and joined into the far-field water because of the wind-induced mixing and the northeastward Ekman transport. The Changjiang River plume turned to the northeastward at 122.5°E (**Figure 8B**), almost the same place as the no-wind case (**Figure 6B**).

The minor southeastward branch of the Changjiang River plume can be identified during spring tide (**Figure 8B**). The bifurcation point was near the head of the submarine canyon. A strong southeastward residual current occurred on the slope, which was almost the same as that of Exp2 (**Figure 6B**), which resulted from tidal rectification. Such a residual current favors the diluted water flowing southward along the Zhejiang Coast. However, if we do not include the tide, the southward extended branch of the Changjiang River plume is greatly weakened, as is shown in **Figure 8A**.

5.5. Effect of wind direction

The wind field of the Y ECS region varies significantly both temporally and spatially. Therefore, the observed salinity distribution of the Changjiang River mouth was often distinct from the climatological situation. Here, we investigate how the Changjiang River plume is altered under different wind directions (i.e., the southeasterly wind (Exp5) and southwesterly wind (Exp6), respectively) with the same wind speed of 4 m s⁻¹.

Only the results during spring are shown (**Figure 9**). A major difference occurs in the far-field plume regions. A southeast wind results in a northeast Ekman transport, and therefore in the far field, the northeastward plume branch was better developed and was toward the Jeju Island. The southeastward plume branch that bifurcated at the head of the canyon had almost vanished. The southwest wind produced a southeast Ekman pumping, resulting in a southeastward extension of the Changjiang River plume in the far field. The southeastward plume branch was more evident than the case of south or southeast wind, but the northeastward plume branch was less evident. Nevertheless, in the near field, the plume pattern remained the same under all wind directions, even under the no-wind condition. This indicated that the tidal modulation is an essential mechanism in shifting the Changjiang River plume to the northeastward in summer.

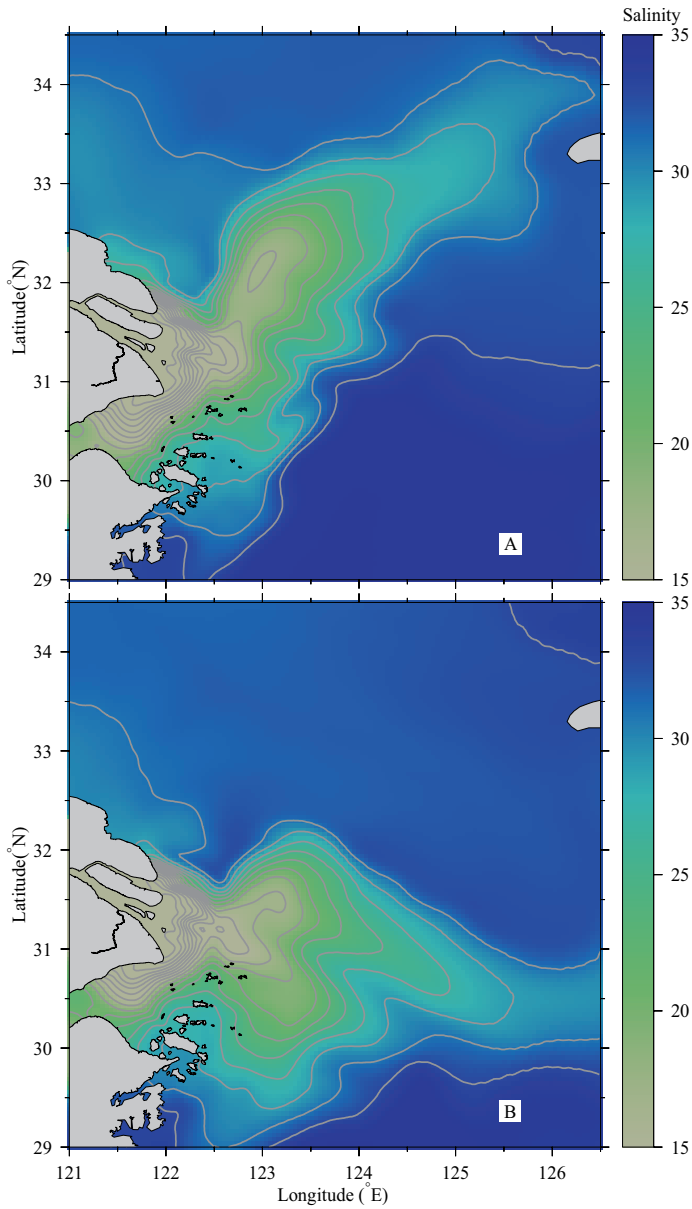


Figure 9. Tidally averaged surface salinity during spring tide under (A) southeasterly wind (i.e., Exp5) and (B) southwesterly wind (i.e., Exp6).

6. Characteristics of the Changjiang River plume under realistic forcings

In climatological model results, the Changjiang River plume spreads to the south along the Zhejiang Coast in winter, whereas turns to the northeast and can even reach the Jeju Island

in summer. It is important to know whether these plume patterns obtained via climatological run are still significant in the realistic environment. Therefore, we conducted a long-term (2000–2008) realistic simulation of the Changjiang River plume and analyzed the modeled surface salinity with empirical orthogonal function (EOF) [50]. The modeled hourly SSSs from year 2001 to 2008 were output and interpolated to a $0.25^\circ \times 0.25^\circ$ mesh to save the computational cost. The SSS time series at each grid point was low-pass filtered with a cutoff window of 34 h to remove the tidal signals, and the filtered salinity field on each day was analyzed with the EOF method.

Three leading EOF modes are shown in **Figure 10**, which contributed 42.9, 14.6, and 9.5%, respectively, of a total of 67%, for the total variance. Mode 1 (**Figure 10A and B**) shows the

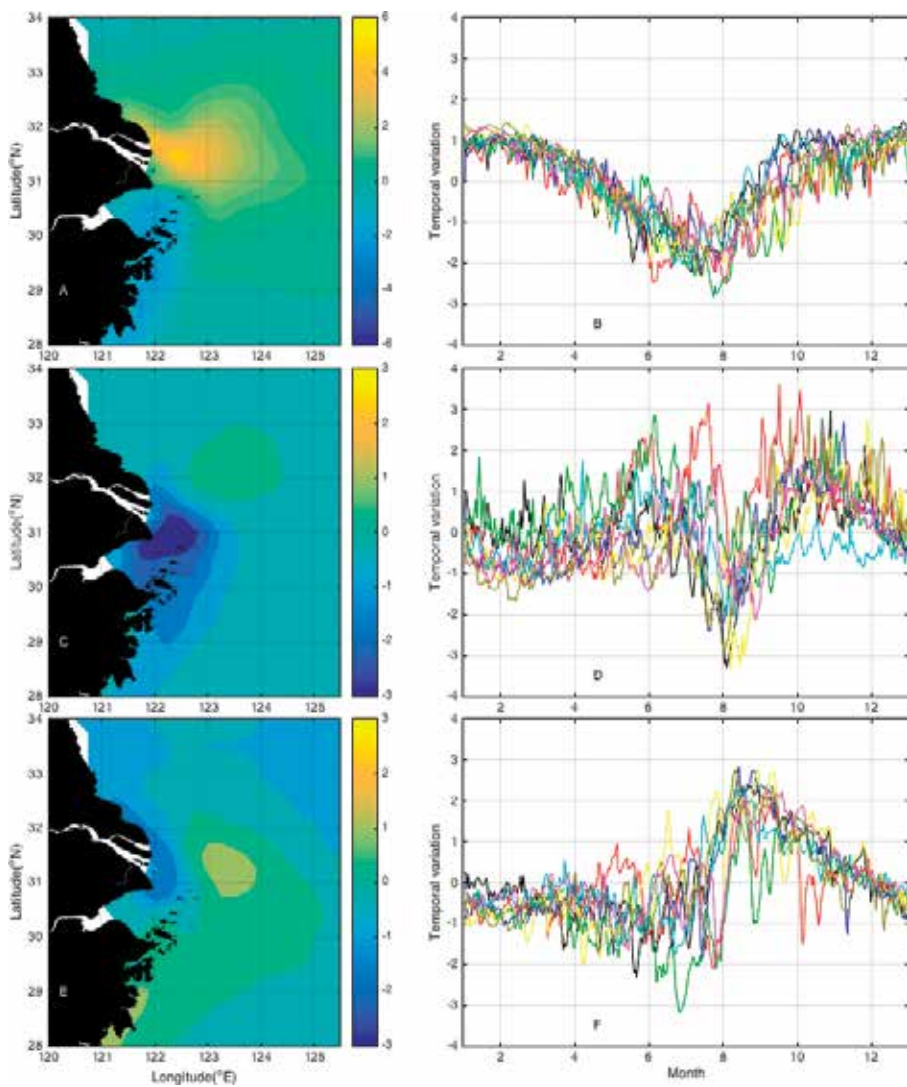


Figure 10. Three leading EOFs (A, C, and E) of the surface salinity anomaly and their PCs (B, D, and F).

two major branches of the Changjiang River plume. From May to August, there is a negative salinity anomaly located northeast to the river mouth. In the remaining months, the negative salinity anomaly is located along the Zhejiang Coast. This remarkable seasonal variation is consistent with the northeastward and southward plume branches. Mode 2 (**Figure 10C and D**) shows that the plume salinity is periodically increased near the river mouth but decreased northeast to the river mouth. The latter one has been recognized as the plume detachment in recent years based on a series of observational studies (e.g., [27]) and modeling studies [34, 37, 39, 49, 52]. Mode 3 (**Figure 10E and F**) suggests that there is a negative salinity anomaly located along the Jiangsu Coast mostly in summer and autumn seasons, corresponding to the northward plume extension.

By analyzing the PCs of EOF (**Figure 10B, D and F**), we can understand the variations of EOF modes at different time scales. We separated the time scales as short (<20 days) and long (>20 days) based on the spectrum analysis. The long-term scale represents the seasonal variations, while the short-term scale represents the variations due to tide and weather events. In this way, we found that the Mode 1, that is, the alternation between propagating northeastward and southward, is mainly controlled by runoff and wind at seasonal time scales. It is also significantly modulated by tide and synoptic wind events. Mode 2, that is, the plume detachment and salinity change near the river mouth, is mainly correlated to the tidal range. This confirmed the previous study that the plume detachment northeast of the Changjiang River is mainly caused by the intense tidal mixing in spring tide [34, 49]. Mode 3, that is, part of the Changjiang River plume extending along the Jiangsu Coast, is mainly correlated to the tidal range but insensitive to the river discharge and wind.

Overall, from the EOF analysis, it can be seen that the Changjiang River plume mainly extends in three pathways, that is, the northeastward, southward, and northward branches. The former two branches are accounted for by Mode 1, which represents the dominant seasonal variation of the Changjiang River plume. The northeastward plume branch dominates during the flood season when the Changjiang discharge is huge and the wind is southerly. During the dry season with reduced discharge and enhanced northerly wind, the southward branch is developed, and the northeastward one vanishes. The northward plume branch along the Jiangsu Coast is a new finding, which occurs mostly in summer and autumn seasons.

7. Extension of Changjiang River plume to the Jiangsu Coast

The above analysis indicates that a small portion of the Changjiang River plume extends to the Jiangsu Coast, even in autumn when the wind turns northerly. Such an extension is in a direction opposite to that of the coastally trapped wave (i.e., the upstream direction). Unlike the massive up-shelf intrusion simulated by nontidal plume models (**Figure 6A**), this plume branch is weak. Such a weak plume extension diluted the seawater in the Subei Coastal Water, producing the so-called Subei low salinity water, which has been observed by numerous surveys (e.g., [33, 46, 61]) and is shown in climatological data ([2, 41]).

7.1. Freshwater flux into the Subei Coastal Water

To explore the dynamics that transports the Changjiang River plume to the Subei Coastal Water, we applied the flux decomposing method along a section SEC crossing this plume branch at 32.5°N. Considering the freshwater “concentration” $f = (s_o - s)/s_o$, the freshwater transport at a unit width of water column over a tidal cycle is defined as:

$$T = \left\langle \int_{-H}^0 v f dz \right\rangle \quad (1)$$

where v is the velocity component normal to the section (i.e., northward component); $\langle \rangle$ is a low-pass filter operator (with a cutoff window of 34 h). Decompose the freshwater concentration f into:

$$f = \langle \bar{f} \rangle + \bar{f}' + f \quad (2)$$

where \bar{f} is the depth averaged freshwater concentration, $\bar{f}' = \bar{f} - \langle \bar{f} \rangle$ is the tidal oscillatory term of the depth averaged freshwater concentration, and $f = f - \bar{f}$ is the vertical deviation of the freshwater concentration. v is treated in the same way. For the water depth, $H = \langle H \rangle + H'$. Therefore,

$$\begin{aligned} T &= \langle H \rangle \langle \bar{v} \rangle \langle \bar{f} \rangle + \langle H' \bar{v}' \rangle \langle \bar{f} \rangle + \langle H' \bar{f}' \rangle \langle \bar{v} \rangle + \langle H \bar{v}' \bar{f}' \rangle + \langle H \bar{v}' f' \rangle \\ &= T_1 + T_2 + T_3 + T_4 + T_5 \end{aligned} \quad (3)$$

in which T_1 is the Eulerian transport that is related to mean flow. T_2 is the Stokes transport that results from the nonlinear interaction between the sea surface tidal fluctuation and the tidal current. T_1 and T_2 represent the transport due to sub-tidal water mass transport. T_3 is almost zero in this study, and the sum of T_3 and T_4 is the tidal pumping transport that results from the tidal asymmetry among the freshwater concentration, water depth, and velocity. T_5 is the shear transport due to the vertically sheared structure of the concentration and velocity. T and T_1 through T_5 were integrated along SEC, respectively.

The freshwater transport across SEC is northward from March to November (**Figure 11**), although the northward plume branch mainly appears from July to October, possibly because of the inaccurate ambient ocean salinity (34 psu) in this region. Nevertheless, it means that the northward water mass transport persists along the Jiangsu Coast. The northward freshwater transport is mainly contributed by the Stokes transport and is enhanced in summer but weakened in winter by the Eulerian transport. The shear transport and tidal pumping transport were generally small.

As the Stokes transport dominates the northward freshwater transport along the Jiangsu Coast, even in the months with the northerly wind, the northward plume can develop. Under the persistent northward Stokes transport, once the Changjiang discharge rises and thereby increases the $\langle f \rangle$, or the wind causes the Eulerian transport to also be northward, the northward plume branch develops.

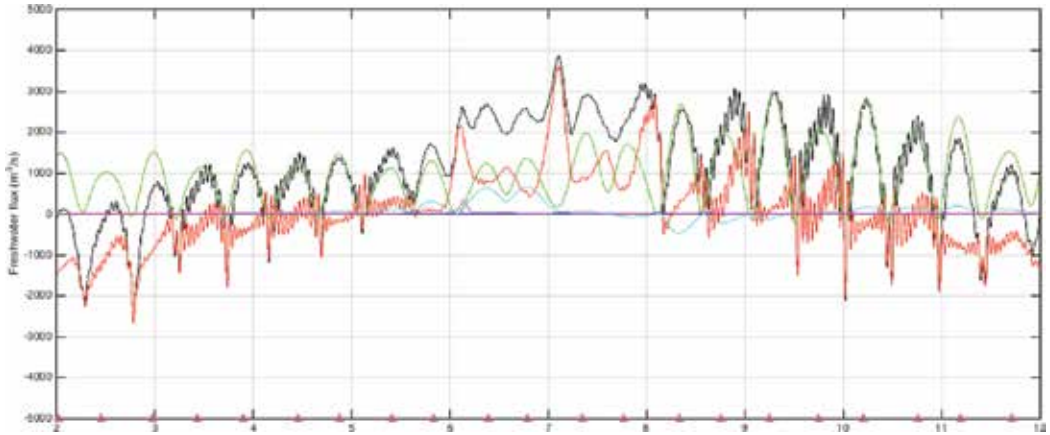


Figure 11. Freshwater flux and their decomposed components across the northward plume branch, with positive values to the north. Triangles at the bottom signify the times of the spring tides. Black line: total freshwater flux (T). Red line: Eulerian transport (T1). Green line: Stokes transport (T2). Blue line: T3. Light blue line: T4. Purple line: stress transport (T5).

7.2. Residual currents in response to wind and tide

Since the transport of the northward plume branch is determined by the sub-tidal water mass transport, we can understand its dynamics by investigating the residual currents around the Jiangsu coastal waters. Tide and wind are two most energetic forcings in the Jiangsu coastal waters. In fact, tide-induced residual currents are general in coastal regions [20, 24, 43], with their direction consistent to the projection of the major flood vector on the coast [56]. Two diagnostic numerical experiments were set, both of which only included the tide and 5 m s⁻¹ wind forcing, with directions of southerly and northerly, respectively, representing the summer and autumn seasons.

Eulerian and Stokes transports of the Changjiang diluted water in Eq. (3) is determined by the residual water mass transport, which can be decomposed into:

$$\langle \int_{-H}^0 \bar{v} dz \rangle = \langle H \bar{v} \rangle = \langle H \rangle \langle \bar{v} \rangle + \langle H' \bar{v} \rangle \quad (4)$$

by using the same method as Eq. (2). Normalized by tidally averaged depth, one can get:

$$\vec{V}_L = \vec{V}_E + \vec{V}_S \quad (5)$$

where

$$\vec{V}_L = \langle \int_{-H}^0 \bar{v} dz \rangle / \langle H \rangle, \vec{V}_E = \langle \bar{v} \rangle, \vec{V}_S = \langle H' \bar{v} \rangle / \langle H \rangle \quad (6)$$

\vec{V}_E is the traditional depth averaged Eulerian residual current; \vec{V}_S is noted as the mass transport Stokes drift [18, 43]; and their sum \vec{V}_L is the residual transport velocity. As the contributions of tidal pumping and shear transport are negligible for the northward plume branch, \vec{V}_E , \vec{V}_S , and \vec{V}_L can represent the transport of diluted water.

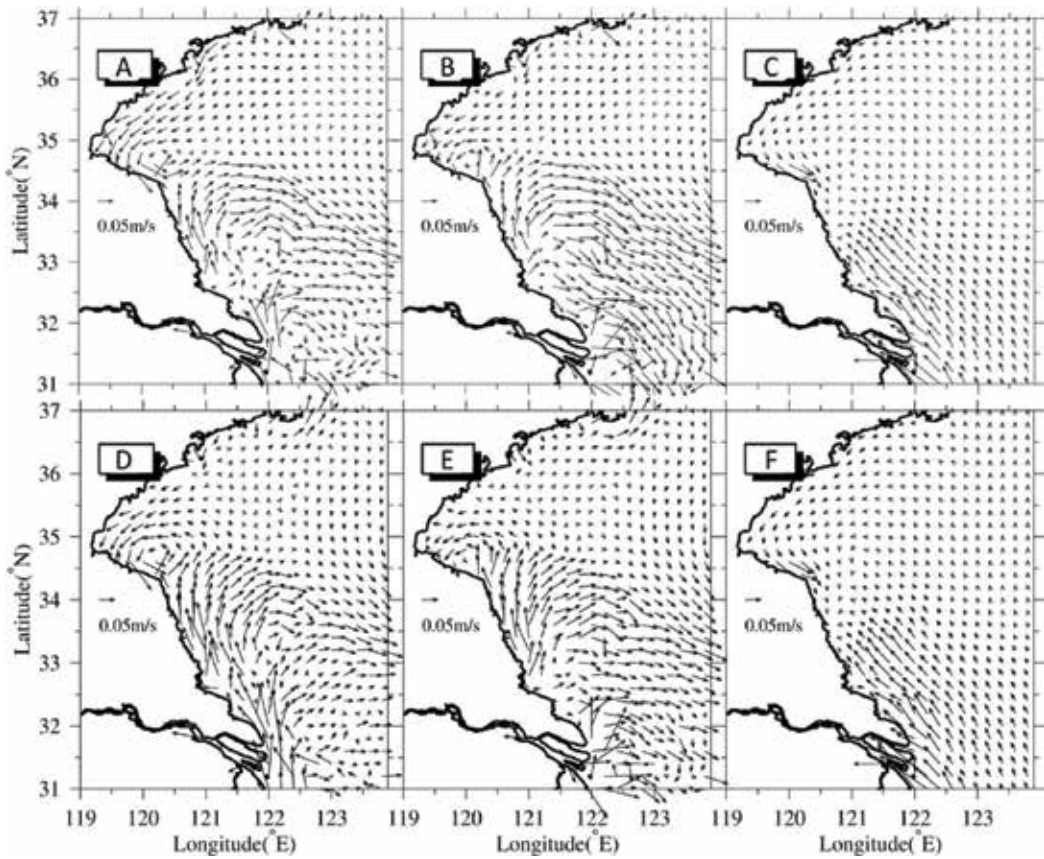


Figure 12. Residual transport velocity (A and D) and its decompositions of the Eulerian residual current (B and E) and the Stokes drift (C and F) during the spring tide. A, B, and C are the results under the 5 m s^{-1} northerly wind; D, E, and F are the results under the 5 m s^{-1} southerly wind.

Strong nonlinear interaction between wind and tide can be found from **Figures 12** and **13**. During the neap tide, \vec{v}_L is controlled by the Eulerian residual current, while the Stokes drift is negligible since the tidal range is small. The Eulerian residual current is northward when the wind is southerly but reverses when the wind turns to northerly. During the spring tide, however, the wind-driven circulation seems to be dampened significantly, and the residual current patterns are nearly under different wind directions. Although \vec{v}_L reverses its direction during neap tide as the wind direction changes, during the spring tide, it is basically northward from the Changjiang River mouth to $\sim 34^\circ\text{N}$ along the Jiangsu Coast.

From **Figures 12** and **13**, it can be seen that the Stokes drift essentially drives the up-shelf transport in the Subei Coastal Water, thus the extension of Changjiang River plume in this area. The formation mechanism of tide-induced Stokes drift is the nonlinear interaction between tidal elevation and tidal current, which is determined by tide tidal wave regime in the East China Sea and Yellow Sea [50]. Stokes transport is stable under various wind directions. This explains why the northward plume branch can exist not only during summer when the wind is southerly, but also can maintain itself in autumn when the wind has already turned to northerly.

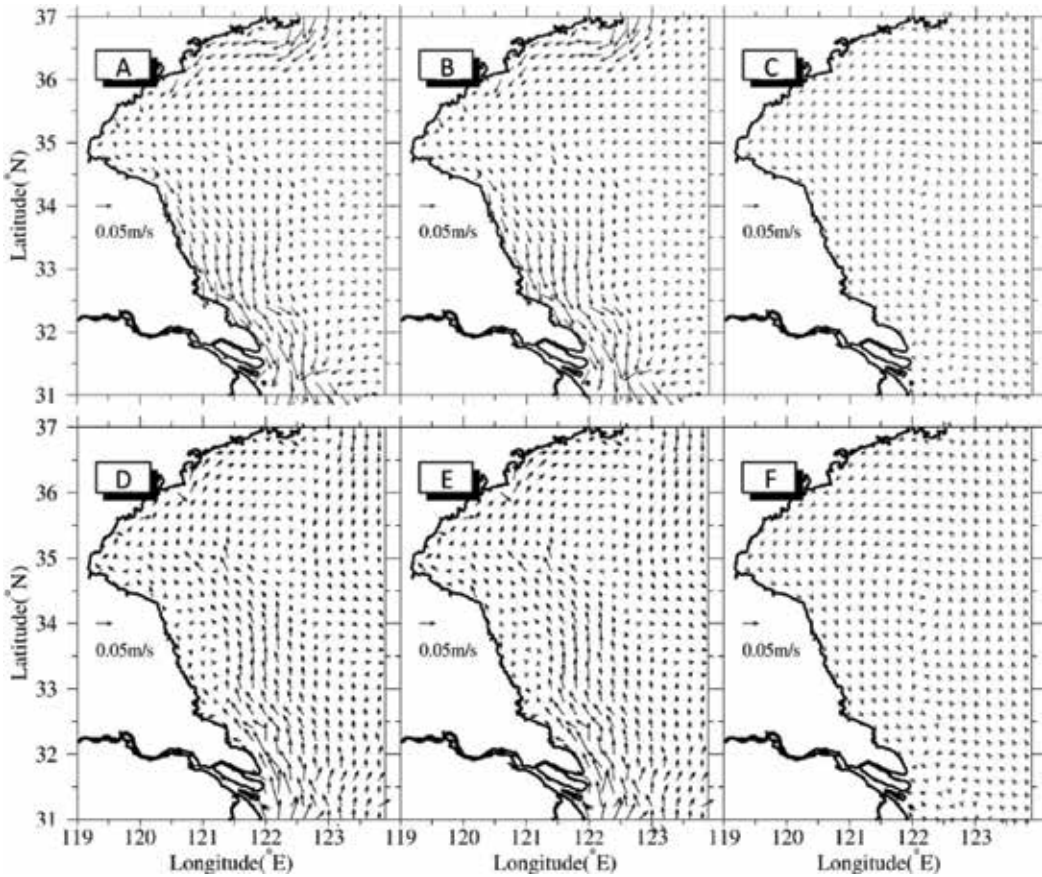


Figure 13. Same as Figure 12, except during the neap tide.

8. Conclusion

Researchers have worked on the Changjiang River plume for more than 60 years, which substantially promoted the understandings on the dynamics and environments in the Yellow and East China Sea. Looking back at the history, the academic studies on Changjiang River plume began very early in 1960s, when the basic characteristics were revealed. The research was interrupted by the Cultural Revolution in 1970s, and then resurged in 1980s and 1990s with numerous fantastic theoretical studies that attempted to reveal the dynamic mechanisms. No consensus, however, was reached during that period. In 1990s and 2010s, numerical simulation became a major method to study the Changjiang River plume, but the study was less active than those in 1980s and 1990s. One reason was that many physical oceanographers in China changed their research focus to the open ocean. Another reason, perhaps more importantly, is that the modeled river plume was often distinct from reality, which made the numerical models doubtful.

Since 2010, the tidal effect was found to be of essential importance in determining the characteristics of the Changjiang River plume. Moon et al. [34] and Rong and Li [37] found that it is

the tide that generates the massive plume detachment at specific locations. Li and Rong [26] found that it is the tide that remarkably strengthens the down-shelf transport of Changjiang River plume. Wu et al. [49] found that it is the tide that prevents the up-shelf plume intrusion, shifts the Changjiang River plume to the northeast outside the river mouth, and bifurcates the plume at the head of submarine canyon. Wu et al. [50] found that it is the tide that transports part of the Changjiang River plume to the Subei Coastal Water. Recently, Wu [51] further found that it is the tide that generates the cross-shelf penetration of Changjiang River plume in the Zhejiang-Fujian coastal water.

It is not to say that tide is the only important factor controlling the dynamics of the Changjiang River plume. Winds, shelf currents, and the river discharge itself are of course important in determining the dynamics around the Changjiang River Estuary. But the tidal effects were often overlooked before 2010, although it is no doubting that the tide is the most energetic movements around the Changjiang River Estuary. The reason could be that the tidal effect is highly nonlinear, and hence an elegant theory on dynamics can hardly be established. Most early studies just ignored the tidal forcing in theoretical or numerical studies. The existent classic plume theories, such as Yankovsky and Chapman [54] and Chapman and Lentz [9], were developed without considering the tidal effects. A question arises that on what degree these theories can be applied in and tidal area. Yellow and East China Seas is a perfect place to study the river plume, since this area is confluenced by massive river discharge, strong tide, energetic shelf circulation, and a typical seasonal monsoon. Many have been done, more await to be explored.

Acknowledgements

We appreciate Prof. Xiangshan Liang for his kind invitation for us to write this chapter. Some materials of this chapter have been previously published in journal articles, and the authors want to appreciate the previous reviewers and editors once again for their insightful comments and suggestions. This work was supported by National Natural Science Foundation of China (Grant no. 40806034) and the National Basic Research Program of China (2011CB409801).

Author details

Hui Wu^{1*}, Tianning Wu¹, Jian Shen² and Jianrong Zhu¹

*Address all correspondence to: hwu@sklec.ecnu.edu.cn

1 State Key Laboratory of Estuarine and Coastal Research, East China Normal University, Shanghai, P.R. China

2 Virginia Institute of Marine Science, College of William and Mary, Gloucester Point, Virginia, USA

References

- [1] Ahsan AQ, Blumberg AF. Three-dimensional hydrothermal model of Onondaga Lake, New York. *Journal of Hydraulic Engineering*. 1999;**125**(9):912-923
- [2] Editorial Board for Marine Atlas. *Ocean Atlas in Huanghai Sea and East China Sea (Hydrology)*. Beijing: China Ocean Press; 1992
- [3] Bai XZ, Wang F. Numerical study on the mechanism of the expansion of the Changjiang River diluted water in summer. *Oceanologia et Limnologia Sinica*. 2003;**34**(6):593-603
- [4] Beardsley R. Structure of the Changjiang river plume in the East China Sea during June 1980. In: *Paper Presented at Proceedings of International Symposium on Sedimentation on the Continental Shelf, with Special Reference to the East China Sea*. China Ocean Press; 1983
- [5] Blumberg A. A primer for ECOM-si, Technical report of HydroQual, 66. 1994
- [6] Chang PH, Isobe A. A numerical study on the Changjiang diluted water in the Yellow and East China Seas. *Journal of Geophysical Research: Oceans*. 2003;**108**(C9):3299
- [7] Chao S-Y. River-forced estuarine plumes. *Journal of Physical Oceanography*. 1988;**18**(1):72-88
- [8] Chao S-Y, Boicourt WC. Onset of estuarine plumes. *Journal of Physical Oceanography*. 1986;**16**(12):2137-2149
- [9] Chapman DC, Lentz SJ. Trapping of a coastal density front by the bottom boundary layer. *Journal of Physical Oceanography*. 1994;**24**(7):1464-1479
- [10] Chen C, Xue P, Ding P, Beardsley RC, Xu Q, Mao X, et al. Physical mechanisms for the offshore detachment of the Changjiang diluted water in the East China Sea. *Journal of Geophysical Research: Oceans*. 2008;**113**(C2):C02002
- [11] Dong L, Guan W, Chen Q, Li X, Liu X, Zeng X. Sediment transport in the Yellow Sea and East China Sea. *Estuarine, Coastal and Shelf Science*. 2011;**93**(3):248-258
- [12] Fong DA. *Dynamics of Freshwater Plumes: Observations and Numerical Modeling of the Wind-Forced Response and Alongshore Freshwater Transport*. Massachusetts Institute of Technology and Woods Hole Oceanographic Institution; Ph.D. thesis; Woods Hole; 1998
- [13] Galperin B, Kantha L, Hassid S, Rosati A. A quasi-equilibrium turbulent energy model for geophysical flows. *Journal of the Atmospheric Sciences*. 1988;**45**(1):55-62
- [14] Gao L, Li D-J, Ding P-X. Quasi-simultaneous observation of currents, salinity and nutrients in the Changjiang (Yangtze River) plume on the tidal timescale. *Journal of Marine Systems*. 2009;**75**(1):265-279
- [15] Gao S, Collins M. Holocene sedimentary systems on continental shelves. *Marine Geology*. 2014;**352**:268-294

- [16] Garvine RW. Penetration of buoyant coastal discharge onto the continental shelf: A numerical model experiment. *Journal of Physical Oceanography*. 1999;**29**(8):1892-1909
- [17] Garvine RW. The impact of model configuration in studies of buoyant coastal discharge. *Journal of Marine Research*. 2001;**59**(2):193-225
- [18] Hunter J. An investigation into the circulation of the Irish Sea. Oceanography Report 72-1. Menai Bridge, UK: Marine Science Laboratories, University College of North Wales; 1972
- [19] Hur H, Jacobs G, Teague W. Monthly variations of water masses in the Yellow and East China Seas, November 6, 1998. *Journal of Oceanography*. 1999;**55**(2):171-184
- [20] Ianniello J. Tidally induced residual currents in estuaries with constant breadth and depth. *Journal of Marine Research*. 1977;**35**:755-786
- [21] Isobe A, Ando M, Watanabe T, Senjyu T, Sugihara S, Manda A. Freshwater and temperature transports through the Tsushima-Korea Straits. *Journal of Geophysical Research: Oceans*. 2002;**107**(C7):3065
- [22] Kourafalou VH, Oey LY, Wang JD, Lee TN. The fate of river discharge on the continental shelf: 1. Modeling the river plume and the inner shelf coastal current. *Journal of Geophysical Research: Oceans*. 1996;**101**(C2):3415-3434
- [23] Le K-T. A preliminary study of the path of the Changjiang diluted water. *Oceanologia et Limnologia Sinica*. 1984;**15**(2):157-167
- [24] Li C, O'Donnell J. Tidally driven residual circulation in shallow estuaries with lateral depth variation. *Journal of Geophysical Research: Oceans*. 1997;**102**(C13):27915-27929
- [25] Li D, Zhang J, Huang D, Wu Y, Liang J. Oxygen depletion off the Changjiang (Yangtze River) estuary. *Science in China Series D: Earth Sciences*. 2002;**45**(12):1137-1146
- [26] Li M, Rong Z. Effects of tides on freshwater and volume transports in the Changjiang River plume. *Journal of Geophysical Research: Oceans*. 2012;**117**(C6):C06027
- [27] Lie HJ, Cho CH, Lee JH, Lee S. Structure and eastward extension of the Changjiang River plume in the East China Sea. *Journal of Geophysical Research: Oceans*. 2003;**108**(C3):3077
- [28] Liu Z, Xia D. A preliminary study of tidal current ridges. *Chinese Journal of Oceanology and Limnology*. 1985;**3**(1):118-133
- [29] Liu Z, Hu D. Preliminary study on the Huanghai Sea coastal current and its relationship with local wind in summer. *Acta Oceanologica Sinica*. 2009;**31**(2):1-7
- [30] Mao H, Gan Z-J, Lan S-F. A preliminary study of the Yangtze diluted water and its mixing processes. *Oceanologia et Limnologia Sinica*. 1963;**5**(3):183-206
- [31] Matano RP, Palma ED. The upstream spreading of bottom-trapped plumes. *Journal of Physical Oceanography*. 2010;**40**(7):1631-1650
- [32] Mellor GL, Yamada T. Development of a turbulence closure model for geophysical fluid problems. *Reviews of Geophysics*. 1982;**20**(4):851-875

- [33] Mi T-Z, Yao Q-Z, Meng J, Zhang X-L, Liu S-M. Distributions of nutrients in the southern Yellow Sea and East China Sea in spring and summer 2011. *Oceanologia et Limnologia Sinica*. 2012;**43**:678-688
- [34] Moon J-H, Hirose N, Yoon J-H, Pang I-C. Offshore detachment process of the low-salinity water around Changjiang Bank in the East China Sea. *Journal of Physical Oceanography*. 2010;**40**(5):1035-1053
- [35] Pan Y, Wang K, Huang S. Analysis on the path of transportation and diffusion of Changjiang diluted water. *Donghai Marine Science*. 1997;**15**(2):25-34
- [36] Pu Y, Xu X. The expansion of diluted water in the Changjiang (Yangtze R.) as seen from the variations in the runoff, water level and salinity. *Marine Science Bulletin*. 1983;**2**(3):1-7
- [37] Rong Z, Li M. Tidal effects on the bulge region of Changjiang River plume. *Estuarine, Coastal and Shelf Science*. 2012;**97**:149-160
- [38] Shen H. *Material Flux of the Changjiang Estuary*. Beijing: China Ocean Press; 2001
- [39] Shi JZ, Lu L-F. A short note on the dispersion, mixing, stratification and circulation within the plume of the partially-mixed Changjiang River Estuary, China. *Journal of Hydro-Environment Research*. 2011;**5**(2):111-126
- [40] Smagorinsky J. General circulation experiments with the primitive equations: I. The basic experiment. *Monthly Weather Review*. 1963;**91**(3):99-164
- [41] Su J, Yuan Y. *Oceanography of China Seas*. Beijing: China Ocean Press; 2005
- [42] Tang D, Di B, Wei G, Ni I-H, Wang S. Spatial, seasonal and species variations of harmful algal blooms in the South Yellow Sea and East China Sea. *Hydrobiologia*. 2006;**568**(1): 245-253
- [43] Tee K-T. Tide-induced residual currents, a 2-D nonlinear tidal model. *Journal of Marine Research*. 1976;**34**:603-628
- [44] Tong Y, Zhao Y, Zhen G, Chi J, Liu X, Lu Y, et al. Nutrient loads flowing into coastal waters from the main rivers of China (2006-2012). *Scientific Reports*. 2015;**5**:16678
- [45] Wang B, Xie L, Sun X. Water quality in marginal seas off China in the last two decades. *International Journal of Oceanography*. 2011;**2011**:731828
- [46] Wei Q, Zang J, Wei X, Liu L. The distribution of nutrients and the relationship of them with the circulation condition in the western southern Huanghai Sea in autumn. *Acta Oceanologica Sinica*. 2011;**33**(1):74-82
- [47] Wu H, Zhu J. Advection scheme with 3rd high-order spatial interpolation at the middle temporal level and its application to saltwater intrusion in the Changjiang Estuary. *Ocean Modelling*. 2010;**33**(1):33-51
- [48] Wu H, Zhu J, Choi BH. Links between saltwater intrusion and subtidal circulation in the Changjiang Estuary: A model-guided study. *Continental Shelf Research*. 2010;**30**(17): 1891-1905

- [49] Wu H, Zhu J, Shen J, Wang H. Tidal modulation on the Changjiang River plume in summer. *Journal of Geophysical Research: Oceans*. 2011;**116**(C8):C08017
- [50] Wu H, Shen J, Zhu J, Zhang J, Li L. Characteristics of the Changjiang plume and its extension along the Jiangsu Coast. *Continental Shelf Research*. 2014;**76**:108-123
- [51] Wu H. Cross-shelf penetrating fronts: A response of buoyant coastal water to ambient pycnocline undulation. *Journal of Geophysical Research: Oceans*. 2015;**120**(7):5101-5119
- [52] Xuan JL, Huang D, Zhou F, Zhu XH, Fan X. The role of wind on the detachment of low salinity water in the Changjiang Estuary in summer. *Journal of Geophysical Research: Oceans*. 2012;**117**(C10):C10004
- [53] Yang SL, Milliman JD, Xu KH, Deng B, Zhang X, Luo X. Downstream sedimentary and geomorphic impacts of the Three Gorges Dam on the Yangtze River. *Earth-Science Reviews*. 2014;**138**:469-486
- [54] Yankovsky AE, Chapman DC. A simple theory for the fate of buoyant coastal discharges. *Journal of Physical Oceanography*. 1997;**27**(7):1386-1401
- [55] Yankovsky AE. The cyclonic turning and propagation of buoyant coastal discharge along the shelf. *Journal of Marine Research*. 2000;**58**(4):585-607
- [56] Ye J, Garvine RW. A model study of estuary and shelf tidally driven circulation. *Continental Shelf Research*. 1998;**18**(10):1125-1155
- [57] Yu K. Two dimensional numerical calculation of residual current and salinity at the Changjiang River Estuary. *Oceanologia et Limnologia Sinica*. 1990;**21**(1):92-96
- [58] Yuan D, Zhu J, Li C, Hu D. Cross-shelf circulation in the Yellow and East China Seas indicated by MODIS satellite observations. *Journal of Marine Systems*. 2008;**70**(1):134-149
- [59] Zhang S, Wang Q, Lü Y, Cui H, Yuan Y. Observation of the seasonal evolution of the Yellow Sea Cold Water Mass in 1996-1998. *Continental Shelf Research*. 2008;**28**(3):442-457
- [60] Zhao B. On the extension of Changjiang diluted water. *Acta Oceanologica Sinica*. 1991;**13**(5):600-610
- [61] Zhou F, Su J, Huang D. Study on the intrusion of coastal low salinity water in the west of southern Huanghai Sea during spring and summer. *Acta Oceanologica Sinica (in Chinese)*. 2004;**26**(5):34-44
- [62] Zhu J, Li Y, Shen H. Numerical simulation of the wind field's impact on the expansion of the changjiang river diluted water in summer. *Oceanologia et Limnologia Sinica*. 1997;**28**(1):72-79
- [63] Zhu J, Xiao C, Shen H. Numerical model simulation of expansion of Changjiang diluted water in summer. *Acta Oceanologica Sinica*. 1998;**20**(5):13-22
- [64] Zhu C, Wang Z-H, Xue B, Yu P-S, Pan J-M, Wagner T, et al. Characterizing the depositional settings for sedimentary organic matter distributions in the Lower Yangtze River-East China Sea Shelf System. *Estuarine, Coastal and Shelf Science*. 2011;**93**(3):182-191

Coastal Pollution

Marine Ecological Disasters and Their Physical Controlling Mechanisms in Jiangsu Coastal Area

Min Bao, Weibing Guan, Zhenyi Cao, Qi Chen and Yun Yang

Additional information is available at the end of the chapter

<http://dx.doi.org/10.5772/intechopen.80015>

Abstract

The studies in this chapter are focused on marine ecological disasters in Jiangsu coastal area. Three kinds of algal blooms occurred in this region, namely, red tide associated with *Dinoflagellate*, green tide associated with *Ulvaprolifera* and golden tide associated with *Sargassum*. Numerical model results demonstrated that red tides in Haizhou Bay originated locally, because most of *Dinoflagellates* near Zhoushan Islands would be transported northeastward by the Changjiang diluted water, and even the lucky ones that entered the south of Jiangsu coastal area would die in the Subei Shoal due to high turbidity there. Due to the Changjiang diluted water and the prevailing southerly wind, *Ulvaprolifera* could not drift southward, either. Seawater with high turbidity in the Subei Shoal limited sunlight penetration into deep water column, and further inhibited the growth of *Ulvaprolifera* suspending in the water column. In this chapter, we use drift bottles and satellite-tracked Argos drifters to provide solid direct dynamic evidence that *Ulvaprolifera* could drift from the Subei Shoal to Qingdao coastal area and even further north. The sand ridges limited the traveling path of *Ulvaprolifera* in the Subei Shoal, and wind-driven currents and other baroclinic processes helped *Ulvaprolifera* travel farther to the north.

Keywords: red tide, green tide, golden tide, physical controlling mechanism, Jiangsu coastal area

1. Marine ecological disaster and research contents of this chapter

1.1. Eutrophication

Since the end of the last century, marine environmental quality has become worse and worse as local economy developed rapidly in Jiangsu [1]. Chinese national water quality distribution showed that the pollution problems in China were especially serious in the Changjiang estuary and Jiangsu coastal area. Water pollutions have a series of negative effects on inshore cultivation, wetland protection, among others. Similar as water quality situation, eutrophication problems along the Jiangsu coast were conspicuous. Seawater pollution in China was mainly caused by the discharge of land-sourced pollutants, and coastal cities including Nantong city, Yancheng city and Lianyungang city were affected mostly. The most polluted coastal waters were near estuaries, sewage outlets and their adjacent seas. It was obvious that the seawater near the coast was much more polluted than that of farther offshore. The main pollutants were inorganic nitrogen, active phosphate and petroleum. As the equation of eutrophication index showed [2], the most polluted seawaters were the most eutrophic seawaters. Increment of inorganic nitrogen and active phosphate caused eutrophication in the coastal waters, and this situation has been going on for a long time. There was no obvious inter-annual variation of the polluted sea area in Jiangsu, with the largest area of seriously polluted waters to be 14,371 km² in 2012. Generally, eutrophication gradually worsened from spring to autumn during a year. In spring, the seawaters were in the critical state of eutrophication; eutrophication gradually accelerated during summer and finally seawaters became seriously polluted along the Jiangsu coast [1]. Nutrients were sufficient for algal growth in the Jiangsu coastal region. Some algae can produce toxin poisoning shellfish, fish and other marine organisms. Even for nontoxic algal blooms, the excessive reproduction of algae can also cause blockage or damage to gills, and marine organisms can be asphyxiated in the poor oxygen waters [3]. At present, the major marine disasters suffered in the Jiangsu coast were red tide and green tide; but in 2017, golden tide seemed to join in.

1. Red tide

Red tide is a kind of algal bloom with a red or brown color caused by some species of *dinoflagellates* [4]. According to the records of red tides in the Jiangsu Marine Environment Quality Bulletins and National Marine Disaster Bulletins (**Figure 1**), Jiangsu coastal area was not a region with frequent red tides. Nevertheless, they happened nearly every year in the area; especially in 2005, breaking out four times in the Jiangsu coast with a total size of 1274 m² (**Figure 2**). Among them, the red tide from September 23 to September 27 was the largest since the red-tide-monitoring area was established in 2005, with a single size of 1000 m². According to the statistical data, this kind of tides in this region usually happened from April to September, especially in May and June. The frequency was the lowest in August. In Jiangsu coast, they mainly occurred in the waters of Haizhou Bay and Nantong offshore area, with 78% in Haizhou Bay. The dominant species of red tides in this region was *Skeletonema macostatum* (**Table 1**). The red tides in Haizhou Bay were mostly poisonous dinoflagellate, and those in Nantong offshore area were often diatom. Since poisonous blooms were very harmful, the State Oceanic Administration set up a red-tide-monitoring area in Haizhou Bay

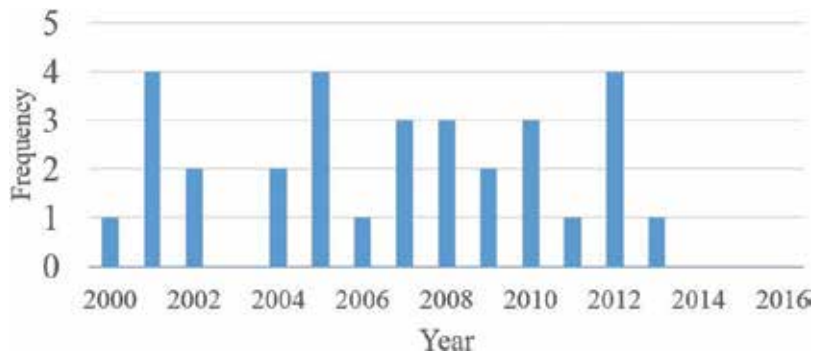


Figure 1. Frequency of red tides in Jiangsu coastal area from 2000 to 2016.

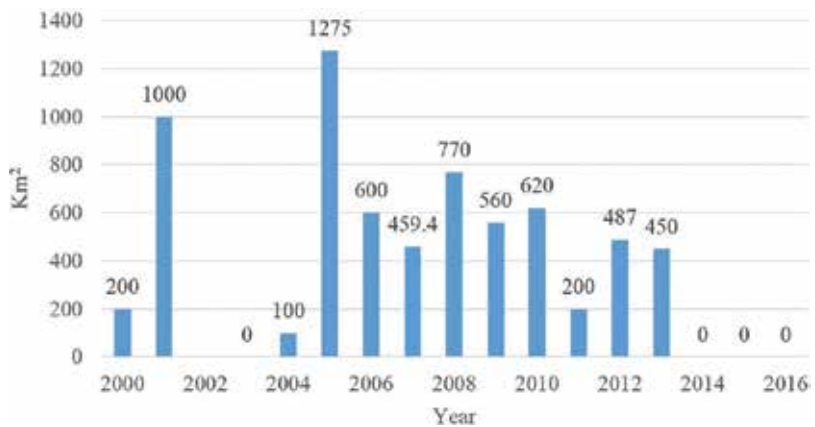


Figure 2. Area variation of red tide in Jiangsu coastal area from 2000 to 2016.

(119°31'E-119°35'E, 34°44'N-34°48'N), where high-frequency monitoring was carried out. Note that although the Jiangsu coastal water was still in a state of eutrophication and has potential risk of red tide, red tide never happened after 2014.

2. Green tide

Algal blooms caused by excessive growth of green algae, such as *Ulva prolifera*, and their gathering in high density are referred to as green tide [5]. *Ulva prolifera* is nontoxic and edible with high protein, high dietary fiber, low fat, low energy, rich minerals and rich vitamins. However, massive gathering of *Ulva prolifera* is regarded as a kind of marine disaster, because green tide blocks sunlight penetration into the water column below the surface, which will affect the growth of other kinds of algae. Anoxia during the demise of green tide causes other marine organisms to be asphyxiated in the poor oxygen waters. Green tide can seriously interfere with human activities along the coast.

Since 2007, green tide erupted in 11 consecutive years and has become a common marine disaster in Jiangsu and Shandong coastal seas. According to some studies [6, 7], *Ulva prolifera*

Dominant species of red tide	Frequency	Year
<i>Gonyaulax polygramma</i>	1	2004
<i>Noctiluca scientillans</i>	1	2004
<i>Skeletonema macostatum</i>	5	2001, 2005, 2010, 2011, 2012
<i>Eucampia zodiacus</i>	2	2006, 2008
<i>Gymnodinium catenatum</i>	3	2005, 2006, 2010
<i>Heterosigma akashiwo</i>	3	2007, 2008, 2013
<i>Thalassiosira</i> sp.	1	2007
<i>Asterionella japonica</i>	1	2008
<i>Karenia mikimotoi</i>	1	2009

Table 1. Dominant species of red tide in Jiangsu coastal area from 2000 to 2016.

originated from the Subei Shoal, which was usually attached to the rafts of *Porphyra* aquaculture facilities (**Figure 3a**). During the harvest season, *Ulvaprolifera* was peeled off from the rafts and moved with tidal currents into the seawater with high turbidity (**Figure 3b**). At the beginning, *Ulvaprolifera* was suspended in the water column (**Figure 3c**); after drifting into clear water, band-shaped green tide was generated with excessive growth (**Figure 3d**). Green tides usually occur from March to August. Sporadic *Ulvaprolifera* could be detected around the Jiangsu coastal sea in late-March. Massive green tides often arrived at the Qingdao coast in early to mid-June. The demise of green tide started from July and ended in August. Green tide in the Jiangsu coastal area was much smaller in size than that in Shandong. In the Jiangsu coastal sea, green tide usually gathered in the north, with less in the southern region. Only sporadic *Ulvaprolifera* could be found in the Subei Shoal, while in the offshore seas of Yancheng and Haizhou Bay band-shaped green tides with different sizes have been observed. Green tides either landed on the coast or gathered near shore to the north of Jiangsu during different years. According to the data, both the largest distribution area and the largest affected area both reached maxima in 2009, being 58,000 km² and 2100 km², respectively. In 2016, the largest distribution area was 57,500 km², but the largest affected area was only 554 km². Generally, green tides off Jiangsu accounted for one-third of the whole *Ulvaprolifera*, and most *Ulvaprolifera* in this region floated in the offshore sea, with a small amount landed in the northern coast of Jiangsu province.

3. Golden tide

Sargassum is a genus of brown macroalgae, so *Sargassum* blooms are commonly referred to as "Golden tides" [8]. Golden tide is new as a marine disaster in the Jiangsu coastal sea (**Figure 4**). The *Porphyra* aquaculture in the Jiangsu coast will be destroyed since there is a competitive growth between *Porphyra* and *Sargassum*. *Sargassum* was believed to originate in the open sea. In the previous years, green tides were often mixed with a small amount of *Sargassum*. For instance, R/V "KeXue #3" detected that the mixing ratio of *Ulvaprolifera* to *Sargassum* was 95:5 on June 8, 2016. As the China Ocean News reported, in late-December of 2016, golden tide suddenly appeared in the Jiangsu coastal area and lasted until late-February



Figure 3. *Ulvaproliifera* (a) attached on the rafts of *Porphyra* aquaculture facilities, (b) on the tidal flats, (c) in the water with high turbidity and (d) in clean water.



Figure 4. *Sargassum* in the offshore area of Dafeng in Jiangsu.

of 2017. A lot of *Porphyra* aquaculture facilities collapsed due to this golden tide event. The satellite image in late April of 2017 showed that massive *Sargassum* floated in the open sea and moved landward gradually. The mixing ratio of *Ulvaproliifera* to *Sargassum* detected on June 9, 2017 was 60:40. In future, the Jiangsu coastal sea may face a situation when three kinds of macroalgae occur at the same time.

1.2. Research contents in this chapter

Though being the two main kinds of algal blooms in Jiangsu province, red tide and green tide rarely caused related algal blooms in Zhejiang province, especially in the north of Zhejiang coastal area, which is adjacent to the southern Jiangsu coastal area. Red tides of Zhejiang coast, a province with the most frequent red tides in the country, usually happened around Zhoushan Islands near the Changjiang estuary, while Haizhou Bay in the northern Jiangsu province was a place with frequent red tides. These two provinces are close to each other, but their algal bloom distribution patterns are so different. What separates these red tides is the first question we want to answer in this chapter.

Another emphasis in this chapter is on *Ulvaprolifera* in the Jiangsu coastal area. Previous studies have shown that *Ulvaprolifera* originated from the *Porphyra* aquaculture area in the Subei Shoal in the western Yellow Sea. But little direct dynamic evidence was provided to support this. The Subei Shoal is characterized by complex topography, with a lot of radial sand ridges and broad tidal flats. *Porphyra* aquaculture facilities were placed over the tidal flats, which were believed to be the source of *Ulvaprolifera*. Therefore, it can be summarized as three questions as follows. (1) Could algae in the Subei Shoal move out of this region into the deep waters? (2) If so, could algae subsequently travel northward the Qingdao coast or even further north? (3) Why did green tides break out in Qingdao coast and its adjacent seas, but not in the source region of the Subei Shoal? What was the physical mechanism behind this?

In the following subsections, we will answer these questions and reveal the physical mechanisms for the drifting and development of *Ulvaprolifera*.

2. Observation and research plans

2.1. Hydrological and meteorological data collection

Data used in this study were from field observations and satellite remote sensing products. The data of temperature, salinity, currents, transparency, suspended particulate matter (SPM) and photosynthetically available radiation (PAR) were collected from the field observations. Conductivity-temperature-depth (CTD) instruments deployed at two mooring stations collected long time series of temperature and salinity data. Current data were obtained using the acoustic Doppler current profilers (ADCPs) installed at two anchored and two moored stations. *In-situ* temperature, salinity and PAR data were collected during the four field surveys. We collected transparency values using the Secchi disk, which will be used to calculate *in-situ* SPM concentration.

MODIS-Aqua images from April to June 2012 were used to retrieve monthly averaged SPM data [9]. The wind data were from a blended sea wind data product supported by the US National Oceanic and Atmospheric Administration (<http://www.ncdc.noaa.gov/oa/rsad/air-sea/seawinds.html>).

2.2. Drift bottles and satellite-tracked Argos drifters

The Subei Shoal is too shallow to deploy satellite-tracked Argos drifters. As a result, house-made drift bottles were used, and 80 were released at $33^{\circ}13.3'N$, $121^{\circ}10.2'E$ in 2012 (Figure 5). Half of the bottles were empty, to insure that they can float near the surface, and the rest were filled with sand to make them submersed under the surface as some *Ulvaprolifera* suspends in the water column.

Outside the Subei Shoal, four satellite-tracked Argos drifters were deployed in June 2011 in the deep waters, and six were released in June 2011 (Figure 5). Location information collected hourly was transmitted to the laboratory via satellite.

2.3. Numerical model

The Regional Oceanic Modeling System (ROMS; citations needed) was used to build the 3D hydrodynamic model for the East China Sea with three-layer nested grids. Table 2 shows the domains and related information of the three-layer nested models. After being validated, the model can reproduce main currents and their annual variation in the East China Sea,

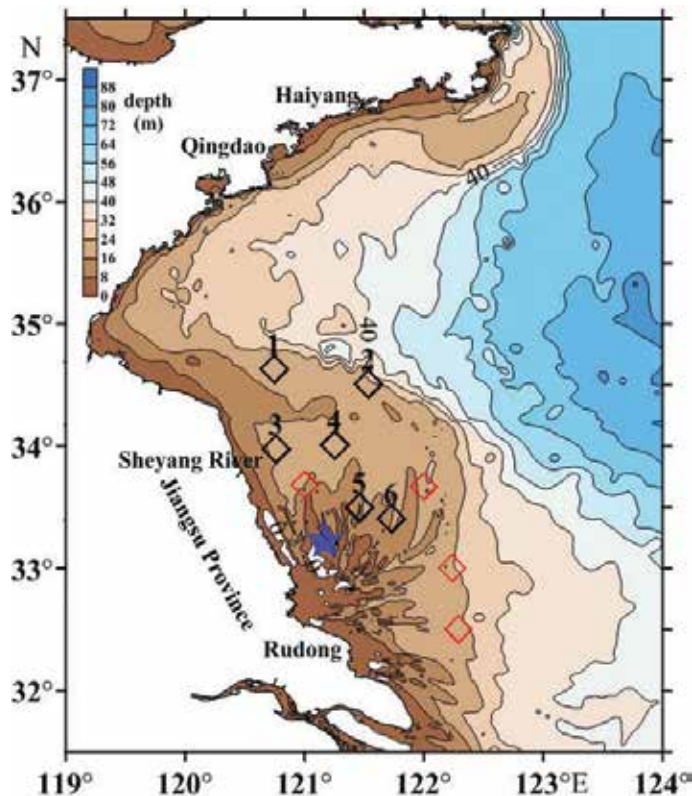


Figure 5. Topography of the southwestern Yellow Sea with release location of drift bottles (blue ★) and satellite-tracked surface Argos drifters released in 2011 (red ◇) and 2012 (red ◇).

Model	Domain	Resolution (°)	Depth (m)	Vertical layers
I	18°S-63°N, 99°E-165°E	1/6	5-5500	20
II	15°N-47.5°N, 105.5°E-139°E	1/12	5-5500	20
III	22.75°N-41°N, 115.75°E-131°E	1/24	5-5500	20

Table 2. Related information for three-layer nested models.

including the Kuroshio current, the Taiwan warm current, the Min-Zhe coastal currents, and so on. In addition, a coastal numerical model built for the Subei Shoal will be described in the following paragraphs.

An unstructured grid, finite-volume, primitive equation community ocean model (FVCOM) was used to build the Subei Shoal coastal numerical model. The model domain was large enough to ensure that the open boundary was far from the Subei Shoal. The resolution in the ridge area was refined to be ~140 m, while the grid was 15,000 m near the open boundary. The model included 56,548 elements and 28,456 nodes in the horizontal direction and 11 sigma levels in the vertical direction. Tidal forcing along the open boundaries was added hourly, which was derived from the Oregon State University Tidal Inversion Software (OTIS) Regional Tidal Solutions and included tidal constituents of M_2 , S_2 , N_2 , K_2 , K_1 , P_1 , O_1 and Q_1 . Time step was 1 s for the external mode, and the time split was 10. Finally, the results from this model were validated by observations [10].

3. Main results

3.1. Controlling effects of Changjiang diluted water on the algal distribution in the East China Sea and the Yellow Sea

The Changjiang is the largest river in China; its average annual sediment discharge of 4.86 tons and runoff of 924 billion cubic meters ranked the third and fourth, respectively, in the world. Such large amounts of sediment and runoff will inevitably have important impacts on the physical environment of the East China Sea. The Changjiang River is also a main source of nutrients for our study domain. The Changjiang diluted water also plays an important role on nutrient distribution and its variation trend and affects distribution pattern of algal disaster.

Based on the observation data, the ROMS numerical model was applied to study the extension of the Changjiang diluted water and its effect on nutrient distribution pattern. The results in **Figure 6** show that the Subei coastal current, the Changjiang diluted water and the Min-Zhe coastal current flow southward under the strong northeast winter monsoon; furthermore, the Changjiang diluted water and the Min-Zhe coastal current flow close to the shore. The Subei coastal current appeared to invade the northern part of the East China Sea, and the Min-Zhe coastal current still tended to move northward but was obviously slowed down. In summer, the Changjiang diluted water turned toward northeast, heading to Jeju Island. Both the Min-Zhe coastal current and Taiwan warm current moved northeastward with speeds larger than those in the other months. The Subei coastal current had an obvious tendency to move northward along

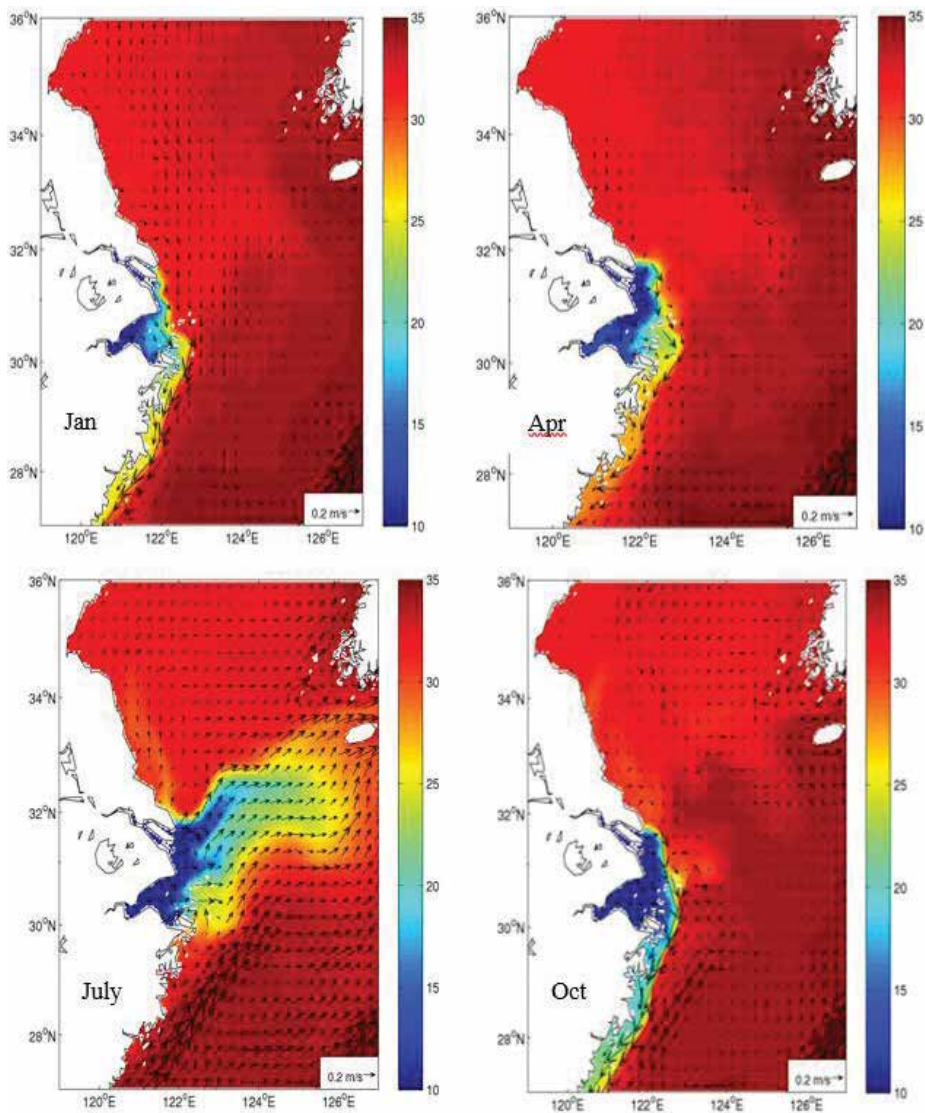


Figure 6. Current and salinity patterns of the 1-m layer in the Changjiang estuary and its adjacent region.

the coast. Spring and summer were transition seasons. The diluted water in the offshore area was limited in the surface layer, and basically there was no evidence of diluted water in the 20-m layer. This was consistent with the characteristics of observed diluted water distribution pattern.

In addition, algal migration paths in the red tide were studied. Assuming that at the end of April, red tide appeared constantly in the Zhoushan coastal area. Simulation through September 1st showed the algal drifting as neutral particles. The trajectories of all particles are shown in **Figure 7**. Most (~89%) of them moved to the Changjiang estuary and the Kuroshio region, and a few (6%) of them were transported to the Tsushima Strait. Satellite images and *in-situ* photos show that the seawater in the Subei Shoal was of high turbidity, but the seawater in the Haizhou Bay was much clearer (**Figure 8**). About 5% of the particles from Zhoushan entered the Yellow

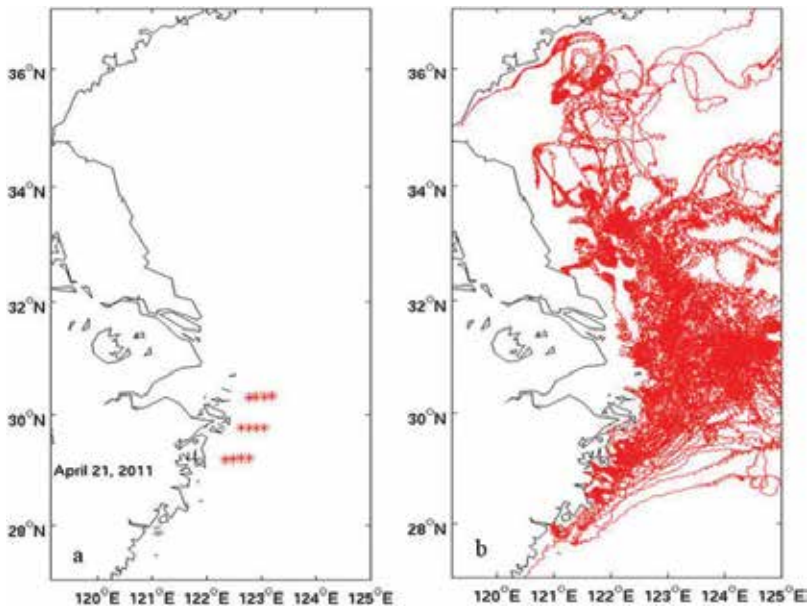


Figure 7. (a) Released locations for all particles and (b) trajectories of all neutral particles released in Zhoushan coastal area in 2011.

Sea, but most of them went through the waters with high suspended sediment concentration in the Subei area for a long time, where they could not grow well and even died in the turbid water. Therefore, it can be concluded that the red tide in the East China Sea can hardly invade the Yellow Sea, and that the red tides happened in Haizhou Bay, Jiangsu province were local events.

For green tides, it is assumed that *Ulva prolifera* moved like neutral particles, and they appeared continuously in the Subei Shoal for 100 days from April 21, 2011. The trajectories for all particles are shown in **Figure 9**. From late April to early May, green tide moved northward under the prevailing southerly wind. Green tide can transport southward by occasional northerly wind and Subei coastal current outside the 40-m isobath, but they will eventually drift with the northwestward Changjiang diluted water and head toward Korea. They cannot enter the East China Sea. According to the above results, the Changjiang diluted water blocked the way of red tide in the Changjiang estuary and Zhoushan Islands, and it also prevented *Ulva prolifera* in the Subei Shoal from moving to the East China Sea.

3.2. Direct dynamic evidence for *Ulva prolifera* moving from south to north

Many (~80) drift bottles were deployed on May 2, 2012, and two were retrieved (**Figure 10a**) with one being an empty bottle near the Jiaozhou Bay mouth on May 28, 2012 and the other being sand-filled bottle at 121°15.2'E, 36°30.4'N (near Haiyang) on June 11, 2012. If only looking at the start and the end points, the empty bottle and the sand-filled bottle drifted north by west and east, respectively. They all landed on the coast of Shandong province. This means *Ulva prolifera* can move out of the Subei Shoal and be further transported to the coastal area of Shandong during spring and summer. Similar as drift bottles but with more details, six satellite-tracked surface-following drifters were released in early June of 2012. The trajectories

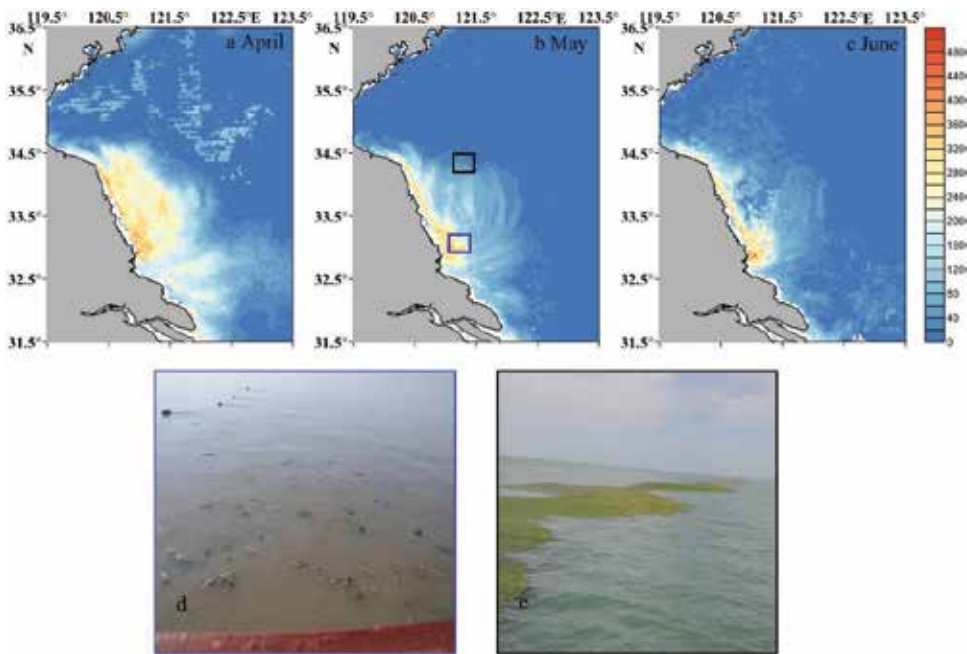


Figure 8. Monthly averaged MODIS-aqua images of surface SPM concentration in April (a), may (b) and June (c) of 2012. *Ulvaprolifera* (d) in the muddy water in the Subei shoal (blue rectangle in (b)) and (e) in clear water outside the Subei shoal (black rectangle in (b)).

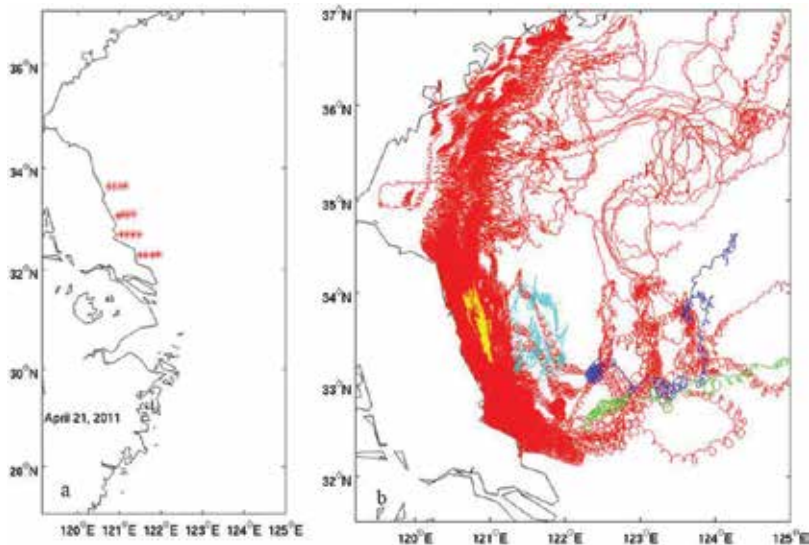


Figure 9. (a) Released locations for all particles, and (b) trajectories of all neutral particles released in the Subei area in 2011 (red) and satellite-tracked Argos drifters (other colors) at the same time.

also indicate that *Ulvaprolifera* can drift from Jiangsu to Shandong coastal area (**Figure 10a**). On average, the drifters drifted at a speed of 11.1 cm s^{-1} ($288.8 \text{ km month}^{-1}$), which is approximately equal to the speed of floating *Ulvaprolifera* patches.

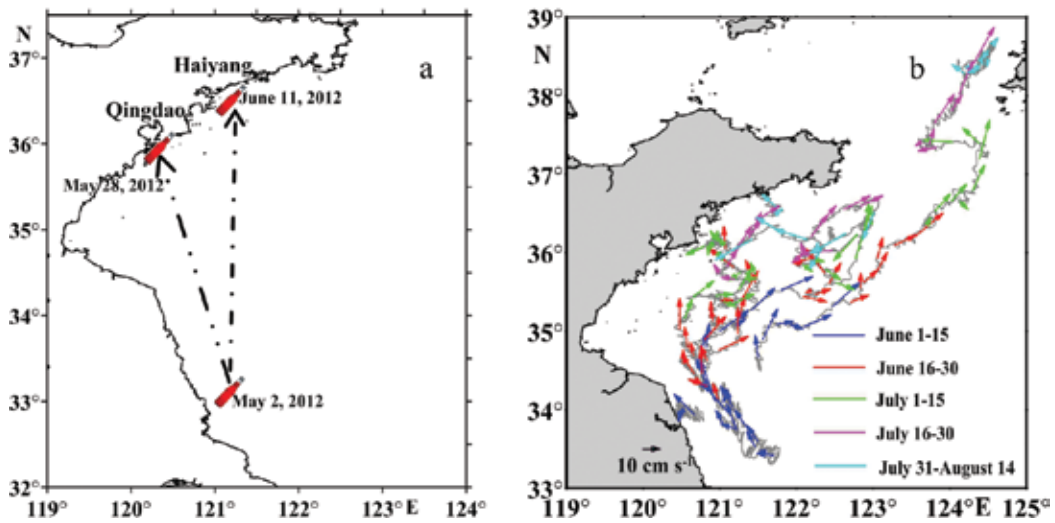


Figure 10. (a) The start and end locations of drifter bottles; (b) the trajectories of six satellite-tracked surface drifters (gray line) and velocity vectors of tide-filtered surface drifter data, with only every other velocity vector being plotted to show the results more clearly.

Numerous small-scale spiral oscillations were observed in the trajectories, indicating strong tidal currents or meso-scale eddies. Net movement of drifters was partly covered by the periodical movements. A low-pass filter at a cutoff period of 25 h was applied to obtain the tide-filtered velocity vectors of the drifters (**Figure 10b**). In the south of 34°30.0'N, most of the vectors nearly kept the same pace as others pointed toward the northwest. This means these vectors are dominated by the same Lagrangian residual current direction. After crossing 34°30.0'N, the consistent pace was broken. The vectors in the north were likely to be affected by complex dynamics there, with the wind being one of the important factors.

To explain the potential relationship with wind, we compared the wind speed data and the clockwise direction deflection angle between wind and drifter velocity (**Figure 11**). Theoretically, in terms of the Ekman theory, the surface current should be 45° to the right of the wind in the Northern Hemisphere. In reality, the angle is less than 45° in the shallow coastal waters. But in our case, the comparison results show only 33% of the angle was between 0 and 45° (**Figure 11a**). It suggests that the trajectories cannot be totally explained by the wind-driven Ekman theory, and other baroclinic processes must also influence the trajectories.

In **Figure 11a**, when wind speeds were larger than 7 m s⁻¹, the wind-driven component dominated the drifter direction, and more data fell within (or close to) 0–45°. For those vectors with angles between 0 and 45°, correlation analysis was done between wind speed and drifter velocity (as a proxy for the wind drift current). The results show that they have significant linear relationship through the origin ($n = 49$; $r^2 = 0.88$, slope = 0.023) (**Figure 11b**). This also indicates that in the western Yellow Sea during spring and summer 2012, the wind-driven component of drifter velocity was 2.3% of the wind speed on average.

With the field experiments, we obtained first solid evidence that *Ulvaprolifera* can leave the Subei Shoal and move to the coastal ocean of Shandong province or even further north.

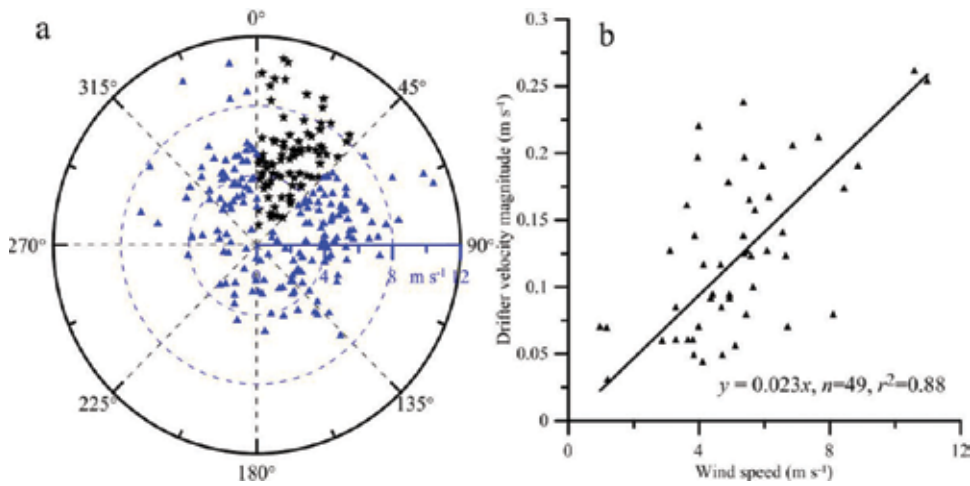


Figure 11. (a) Polar scatterplot of wind speed and clockwise deflection angle between wind direction and drifter velocity direction. The radius axis is the wind speed, while the angle axis is the clockwise deflection angle. Black symbols represent points with deflection angles between 0 and 45°; and blue symbols denote the rest. (b) Scatterplot of wind speed and drifter velocity magnitude for black dots in (a). The black line denotes the linear regression through the origin. n is the number of data points used, and r^2 is the coefficient of determination.

3.3. *Ulvaprolifera* drifting patterns in the Subei area

Figure 12a comes from the comparison of the satellite images related to raft distribution of *Porphyra* aquaculture in the Jiangsu coast between 2004 and 2007. A high-resolution model was built for the Subei coastal ocean to simulate the *Ulvaprolifera* movement after it peeled off from the raft during the *Porphyra* harvest in 2004 and 2007 (**Figure 12a**). Simulation started from May 1st, and neutral particles (representing *Ulvaprolifera*) were released daily every half an hour between 6:00 and 18:00 local time during the harvest season. The harvest duration was supposed to be 5 days, and the drifting simulation lasted half a month. Green dots represent *Ulvaprolifera* peeled off from the rafts added between 2004 and 2007, and red dots were those peeled off from rafts that already existed before 2004. Simulation results illustrated bands of *Ulvaprolifera* and their small bands were generated in the Subei Shoal. These bands were determined by the joint influence of the unique topography, radial tidal currents and wind. Driven by the South-Southeast wind (**Figure 12b**), the red particles traveled more seaward than the green ones. The modeled trajectories using the real wind in 2012 are shown in **Figure 12c**, and less red dots left the Subei Shoal in comparison with the results at the same time in Fig 21b. Why? Looking at **Figure 12a**, *Porphyra* rafts were mainly distributed south of 32.6°N, while the monthly averaged wind (**Figure 13**) appeared primarily as the easterly. Such wind took the *Ulvaprolifera* landward, and it died after being piled up on the coast. The wind direction and the change of the *Porphyra* aquaculture scale were the main reasons for no green tides before 2007.

The FVCOM Subei Shoal coastal numerical model showed that, without wind forcing, *Ulvaprolifera* could not leave the shoal area, which was the same as in the northerly wind case. Under both southerly and southeasterly winds, *Ulvaprolifera* in the study domain could move out of the Subei Shoal and even went further northward. Under the SSE wind condition, when traveling northward, *Ulvaprolifera* north of 32.6°N peeled off from the rafts that existed before

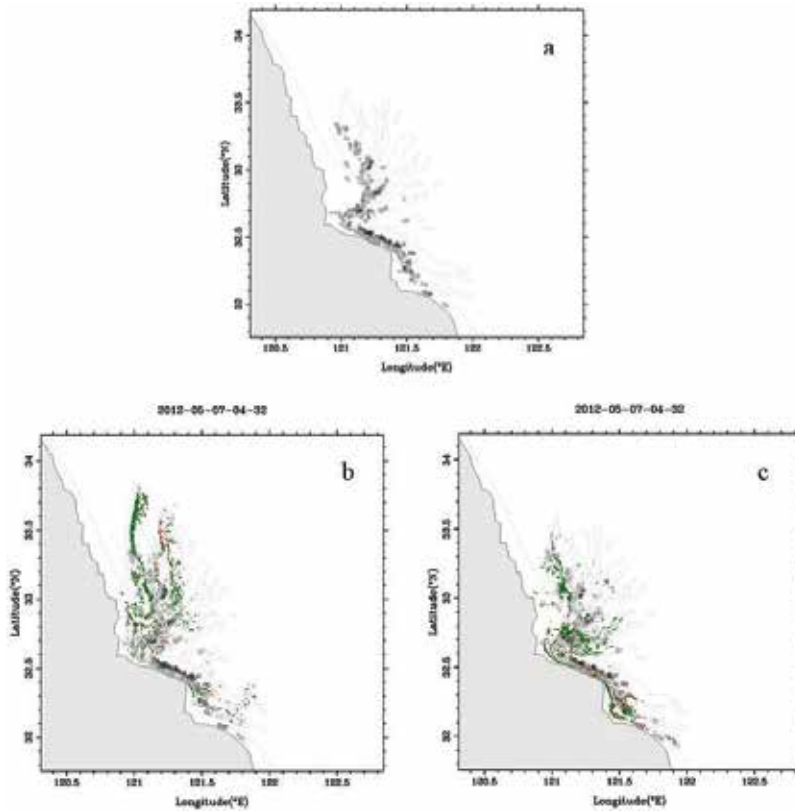


Figure 12. (a) The distribution pattern of *Porphyra* rafts: Red dots for the rafts existed before 2004, green dots for the rafts added between 2004 and 2007. Particles distribution pattern at a moment under the SSE wind (b) and under realistic wind in 2012 (c).

2004 drifted seaward more than that from the rafts added between 2004 and 2007. Wind speed and direction were important during the drifting process. In the case with the southerly wind, *Ulvaprolifera* paths directed northward, while in the latter case, *Ulvaprolifera* generally moved north by west. Particles distributed in different patterns under different wind conditions. This means *Ulvaprolifera* drifting process was influenced by both tidal currents and wind in the Subei Shoal. Tidal currents played the dominant roles within the radial sand ridges, with particles mainly moved along the channels. Outside of the Subei Shoal, wind speed and direction were more important for the trajectories. These findings are consistent with the results of drift bottles and satellite-tracked surface Argos deployed during spring and summer 2012.

3.4. Physical controlling mechanisms of spatial and temporal distribution of *Ulvaprolifera*

Many studies have been carried out in the southwestern Yellow Sea. But specific to the Subei Shoal and its northern waters, field data of physical oceanography were few and precious, not to mention the field data during green tides. In this study, field data were collected in the Subei Shoal and its northern waters during green tides. More importantly, the survey domain

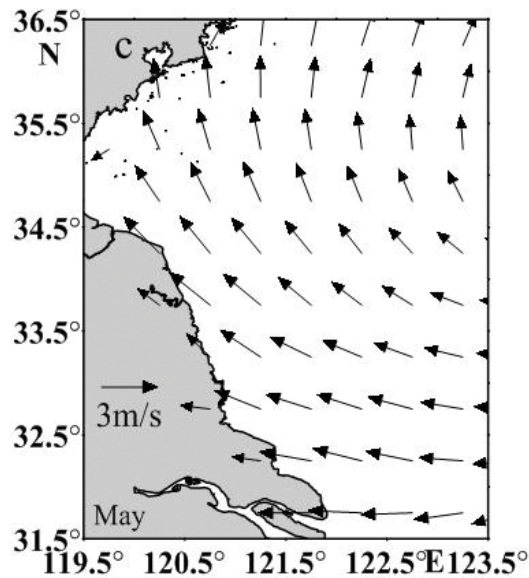


Figure 13. Monthly averaged wind of May 2012.

included the Subei Shoal and the relatively deep waters. The results given in the following paragraphs are about currents, temperature, salinity, SPM and PAR.

The currents in the Subei Shoal were dominated by M_2 tides. The current pattern was significantly limited by the topography, and the back-and-forth current directions were highly consistent with the channel directions. At the four stations, the maximum current speed reached 1.73 m s^{-1} . Harmonic analysis was done for one-month-long current data from Stations M1 and M2. The lengths of the semimajor axes of the surface tidal current ellipses for the M_2 constituent at both stations were about 0.74 m s^{-1} , while the values for the semiminor axes were 0.05 m s^{-1} at Station M1 and 0.32 m s^{-1} at Station M2. This result means that the tidal currents were typical alternating and rotational for Station M1 and Station M2, respectively. The maximum subtidal current speed at Stations M1 and M2 was less than the observed total current by one order of magnitude. The direction of subtidal current was mainly affected by the wind. During spring and summer with the prevailing southerly wind, *Ulvaprolifera* moved back and forth, and the subtidal currents drove *Ulvaprolifera* northward.

The temperature pattern at the two mooring stations shows that temperature was going up from late-April to early June with the increasing rate of $0.15^\circ\text{C}/\text{day}$ (Figure 14). The diurnal temperature variation was less than 2.21°C . The field observation data during all four periods indicate that a zone with cold surface water existed around the Jiangsu coast between isobaths of 20 m and 30 m (Figure 15). These cold zones were speculated to be produced by strong mixing from strong tidal currents and upwelling. The optimum temperature for *Ulvaprolifera* is $15\text{--}20^\circ\text{C}$. From the third survey, temperature in the survey domain was all above 17°C .

The opposite change between salinity and temperature in Figure 15a illustrates this station was influenced by the intrusion of Changjiang diluted water. The horizontal salinity pattern shows the intrusion path of Changjiang diluted water (Figure 15b). The local diluted water around the

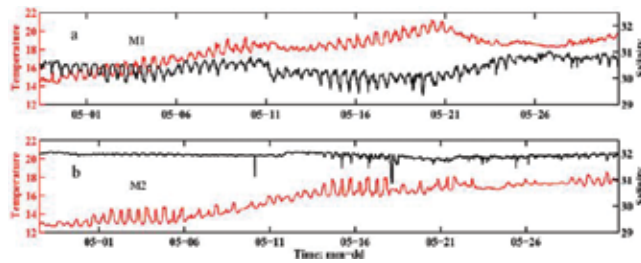


Figure 14. Temporal variations of temperature (red) and salinity (black) at stations M1 (a) and M2 (b).

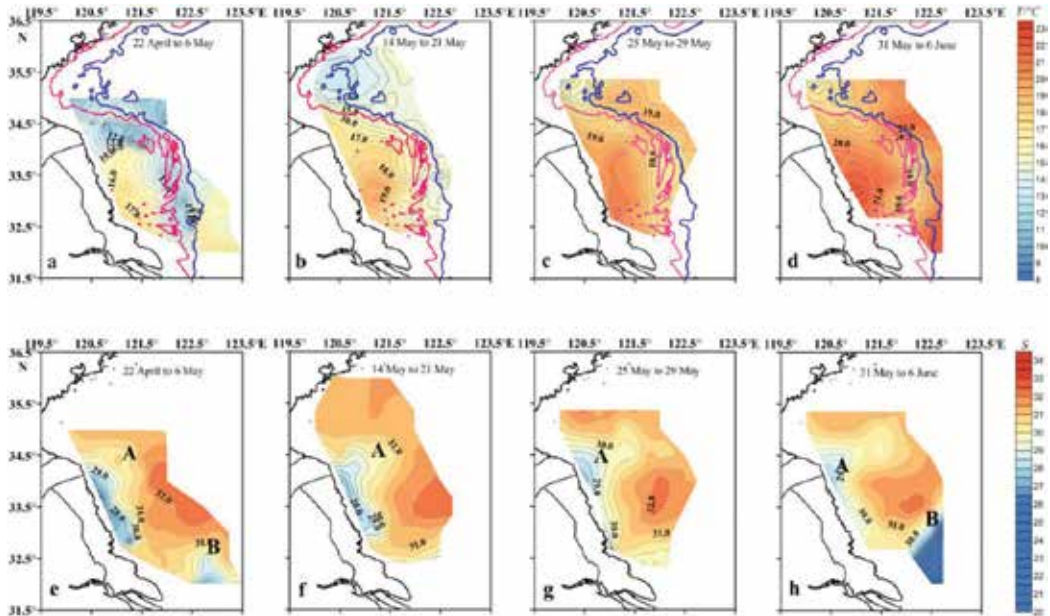


Figure 15. Distribution patterns of surface temperature ($^{\circ}\text{C}$, upper panels) and salinity (lower panels) from April 22 to may 6 (a, e), from may 14 to may 21 (b, f), from may 25 to may 29 (c, g), and from may 31 to June 6 (d, h) in 2012. The red and blue curves are the 20- and 30-m isobaths, respectively.

Subei Coast was produced by the river discharge in Jiangsu province, which was slowly converging to the north end of Jiangsu coast from late-April to early June with its initial pattern evenly distributed along the coast. From this, we can see that there existed certain kind of relation between Subei diluted water and Changjiang diluted water. When the tongue of Changjiang diluted water went further northward, Subei diluted water was concentrated in the north. Otherwise, Subei diluted water was evenly distributed along the coast. Saline water with salinity more than 5 psu was a hospitable situation for *Ulvaprolifera*, and all coastal seawaters can meet this requirement.

The sea surface SPM concentration determined the penetration of PAR through the seawater column. *Ulvaprolifera* peeled off from the *Porphyra* raft suspended in the water column at first; after growing independently for a certain time, it produced gas inside and was able to float (Figure 16). Therefore, before floating, the sea surface SPM concentration would influence the growth of *Ulvaprolifera* (Figure 16c). The satellite images of monthly averaged SPM

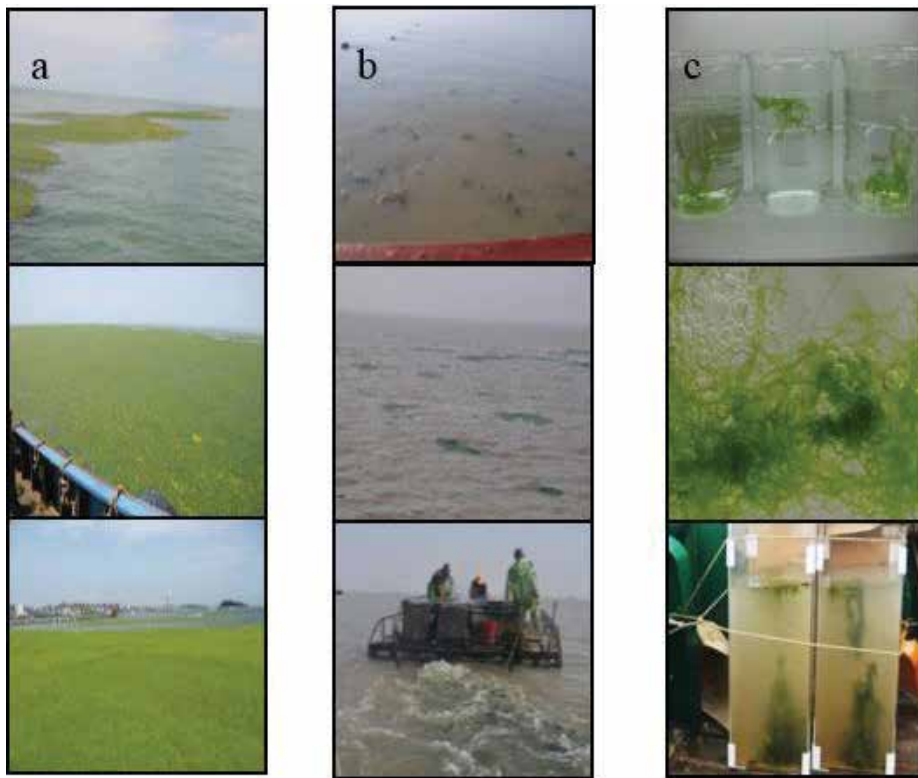


Figure 16. (a) Massive *Ulvaprolifera* and band-shaped green tide, (b) sporadic *Ulvaprolifera* in the Subei shoal with high turbidity and (c) *Ulvaprolifera* suspended in the water column in the laboratory.

concentration in April, May and June (**Figure 8a–c**) illustrate that the SPM decreased month by month as the ocean wave decreased because of the weakening wind. However, the SPM concentration in the Subei Shoal was much larger than that in the other areas. The three-month-averaged SPM concentration was 140.1 mg/dm^3 in the Subei Shoal and 11 mg/dm^3 north of 34.5°N . As shown in **Figure 17**, there was a regression relationship between SPM concentration and transparency, and there existed another exponential relationship between depth and PAR. The quantitative relationship equation could be worked out among SPM, transparency and PAR attenuation coefficient. Based on this equation, the ratio of PAR 10 cm under the water surface to that at the surface could be calculated (**Figure 18a–c**). In the Subei Shoal, the ratio was about 30%; but in the other clear seawater, it could be above 90%.

In short, *Ulvaprolifera* in the Subei Shoal can leave the area due to wind-driven currents and southerly wind. According to the average drifting velocity, *Ulvaprolifera* spent less than 20 days in the region south of 34.6°N . In the Subei Shoal, temperature, salinity and nutrients were suitable for the growth of *Ulvaprolifera*. But the vital disadvantage was the high SPM concentration, which limited light transmission in the water for photosynthesis before floating (**Figure 16b**). As *Ulvaprolifera* traveled northward, temperature in the northern area increased (**Figure 16a**). There, with clear local water and sufficient nutrients, *Ulvaprolifera* grew rapidly. Actually, the seawater near 34.6°N was jointly influenced by cold front and local diluted water, where sufficient nutrients existed.

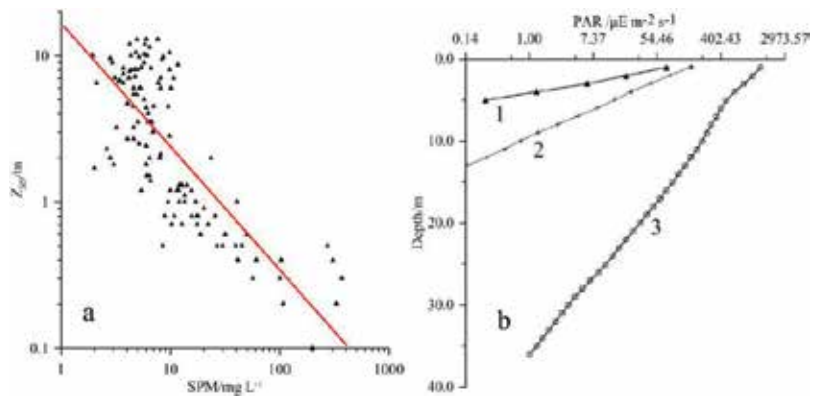


Figure 17. (a) Relation between SPM and Secchi disk depth (Z_{sd}), as well as least square regression line (red), for the southwestern Yellow Sea during spring 2012. (b) Vertical profiles of the PAR observed in the southwestern Yellow Sea during spring 2012.

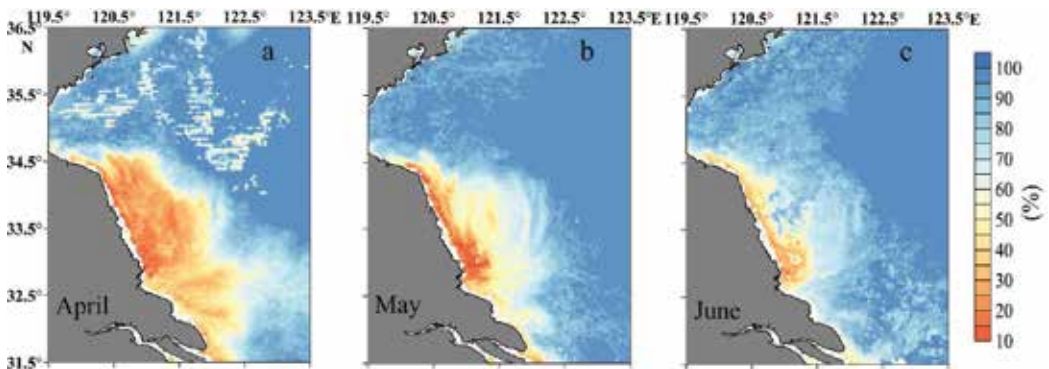


Figure 18. Similar to Figure 8a–c, except for the ratio of PAR 10 cm under the water surface to that at the surface.

4. Summary and discussion

Three marine disasters caused by algal blooms in the Jiangsu coastal region were described in detail in this chapter. Red tide was the first kind of algae bloom in the region, green tide has lasted for 11 years since 2007 and golden tide was new but likely to be another common algal bloom. Now, *Sargassum* is considered to originate in the open sea and may be related to global warming (only a hypothesis that needs to be tested). The Jiangsu coastal region now faces a new possibility with three kinds of algal bloom occurring concurrently. Among them, the green tide in the Subei Shoal was the focus of this chapter. With the data from observations and satellite data set, some findings have been obtained.

The Subei Shoal area is seldom affected by red tides in the Changjiang estuary and Zhejiang province where red tides are frequent. This is because the Changjiang diluted water acts like a barrier, which prevents *Dinoflagellates* in the south from moving northward. Even if some manages to reach the shoal, it will die in the water with high turbidity in the Subei Shoal.

Similarly, *Ulvaprolifera* in the Subei Shoal stops moving southward due to the Changjiang diluted water, and the prevailing southerly wind.

Red tides in the Subei area often happened in Haizhou Bay, which was shown to originate locally. Since 2014, red tide has disappeared from Jiangsu province. This may be caused by the growth inhabitation of *Dinoflagellates* when competing with macroalgae like *Ulvaprolifera*.

The study in this chapter also provided solid direct dynamic evidence that *Ulvaprolifera* can drift from the Subei Shoal to the Qingdao coastal area [11]. Drift bottles and satellite-tracked Argos drifters showed that *Ulvaprolifera* in the Subei Shoal can move out of this region and be transported to the Qingdao coast and even further north. The neutral particle-tracking numerical experiment confirmed this viewpoint.

Physical controlling mechanisms were studied here, and answered the question why *Ulvaprolifera* originated in the Subei Shoal broke out in the Shandong coastal region [12]. Seawater in the Subei Shoal (south of 34.6°N) with high turbidity limited photosynthesis to a certain extent for the young *Ulvaprolifera* there. *Ulvaprolifera* cannot grow well in such waters. Wind-driven currents and southerly wind can drive *Ulvaprolifera* northward to the clear water outside of the Subei Shoal. When green tide arrived in the northern region, temperature there gradually rose to be appropriate for the growth of *Ulvaprolifera*. The PAR near surface enhanced in the clear water, and *Ulvaprolifera* can grow rapidly with suitable temperature, salinity and abundant nutrients.

Acknowledgements

This study was carried out within the framework of the National Key Research and Development Program of China (grant 2017YFC1404300). It was jointly supported by the National Nature Science Foundation of China (grant 41506027), by the Strategic Priority Research Program of the Chinese Academy of Sciences (grant XDA11020304), by the National Programme on Global Change and Air-Sea Interaction (grant GASI-IPOVAI-04), and the Project of the State Key Laboratory of Satellite Ocean Environment Dynamics, the Second Institute of Oceanography (grants SOEDZZ1503 and SOEDZZ1805). We thank Zuojun Yu for improving English writing.

Author details

Min Bao¹, Weibing Guan^{1,2*}, Zhenyi Cao¹, Qi Chen¹ and Yun Yang¹

*Address all correspondence to: gwb@sio.org.cn

1 State Key Laboratory of Satellite Ocean Environment Dynamics, Second Institute of Oceanography, State Oceanic Administration, Hangzhou, P.R. China

2 Institute of Physical Oceanography, Ocean College, Zhejiang University, Hangzhou, P.R. China

References

- [1] Ding Y. Research on the variation characteristics of water quality in Jiangsu coastal waters [Master degree dissertations]. [Nanjing]: Nanjing Normal University; 2014
- [2] Jiang S, Li J, Zhang Y, Niu Z, Jin Y. The eutrophication evaluation and cause analysis in Jiangsu coastal sea area. *The Administration and Technique of Environmental Monitoring*. 2012;**24**(4):26-29
- [3] Su J. Harmful algal bloom and its research in China. *Bulletin of the Chinese Academy of Sciences*. 2001;**5**
- [4] Zhou M, Zhu M, Zhang J. Status of harmful algal blooms and related research activities in China. *Chinese Bulletin of Life Sciences*. 2001;**13**(2):54-59
- [5] Liu D, Keesing JK, Xing Q, Shi P. World's largest macroalgal bloom caused by expansion of seaweed aquaculture in China. *Marine Pollution Bulletin*. 2009;**58**(6):888-895
- [6] Lü X, Qiao F. Distribution of sunken macroalgae against the background of tidal circulation in the coastal waters of Qingdao, China, in summer 2008. *Geophysical Research Letters*. 2008;**35**(23):L23614
- [7] Qiao F, Dai D, Simpson J, Svendsen H. Banded structure of drifting macroalgae. *Marine Pollution Bulletin*. 2009;**58**(12):1792-1795
- [8] Huang BX, Ding LP, Tan HQ, Sun GD. Diversity and distribution of genus *Sargassum* in China seas. *Oceanologia Et Limnologia Sinica*. 2013;**44**(1):69-76
- [9] Wang XH, Qiao F, Lu J, Gong F. The turbidity maxima of the northern Jiangsu shoal-water in the Yellow Sea, China. *Estuarine, Coastal and Shelf Science*. 2011;**93**(3):202-211
- [10] Chen C, Liu H, Beardsley RC. An unstructured grid, finite-volume, three-dimensional, primitive equations ocean model: Application to coastal ocean and estuaries. *Journal of Atmospheric and Oceanic Technology*. 2003;**20**(1):159-186
- [11] Bao M, Guan W, Yang Y, Cao Z, Chen Q. Drifting trajectories of green algae in the western Yellow Sea during the spring and summer of 2012. *Estuarine, Coastal and Shelf Science*. 2015;**163**(Part A):9-16
- [12] Bao M, Guan W, Wang Z, Wang D, Cao Z, Chen Q. Features of the physical environment associated with green tide in the southwestern Yellow Sea during spring. *Acta Oceanologica Sinica*. 2015;**34**(7):97-104

Nuclear Pollution in the East China Sea from the Fukushima Disaster

X. San Liang and Yineng Rong

Additional information is available at the end of the chapter

<http://dx.doi.org/10.5772/intechopen.80016>

Abstract

Nuclear pollution has become a new form and perhaps more harmful type of pollution that obsesses coastal regions; it has been of increasing concern after the disastrous Fukushima nuclear leak on March 11, 2011. In order to assess the impact of the Fukushima accident on the East China Sea (ECS), a highly resolved model is set up to simulate the evolution of the ^{137}Cs concentration. Different from previous studies in this regard, here we take into account the radionuclides originally existing in the ocean. It is found that the radionuclides from the Fukushima leak do have reached ECS, though with a concentration far below the harmful level. The major waterways that inlet the radionuclides are Taiwan Strait and the waterway east of Taiwan. The radioactive material tends to accumulate in the ECS until reaching its peak in 2019; afterward, the outflux through Tokara Strait and Tsushima exceeds the influx through the two southern waterways, and the material resumes in 2021 to its original state. The concentration is neither homogeneously nor stationarily distributed; for example, usually in summer, there is a high center over the Subei Bank in the Yellow Sea. This study is expected, should a similar accident happen again, to help decide where to monitor the ocean, and, hopefully, how to get the pollution under control.

Keywords: Yellow Sea, East China Sea, Fukushima nuclear leak, nested ocean modeling

1. Introduction

The coastal seas are the most severely polluted waters in the world ocean. As shown in the preceding chapter, runoff from urban areas and agricultural fields, plus the deposition from

the atmosphere, may lead to harmful algal bloom and the formation of dead zone due to hypoxia and eutrophication. In recent years, a new type of coastal pollution has been of great concern, that is, the nuclear pollution due to nuclear power plant failure.

Historically, the most disastrous catastrophic nuclear disaster, in terms of cost and casualty, is the Chernobyl accident. The disaster began on April 26, 1986, with a late-night safety test at the fourth light water graphite moderated reactor at the Chernobyl Nuclear Power Plant, Ukrainian Soviet Socialist Republic of the former Soviet Union, which, however, ended with a destructive steam explosion that lofted plumes of fission products into the atmosphere (emission of radionuclides totals up to $13,000 \times 10^{15}$ Bq; [1]), exerting a widespread influence on Europe, Asia, and America [2]. Second to it is the nuclear energy disaster at Fukushima Daiichi Nuclear Power Plant, 150 miles northeast of Tokyo, Japan, which is also of the maximum classification (classified as a level 7 event on the International Nuclear Event Scale). An earthquake of magnitude 9.0 (Tōhoku earthquake) on March 11, 2011, caused a devastating tsunami with a wave reaching as high as 16 meters, overwhelming the Fukushima I Nuclear Power Plant's seawall (10 m high). The cooling systems of the plant were knocked out, and the insufficient cooling resulted in a series of nuclear meltdowns, hydrogen-air chemical explosions, and the release of radioactive material into the ambient environment [3].

The impact of the Fukushima accident can never be overestimated; it has been ranked as the world's worst nuclear accident in 25 years. The radionuclides have been widely spread with the winds and oceanic circulations; particularly, it is reported that they arrive above North America just 4 days after [4]. Although the emission is claimed to have been under control, the impact, particularly the impact on the oceans, remains [5, 6]. For example, the concentration of ^{137}Cs off Japan, though has been on decline ever since the accident, remains as high as 100 times that before the accident by October 2014 [7]. By simulation, the radionuclides may reach the US coast in 4–5 years [8, 9] and then come back along the equator, impacting the coastal oceans in Southeast Asia. In this chapter, we focus on its impact on the East China coast, one of the most densely populated regions in the world. Since ^{137}Cs has the longest life cycle (with a half-life period $\tau = 30$ year), in the following, only ^{137}Cs is considered.

Previously, the East China coast is believed to be not or less influenced by the accident [10]. Research during the past few years, however, shows that the Fukushima-originated ^{137}Cs has already arrived in the China Seas. By Zhao et al. [11] and Rong et al. [12], it arrives in 2013 and will continue to accumulate in the following 5–6 years. Considering that the previous modeling studies do not take into account the background ^{137}Cs distributions, and may generally have too coarse a resolution for the East China Sea, recently Rong and Liang [13] reexamine the problem with a highly resolved numerical model, plus a sequential updating strategy to assimilate the background ^{137}Cs concentration, and reveal how the intruded radionuclide may move, evolve, reside, or disappear. This chapter is a summary of these results. The following is mainly based on Rong et al. [12] and Rong and Liang [13], where Sections 2 and 3 give a brief introduction of the model configuration and simulation strategy, Section 4 is a validation, Section 5 shows the results, and Section 6 concludes the study.

2. Model setup

In Rong and Liang [13], the Regional Ocean Modeling System (ROMS) is adopted for the simulation and prediction of the radionuclide transport. ROMS is a widely applied incompressible ocean model with free surface, hydrostatic, and Boussinesq approximations; it uses the Reynolds average Navier-Stokes equations as governing equations (e.g., [14]). In Cartesian coordinates (x, y, z) , these equations are:

$$\frac{\partial u}{\partial t} + \vec{v} \cdot \nabla u - fv = -\frac{1}{\rho_0} \frac{\partial P}{\partial x} - \frac{\partial}{\partial z} \left(\overline{u'w'} - \gamma \frac{\partial u}{\partial z} \right) + F_u + D_u \quad (1)$$

$$\frac{\partial v}{\partial t} + \vec{v} \cdot \nabla v - fu = -\frac{1}{\rho_0} \frac{\partial P}{\partial y} - \frac{\partial}{\partial z} \left(\overline{v'w'} - \gamma \frac{\partial v}{\partial z} \right) + F_v + D_v \quad (2)$$

$$\frac{\partial P}{\partial z} = -\rho g \quad (3)$$

$$\frac{\partial u}{\partial x} + \frac{\partial v}{\partial y} + \frac{\partial w}{\partial z} = 0 \quad (4)$$

$$\frac{\partial C}{\partial t} + \vec{v} \cdot \nabla C = -\frac{\partial}{\partial z} \left(\overline{C'w'} - \gamma_\theta \frac{\partial C}{\partial z} \right) + F_C + D_C \quad (5)$$

where $\vec{v} = (u, v, w)$ is the three-dimensional velocity vector, C is the concentration of some tracer, F denotes external forcing, D represents the horizontal dissipation/diffusion processes, and the other symbols are conventional. This equation set is closed with an equation of state:

$$\rho = \rho(T, S, P) \quad (6)$$

and parameterized turbulent fluxes; particularly, the vertical mixing is parameterized with a nonlocal, K-profile parameterization (KPP) scheme [15]. The closed set of equations are transformed into terrain-following coordinates (x, y, σ) and then solved using a split-explicit scheme.

A one-way nesting strategy is used, and hence two model domains are considered (**Figure 1**). The outer domain (L0) comprises the whole North Pacific Ocean, from the equator to Bering Strait. The inner domain (L1) covers the East China Sea (ECS) region. For both domains, there are 22 sigma levels in the vertical, while horizontally the resolutions for L0 and L1 are roughly 10.1 and 3.6 km, respectively. Other parameters are referred to **Table 1**. The bottom topography is extracted from the ETOPO1 data by National Oceanic and Atmosphere Administration (NOAA). A Hanning filter is applied to the topography to make sure that pressure gradient force is computed accurately [16].

The horizontal boundaries for model L0 are all taken as closed. This makes sense because (1) Bering Strait is very narrow and shallow and (2) the equator is a dynamically closed boundary, though in reality there does exist cross-equator water exchange. This makes the long-time integration much reliable. For model L1, the boundary fluxes are supplied by the outputs from

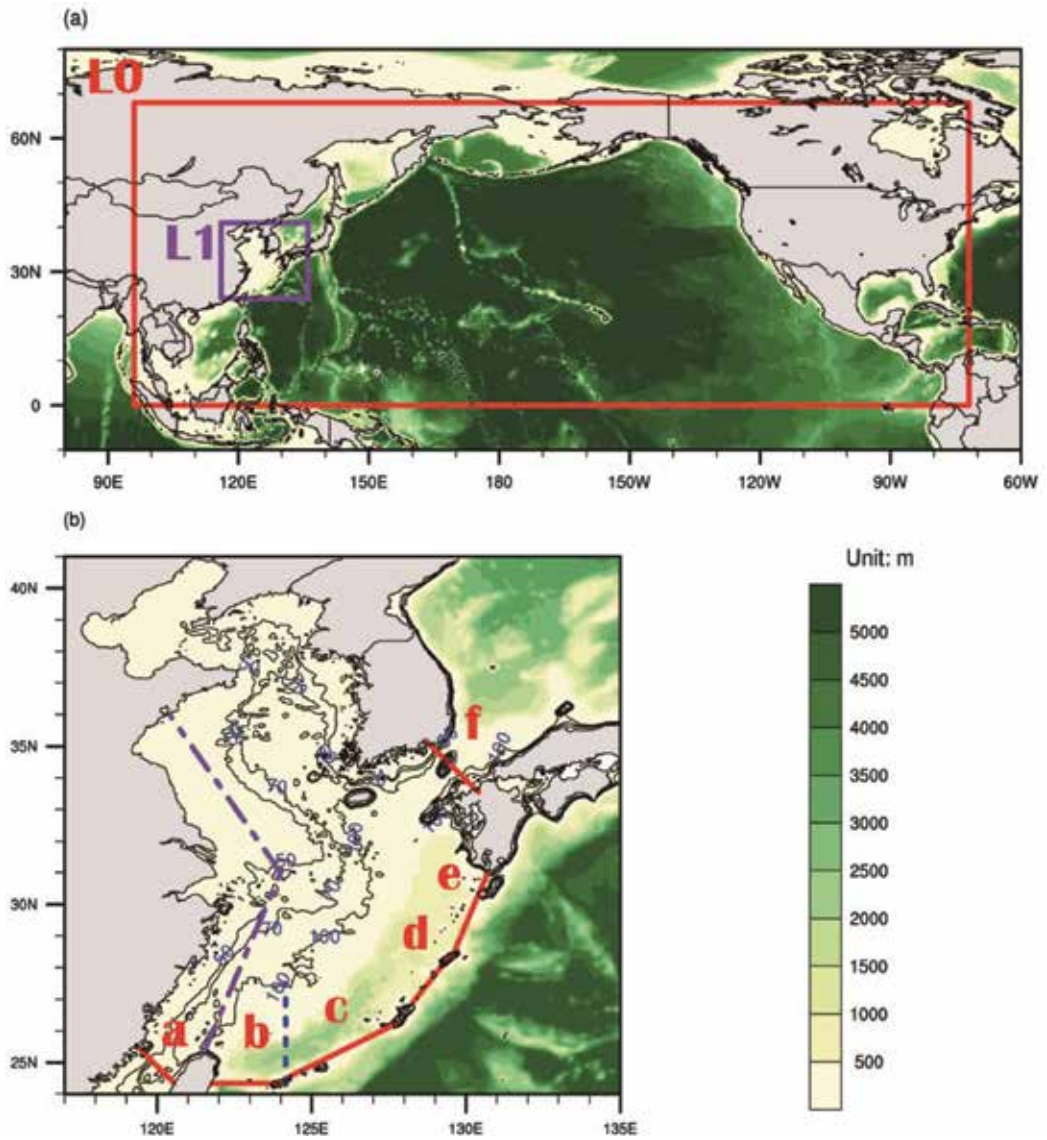


Figure 1. Bathymetry (in m) for the two-domain, one-way nesting model. Shown are the positions where the fluxes are calculated: a. Taiwan Strait, b. East of Taiwan, c. Ishigaki to Naha, d. Naha to Amami, e. Tokara Strait, f. Tsushima Strait. Also marked is a section of East China coast (green line).

Domain	Maximum depth (m)	Minimum depth (m)	Latitude (°N)	Longitude (°E)	Resolution (km)	Time step (s)
L0	5000	15	0–68	96–288	10.1	900
L1	5000	10	24–41	117–135	3.6	90

Table 1. Parameters for the two-domain nested ROMS model.

coarse model. The nesting is realized through the pointer-based ROMS2ROMS Matlab (Agrif) package [17]. To this model, tides are applied; specifically, the 10 tidal constituents, M2, S2, N2, K2, K1, O1, P1, Q1, Mf, and Mm, are considered here (data from Oregon State University; see [18, 19]). In the vertical direction, the no-flux condition is applied at the bottom. At the surface, wind stress, heat, and freshwater fluxes are prescribed. The stress and fluxes are from two datasets. Between January 2001 and August 2015, they are from the reanalysis data of National Centers for Environmental Prediction (NCEP, daily, 2.5° (lat) \times 2.5° (lon)). After August 2015, the predicted data of Geophysical Fluid Dynamics Laboratory (GFDL, 3 hour, 2° (lat) \times 2.5° (lon)) are used.

The model is initialized with the fields of temperature, salinity, velocity, and sea surface height derived from the HYbrid Coordinate Ocean Model (HYCOM, $1/12^\circ$) reanalysis dataset. The ^{137}Cs concentration is prescribed at two steps. (1) Initially, it is estimated using the data from International Atomic Energy Agency (IAEA, <https://maris.iaea.org/Search/Search.aspx>) with a simple assimilation scheme (see below). (2) Upon occurrence of the accident, the released ^{137}Cs is poured into the ocean. Here arise the following issues: how much is the pollutant; when and where to introduce the pollutant. Note that the total amount of the leaked ^{137}Cs remains largely unknown. It has been estimated that the release into the atmosphere of ^{137}Cs is in the range of 13–15 PBq (1 PBq = 10^{15} Bq; Chino et al., 2011) and that poured directly into the ocean is 2.3–27 PBq [20–22]; we will choose 5 PBq in the standard run and do some experiments with the amount in this range. Second, the release of the ^{137}Cs is actually continuous at one grid point during March–April 2011 [5, 20, 23]. But since it has been found [24] that, for a long-time simulation, no significant difference shows for different release strategies, it is assumed that the leak is instantaneous on April 1, 2011. Besides, to avoid shock, the radionuclide is homogeneously distributed within an area centered at the leak location (37.42°N , 141.03°E) with a radius of 2° ; vertically, it has a profile gradually decreasing linearly from the surface to 0 at 100 m deep.

3. Assimilation of the background ^{137}Cs concentration

During 1950–1990, plenty of radioactive substances had been poured into the oceans until the Chernobyl accident occurred and the Comprehensive Nuclear-Test-Ban Treaty was signed; it is believed that, by 1986, the ^{137}Cs in the oceans has totaled 800 PBq [25]. Considering that the release in this accident is no more than 42 PBq [21], the major part of the ^{137}Cs in the Pacific cannot be from Fukushima. This is particularly true for regions far away from the Plant. As an evidence, the IAEA data show that the average ^{137}Cs concentration in the surface layer (0.5 m) of the North Pacific is 1.54 Bq/m^3 during the decade before the accident, while previous studies neglecting the contribution from the background concentration (e.g., [9, 11, 23, 26]) reveal a maximum after-accident concentration less than 0.5 Bq/m^3 in ECS, which is, obviously, far below the observation.

The ^{137}Cs distribution before the accident thence must be taken into account. In this study, two different simulations are performed. Run 1 as a control run does not have the background concentration; 5PBq of ^{137}Cs is directly poured into the ocean at the accident time just as

Hideyuki et al. [27] and Zhao et al. [11]. Run 1 runs from April 1, 2011 to March 31, 2021. Assume that the regions where the ^{137}Cs concentration in Run 1 is less than 0.001 Bq/m^3 are not affected by the pollutant directly poured into the Pacific. The observational data in these regions from January 2001 to February 2011 are then used as the observed ^{137}Cs concentration. These data are assimilated into the model to form an optimal estimate of the field, which is taken as the background concentration for the next run, i.e., Run 2.

The assimilation is through a scheme called sequential updating which, albeit simple, has been successfully utilized in the many operational ocean forecasts, such as in the forecast of the Iceland-Faeroe frontal variability [28, 31]. It is made up of two steps. First, use objective analysis (OA) to prepare the observational field for assimilation. The e-folding time and distance for OA are, respectively, 360 days and 40° . An error field is obtained accordingly. Second, an optimal interpolation (OI) is performed to combine the model output and the OAd field, with the inverse of the error field as the weight. The OI may be performed globally or pointwise. The two do not seem to make much difference; for ease to implement, the latter is hence adopted. In this way, the model output is sequentially updated with the observation.

Table 2 lists the observed surface (0.5 m) ^{137}Cs concentrations in the China Seas before the accident [29] and our corresponding results. For all the six available observations, the mean relative error is 10.3%. Compared to the zero distribution in previous studies, our model works well to produce the ^{137}Cs distribution before the accident.

Since only the surface observation is available, the vertical ^{137}Cs distribution has to be empirically set. We follow Tsumune et al. [30] to set:

$$C(z) = C_0 \times 10^{-0.0005z}, \quad (7)$$

where C (in Bq/m^3) indicates the ^{137}Cs concentration; particularly, C_0 is the surface concentration. This, together with the measurements/estimates of the ^{137}Cs concentration immediately after the accident, furnishes the initial condition for Run 2, which is used for the simulation and prediction.

Latitude	Longitude	Observations (Bq/m^3)	Simulation results	
			Concentration (Bq/m^3)	Relative errors (%)
32.01	126.48	1.01 ± 0.06	1.22	20
36.05	123.50	1.10 ± 0.07	1.20	10
20.50	122.29	1.14 ± 0.07	1.25	9
29.64	123.04	1.32 ± 0.13	1.19	-10
32.00	124.00	1.33 ± 0.10	1.19	-11
18.00	116.00	1.42 ± 0.09	1.38	-2

Table 2. Comparison of surface layer (0.5 m) ^{137}Cs radioactive concentration between the observations [29] and simulations in this study.

4. Validation

4.1. Outer domain: SST and currents

Our simulated result has been compared with the data derived from the Simple Ocean Data Assimilation (SODA). **Figure 2** shows the 2009 annual mean sea surface temperature (SST) and flow from our simulation (**Figure 2a**) and SODA (**Figure 2b**). It is easily seen that the major features of the SST have been well reproduced. For example, shown in the figure are the east-west asymmetry of the temperature in the tropic and the warm pool in the western equatorial Pacific. The large-scale circulations have also been well reproduced. The North Equatorial Current flows westward, encounters the west boundary, and forms the Kuroshio and the much more energetic current, the Ryukyu Current. Upon passing the Luzon, part of the Kuroshio may intrude into the northern South China Sea (SCS) in an anticyclonic form, but the mainstream keeps moving northward into the ECS. The Kuroshio in ECS branches to the northeast of Taiwan. One branch intrudes onto the shelf, forming the outer part of the Taiwan Warm Current and then merging back into the mainstream at a higher latitude. The Kuroshio flows out of the ECS through Tokara Strait, meeting the Oyashio Current off the Japan coast near Fukushima. It then flows eastward, in a meandering form, and makes the Kuroshio Extension System. These currents are evident in both **Figure 2a** and **b**, and they in these two subfigures are similar in magnitude and location. Our simulation of the large-scale system is therefore successful.

4.2. East China Sea: SST and currents

The comparison of the ECS circulation and SST is with the HYCOM product. **Figure 3** shows the monthly mean (2006–2011) ECS SST and velocity. The left and right panels are, respectively, the simulated result and the HYCOM data. Note that East Asia has a monsoon climate; correspondingly, the ocean fields have strong seasonal variations. By comparing the SST and flow season by season, clearly the two panels agree well in both summer and winter, except in

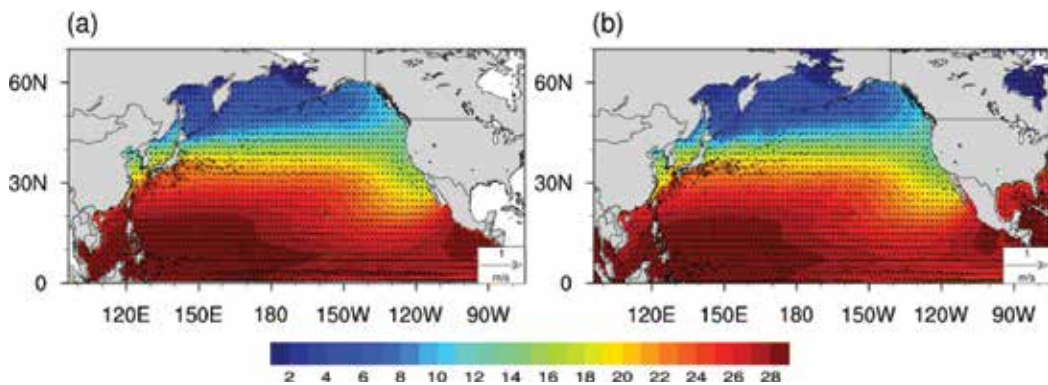


Figure 2. Annual mean SST (shaded) and surface velocity (vector) of 2009 in North Pacific: (a) model output, (b) SODA data.

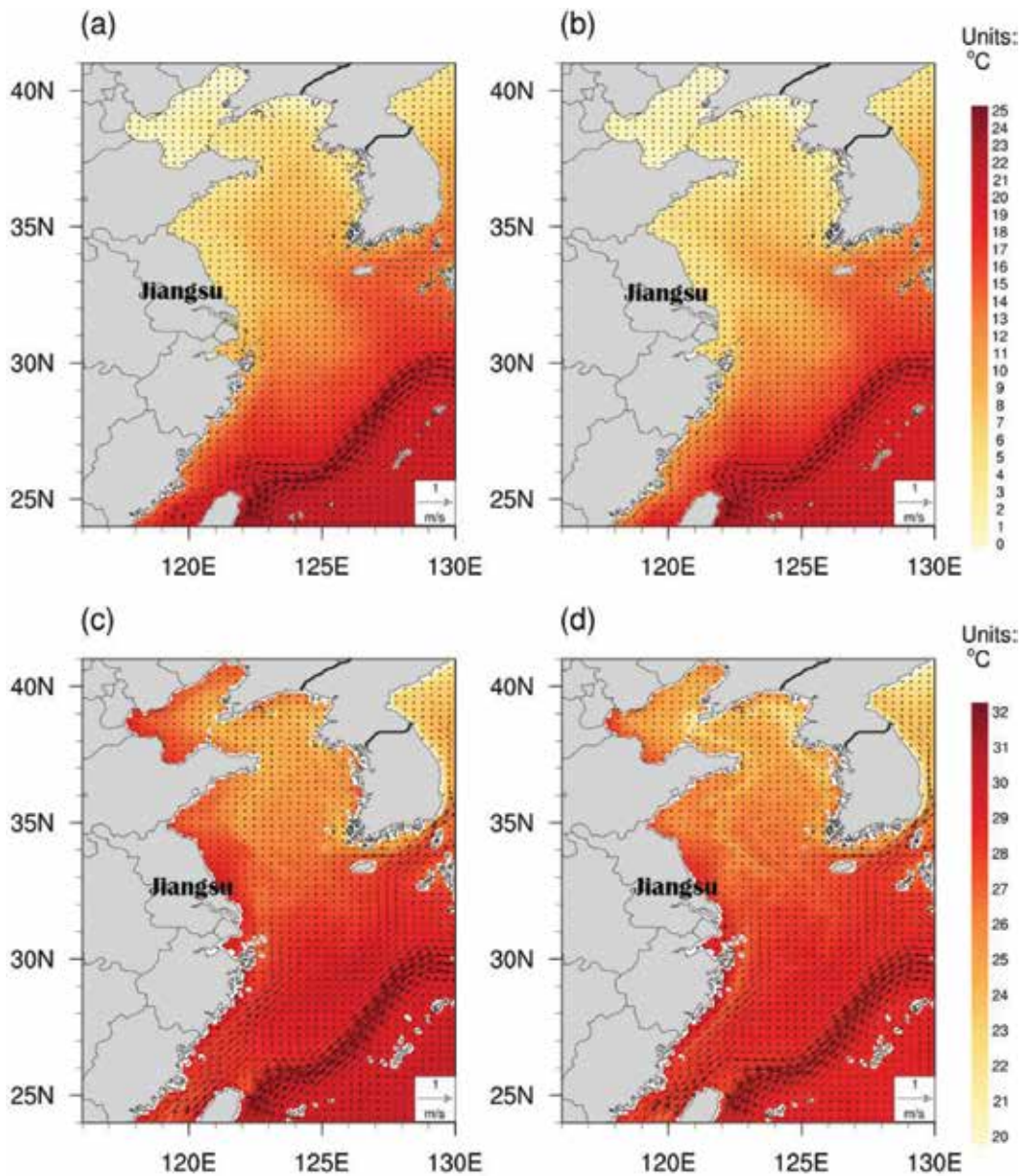


Figure 3. The ECS SST (shaded) and velocity (vector) in winter and summer: (a) ROMS outputs, February; (b) HYCOM result, February; (c) ROMS outputs, August; (d) HYCOM result, August.

August when HYCOM displays a higher SST at the mouth of the Bohai Sea. The general features of the ECS circulation system have all been captured. For example, in winter (February), the coastal SST is lower than the open sea. West of Cheju Island, a warm tongue intrudes northwestward into the waters south of Shandong Peninsula. At this time, the Kuroshio, the Taiwan Warm Current, and the Tsushima Current are weak, and the Zhe-Min Coastal Current

is southward. In summer (August, **Figure 3c** and **d**), the Kuroshio and its branch are strong, and the Zhe-Min Coastal Current flows northward. Scattered in the Yellow Sea are isolated cold patches; they are especially clear off the tips of Shandon Peninsula. These features are well known and have been successfully reproduced here. This completes the validation.

4.3. A comparison of the ^{137}Cs distribution simulations with and without background concentration assimilation

Table 3 shows the differences between simulations with (Run 2) and without (Run 1) assimilating the ^{137}Cs background radioactive concentration in the North Pacific. Clearly, in Run 1, there are many regions where ^{137}Cs has been observed, but the simulated concentration is zero. This simulation has been greatly improved in Run 2, where the concentrations at these

Date	Latitude (°N)	Longitude (°E)	Observation (Bq/m ³)	Run 1 (Bq/m ³)	Run 2 (Bq/m ³)
3/01/2012	22.11	191.46	1.6	0	1.49
05/01/2012	22.97	179.98	1.6	0	1.48
21/01/2012	34.45	130.08	1.7	0	1.22
21/01/2012	34.45	130.08	1.4	0	1.22
22/01/2012	32.53	132.98	1.6	0	1.34
22/01/2012	32.53	132.98	1.3	0	1.34
29/01/2012	26.89	182.06	1.6	0.01	1.75
30/01/2012	27.84	189.1	2.1	0	1.76
31/01/2012	32.98	197.06	1.7	4.08	2.55
01/02/2012	33.05	204.72	1.6	0	3.01
02/02/2012	34.26	213.1	2	0	1.69
03/02/2012	35.16	220.91	2.2	0	1.7
04/02/2012	48.99	219.18	1.3	0	1.41
04/02/2012	36.36	228.83	1.7	0	1.66
05/02/2012	47.53	228.13	1.4	0	1.41
17/02/2012	26.82	173.34	2.4	0.12	1.6
24/02/2012	32.29	206.67	1.6	0	4.08
29/02/2012	34.53	175.9	9.6	1.81	5.72
02/03/2012	33.42	196.11	2.1	1.61	2.18
02/03/2012	39.46	177.47	13.6	4.53	12.38
04/03/2012	30.09	211.27	1.7	0	1.58
09/03/2012	40.45	133.84	1.7	0	1.11
16/03/2012	31.92	223.18	1.6	0	1.71
21/03/2012	34.86	177.27	5.8	3.77	2.34

Table 3. ^{137}Cs concentrations from the IAEA observations, Run 1 and Run 2 (January–March, 2012).

locations are now close to the observations. As another issue, concentration may vary dramatically in 1 day (such as January 21, 2012, in **Table 3**). By comparing the observations from IAEA (124 different stations from June, 2011, to September, 2012, throughout the North Pacific) with the two Runs, it is found that the average relative deviation of the Run 1 simulations from the observations is 103.06%. In contrast, that of the Run 2 simulations is only 27.58%. If one recalls that the average relative interdiurnal variation of the observations is as high as 20.69%, the success of Run 2 is really remarkable. That is to say, the ^{137}Cs simulation has been greatly improved with the background concentration assimilated.

5. Impact on the East China coast

5.1. ^{137}Cs flux

The ECS is a half-closed marginal sea in the Northwest Pacific, connected to the open ocean through several narrow waterways, which include Taiwan Strait, Tokara Strait, Tsushima Strait, and the channels between Taiwan and Yonaguni, Ishigaki and Naha, and Naha and Amami. To see how the Fukushima nuclear substances may intrude into ECS, the ^{137}Cs fluxes across these six waterways are computed. From **Figure 4**, Taiwan Strait (**Figure 4a**) and the Taiwan-Yonaguni channel (**Figure 4b**) are the major straits that introduce the pollutants. The influx of ^{137}Cs East of Taiwan is, on average, $3.99 \times 10^7 \text{Bq/s}$, which is an order larger than that through Taiwan Strait ($3.82 \times 10^6 \text{Bq/s}$). However, considering that the Kuroshio Branch Current makes only a small fraction of Kuroshio, its impacts on the China coastal regions could be of the same order. Generally, these fluxes show significant temporal variabilities. For the flux through Taiwan Strait, seasonality is obvious, with a high concentration in summer and a low concentration in winter. Meanwhile, there also exists a clear interannual variability: the flux is increasing during 2014–2017 and decreasing otherwise. For the strait east of Taiwan, the variability is mostly interannual. Before 2013, the flux grows rapidly. It finds its second growth in early 2014, reaching its peak in 2017. After that, it declines gradually.

The other waterways near Taiwan include the section from Ishigaki to Naha (**Figure 4c**) and that from Naha to Amami Islands (**Figure 4d**). These sections are roughly parallel to the Kuroshio axis. With a water depth of 1500 m or so, they are also the main straits that connect ECS with Northwest Pacific. From the figure, it is seen that large amount of ^{137}Cs is transported between Northwest Pacific and ECS. But because of the alignment, which is parallel to the Kuroshio path, the average fluxes in both waterways are orders smaller (respectively, $4.44 \times 10^5 \text{Bq/s}$ and $5.79 \times 10^5 \text{Bq/s}$) than those east of Taiwan and through Tokara Strait (see below).

Tokara Strait (**Figure 4e**) and Tsushima Strait (**Figure 4f**) are the two waterways that outlet the ECS radionuclides. The flux through the latter is $2.58 \times 10^6 \text{Bq/s}$, while that through the former is an order larger, reaching $4.26 \times 10^7 \text{Bq/s}$. It is interesting to note that the fluxes east of Taiwan and that through Tokara Strait are similar in magnitude and in variation pattern. This implies that most of the ^{137}Cs into ECS along the Kuroshio actually does not stay within the

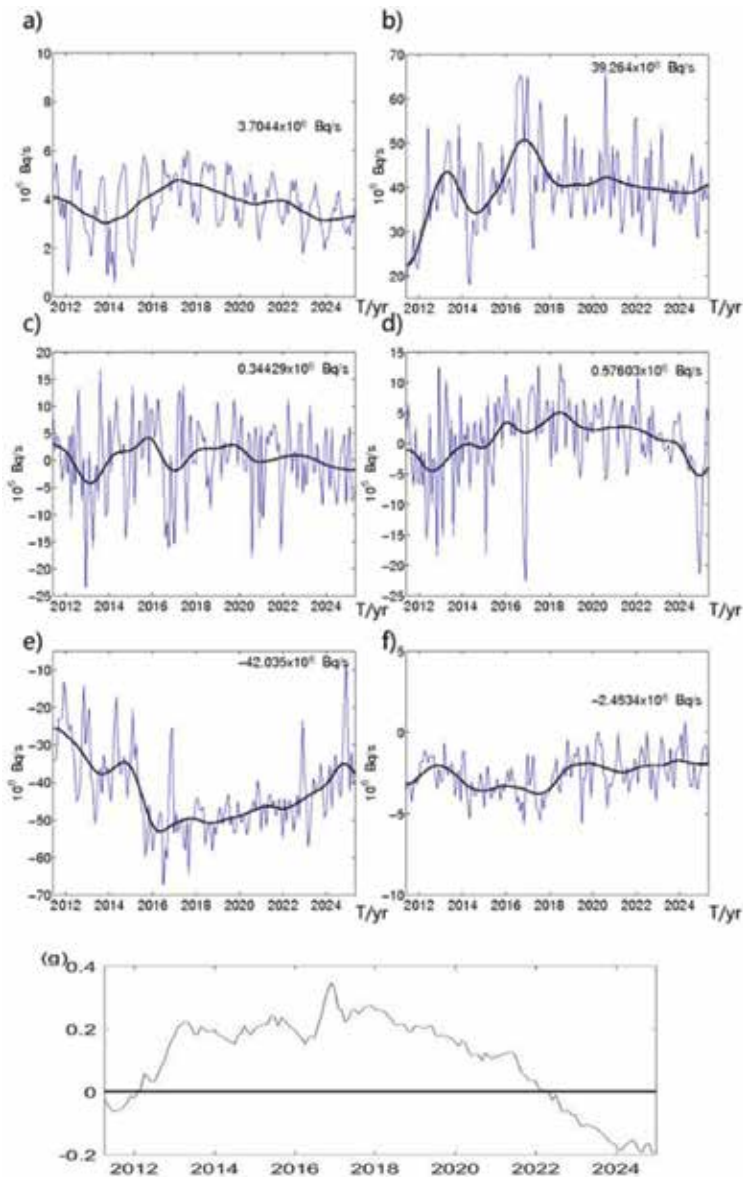


Figure 4. Time series of the ^{137}Cs fluxes across the six waterways indicated in **Figure 1b** (a–f; unit: $\frac{10^6 \text{ Bq}}{\text{s}}$; positive values indicate fluxes into ECS; black lines are moving averages), and the total accumulation of nuclear pollutants in ECS (g; unit: PBq).

sea. Another feature is that the outfluxes through Tsushima Strait and Tokara Strait are weak in winter and strong in summer, in accordance with the seasonal variation of Kuroshio.

To see the net influx of the pollutant, we take a cumulative sum of the fluxes through the six waterways from April 2011 to December 2025. Shown in **Figure 4g** is the cumulant. Note the negative value before 2012. That means there is a net outflux of nuclear substance during that

period; in other words, the main part of ^{137}Cs in the ocean has not arrived in ECS. After 2012, the nuclear substance begins to accumulate, though gradually, and reaches its peak in 2018 (0.13 PBq). In 2021, the sum is below zero again, implying that, in ECS, it takes about a decade for the radionuclide concentration to get back to its original level.

5.2. Nearshore distribution

Because of the dense population, we pay particular attention to the coastal regions. **Figure 5a** shows that the surface ^{137}Cs concentration in ECS takes a maximum around $1.3\text{--}1.8\text{ Bq/m}^3$, depending on the location. Generally, it is high in the southeast of ECS and low in the northwest. The maximum is attained in 3 years after the accident along the Ryukyu Islands from Taiwan to

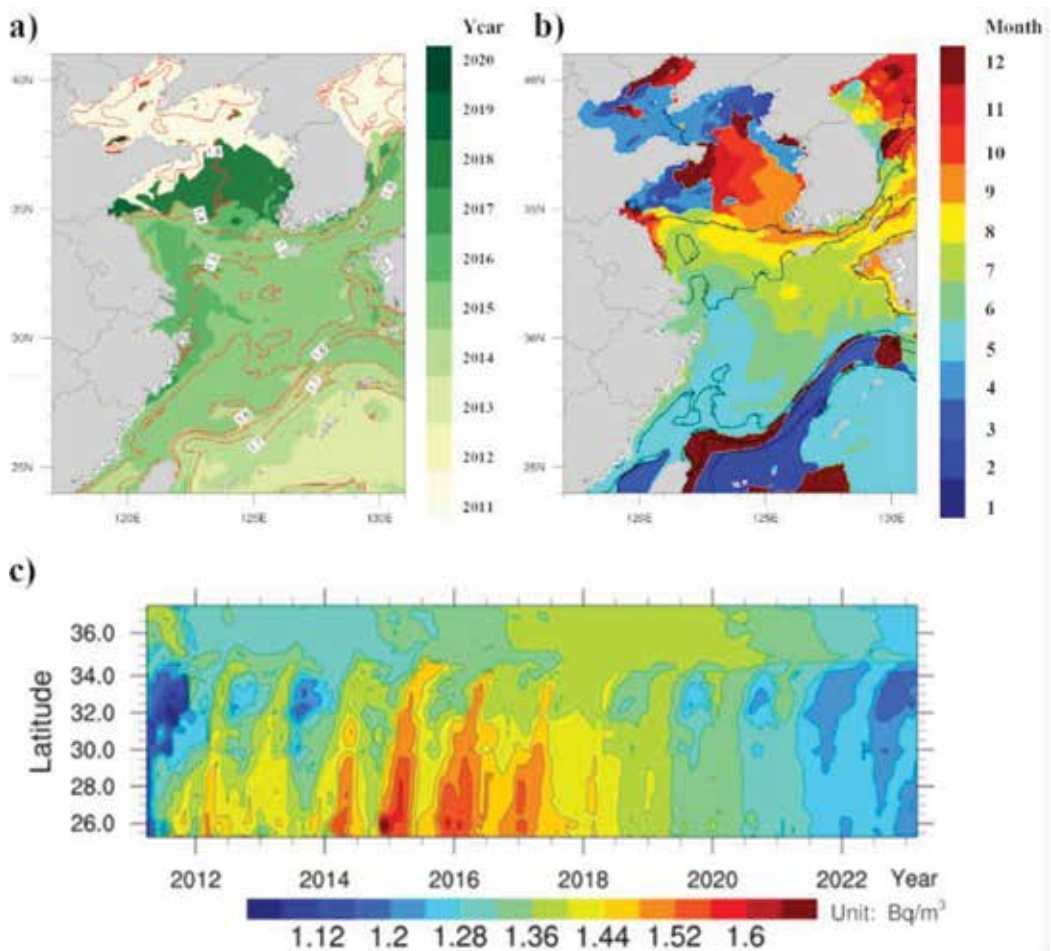


Figure 5. (a) Distribution of the simulated maximum surface ^{137}Cs concentration (lines, in Bq/m^3) and the year when it is attained (shaded). (b) Distribution of the maximal monthly mean ^{137}Cs radioactive concentration (lines, in Bq/m^3) and the months when the maximum is attained (shaded). The monthly mean is taken over the same months during 2014–2019. (c) Hovmöller diagram of the ^{137}Cs concentration (shaded, in Bq/m^3) between 25°N and 35°N (green line in **Figure 1b**) along the East China coast from 2011 to 2023.

Tokara Strait. On the whole, it peaks in 2014, except along the Zhejiang coast, where the peak appears 1 year later. In the Yellow Sea, the scenario looks much more complex. The maximal concentration is about 1.4–1.5 Bq/m³, but it varies with space and time. To the east of Harbor Lianyung, the maximum shows up in 2018; from Subei Shoal to Cheju Island, it appeared during 2014–2015; but from South Korea to Shandong Peninsula, it was attained in 2016. The concentrations in the Bohai Sea and Northern Yellow Sea and around the Shandong Peninsula remain at a level as that before the accident. That is to say, these regions are essentially not affected.

Based on the above, the East China coast is most severely affected during the period 2014–2018. A particular observation is that there exists a local high ¹³⁷Cs region (exceeding 1.45 Bq/m³) on the eastern side of the Subei Bank, a shallow water region off the middle Jiangsu coast.

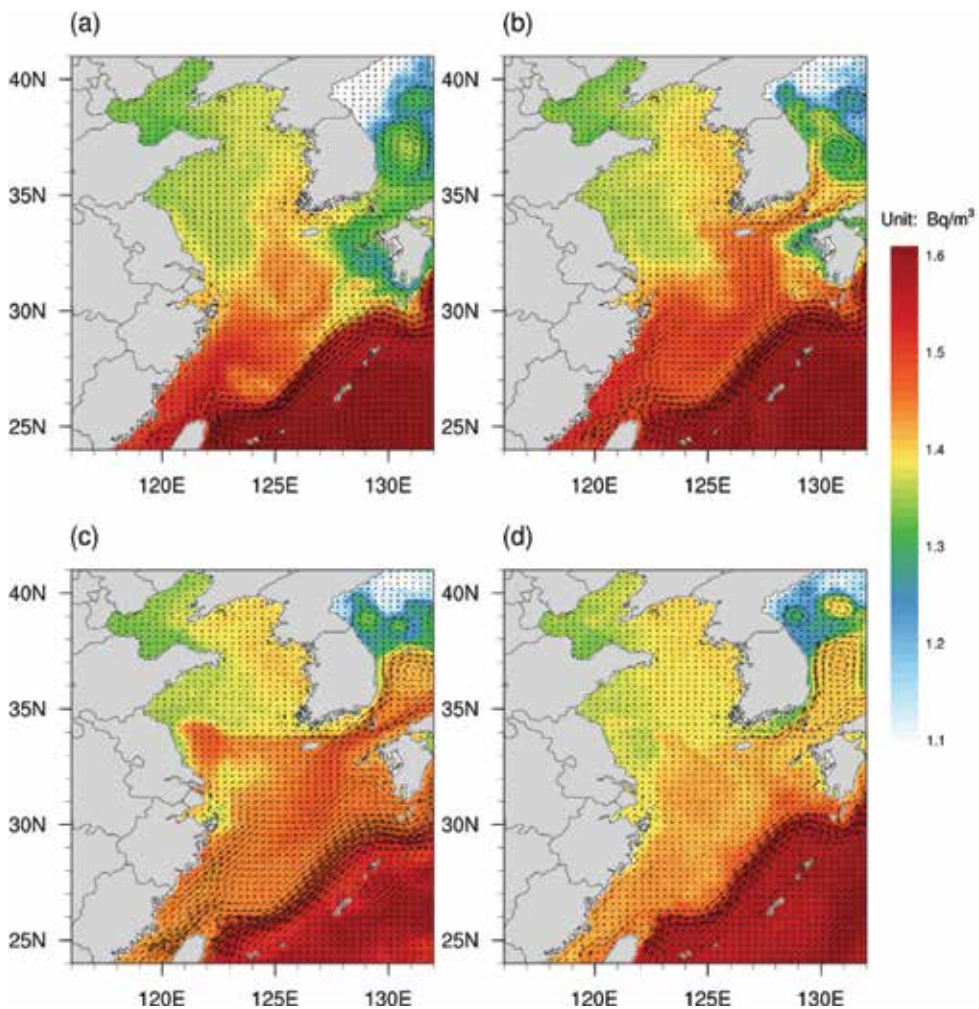


Figure 6. Distributions of the monthly mean surface ¹³⁷Cs concentration in ECS for (a) January, (b) April, (c) July, and (d) October of 2017.

Figure 5c is a Hovmöller diagram between 25°N and 35°N along the East China coast. From it, the maxima occur in the winter of every year before 2019 in the northern part of Taiwan Strait, spreading northward all the way to Subei Bank till summer.

In the Kuroshio region, the ^{137}Cs concentration is high, and so is its horizontal gradient; that is to say, the strong current somehow functions to trap the radionuclide. Following the Kuroshio path to 35°N, one sees a concentration high in May-July. Along the Subei Coast, the maximum concentration is attained in August-November, while in the center of the Yellow Sea, the maximum takes place during September-November. For other regions such as the Bohai Sea and North Yellow Sea, the maximum appears in winter or early spring.

5.3. Seasonal variability

The above suggests that the surface ^{137}Cs concentration in ECS varies considerably from season to season. To see more about this, **Figure 6** shows a sequence of the surface distribution in 2017. On the whole, the concentration displays a gradually decreasing trend northward, from roughly 1.7 Bq/m³ in the southeast to 1.4 Bq/m³ in the northwest. High-concentration water masses move mainly along the shelf break, following the Kuroshio path, from Taiwan toward Tokara Strait. That is to say, most of the nuclear substance influx from east of Taiwan actually flows out of ECS; the major parts that affect the China coast are thence from within Taiwan Strait and through the Kuroshio Branch Current. In other words, they are with the Taiwan Warm Current (TWC), by which they are carried forth along the Zhe-Min Coast and Jiangsu Coast, and are finally transported out of ECS into the Sea of Japan through Tsushima Strait (**Figure 6d**). In the course, the remnants mostly stay along the Jiangsu Coast, leaving around the Subei Bank a high ^{137}Cs concentration spot in summer (**Figure 6a** and **d**). We have also observed such a hotspot in other studies; see Chapter 2 for an example.

6. Concluding remarks

More than 6 years have passed since the Fukushima accident. The radionuclides from the disastrous nuclear leak have been identified in a lot of places in the world. Though there have been many studies, the impact of the accident on the local and global environment has not been well assessed. In this study, we find that the East China Sea (ECS), which was previously believed to be non- or less affected, actually has been full of the Fukushima pollutant, albeit the concentration is still far below a hazardous level.

Using a two-domain, one-way nesting ROMS model, we have simulated and predicted the ^{137}Cs distribution and evolution in the ECS. The outer domain encloses the whole North Pacific which largely avoids the open boundary problem and hence allows for a reliable longer integration. The external forcings (winds, heat and freshwater fluxes, etc.) are either real (from available NCEP reanalysis data) or derived from the GFDL predictions. Different from the previous studies, this model takes into account the background concentration of the

radioactive ^{137}Cs and has observations assimilated. The results have been carefully compared with the existing studies and observations and have been successfully validated.

By the simulation and prediction, the accumulated ^{137}Cs in the ECS reaches its peak in 2018; after 10 years, it falls back to the level before the accident. The straits on both of Taiwan form the main waterways that inlet the radionuclide into ECS, and Tokara Strait and Tsushima Strait are the two through which they leave the region. It is found that the ^{137}Cs concentration, especially that along the coast, varies from season to season. Usually, the pollution is most severe in winter; the maximal concentration along the East China coast reaches 1.3–1.8 Bq/m³. A conspicuous feature is the existence of a hotspot of high ^{137}Cs concentration in summer around the Subei Bank, a shallow water region off Jiangsu, the most populous province of China. The times that the maxima are attained vary from 2014 to 2018, depending on the latitude. Generally, the higher the latitude, the later the maximum is attained.

We hope the above findings can help us to make policy for a rapid response to such kind of disasters. For example, should a more severe but similar leak happen again, we would first monitor the waterways on both sides of Taiwan, and the coastal regions such as the Subei Bank. Moreover, we can take actions in the waterways west and east of Taiwan in order to mitigate the situation and even get the pollution under control.

Acknowledgements

We are grateful to IAEA for the ^{137}Cs observations, to NGDC for the ETOPO1 data, to NOPP for the HYCOM data, and to NOAA for the SODA data, the reanalysis data, and the prediction data. This study was supported by the Jiangsu Provincial Government through 2015 Jiangsu Program for Innovation Research and Entrepreneurship Groups and through the Jiangsu Chair Professorship to XSL.

Author details

X. San Liang* and Yineng Rong

*Address all correspondence to: x.san.liang@gmail.com

School of Atmospheric Sciences and School of Marine Sciences, Nanjing University of Information Science and Technology, Nanjing, China

References

- [1] Saenko V, Ivanov V, Tsyb A, Bogdanova T, Tronko M, Demidchik Y, et al. The Chernobyl accident and its consequences. *Clinical Oncology*. 2011;**23**(4):234-243. DOI: 10.1016/j.clon.2011.01.502

- [2] Povinec P, Chudý M, Sýkora I, Szarka J, Pikna M, Holý K. Aerosol radioactivity monitoring in Bratislava following the Chernobyl accident. *Journal of Radioanalytical and Nuclear Chemistry*. 1988;**126**(6):467-478. DOI: 10.1007/BF02164550
- [3] Tsunami Joint Survey Group, The 2011 Tohoku Earthquake. Nationwide field survey of the 2011 off the Pacific coast of Tohoku earthquake tsunami. *Journal of Japan Society of Civil Engineers, Ser. B2 (Coastal Engineering)*. 2011;**67**(1):63-66. DOI: 10.2208/kaigan.67.63
- [4] Takemura T, Nakamura H, Takigawa M, Kondo H, Satomura T, Miyasaka T, et al. A numerical simulation of global transport of atmospheric particles emitted from the Fukushima Daiichi nuclear power plant. *Scientific Online Letters on the Atmosphere*. 2011;**7**(1):101-104. DOI: 10.2151/sola.2011-026
- [5] Hirose K. 2011 Fukushima Dai-ichi nuclear power plant accident: Summary of regional radioactive deposition monitoring results. *Journal of Environmental Radioactivity*. 2012;**111**(5):13-17. DOI: 10.1016/j.jenvrad.2011.09.003
- [6] Lai Z, Chen C, Beardsley R, Lin H. Initial spread of ^{137}Cs over the shelf of Japan: A study using the high-resolution global-coastal nesting ocean model. *Biogeosciences Discussions*. 2013;**10**(2):1929-1955. DOI: 10.5194/bgd-10-1929-2013
- [7] Buesseler K, Aoyama M, Fukasawa M. Impacts of the Fukushima nuclear power plants on marine radioactivity. *Environmental Science & Technology*. 2011;**45**(23):9931-9935. DOI: 10.1021/es202816c
- [8] Behrens E, Schwarzkopf FU, Lübbecke JF, Böning CW. Model simulations on the long-term dispersal of ^{137}Cs released into the Pacific Ocean off Fukushima. *Environmental Research Letters*. 2012;**7**(3):34004-34013(10). DOI: 10.1088/1748-9326/7/3/034004
- [9] Nakano M, Povinec PP. Long-term simulations of the ^{137}Cs dispersion from the Fukushima accident in the world ocean. *Journal of Environmental Radioactivity*. 2012;**111**(111):109-115. DOI: 10.1016/j.jenvrad.2011.12.001
- [10] Wang H, Wang ZY, Zhu XM, Wang DK, Liu GM. Numerical study and prediction of nuclear contaminant transport from Fukushima Daiichi nuclear power plant in the North Pacific Ocean. *Chinese Science Bulletin*. 2012;**57**(26):3518-3524. DOI: 10.1007/s11434-012-5171-6
- [11] Zhao C, Qiao FL, Wang GS, Xia CS, Jung KT. 福岛核事故泄漏进入海洋的 ^{137}Cs 对中国近海影响的模拟与预测 [Simulation and prediction of ^{137}Cs from the Fukushima accident in the China seas]. *Chinese Science Bulletin*. 2014;**59**(34):3416-3423. DOI: 10.1360/N972014-00012
- [12] Rong YN, Xu R, Liang XS, Zhao YB. A study of the possible radioactive contamination in the China Seas from the Fukushima nuclear disaster. *Acta Scientiae Circumstantiae*. 2016;**36**(9):3146-3159; (in Chinese)
- [13] Rong YN, Liang XS. A study of the impact of the Fukushima nuclear leak on the East China coastal regions. *Atmosphere-Ocean*. 2018. DOI: 10.1080/07055900.2017.1421139

- [14] Shchepetkin AF, McWilliams JC. The regional oceanic modeling system (ROMS): A split-explicit, free-surface, topography-following coordinate model. *Ocean Modeling*. 2005;**9**(4): 347-404
- [15] Large WG, McWilliams JC, Doney SC. Oceanic vertical mixing: A review and a model with a nonlocal boundary layer parameterization. *Reviews of Geophysics*. 1994;**32**:363-403
- [16] Beckmann A, Haidvogel DB. Numerical simulation of flow around a tall isolated seamount. Part I: Problem formulation and model accuracy. *Journal of Physical Oceanography*. 1993;**23**:1736-1753
- [17] Mason E, Molemaker J, Shchepetkin AF, Colas F, McWilliams JC, Sangrà P. Procedures for offline grid nesting in regional ocean models. *Ocean Modelling*. 2010;**35**(1-2):1-15. DOI: 10.1016/j.ocemod.2010.05.007
- [18] Egbert GD, Bennett AF, Foreman MGG. TOPEX/Poseidon tides estimated using a global inverse model. *Journal of Geophysical Research*. 1994;**99**(C12):24821-24852. DOI: 10.1029/94JC01894
- [19] Egbert GD, Erofeeva SY. Efficient inverse modeling of barotropic ocean tides. *Journal of Atmospheric and Oceanic Technology*. 2002;**19**(2):183-204. DOI: 10.1175/1520-0426
- [20] Kawamura H, Kobayashi T, Furuno A, In T, Ishikawa Y, Nakayama Y, et al. Preliminary numerical experiments on oceanic dispersion of ^{131}I and ^{137}Cs discharged into the ocean because of the Fukushima Daiichi nuclear power plant disaster. *Journal of Nuclear Science and Technology*. 2011;**48**(11):1349-1356. DOI: 10.1080/18811248.2011.9711826
- [21] Bois PBD, Laguionie P, Boust D, Korsakissok I, Didier D, Fiévet B. Estimation of marine source-term following Fukushima Dai-ichi accident. *Journal of Environmental Radioactivity*. 2012;**114**(12):2-9. DOI: 10.1016/j.jenvrad.2011.11.015
- [22] Tsumune D, Tsubono T, Aoyama M, Hirose K. Distribution of oceanic ^{137}Cs from the Fukushima Dai-ichi nuclear power plant simulated numerically by a regional ocean model. *Journal of Environmental Radioactivity*. 2012;**111**:100-108. DOI: 10.1016/j.jenvrad.2011.10.007
- [23] Povinec PP, Gera M, Holý K, Hirose K, Lujaniené G, Nakano M, et al. Dispersion of Fukushima radionuclides in the global atmosphere and the ocean. *Applied Radiation and Isotopes*. 2013;**81**(2):383-392. DOI: 10.1016/j.apradiso.2013.03.058
- [24] He YC, Gao YQ, Wang HJ, Ola JM, Yu L. 年日本福岛核电站泄漏在海洋中的传输 [Transport of nuclear leakage from Fukushima nuclear power plant in the North Pacific]. *Acta Oceanologica Sinica*. 2012;**34**(4):12-20
- [25] Zhao C, Qiao F, Wang G, Shu Q, Xia C. 历次核试验进入海洋的 ^{137}Cs 对中国近海影响的模拟研究 [Simulation of the influence of ^{137}Cs from nuclear experiments on China seas]. *Acta Oceanologica Sinica*. 2015;**37**(3):15-24. DOI: 10.369/j/issn.0253-4193.2015.03.002
- [26] Aoyama M, Uematsu M, Tsumune D, Hamajima Y. Surface pathway of radioactive plume of TEPCO Fukushima npp1 released ^{134}Cs and ^{137}Cs . *Biogeosciences*. 2013;**10**(5):3067-3078. DOI: 10.5194/bg-10-3067-2013

- [27] Hideyuki K, Takuya K, Akiko F, Teiji I, Yoichi I, Tomoharu N, et al. Preliminary numerical experiments on oceanic dispersion of I and Cs discharged into the ocean because of the Fukushima Daiichi nuclear power plant disaster. *Journal of Nuclear Science and Technology*. 2012;**48**(11):1349-1356. DOI: 10.3327/jnst.48.1349
- [28] Liang XS, Robinson AR. Absolute and convective instabilities and their roles in the forecasting of large frontal meanderings. *Journal of Geophysical Research: Oceans*. 2013; **118**(10):5686-5702
- [29] Wu JW, Zhou KB, Dai MH. Impacts of the Fukushima nuclear accident on the China seas: Evaluation based on anthropogenic radionuclide ¹³⁷Cs. *Chinese Science Bulletin*. 2013;**58** (4-5):552-558. DOI: 10.1007/s11434-012-5426-2
- [30] Tsumune D, Aoyama M, Hirose K. Behavior of ¹³⁷Cs concentrations in the north pacific in an ocean general circulation model. *Journal of Geophysical Research*. 2003;**108**(108):18-11. DOI: 10.1029/2002JC001434
- [31] Liang XS. Wavelet-based multiscale window transform and energy and vorticity analysis. *Harvard Reports in Physical/Interdisciplinary Ocean Science*, Rep. No. 66. Cambridge, MA, USA: Harvard University; 2002. 411 pp

Climate Change and Impact (Sea Level Rise)

Long-Term Sea Level Variability in the Yellow Sea and East China Sea

Ying Xu, Mingsen Lin and Quanan Zheng

Additional information is available at the end of the chapter

<http://dx.doi.org/10.5772/intechopen.80735>

Abstract

Using the satellite altimeter maps of sea level anomaly (MSLA) and tidal gauge data, this chapter gives an investigation of the long-term sea level variability (SLV) and sea level rise (SLR) rate in the Yellow Sea (YS) and East China Sea (ECS). Correlation analysis shows that the satellite altimeter is effective and capable of revealing the coastal SLV. To investigate the regional correlation of SLV in the YS and ECS, tidal gauge station data are used as references. Based on the monthly maps of correlation coefficient (CC) of SLV at tidal stations with the gridded MSLA data, we find that the existence of Kuroshio decreases the correlation between the coastal and Pacific sea levels. The empirical mode decomposition (EMD) method is applied to derive the SLR trend on each MSLA grid point in the YS and ECS. According to the two-dimensional geographical distribution of the SLR rate, one can see that the sea level on the eastern side of the Kuroshio mainstream rises faster than that on the western side. Both the YS and ECS SLR rates averaged over 1993–2010 are slower than the globally averaged SLR rate. This implies that although the SLV in the two seas is affected by global climate change, it could be mostly influenced by local effects.

Keywords: East China Sea, Yellow Sea, sea level variability, empirical mode decomposition

1. Introduction

Long-term sea level variability (SLV) is critical for understanding global climate change. Meanwhile, accelerating sea level rise (SLR) in response to global warming has become a main issue that concerns the general public. Previous investigations have indicated that the SLR potentially affects human populations in coastal and island regions around the world and

changes natural environments like coastal and marine ecosystems [1–3]. As discussed in the fifth Intergovernmental Panel on Climate Change (IPCC) report, due to sea level rise projected throughout the twenty-first century and beyond, coastal systems and low-lying areas will increasingly experience adverse impacts such as submergence, coastal flooding and coastal erosion¹[4].

Global average sea levels rose 195 mm from 1870 to 2004 and showed an average annual rise of $1.44 \text{ mm}\cdot\text{a}^{-1}$ [5]. However, the recent SLR rate has reached about $3.00 \text{ mm}\cdot\text{a}^{-1}$ which is faster than previous estimation [6]. Researchers found that the distribution of SLV trend was not uniform around the world and the local characteristics of SLV trend were significant for prediction [7–8]. Eustatic changes, steric changes and geologic changes are the main influence factors of sea level variability [9]. To detect these changes as accurately as possible, researchers developed various methods. The analysis of tidal gauge data was the main approach for extracting sea level change signals before 1990s [10]. The combined analysis of satellite altimetry data and tidal gauge data has become an often-used tool for estimating global or regional SLV since 1990s [6, 11–14].

The applicability of satellite altimeter data in coastal sea areas has been validated by many works. Volkov et al. studied the performance of a corrected altimeter data over the north-west European shelf [15]. Their results demonstrated that although local tides effect should be further featured, the altimeter data can be effectively used in monitoring sea level variability over continental shelves. Cheng et al. jointly used satellite altimeter data and tide gauge data to predict the coastal sea level at the west and north coasts of the United Kingdom [16]. Their study showed tidal gauge data are consistent with satellite altimeter data for the annual change during 1993–2010. The annual amplitude correlation is 0.79 and the annual phase correlation is 0.80.

The coastal region off East China is vulnerable to SLR because of the geographical distribution of many low lands and river deltas. In addition, it is the most economically developed and densely populated region in China. Thus, the research on SLR and its impacts has been intensively investigated in China, particularly since 2000. From altimeter observations, Liu et al. calculated that the linear trend of SLR rate in the Yellow Sea (YS) was $5.05 \text{ mm}\cdot\text{a}^{-1}$ from 1992 to 2005 [17]. Zhan et al. used normal Morlet wavelet transform to investigate SLR trend in the China Seas and found that the SLR rate in the YS was $(4.01 \pm 0.49) \text{ mm}\cdot\text{a}^{-1}$ during 1992–2006 and the geographical distribution of the rate presented large differences [18]. Using 11 years altimeter data from 1992 to 2004, Qiao and Chen investigated the spatial-temporal SLV of the China Seas. Their results showed the major variation period was 1 year in the YS and East China Sea (ECS), with the SLR rate of the YS and ECS being 5.17 and $6.83 \text{ mm}\cdot\text{a}^{-1}$, respectively [19]. Liu et al. reported that the SLR rate reached $2.92 \text{ mm}\cdot\text{a}^{-1}$ in the southern part of the ECS (south of 30°N) [20]. The China Sea Level Bulletin 2010 indicates that the sea level in the Chinese Coastal Seas shows an overall fluctuating upward trend during the past 30 years, and that the SLR rate in both the YS and ECS was $2.8 \text{ mm}\cdot\text{a}^{-1}$ [21]. With wavelet transform method, Wang et al. studied the sea level change multi-scale cycle of the ECS. They found that the sea level in the ECS

¹**Foundation item:** The National Natural Science Foundation of China under contract No.41506207; the National Programme on Global Change and Air-Sea Interaction under contract No.GASI-02-SCS-YGST2-02.

showed upward trend and the SLR rate was up to $3.9 \text{ mm}\cdot\text{a}^{-1}$ between 1992 and 2009 [22]. Zuo et al. predicted the flooded area for the coastal regions of Shanghai City, Jiangsu Province and northern Zhejiang Province. Their results indicated that, on the condition of current SLR rate of $3.00 \text{ mm}\cdot\text{a}^{-1}$, the flooded area would be $64.1 \times 10^3 \text{ km}^2$ in 2050 and $67.8 \times 10^3 \text{ km}^2$ in 2080 [23]. Xu et al. studied the average SLR rate in the ECS between 1993 and 2010. The results showed the rising rate was $2.5 \text{ mm}\cdot\text{a}^{-1}$ and it was slower than global average [24].

In this chapter, we examine the SLV in the YS and ECS by using the combination of satellite altimeter data and tidal gauge data. Using the tidal gauge data as reference, the regional correlations of SLV in the YS and ECS are analyzed. Furthermore, long-term SLV trend and its two-dimensional distribution features in the entire YS and ECS are derived by using the empirical mode decomposition (EMD) method.

2. Data and method

2.1. Tidal gauge data

In-situ tidal gauge measures relative sea level variations with respect to a crustal reference point. It can provide a long and fine temporal resolution sea level record. However, there are two main problems when using tidal gauge data to investigate SLR. First, the crustal reference point itself may have vertical motions. Second, the limited spatial distribution of tidal stations has constrained the investigation of SLR, especially in the open seas.

In this chapter, we use the tidal gauge data from the University of Hawaii Sea Level Center (UHSLC), USA. It provides three kinds of sea level data including the research quality data, the fast delivery data (GLOSS/CLIVAR “fast delivery” data) and the SLP-Pac data (JCOMM Sea Level Program in the Pacific map data).

We select the daily research quality data, with six stations available near the coasts of the YS and ECS. Among all the data, only the time series with the same overlapping period as the satellite altimeter data are used. These daily data have been climatologically averaged to eliminate abnormal values. The locations and time spans of the six stations are listed in **Table 1**.

Station name	Latitude (N)	Longitude (E)	Time span	Station #
Laohutan	38°52′	121°41′	1993–1997	631
Shijiusuo	35°23′	119°33′	1993–1997	642
Lvsi	32°08′	121°37′	1993–1996	633
Kanmen	28°05′	121°17′	1993–1997	632
Xiamen	24°27′	118°04′	1993–1997	376
Shanwei	22°45′	115°21′	1993–1997	641

Table 1. Seven tidal stations in the Yellow Sea and East China Sea.

2.2. Satellite altimeter data

Being different from tidal gauge, satellite altimeter provides absolute measurements of sea level variations with respect to the Earth's center-of-mass. It gives independent measurements to investigate SLR with truly global coverage. The major disadvantage of satellite altimeter is its relatively shorter record duration compared to the tidal gauge data. Although the earlier altimeter data had some limitation due to orbit determination and measurement corrections, recent reprocessing of satellite data has shown great improvement and makes it possible to precisely measuring long-term SLVs.

The Archiving, Validation and Interpretation of Satellite Oceanographic data (AVISO) has distributed series of satellite altimetry products since 1992. Precise Orbit Ephemeris (POE) orbit and a centered computation time-window are applied to generate the delayed time (DT) products to achieve better accuracy. Therefore, the DT products are more suitable for sea level research.

In this chapter, we use daily global DT maps of sea level anomaly (MSLA) products as satellite altimeter data. The MSLA is a daily gridded data set which is provided on $(1/3)^\circ \times (1/3)^\circ$ Mercator grid for global coverage. With the daily resolution MSLA from October 14, 1992 to January 19, 2011, more data can be included in EMD trend extraction. And this helps us extract the trend more accurately.

2.3. Empirical mode decomposition

There are two kinds of models for investigation and prediction of SLR trend: numerical models based on physical processes and statistical models based on long-term observations [25]. As a physical approach, a hierarchy of numerical models have been used to estimate past changes and to project future changes in sea level for the IPCC. Meanwhile, a number of statistical approaches have been used to determine SLV, such as the empirical orthogonal function (EOF) analysis [6, 26], the regression method [14, 16], the semi-empirical method [27], spectral analysis [28] and the EMD analysis [29].

EMD introduced by Huang et al. [30] is used to extract sea level trend signals in this chapter. It is a powerful time series analysis tool, particularly for dealing with data from non-stationary and nonlinear processes. The EMD method, in contrast to almost all the other methods, is empirical, intuitive, direct and adaptive [31]. It is based on the assumption that time series data consist of different simple intrinsic modes of oscillations. Each of these linear or nonlinear modes is represented by an intrinsic mode function (IMF), which can have a variable amplitude and frequency as a function of time. Thus, EMD depends on the nature of the data sets. With the specific definition for the IMF and repeated siftings, one can decompose any function into IMFs, and the residue should be a trend.

In this chapter, the sea level data on each MSLA grid point can be describe as a time series function $x(t)$. The sifting process is shown in **Figure 1**.

During the first EMD sifting process, we identify all the local maxima and minima, and then use a cubic spline line to generate upper and lower envelopes. The mean of the upper and

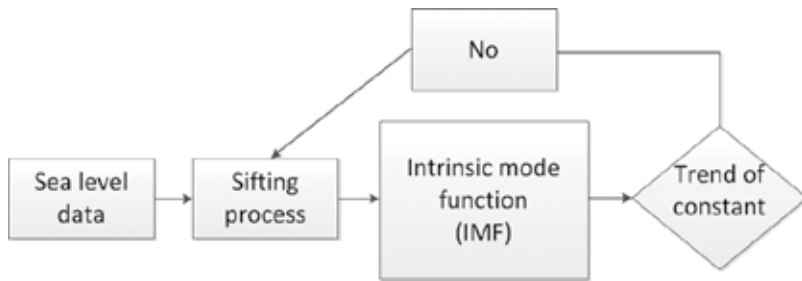


Figure 1. Sifting process of the empirical mode decomposition.

lower envelopes is designated as m_1 , and the difference between the data $x(t)$ and m_1 is the first component h_1 ,

$$h_1 = x(t) - m_1 \quad (1)$$

In the subsequent sifting processes, h_1 can be treated as the data, then

$$h_{11} = h_1 - m_{11} \quad (2)$$

After sifting process being repeated in this manner, when h_{1k} meets the specific definition of the IMF, h_{1k} becomes an IMF, that is,

$$h_{1k} = h_{1(k-1)} - m_{1k} \quad (3)$$

Then, the first IMF is designated as

$$c_1 = h_{1k} \quad (4)$$

Overall, c_1 should contain the finest scale of the shortest period component of the sea level signal. We empirically select n as the number of IMFs. Thus, the sifting process will stop when the number of IMFs is higher than n ,

$$n = \log_2(N) - 1 \quad (5)$$

where N is the number of sea level data. Thus, a decomposition of a MSLA grid-point data into n -empirical modes is achieved, and a residue r_n is obtained which can be the mean sea level trend. Finally, $x(t)$ is represented by

$$x(t) = \sum_{j=1}^n c_j + r_n \quad (6)$$

where IMF and trend are denoted as c_1, \dots, c_n and r_n , respectively. **Figure 2** shows the EMD analysis of the sea level on a MSLA grid point.

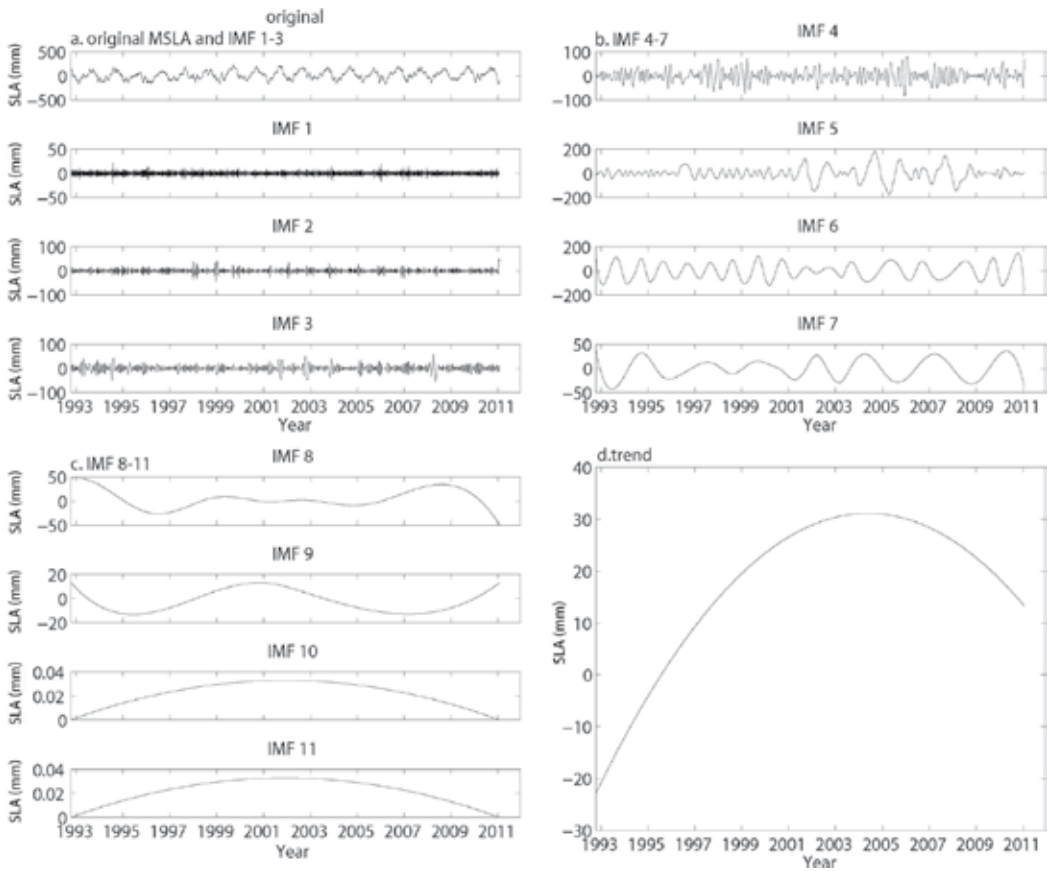


Figure 2. The EMD results at a MSLA grid point. The original is raw tidal gauge data, and IMFs 1–11 are the intrinsic oscillating modes. The trend is the SLR trend of a MSLA grid point from October 14, 1992 to January 19, 2011.

3. Regional correlation of sea level variability

3.1. Validation of maps of sea level anomaly

To accurately derive SLV and the trend, it is necessary to validate the applicability of MSLA in the YS and SCS. We calculate the correlation coefficient (CC) between tidal gauge data and the closest MSLA grid-point data. Both data sets are monthly-averaged to eliminate short-term fluctuations. With a maximum distance of 0.5' between the two types of data, the CCs at Laohutan, Shijiusuo, Lvsu, Kanmen, Xiamen and Shanwei stations are 0.89, 0.40, 0.65, 0.73, 0.79 and 0.81, respectively. The CC of Shijiusuo is relatively low but still in the moderate interval (0.30–0.50). The correlation suggests that satellite MSLA data are effective in sea level monitoring and research in the YS and ECS. **Figure 3** shows the CCs, the curves of the monthly-averaged sea level data and the closest MSLA grid-point data of the seven tidal stations.

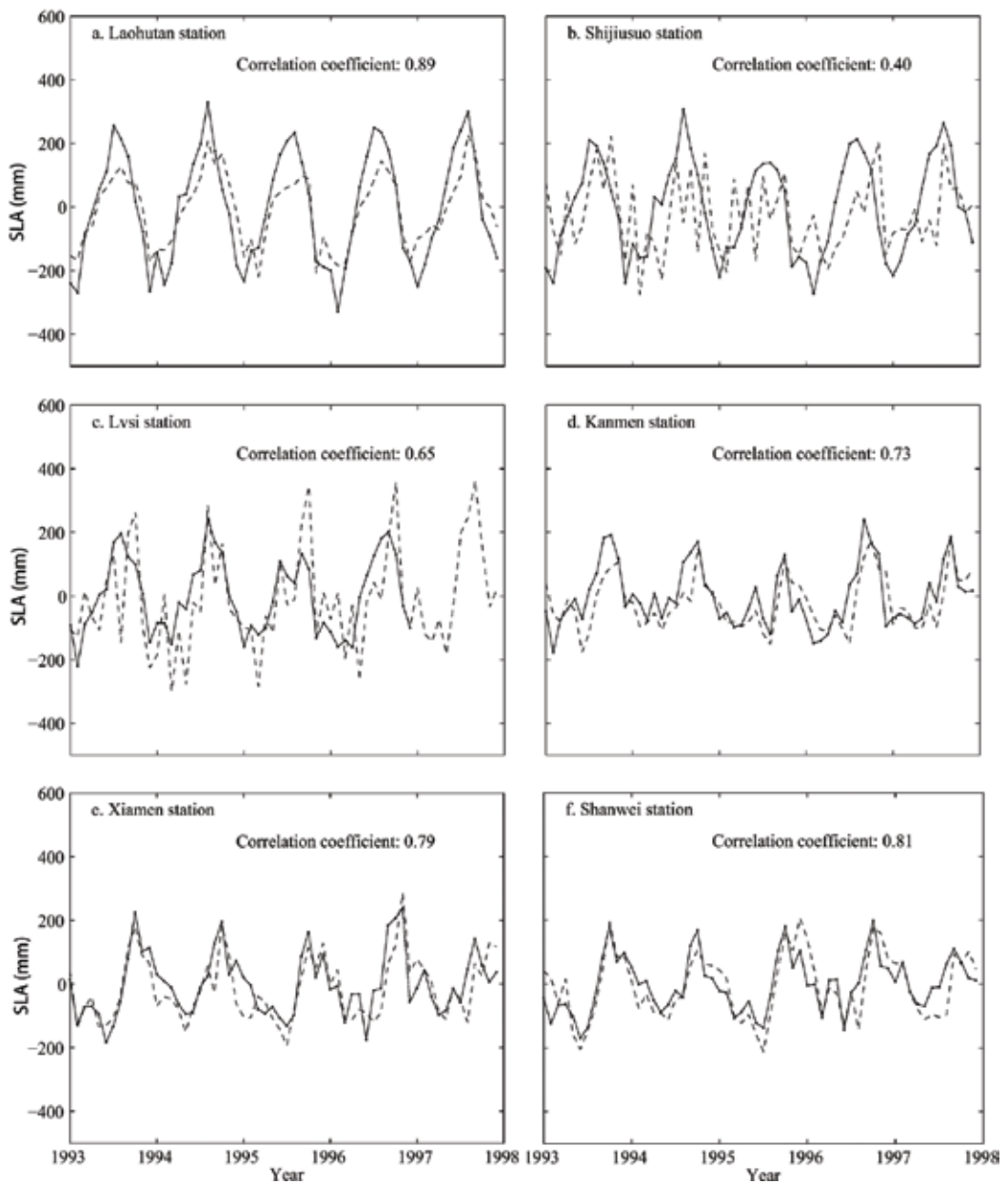


Figure 3. The correlation coefficient with gauge data at the most closest MSLA point of the Laohutan (a), Shijiusuo (b), Lvsi (c), Kanmen (d), Xiamen (e) and Shanwei (f) stations. Solid line is the monthly-averaged sea level data of a tidal station, and dashed line is the monthly-averaged data of the closest MSLA grid point to a selected station.

3.2. Regional correlation of sea level variability in the Yellow Sea

To study the geographical distribution features of the correlation of SLV between tidal gauge and MSLA points in the YS, we employ correlation analysis between the Laohutan, Shijiusuo

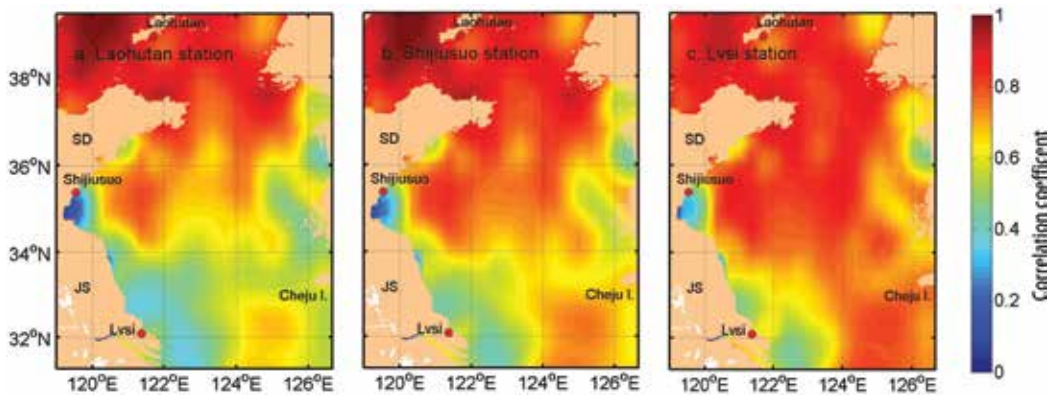


Figure 4. Monthly maps of correlation coefficient (CC) of SLV at Laohutan Station (a), Shijiusuo Station (b) and Lvsi Station (c) with that in the Yellow Sea. SD: Shandong Province; JS: Jiangsu Province.

and Lvsi stations and all the MSLA grid points in the entire YS. With this method, tidal gauge data are used as references to investigate the monthly regional correlation of SLV in the YS.

Figure 4 shows that the SLV at Laohutan station is highly correlated ($0.70 < CC < 0.80$) with that in its adjacent coastal region and the northern YS. The correlations of SLV at Shijiusuo and Lvsi stations with its adjacent coastal region is low ($0.20 < CC < 0.35$), but they are high ($0.7 < CC < 0.85$) with the northern, central and south-eastern regions of the YS. All three panels in **Figure 4** show that the SLV in northern, central and south-eastern regions of the YS (the open sea of the YS) is coherent. The SLV along the western coastal region of the YS also shows coherence between the two data sets.

The circulation in the YS is mainly composed of coastal ocean current system (west coastal current and east coastal current) and the open sea current system (Yellow Sea warm current) and Yellow Sea cold water mass circulation [32–33]. The distribution of CCs indicates on the monthly scale, the SLV in the YS is dominated by open sea and coastal ocean current systems of the YS, respectively.

3.3. Regional correlation of sea level variability in the East China Sea

Similarly, **Figure 5** is the monthly maps of the CC between the four tidal stations and the entire study area of the ECS. Using Lvsi station as reference, the result (**Figure 5a**) shows that the SLV in the northern and central regions of the ECS is highly correlated ($CC > 0.80$). While it is weakly correlated ($0.50 < CC < 0.70$) with the coastal ocean, and negatively correlated with the coastal seas of Fujian and Guangdong Province. At Kanmen Station (**Figure 5b**), we find a similar signature with Lvsi station. The highly correlated region ($CC > 0.80$) is mainly located in the northern and central regions of the ECS. However, the CCs in coastal regions of **Figure 5b** ($CC > 0.7$) are higher than **Figure 5a**. At Xiamen (**Figure 5c**) and Shanwei Station (**Figure 5d**), the highest correlation region ($CC > 0.80$) is located in the coastal seas of Zhejiang, Fujian and Guangdong province. And the CCs with the northern and central regions of the ECS are relatively weak. The Kuroshio can be clearly identified in all the panels of **Figure 5**. And the correlation show different characteristics on the left-hand side and the right-hand side of the Kuroshio core.

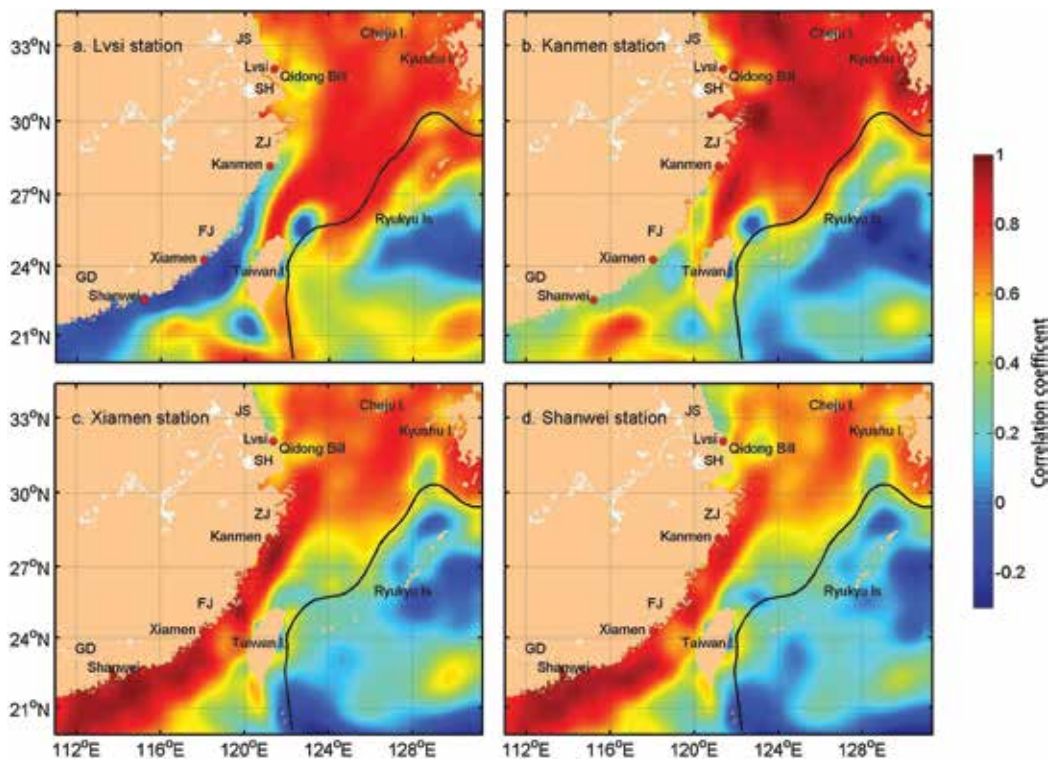


Figure 5. Monthly maps of correlation coefficient of SLV at Lvsai Station (a), Kanmen Station (b), Xiamen Station (c) and Shanwei Station (d) with the grid-point data in the East China Sea. JS: Jiangsu Province; ZJ: Zhejiang Province; FJ: Fujian Province and GD: Guangdong Province.

The circulation in the ECS is mainly composed of warm current (the Kuroshio) and coastal ocean current system (coastal current of Zhejiang and Fujian) [32–33]. The distribution of CCs indicates that the major water mass and the coastal regions in the ECS are dominated by different mechanism on the monthly scale. The Kuroshio blocks the link of SLV between the left-hand and right-hand of its flow core.

4. Long-term sea level variability trend

4.1. Two-dimensional distribution features of trend in the Yellow Sea

Sea level trend at a few MSLA grid points cannot give the detailed pattern in the YS. To better understand the geographical distribution of SLR trend, we calculate the annual-average SLR rate and generate the maps of the rate in the YS from 1993 to 2010, from 1993 to 1998 and from 1999 to 2010, respectively. **Figure 6** shows the distributions in the three phases.

Overall, the annual-average SLR rate in the YS between 1993 and 2010 was (1.03 ± 3.16) $\text{mm}\cdot\text{a}^{-1}$. The fastest SLR regions were located along the west coast and in the southern part of

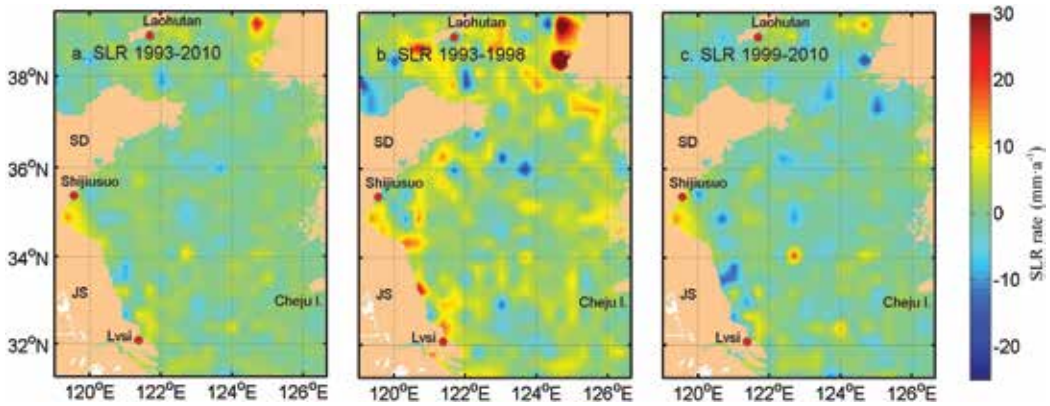


Figure 6. Distributions of SLR rates in the Yellow Sea obtained using the EMD: (a) 1993–2010, (b) 1993–1998 and (c) 1999–2010.

the YS. In the central part of the YS, the SLR rates were negative. The SLR rates from 1993 to 1998 and from 1999 to 2010 were $3.54 \pm 7.08 \text{ mm}\cdot\text{a}^{-1}$ and $-0.01 \pm 4.04 \text{ mm}\cdot\text{a}^{-1}$, respectively. The geographical distributions of the fastest SLR rates in the periods of 1993–1998 and 1999–2010 show similar characteristics to the period of 1993–2010. It is worth noting that the rate of SLR turned from positive to negative value since 1999.

4.2. Two-dimensional distribution features of the trend in the East China Sea

Figure 7 shows the geographical distribution of SLR rate in the ECS. Between 1993 and 2010, the annual-average SLR rate in the ECS was $2.50 \pm 3.64 \text{ mm}\cdot\text{a}^{-1}$. The SLR rates from 1993 to 1998 and from 1999 to 2010 were $4.08 \pm 6.95 \text{ mm}\cdot\text{a}^{-1}$ and $1.88 \pm 4.80 \text{ mm}\cdot\text{a}^{-1}$, respectively. However, the rate was neither uniformly nor simultaneously distributed in the ECS. We can see the rate on the right-hand side of the Kuroshio core was faster than on the left-hand side in all the panels of **Figure 7**. That may indicate the role of warm water transportation of the Kuroshio in SLR is not more important than the local processes in the ECS.

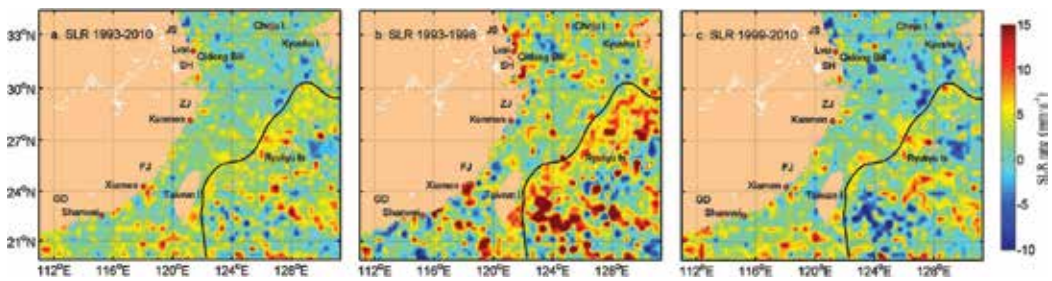


Figure 7. Distributions of SLR rates in the East China Sea obtained using from the EMD: (a) 1993–2010, (b) 1993–1998 and (c) 1999–2010.

5. Summary

In this chapter, we deal with long-term SLV in the YS and ECS using satellite altimeter MSLA data from 1992 to 2011, as well as data from six tidal gauges from 1996 to 1999. Major findings are summarized as follows.

(1) Using correlation analysis method, we first calculate the monthly-averaged correlation coefficients between the tidal gauge data and the closest MSLA grid-point data to validate the applicability of MSLA in the YS and ECS.

The results indicate that, in addition to Shijiusuo station where the CC is 0.40 (in the moderate interval), the CCs at the other five tidal station show high correlations. The maximum value of the correlation coefficients is 0.89 at Laohutan Station. These results confirm that using satellites to observe coastal SLV is effective and feasible when MSLA data is monthly-averaged.

(2) Furthermore, we apply the correlation analysis between MSLA and tidal gauge data in the YS and ECS. The regional correlation of SLV in the YS and ECS between the two data sets is investigated using the tidal station data as the reference.

For the YS, according to the correlation coefficient map, the monthly SLV in the northern, central and south-eastern regions of the YS (the open sea of the YS) and that along the western coastal region of the YS show coherence, respectively.

For the ECS, the monthly SLV in the northern and central regions of the ECS and that along the coastal regions of Zhejiang, Fujian and Guangdong province show coherence, respectively. The existence of the Kuroshio decreases the correlation or generates negative correlation between coastal sea level and Pacific sea level.

The geographical distributions of CCs show that the SLV in the YS and ECS are affected by the circulation systems on monthly scale. The Kuroshio acts like a barrier, which blocks the effect of the Pacific and global change.

(3) The EMD method is used to derive sea level trend in the YS and ECS. Then the SLR rate is calculated based on the trend, and its two-dimensional geographical distribution is investigated. The important findings are given below.

In the YS, the SLR rate turned from positive to negative value in 1999–2010, and the fastest SLR regions were located along the west coast and in the southern region of the YS. In the ECS, the SLR rate significantly slowed down in 1999–2010, and the sea level on the right-hand side of the Kuroshio core rose distinctly faster than on the left-hand side of the Kuroshio. This further supports the barrier effect of the Kuroshio in the ECS.

A recent study shows that the global warming has paused while the deep ocean takes the heat instead [34]. In this study, we found the SLR rate after 1999 also slowed down significantly in the YS and ECS. This kind of change shows that SLR in YS and ECS is affected by global climate change. Moreover, the SLR rates in the YS ($1.03 \pm 3.16 \text{ mm}\cdot\text{a}^{-1}$) and in the ECS ($2.50 \pm 3.64 \text{ mm}\cdot\text{a}^{-1}$)

during 1993–2010 are lower than the global average ($3.00 \text{ mm}\cdot\text{a}^{-1}$). The lower rate than the global average indicates that local system effects play important roles in the SLR in the YS and ECS.

Both SLR and circulation system in the YS and ECS are complicated. There still are no answers to many critical questions about the ocean dynamics in the YS and ECS. The subject on the SLR in the YS and ECS remains a research focus under debate. We hope that this study will bring some useful information to this debate.

Acknowledgements

We thank to the dedications of MSLA data from AVISO/CNES (<http://www.avisio.altimetry.fr/en/data.html>) and tidal gauge sea level data from UHSLC (University of Hawaii Sea Level Center). We also wish to thank the Department of Atmospheric and Oceanic Science, University of Maryland for resources while the lead author was a visiting scholar there.

Author details

Ying Xu^{1*}, Mingsen Lin¹ and Quanan Zheng²

*Address all correspondence to: xuying@mail.nsoas.org.cn

1 National Satellite Ocean Application Service, Key Laboratory of Space Ocean Remote Sensing and Application, State Oceanic Administration, Beijing, China

2 Department of Atmospheric and Oceanic Science, University of Maryland, MD, USA

References

- [1] Bindoff NL, Willebrand J, Artale V, Cazenave A, Gregory J, Gulev S, et al. Observations: oceanic climate change and sea level. In: Labeyrie L, Wratt D, editors. *Climate Change 2007: The Physical Science Basis. Contribution of Working Group I to the Fourth Assessment Report of the Intergovernmental Panel on Climate Change*. Cambridge, United Kingdom and New York, NY, USA: Cambridge University Press; 2007. pp. 385-432
- [2] Fischlin A, Midgley GF, Price JT, Leemans R, Gopal B, Turley C, et al. Ecosystems, their properties, goods and services. In: Cramer W, Diaz SM, editors. *Climate Change 2007: Impacts, Adaptation and Vulnerability. Contribution of Working Group II to the Fourth Assessment Report of the Intergovernmental Panel on Climate Change*. Cambridge: Cambridge University Press; 2007. pp. 211-272
- [3] Nicholls RJ, Cazenave A. Sea-level rise and its impact on coastal zones. *Science*. 2010; **328**(5985):1527-1520. DOI: 10.1126/science.1185782

- [4] Wong PP, Losada IJ, Gattuso J-P, Hinkel J, Khattabi A, McInnes KL, et al. Coastal systems and low-lying areas. In: Nicholls RJ, Santos F, editors. *Climate Change 2014: Impacts, Adaptation, and Vulnerability. Part A: Global and Sectoral Aspects. Contribution of Working Group II to the Fifth Assessment Report of the Intergovernmental Panel on Climate Change*. Cambridge, United Kingdom and New York, NY, USA: Cambridge University Press; 2014. pp. 361-409
- [5] Church JA, White NJ. A 20th century acceleration in global sea-level rise. *Geophysical Research Letters*. 2006;**33**(1):L01602. DOI: 10.1029/2005GL024826
- [6] Church JA, White NJ. Sea-level rise from the late 19th to the early 21st century. *Surveys in Geophysics*. 2011;**32**(4-5):585-602. DOI: 10.1007/s10712-011-9119-1
- [7] Cazenave A, Nerem RS. Present-day sea-level change observations and causes. *Reviews of Geophysics*. 2004;**42**(3):131-144. DOI: 10.1029/2003RG000139
- [8] Church JA, Gregory JM, Huybrechts P, Kuhn M, Lambeck K, Nhuan MT, et al. Changes in sea level. In: Douglas BC, Ramirez A, editors. *Climate Change 2001: The Scientific Basis, Contribution of Working Group I to the Third Assessment Report of the Intergovernmental Panel on Climate Change*. New York, NY, USA: Cambridge University Press; 2001. pp. 639-693
- [9] Carton JA, Giese BS, Grodsky SA. Sea level rise and the warming of the oceans in the simple ocean data assimilation (SODA) ocean reanalysis. *Journal of Geophysical Research*. 2005;**110**(C9):C09006. DOI: 10.1029/2004JC002817
- [10] Douglas BC. Global sea level acceleration. *Journal of Geophysical Research*. 1992;**97**(C8): 12699-12706. DOI: 10.1029/92JC01133
- [11] Cabanes C, Cazenave A, Le Provost C. Sea level rise during past 40 years determined from satellite and in situ observations. *Science*. 2001;**294**(5543):840-842. DOI: 10.1126/science.1063556
- [12] Mangiarotti S. Coastal sea level trends from TOPEX-POSEIDON satellite altimetry and tide gauge data in the Mediterranean Sea during the 1990s. *Geophysical Journal International*. 2007;**170**(1):132-144. DOI: 10.1111/j.1365-246X.2007.03424.x
- [13] Trisirisatayawong I, Naejie M, Simons W, Fenoglio-Marc L. Sea level change in the Gulf of Thailand from GPS-corrected tide gauge data and multi-satellite. *Global and Planetary Change*. 2011;**76**(3-4):137-151. DOI: 10.1016/j.gloplacha.2010.12.010
- [14] Dean RG, Houston JR. Recent sea level trends and accelerations: comparison of tide gauge and satellite results. *Coastal Engineering*. 2013;**75**(5):4-9. DOI: 10.1016/j.coastaleng.2013.01.001
- [15] Volkov DL, Larnicol G, Dorandeu J. Improving the quality of satellite altimetry data over continental shelves. *Journal of Geophysical Research*. 2007;**112**(C6):C06020. DOI: 10.1029/2006JC003765

- [16] Cheng YC, Andersen OB, Knudsen P. Integrating non-tidal sea level data from altimetry and tide gauges for coastal sea level prediction. *Advances in Space Research*. 2012;**50**(8):1099-1106. DOI: 10.1016/j.asr.2011.11.016
- [17] Liu GF, Ma HQ, Zhang GY. Trends and wavelet correlation analysis of sea level changes in the China Seas and the global area from satellite altimetry (In Chinese). *Science of Surveying and Mapping*. 2007;**32**(6):56-58. DOI: 10.3771/j.issn.1009-2307.2007.06.018
- [18] Zhan JG, Wang Y, Xu HZ, Hao XG, Liu LT. The wavelet analysis of sea level change in China Sea during 1992-2006 (In Chinese). *Acta Geodaetica et Cartographica Sinica*. 2008;**37**(4):438-443. DOI: 10.3321/j.issn:1001-1595.2008.04.007
- [19] Qiao X, Chen G. A preliminary analysis on the China Sea level using 11 years' TOPEX/Poseidon altimeter data (In Chinese). *Marine Sciences*. 2008;**32**(1):60-64. DOI: 1000-3096(2008)01-0060-05
- [20] Liu XY, Liu YG, Guo L, Gu YZ. Change of mean sea level of low-frequency on East China Sea and its relation with ENSO (In Chinese). *Journal of Geodesy and Geodynamics*. 2009;**29**(4):55-63. DOI: 1671-5942(2009)04-0055-09
- [21] State Oceanic Administration, People's Republic of China. China Sea Level Bulletin 2010 (In Chinese) [Internet]. 2011;**4**:22. Available from: http://www.soa.gov.cn/zwgk/hygb/zghpmb/201211/t20121105_5567.html
- [22] Wang GD, Kang JC, Han GQ, Liu C. Analysis and prediction of sea-level-change multi-scale cycle for East China Sea (In Chinese). *Advances in Earth Science*. 2011;**26**(6):678-684. DOI: 1001-8166(2011)06-0678-07
- [23] Zuo JC, Yang YQ, Zhang JL, Chen MX, Xu Q. Prediction of China's submerged coastal areas by sea level rise due to climate change. *Journal of Ocean University of China*. 2013;**12**(3):327-334. DOI: 10.1007/s11802-013-1908-3
- [24] Xu Y, Lin MS, Zheng QA, Ye XM, Li JY, Zhu BL. A study of long-term sea level variability in the East China Sea. *Acta Oceanologica Sinica*. 2015;**34**(11):109-117. DOI: 10.1007/s13131-015-0754-0
- [25] Baart F, Koningsveld MV, Stive MJF. Trends in sea-level trend analysis. *Journal of Coastal Research*. 2012;**28**(2):311-315. DOI: 10.2112/JCOASTRES-11A-00024.1
- [26] Church JA, White NJ, Coleman R, Lambeck K, Mitrovica JX. Estimates of the regional distribution of sea level rise over the 1950-2000 period. *Journal of Climate*. 2004;**17**(13):2609-2625. DOI: 10.1175/1520-0442(2004)017%3C2609:EOTRDO%3E2.0.CO;2
- [27] Rahmstorf S. A Semi-empirical approach to projecting future sea-level rise. *Science*. 2007;**315**(5810):368-370. DOI: 10.1126/science.1135456
- [28] Fenoglio-Marc L. Long-term sea level change in the mediterranean sea from multi-satellite altimetry and tide gauges. *Physics and Chemistry of the Earth, Parts A/B/C*. 2002;**27**(32-34):1419-1431. DOI: 10.1016/S1474-7065(02)00084-0

- [29] Ezer T. Sea level rise, spatially uneven and temporally unsteady: why the U. S. East Coast, the global tide gauge record, and the global altimeter data show different trends. *Geophysical Research Letters*. 2013;**40**(20):5439-5444. DOI: 10.1002/2013GL057952
- [30] Huang NE, Shen Z, Long SR, Wu MC, Shin HH, Zheng QA, et al. The empirical mode decomposition and the Hilbert spectrum for nonlinear and non-stationary time series analysis. *Proceedings of the Royal Society A: Mathematical, Physical and Engineering Sciences*. 1998;**454**(1971):903-995. DOI: 10.1098/rspa.1998.0193
- [31] Huang NE, Shen SSP, editors. *Hilbert-Huang Transform and Its Applications*. 1st ed. Tuck Link, Singapore: World Scientific Publishing Company; 2005. 324 p. DOI: 10.1142/5862
- [32] Guan BX. Patterns and structures of the currents in Bohai, Huanghai and East China Seas. *Oceanology of China seas*. 1994;**1**:17-26
- [33] Qiao FL, editor. *Regional Oceanography of China Seas-Physical Oceanography (In Chinese)*. Beijing, China: China Ocean Press; 2012. 481 p
- [34] Chen XY, Tung KK. Varying planetary heat sink led to global-warming slowdown and acceleration. *Science*. 2014;**345**(6199):897-903. DOI: 10.1126/science.1254937

The Slow Coastal-Trapped Waves off Subei Bank in the Yellow Sea and Their Climatic Change in the Past Decades

X. San Liang

Additional information is available at the end of the chapter

<http://dx.doi.org/10.5772/intechopen.80017>

Abstract

Coastal-trapped waves (CTWs) are a class of subinertial signals in the weather frequency band that play a pivotal role in coastal air-sea interaction. However, this important topic seems to be missing in the heated debate in recent years on coastal environmental change and protection. In this chapter, a brief but self-contained introduction of the CTW theory is presented, in the hope of providing a reference for investigators in the relevant fields. Also presented is a numerical scheme for computing the wave properties. As a demonstration, we have conducted a preliminary study of the CTWs for a section across the Subei Bank in the Yellow Sea. By the results, all the computed slow modes, including a bottom-intensified one, seem to be slowing down since two decades ago. They have particularly slowed down in the event when a strong El Niño is followed by a strong La Niña, such as in the 97–98 and 09–10 El Niño events.

Keywords: coastal-trapped wave, Yellow Sea, Jiangsu coast, climate change, ENSO

1. Introduction

Coastal-trapped waves (CTWs) are a class of subinertial waves within the weather frequency band, which have elegant mathematical formulation; in the Northern Hemisphere, they propagate unidirectionally such that the coast lies on the right. In coastal hazard study, the role of CTWs is rarely touched, though its importance in exchanging mass and energy has been well recognized (e.g., [1]). For example, the wind-driven variabilities over the continental margin can be largely explained in terms of CTW properties. These waves play a key role in coastal oceans' response to atmospheric weather changes; they make a major mechanism in the coastal ocean that spreads the atmospheric energy in the alongshore direction, leading to the formation of the

remotely driven upwelling, and hence regulating coastal processes from far away. Historically, the low-frequency CTW wave motions were first identified along the East Australian coast [2], and soon studied in terms of continental shelf waves (CSW) by Robinson [3], reflecting the early effort in this field at Harvard University ([4], cf. [5]). Systematic CTW studies began with Allen [6], Wang and Mooers [7], Clarke [8], Huthnance [9], to name several. A comprehensive review is referred to Brink [10].

The East China Sea (ECS), including the Yellow Sea (YS), is one of the major marginal seas in the Northwestern Pacific. Despite its long coastline, CTWs are rarely investigated for this region. It seems that most of the CTW studies are in 80s to early 90s, though recently there is a renewed interest with the aid of Hilbert-Huang transform [11]. For example, Feng [12] examined the dissipative trapped waves on a broad shelf; Liu and Qin [13] investigated the

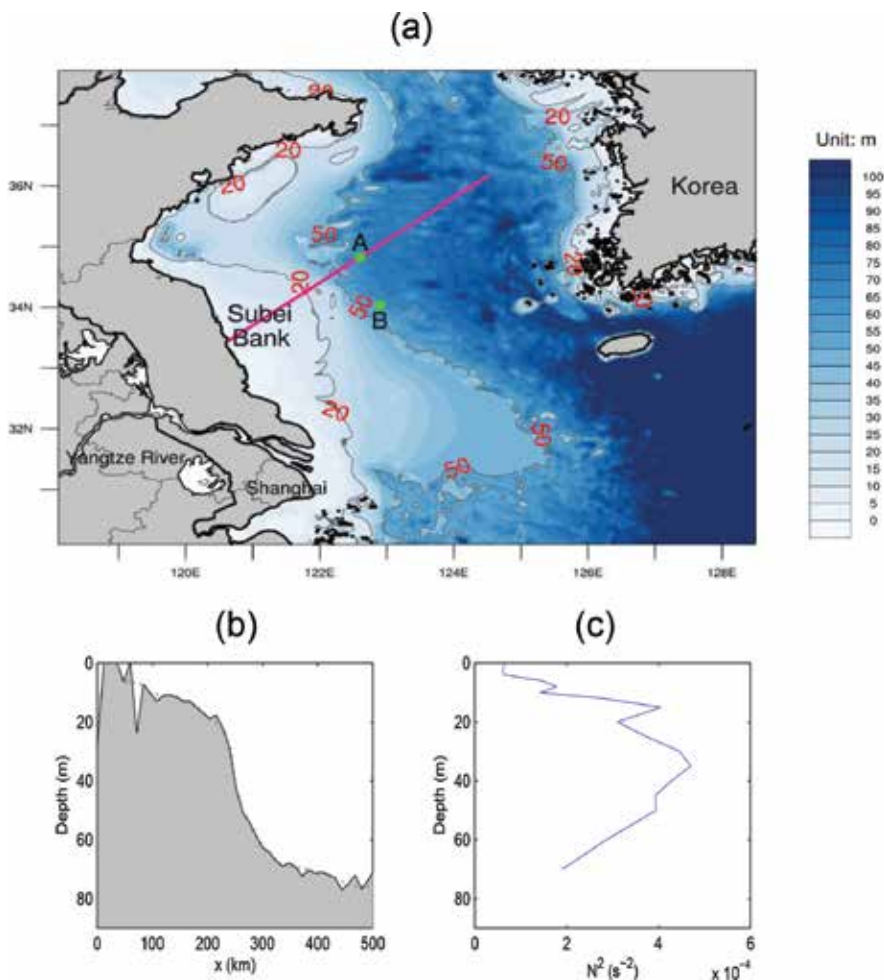


Figure 1. (a) Bathymetry of the Yellow Sea. Abutted to the left is China, while on its right lies Korea. The solid line across Subei Bank marks the cross-section which we will study. Also marked are the points A and B where time series will be extracted from the HYbrid Coordinate Ocean Model (HYCOM) dataset for analysis. (b) The topography along the section marked in (a). (c) A profile of the buoyancy frequency squared N^2 (for 1995).

instability of CTWs; Kong et al. [14] studied the impact of the ECS CTWs on Kuroshio; and Chen and Su [15] gave a systematic investigation of continental shelf waves (CSW) along the East China coast. This is in contrast to the South China Sea (SCS), which has attracted much more interest for CTW research; a recent study is referred to Zheng et al. [16].

As the northern part of the ECS, the YS is even less studied in the light of CTWs. This is because the YS is a nearly closed basin with a broad, shallow double shelf, a deep trough lying in between (**Figure 1**). Strictly speaking, CTWs in the traditional sense may not be significant, and, indeed, the YS wave motion is dominated by tides. But previous studies did confirm the existence of CTWs in the YS. Particularly, Chen and Su [15] found they have frequencies around 0.21–0.32 cycle per day (cpd), and a speed of roughly 15 m/s; Wang et al. [17] identified two free CTWs, with phase speeds of 14–19 m/s. A careful and detailed study of the YS CTW was conducted by Hsueh and his group (cf. Hsueh and Pang [18]); it is particularly for the wave motion along the Korea coast.

So far there is almost no study on the CTWs along the Jiangsu coast (particularly off Subei Bank) in the YS. This may be due to the lack of a deep ocean to its east. But, if we focus on some motions local enough, it is conceivable that the trapping condition, that is, vanishing far field, that admits the CTWs may still hold. Besides, such subinertial signals do have been identified (e.g., [15, 17]). Considering the potential importance of CTWs on the processes off Subei Bank, we henceforth conduct a preliminary study for this region. To fit for the scope of this book, we focus on the slow CTW modes and examine their climatic variabilities (see below). On the other hand, we take this opportunity to present a brief but self-contained introduction of the CTW theory, in order to provide environmentalists a reference for this important topic, which is yet to be explored in coastal hazard research.

2. A brief introduction of the coastal-trapped wave theory

2.1. Governing equations

Take a right-hand coordinate system (x, y, z) with x directing offshore and z upward. With the assumption of hydrostaticity and incompressibility, the linearized Boussinesq equations for the free-wave problem on an f -plane in the absence of a basic flow are

$$u_t - fv = -\frac{1}{\rho_0}P_x + \frac{1}{\rho_0}\tau_z^x \tag{1}$$

$$v_t + fu = -\frac{1}{\rho_0}P_y + \frac{1}{\rho_0}\tau_z^y \tag{2}$$

$$\rho = -\frac{1}{g}P_z \tag{3}$$

$$u_x + v_y + w_z = 0 \tag{4}$$

$$\rho_t - \frac{\rho_0}{g}N^2w = 0 \tag{5}$$

where (u, v, w) , ρ , and P are the perturbation velocity, density, and pressure, respectively. The turbulent stress (τ^x, τ^y) will be needed when bottom drag and wind forcing are applied; otherwise, it is usually neglected in the ocean interior. Here, the density field is decomposed into three parts: $\rho_0 + \bar{\rho}(z) + \rho(x, y, z, t)$ with the perturbation field $\rho \ll \bar{\rho} \ll \rho_0$. ρ_0 (usually taken as 1000 or 1025 kg/m^3) and $g = 9.8 \text{ m/s}^2$ are constants, and $N^2 = -\frac{g}{\rho_0} \frac{\partial \bar{\rho}}{\partial z}$ is the Brunt-Väisälä or buoyancy frequency; $N^2 = N^2(z)$ is given. Suppose that the bottom depth has a dependence on x only, $h = h(x)$, as schematized in **Figure 2**. The boundary conditions are that the perturbation vanishes as $x \rightarrow +\infty$, and that no flux crosses the solid boundary. The former is the very costally trapped condition. In the figure, the location $x = b$ is pretended to be where the coast is. In practice, it has been chosen such that $h(b) = 22.5 \text{ m}$ (Clarke and Brink, 1985), and such that $h(b)$ is equal to three times the Ekman layer e -folding decay scale δ [19].

In the absence of turbulent stress, (1)–(5) can be reduced to one single equation for P . Let $\zeta = \frac{\partial v}{\partial x} - \frac{\partial u}{\partial y}$ and $\mathcal{D} = \frac{\partial u}{\partial x} + \frac{\partial v}{\partial y}$, respectively, be vorticity and divergence, then it is easy to obtain

$$\begin{aligned} \zeta_t + f \mathcal{D} &= 0, \\ \mathcal{D}_t - f \zeta &= -\frac{1}{\rho_0} \nabla^2 P. \end{aligned}$$

But $\mathcal{D} = -\mathcal{W}_z = \frac{\partial}{\partial z} \left(\frac{1}{\rho_0 N^2} P_{zt} \right)$ by the continuity and hydrostatic equations (4) and (5). These yield

$$\left(f^2 + \frac{\partial^2}{\partial t^2} \right) \frac{\partial}{\partial z} \left(\frac{P_{zt}}{N^2} \right) + \nabla^2 P_t = 0. \tag{6}$$

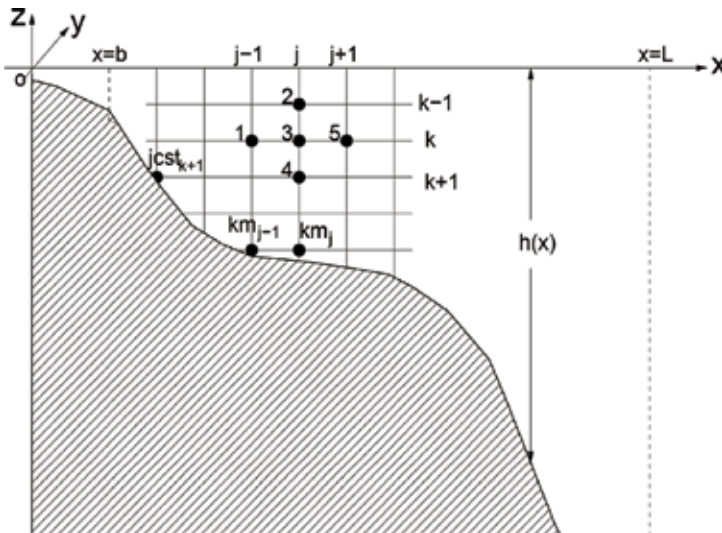


Figure 2. A schematic of the topographic configuration and its discretization (k and j are the indices). The location $x = b$ is pretended to be where the coast lies.

In the “long-wave limit”

$$\partial^2/\partial t^2 \ll f^2, \quad \partial^2/\partial y^2 \ll \partial^2/\partial x^2,$$

the equation is simplified to

$$\frac{P_{xxt}}{f^2} + \left(\frac{P_{zt}}{N^2}\right)_z = 0. \tag{7}$$

With the same long-wave assumption, the boundary conditions are (Clarke and Van Gorder [20]):

$$\text{at } x = b, \quad P_{xt} + \frac{rP_x}{h} + fPy = \frac{f\tau^y}{h} \tag{8}$$

$$\text{at } z = 0, \quad P_z = 0 \text{ (rigid lid), or } P_z + \frac{N^2}{g}P = 0 \text{ (free surface)} \tag{9}$$

$$\text{at } z = -h, \quad \frac{f^2P_{zt}}{N^2} + h_x(P_{xt} + fP_y) + (rP_x)_x - h_x rP_{xz} = 0, \tag{10}$$

$$\text{as } x \rightarrow \infty, \quad P_x \rightarrow 0, \tag{11}$$

where τ^y is the alongshore component of the wind stress, and r is the coefficient of the y -bottom drag in a linear form: $\tau_B^y = \rho_0 r v_B$. Note Eq. (11) is the far field condition; in practice, it may be replaced by another convenient condition ($u_x = 0$ at $x = L$) (see [10]). Eq. (8) is the no-flux condition: $\int_{-h(b)}^0 u dz = 0$.

Eq. (9) is the boundary condition at $z = 0$ for a rigid-lid or a free surface. In this study, we will adopt the rigid-lid assumption, which implies a nondivergent horizontal flow, and effectively filters out the fast external waves. In the YS/ECS case, there have been strong arguments against using it because the number $\Gamma = \frac{(fL)^2}{gH}$, where L is the width of continental shelf and H the typical depth, is not small (e.g., [11, 15, 18]). Here for the purpose of this monograph, we will focus on the climatic variability of the YS CTWs, which are only associated with slow modes. As such, a rigid lid on top of the ocean makes a more convenient configuration. For discussions on the free surface condition, see, e.g., Brink [19].

Motivated by the form of (7), Clarke and Van Gorder [20] introduced a vector

$$\mathbf{M} = \frac{P_x}{f^2} \mathbf{i} + \frac{P_z}{N^2} \mathbf{k}, \tag{12}$$

and the equation is then simply $\nabla \cdot \mathbf{M}_t = 0$.

2.2. Eigenvalue problem

In order to avoid getting into too much technical details, we only consider the frictionless situation: $r = 0$. For free CTWs, $\tau^y = 0$. We seek a wave solution in the form

$$P(x, y, z; t) = F(x, z) \phi(y - ct). \tag{13}$$

Substitution of it back into (7) and the boundary conditions (8)–(11) gives

$$\frac{F_{xx}}{f^2} + \left(\frac{F_z}{N^2}\right)_z = 0, \tag{14}$$

$$\text{at } z = 0, \quad F_z = 0, \tag{15}$$

$$\text{at } x = b, \quad \frac{c}{f} F_x - F = 0, \tag{16}$$

$$\text{at } z = -h(x), \quad c \left(h_x F_x + \frac{f^2}{N^2} F_z \right) - fh_x F = 0, \tag{17}$$

$$\text{as } x \rightarrow \infty, \quad F_x \rightarrow 0. \tag{18}$$

Note the minus signs in the conditions at $x = b$ and $z = -h(x)$; they are positive in Brink [19] and Clarke [8] because a left-hand coordinate system is adopted therein. In terms of the vector \mathbf{M} introduced by Clarke and Van Gorder [20]), the solution form is $\mathbf{M} = \mathbf{B} \phi(y - ct)$, where

$$\mathbf{B} = \frac{F_x}{f^2} \mathbf{i} + \frac{F_z}{N^2} \mathbf{k}. \tag{19}$$

Let the whole domain for the configuration (cf. **Figure 2**) be Ω and denote the boundary that encloses it as $\partial\Omega$. Introduce an inner product space H over Ω . Its inner product $\langle F_m, F_n \rangle_{\mathcal{H}}$ is defined such that, for any $F, G \in H$,

$$\langle F, G_{\mathcal{H}} \rangle = \int_{-h(b)}^0 FG \Big|_{x=b} dz + \int_b^\infty h_x FG \Big|_{z=-h(x)} dx. \tag{20}$$

Considering the vanishing far field condition and the rigid-lid surface condition, this is actually an inner product evaluated at the boundary $\partial\Omega$. This is quite different from the inner product space in the usual sense. It is easy to show that $\langle F_m, F_n \rangle_{\mathcal{H}}$ satisfies the needed axioms.

Let $\{F_m\}$ be a set of the eigenfunctions of (14)–(18). Clearly $F_m \in H$ for all integers m ; they possess the following important property [7, 8]:

Theorem 2.1 $\{F_m\}$ forms an orthogonal set in H ; that is to say, $\langle F_m, F_n \rangle_{\mathcal{H}} = 0$ if $m \neq n$.

PROOF. The orthogonality can be proved in different ways. In Clarke and Van Gorder [20], it is easily obtained through manipulating the identity

$$\nabla \cdot (F_n \mathbf{B}_m - F_m \mathbf{B}_n) = 0,$$

which integrated over Ω must also vanish. By Gauss' theorem,

$$\int_{\partial\Omega} \mathbf{n} \cdot (F_n \mathbf{B}_m - F_m \mathbf{B}_n) ds = 0,$$

where ds is the arc length along $\partial\Omega$. With the boundary conditions taken into account, this becomes

$$\left(\frac{1}{c_n} - \frac{1}{c_m} \right) \left[\int_{x=b} F_m F_n ds + \int_{z=-h(x)} h_x \frac{F_m F_n}{\sqrt{1+h_x^2}} ds \right] = 0.$$

For $m \neq n$, this is

$$\int_{x=b} F_m F_n ds + \int_{z=-h(x)} \frac{h_x}{\sqrt{1+h_x^2}} F_m F_n ds = 0,$$

or

$$\int_{-h(b)}^0 F_m(0, z) F_n(0, z) dz + \int_{x=b}^{\infty} F_m(x, -h(x)) F_n(x, -h(x)) h_x dx = 0. \quad (21)$$

Q.E.D.

This theorem states that the eigenvectors are orthogonal in the inner product space H . They can always be normalized by the induced norm $\|F_m\| = \sqrt{\langle F_m, F_m \rangle_{\mathcal{H}}}$, and then form an orthonormal set. [$\|F_m\|$ is shown to be f ; see Clarke [8]]. Caution should be used, however, in the normalization, which must be made such that energy is conserved as waves propagate through a slowly varying medium [21].

From the orthogonality condition Wang and Mooers [7] connected CTWs to internal Kelvin waves (flat bottom), shelf waves, and topographic Rossby waves ($b = 0$). They also showed that there exists another orthogonality condition over Ω rather than along $\partial\Omega$; that is:

$$\int_b^{\infty} \int_{-h(x)}^0 \left[\left(\frac{\partial F_n}{\partial x} \right) \left(\frac{\partial F_m}{\partial x} \right) + \frac{1}{N^2} \left(\frac{\partial F_n}{\partial z} \right) \left(\frac{\partial F_m}{\partial z} \right) + \ell^2 F_n F_m \right] dx dz = 0,$$

if $c_n \neq c_m$, where ℓ is the wavenumber in y . But whether this satisfies the inner product axioms is yet to be checked.

In addition to orthogonality, it is also possible to prove that $\{F_m\}$ forms a complete set (see Courant and Hilbert, pp. 424–426). That is to say, the normalized $\{F_m\}$ makes a basis of H .

2.3. Excitation of CTWs

By the forgoing argument, $\{F_n\}$ makes a basis of H . Thus, any function of H , P in particular, can be written as a linear combination of F_n , $n = 1, 2, \dots$,

$$P = \sum_{n=1}^{\infty} F_n(x, z)\phi_n(y, t). \tag{22}$$

When a forcing τ^y is applied at the boundary, we can then solve for the amplitudes ϕ_n .

Usually, the amplitude equation can be obtained through taking the inner product of F_n with the governing Eq. (7), or $\nabla \cdot \mathbf{M}_t = 0$. In this particular case, it is not this straightforward because the inner product is evaluated along the boundary $\partial\Omega$, rather than in Ω . Besides multiplying F_n with $\nabla \cdot \mathbf{M}_t$, Clarke and Van Gorder [20] considered a duality $P_t \mathbf{B}_n$. They found that

$$\nabla \cdot (F_n \mathbf{M}_t - P_t \mathbf{B}_n) = 0,$$

which of course vanishes if integrated over Ω . By Gauss' theorem,

$$\oint_{\partial\Omega} \mathbf{n} \cdot (F_n \mathbf{M}_t - P_t \mathbf{B}_n) ds = 0.$$

Expanding and taking into account of the boundary conditions, this is eventually reduced to (see Clarke and Van Gorder [20])

$$\int_{-h(b)}^0 \left[F_n \left(P_y - \frac{P_t}{c_n} \right) \right]_{x=b} dz + \int_{-h(b)}^0 \left(\frac{F_n r P_x}{f h} \right)_{x=b} dz + \int_b^{\infty} \left[F_n \left(P_y - \frac{P_t}{c_n} \right) \right]_{z=-h(x)} dx + \int_b^{\infty} F_n(x, -h) \frac{d}{dx} \left(\frac{r P_x(x, -h(x))}{f} \right) dx = \left(\int_{-h(b)}^0 F_n(b, z) dz \right) \frac{\tau^y(y, t)}{h(b)}.$$

Substitution of (22) for P , and use of the orthogonality property: $\langle F_m, F_n \rangle_{\mathcal{H}} = 0$ if $m \neq n$, yields

$$-\frac{1}{c_n} \frac{\partial \phi_n}{\partial t} + \frac{\partial \phi_n}{\partial y} + \sum_{m=1}^{\infty} a_{mn} \phi_m = b_n \tau^y(y, t),$$

where

$$b_n = \frac{1}{D_n h(b)} \int_{-h(b)}^0 F_n(b, z) dz,$$

$$a_{mn} = \frac{1}{D_n} \left[\int_b^{\infty} F_n(x, -h) \frac{1}{f} \frac{d}{dx} (r F_{mx}(x, -h)) dx + \int_{-h(b)}^0 \left[\frac{F_n r F_{mx}}{f h} \right]_{x=b} dz \right]$$

$$D_n = \langle F_n, F_n \rangle_{\mathcal{H}} = \|F_n\|^2.$$

In the case, only one mode n is excited, there is no coupling: $\sum_1^{\infty} a_{mn} \phi_m = a_{nn} \phi_n$ (e.g., Battisti and Hickey [22]), the amplitude equation can be solved analytically in terms of characteristic coordinates [19].

$$s = t - \int_y^0 c_n^{-1} dy',$$

$$\xi = y.$$

In this case,

$$\phi_n(y, t) = \phi_n \left(0, t - \int_y^0 c_n^{-1} d\xi \right) \cdot e^{-\int_y^0 a_{nn} d\xi} + \int_y^0 b_n(\xi) \tau^y \left(\xi, t - \int_y^\xi c_n^{-1} d\xi' \right) \cdot e^{-\int_y^\xi a_{nn} d\xi'} d\xi,$$

where $y = 0$ signifies the starting point of the calculation. See Brink [19] for details.

Once ϕ is solved, P may be obtained through reconstruction with modes. From (1)–(2), it is easy to obtain $v_{tt} + f^2 v = -\frac{1}{\rho_0} P_{yt} + \frac{f}{\rho_0} P_x$, which in the long-wave limit simply shows the geostrophic balance: $f^2 v = f P_x / \rho_0$. The fields then can be obtained accordingly:

$$\begin{aligned} u &= -\frac{1}{\rho_0 f^2} (P_{xt} + f P_y), \\ v &= \frac{1}{\rho_0 f} P_x, \\ w &= -\frac{P_{zt}}{\rho_0 N^2}, \\ \rho &= -\frac{1}{g} P_z. \end{aligned}$$

3. The CTWs off the Subei Bank in the Yellow Sea

3.1. Background fields

We choose a cross-section outside the Subei Bank as shown in **Figure 1**. It is chosen in the middle since in the north the shelf is too shallow, while in the south the Changjiang diluted water complicates the circulation system very much and hence may disguise the wave propagation. The HYCOM data are used to set up the model; they are advantageous in that tides are excluded in the reanalysis fields. The horizontal resolution is 0.1° in longitude, by 0.0702° in latitude, which results in a horizontal spacing of 12 km along the section. In the vertical direction, the levels are at 0, 2, 4, 6, 8, 10, 12, 15, 20, 25, 30, 35, 40, 45, 50, 60, 70, 80 m, respectively. The data are available for 1993 through 2013. After 2013, the vertical resolution is too coarse for our purpose, and hence they are not considered in this study.

The topography along the section is displayed in **Figure 1b**; it is slightly modified to avoid the bumps (the dashed line). The basic buoyancy frequencies differ year by year. They are calculated from the annual mean density anomaly profiles averaged over along the section. Shown in **Figure 1c** is such an example.

3.2. Eigenvalues and eigenmodes

With the background field, we solve the eigenvalue problem. The solution method is referred to the appendix; it is essentially the same as that by Brink [10], Clarke and Gorder [20], and Wilkin and Chapman [23]. Considering the broad shallow shelf, we artificially set the coastline at the isobath $H = 10$ m. By computation, four typical trapped eigenmodes have been identified. For the year of 2000, the celerities are, in order of magnitude, -0.12 , -0.19 , -0.21 , -0.29 m/s;

the corresponding modes will be henceforth refer to as M1, M2, M3, and M4, respectively. Besides, many slower modes such $c = -0.0046$ m/s have also been found, because the model is too coarsely resolved that we do not consider them here. Similarly, a few higher modes, particularly the one with $c = -0.57$ m/s, are evident. But these higher modes are not trapped to the western topography or coast and hence should be discarded. An observation is that all these celerities are negative; that is to say, all the corresponding waves propagate to the south. This is the very important property of CTW: in the Northern Hemisphere, the wave propagates with the coast on the right hand side.

In order to see whether these eigenvalues indeed exist, we examine the time series at two points $A(122.6^\circ E, 34.825^\circ N)$ and $B(122.9^\circ E, 34.035^\circ N)$ (see **Figure 1**). They are roughly along the isobath $H \approx 64$ m, located ~ 92 km apart. Again, we use the HYCOM reanalysis data to form the time series. Since too many data are missing for the flow field, consider only the density anomaly. The series are from January 01, 1993 through December 31, 2012, with an interval of 1 day.

The dominant modes of the series have periods of 365 and 183 days, respectively; these are the annual and biannual modes (not shown). However, in the weather frequency band, a local peak is also significant. We use the wavelet method to filter out the signal within this band. Choose the series between October 12, 2001 to December 31, 2012 to ensure that they have a length of $4096 = 2^{12}$ steps (a length of power of 2 is required). We use the orthonormalized cubic spline wavelets constructed in Liang and Anderson (2007) to fulfill the filtering. The scale window is chosen to be bounded by periods 2 and 16 days, respectively. This roughly corresponds to the weather frequency band. We then perform a time-delayed correlation analysis with the two band-pass filtered series, written $\rho_A(t)$ and $\rho_B(t)$. Given a delay τ (in days), we then compute the correlation coefficient $\gamma(\tau)$ between $\rho_A(t)$ and $\rho_B(t + \tau)$. (τ should not be too large, in accordance with the weather frequency band requirement.) Suppose that $\gamma(\tau)$ takes its maximum at T , then the phase speed can be estimated to be d/T . Notice that it is not a good idea to compute γ for all the 4096 days, since the CTWs are coastal wind-driven and within the weather frequency band (1 week or 2 weeks or so). Different modes may be excited during different periods. We hence choose to do the correlation analysis every 30 days. The results

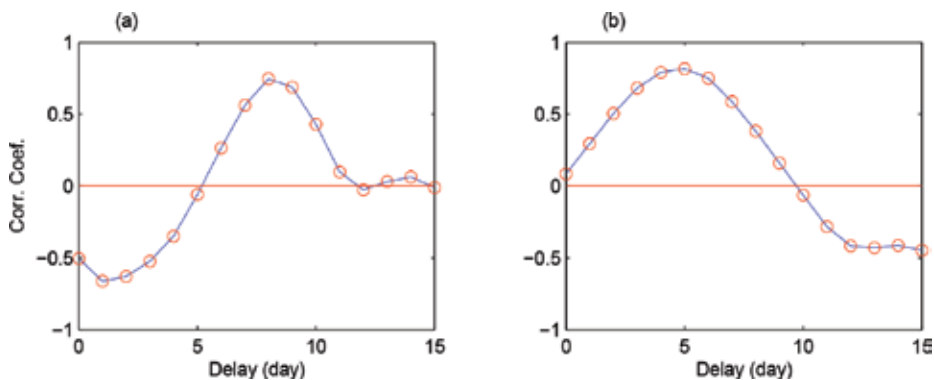


Figure 3. The correlation coefficients between ρ_A and the delayed ρ_B for the periods (a) 12 Aug 2005–2011 Sep 2005 and (b) 04 Feb 2011–2106 Mar 2011. The locations A and B are marked in **Figure 1**.

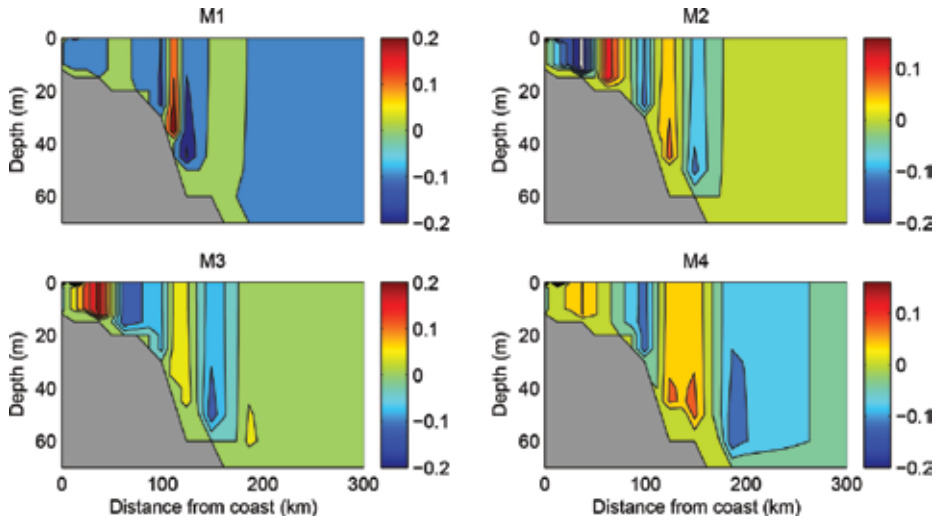


Figure 4. The cross-section structures of the four coastal trapped wave modes M1, M2, M3, and M4, which have celerities of $c = -0.12, -0.19, -0.21, -0.29$ m/s, respectively.

may differ, but the CTW modes consistent with our calculation frequently show up. For example, in **Figure 3a**, the maximum γ takes place at a delay of 8 days for ρ_B , so the modal phase velocity is $92000 / (8 \times 24 \times 3600) = 0.13$ m/s. Similarly, in **Figure 3b**, γ takes its maximum at 5 days, which corresponds to a speed of 0.21 m/s. Considering there may be a slight change in magnitude with time (see below), these celerities agree very well with the celerities of M1 ($c = 0.12$) and M3 ($c = 0.21$) in 2000. We actually find many cases with a speed of 0.53, a high mode that have been discarded, and many other slower modes, which we do not consider here. Note the time resolution (1 day) of the series cannot distinguish M2 and M3.

The eigenmodes corresponding to the four celerities are shown in **Figure 4**. From it we see that, the slower the wave, the more topographically trapped the structure. Particularly, in the first subplot, we see a bottom-trapped mode ($c = -0.12$ m/s).

The modal structures for other years are similar, but the propagating speeds differ. In the next section, we will see more details about this.

4. The change in CTW celerities during the past 20 years

The buoyancy frequency profiles change with time, which will inevitably affect the CTW propagating properties. We have computed the eigenvalues for the six identified modes for all the past 20 years. The results are shown in **Figure 5**.

Interestingly, from the figure, all the identified modes seem to have the same evolutionary trend. On the whole, the computed speeds are all on decline (note the negative sign) during the past 20 years. This might be related to global warming, but what makes it puzzling is that, simply

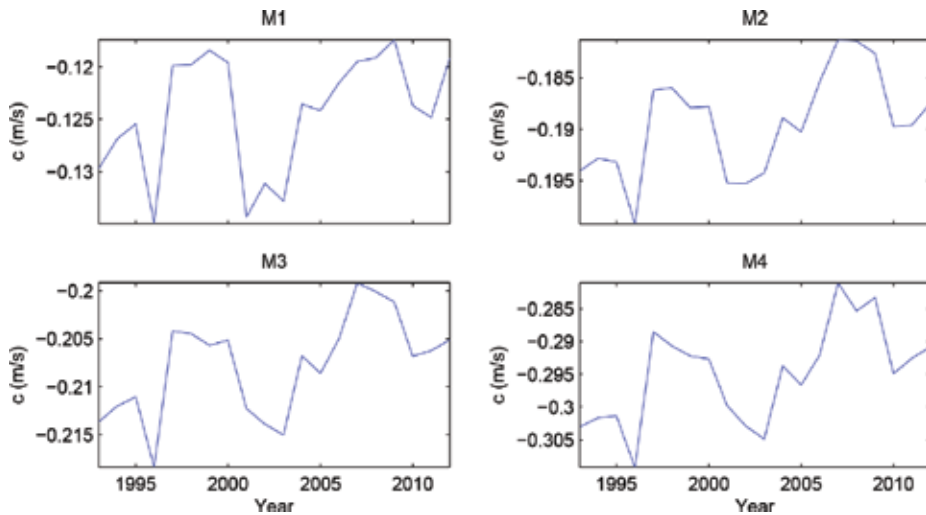


Figure 5. Time variation of the celerities of the four modes M1–M4 as shown in Figure 4.

warming the ocean cannot change the CTW wave propagating; rather, it is the alteration of the vertical stratification that may cause the change. For such a shallow sea, it is still unclear how this can be fulfilled. Even though it is related to global warming, it must be through some third mechanism(s). In the Yellow Sea, a conspicuous hydrographic feature is its cold water mass in summer; maybe that functions to mediate the events—we will explore this in future studies.

Another interesting feature of Figure 5 is the maxima (or minima if magnitude is considered) around 1997 and 2009. This reminds one of El Niño, as around those are the El Niño years; particularly, the 97–98 El Niño is very strong, as shown in Figure 6. However, from the figure one may argue that 02–03 is also a moderately strong El Niño year, while in Figure 5, the c 's reach their respective minima. We hence need to pick more quantity to compare. As shown in Figure 6, the La Niña intensity may be such a candidate. Notice that immediately after the 97–98 El Niño, there is a strong La Niña; same happens after the 09–10 one, while after 2003 no La Niña occurs at all. Therefore, it seems that the CTWs are greatly slowed down when a strong El Niño followed by a strong La Niña occurs.

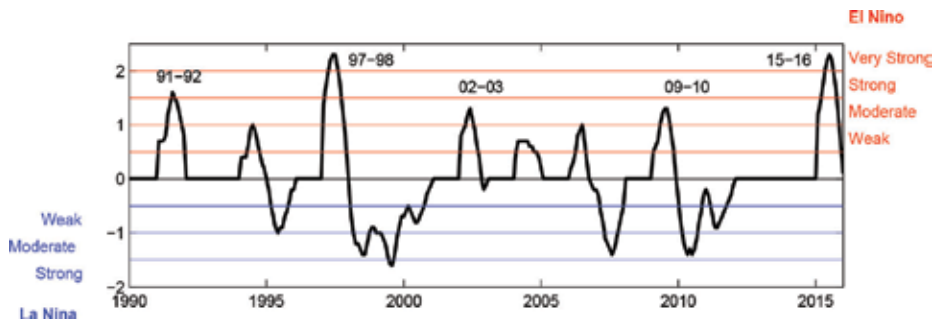


Figure 6. ENSO events and their intensities since 1990. The figure is based on the Oceanic Niño Index; see http://www.cpc.ncep.noaa.gov/products/analysis_monitoring/ensostuff/ensoyears.shtml.

We emphasize that we do not claim that ENSO has caused the slow-down of the CTWs. What we have shown is just a remarkable correlation between the wave property change and the ENSO occurrence—In fact, even correlation may not be an appropriate term here. We should have computed the correlation coefficients between the c 's and some ENSO index, say, the Oceanic Niño Index as shown in **Figure 6**, but the time resolution of the c series are very low; there is only one value per year. We have also tried CTW configurations with monthly mean fields, but the dominating seasonal cycle completely disguises the signal, which just worsens the situation.

5. Concluding remarks

Coastal trapped waves (CTW), which flourished during 60–80s, thanks to the efforts from investigators such as Allen [6], Wang and Mooers [7], Clarke [8], Huthnance [9], Mysak [24], Brink [19], Chapman [25], among many others, play an important role in the processes of coastal and continental oceans (cf. [10]). However, this important topic seems to be missing in the heated debate in recent years on coastal environmental change and protection. In this chapter, we have given a brief but self-contained introduction of the CTW theory, in the hope of gaining renewed interest in this field. The nice properties such as the mutual orthogonality between the eigenmodes make this class of waves not just important in practice, but also theoretically appealing. For reference, a numerical scheme is supplied in the appendix to solve the resulting eigenvalue problem.

As a demonstration, we have conducted a preliminary study of the CTWs for a section across Subei Bank in the Yellow Sea, a region where traditionally the role of CTWs has been overlooked due to its shallow depth. Considering the scope of this monograph, we have particularly focused on the slow wave modes and their variabilities during the past decades. Interestingly, all the identified prominent modes, including a bottom-intensified one, seem to be slowing down during the past 20 years. Particularly, it seems that they are greatly slowed down during the events when a strong El Niño is followed by a strong La Niña, such as the 97–98 and 09–10 El Niño events.

However, caution should be used in interpreting these results. Apart from the poor time resolution (one value per year), the obtained c -series are not long enough for climate variability studies. It would be better if the data can be extended so that decadal variability can be examined; particularly one would like to see how they behave during the two super El Niño years: 1982–1983 and 2015–2016 (currently data are not available). We will investigate this in future studies.

Acknowledgements

Section 2 and Appendix are extracted from an unpublished technique report (Liang [26]) by the author in the former Harvard Ocean Group, which was prepared for the project AOSN-II then (cf. [27]). Thanks are due to Kenneth Brink for the help in drafting that report. The HYCOM group is acknowledged for providing the reanalysis data. Yineng Rong prepared the

background field of the cross-section and the point series for analysis and drew **Figure 1**. This study was partially supported by the 2015 Jiangsu Program for Innovation Research and Entrepreneurship Groups, by the National Program on Global Change and Air-Sea Interaction (GASI-IPOVAI-06), and the National Science Foundation of China under Grant 41,276,032 [28–30].

A. A numerical solver for coastal-trapped waves

The x - z domain is discretized into a mesh grid, as sketched in **Figure 2**. The spacings Δx and Δz may vary with the respective indices j and k . We use j , instead of i , to indicate the x index,

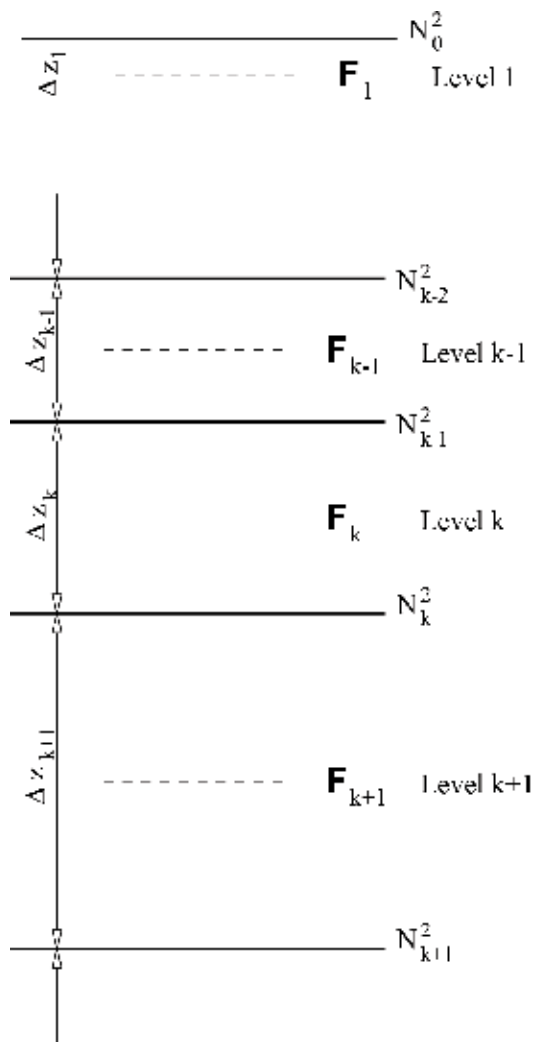


Figure 7. Discretization in the z direction.

in order not to confuse with the complex number $\sqrt{-1}$. In the grid, the eigenfunction F is defined at integer points k , while the buoyancy frequency N^2 is at half integer points (Figure 7).

For j , let j_b and j_m be the boundary limits, which correspond to $x = b$ and $x = L$ (L some large number). Note for each horizontal level k , the limits for j should be $j_{cst}(k)$ and j_m , with j_{cst} dependent on k . Similarly denote the bottom index as k_m , then k runs from 1 to k_m , and the rigid-lid and bottom correspond to $k = \frac{1}{2}$ and $k = k_m + \frac{1}{2}$, respectively. The limit $k_m = k_m(j)$ is a function j , which is determined by the function $h(x)$.

Let

$$\delta(x) = \begin{cases} 1, & x = 0; \\ 0, & x \neq 0, \end{cases}$$

and

$$\begin{aligned} \delta^{sea} &\equiv \delta(j - j_\infty); & c^{sea} &\equiv 1 - \delta^{sea} \\ \delta^{cst} &\equiv \delta(j - j_{cst}(k)); & c^{cst} &\equiv 1 - \delta^{cst} \\ \delta^{top} &\equiv \delta(k - 1); & c^{top} &\equiv 1 - \delta^{top} \\ \delta^{bot} &\equiv \delta(k - k_m(j)); & c^{bot} &\equiv 1 - \delta^{bot}. \end{aligned}$$

Further define

$$\begin{aligned} \Delta_x^+ &\equiv \frac{\Delta x_{j+1} + \Delta x_j}{2}, & \Delta_z^+ &\equiv \frac{\Delta z_{k+1} + \Delta z_k}{2}, \\ \Delta_x^- &\equiv \frac{\Delta x_{j-1} + \Delta x_j}{2}, & \Delta_z^- &\equiv \frac{\Delta z_{k-1} + \Delta z_k}{2}, \\ \gamma_x^+ &\equiv \frac{\Delta x_j - \Delta x_{j+1}}{2(\Delta_x^+ + \Delta_x^-)}, & \gamma_z^+ &\equiv \frac{\Delta z_k - \Delta z_{k+1}}{2(\Delta_z^+ + \Delta_z^-)}, \\ \gamma_x^- &\equiv \frac{\Delta x_{j-1} - \Delta x_j}{2(\Delta_x^+ + \Delta_x^-)}, & \gamma_z^- &\equiv \frac{\Delta z_{k-1} - \Delta z_k}{2(\Delta_z^+ + \Delta_z^-)}. \end{aligned}$$

Then

$$\begin{aligned} \frac{\partial^2 F}{\partial x^2} = & \frac{1}{\Delta x_j} \cdot \left\{ c^{sea} \cdot \left[\frac{F_{j+1,k} - F_{j,k}}{\Delta_x^+} + \gamma_x^+ c^{cst} \left(\frac{F_{j+1,k} - F_{j,k}}{\Delta_x^+} - \frac{F_{j,k} - F_{j-1,k}}{\Delta_x^-} \right) \right] + \delta^{sea} \cdot \left(\frac{\partial F}{\partial x} \right) \Big|_{(\infty,k)} \right. \\ & \left. - c^{cst} \cdot \left[\frac{F_{j,k} - F_{j-1,k}}{\Delta_x^-} + \gamma_x^- c^{sea} \left(\frac{F_{j+1,k} - F_{j,k}}{\Delta_x^+} - \frac{F_{j,k} - F_{j-1,k}}{\Delta_x^-} \right) \right] - \delta^{cst} \cdot \left(\frac{\partial F}{\partial x} \right) \Big|_{(j_{cst}(k),k)} \right\}, \end{aligned}$$

and

$$\begin{aligned}
 f^2 \left(\frac{F_z}{N^2} \right)_z &= \frac{f^2}{\Delta z_k} \cdot \left\{ \frac{c^{top}}{N_{k-1/2}^2} \cdot \left[\frac{F_{j,k-1} - F_{j,k}}{\Delta_z^-} + \gamma_z^- c^{bot} \left(\frac{F_{j,k-1} - F_{j,k}}{\Delta_z^-} - \frac{F_{j,k} - F_{j,k+1}}{\Delta_z^+} \right) \right] \right. \\
 &+ \frac{\delta^{top}}{N_{k-1/2}^2} \cdot \left(\frac{\partial F}{\partial z} \right) \Big|_{(j,1)} - \frac{c^{bot}}{N_{k+1/2}^2} \cdot \left[\frac{F_{j,k} - F_{j,k+1}}{\Delta_z^+} + \gamma_z^+ c^{top} \left(\frac{F_{j,k-1} - F_{j,k}}{\Delta_z^-} - \frac{F_{j,k} - F_{j,k+1}}{\Delta_z^+} \right) \right] \\
 &\left. \times \frac{\delta^{bot}}{N_{k+1/2}^2} \cdot \left(\frac{\partial F}{\partial z} \right) \Big|_{(j,k_m(j))} \right\},
 \end{aligned}$$

where the boundary conditions are

$$\begin{aligned}
 \left(\frac{\partial F}{\partial x} \right) \Big|_{(\infty,k)} &= 0, \\
 \left(\frac{\partial F}{\partial x} \right) \Big|_{(j_{cst}(k),k)} &= \frac{f}{c} F_{j_{cst}(k),k}, \\
 \left(\frac{\partial F}{\partial z} \right) \Big|_{(j,1)} &= 0, \\
 \left(\frac{\partial F}{\partial z} \right) \Big|_{(j,k_m(j))} &= 0.
 \end{aligned}$$

Remarks

- Note here the bottom boundary condition is no longer

$$c \left(h_x F_x + \frac{f^2}{N^2} F_z \right) - f h_x F = 0, \quad \text{at } z = -h(x) \quad (23)$$

as shown before. Because we adopt a staircase-like topography in our discretized domain, (23) is replaced by a horizontal wall condition and a flat-bottom condition.

- In the equation, γ_x^+ , γ_x^- , γ_z^+ , and γ_z^- have been multiplied respectively by c^{cst} , c^{sea} , c^{bot} , and c^{top} to handle those points near the boundary. In this case, the discretization at these points have only precision of order 1 if the mesh is not uniform.

With the above F_{xx} and F_{zz} , the governing equation

$$\frac{F_{xx}}{f^2} + \left(\frac{F_z}{N^2} \right)_z = 0$$

is discretized. Collect the coefficients of $F_{j-1,k}$, $F_{j,k-1}$, $F_{j,k}$, $F_{j,k+1}$, and $F_{j+1,k}$, as correspond to the points 1, 2, 3, 4, and 5 in **Figure 2**. They are:

$$F_{j-1,k} : \frac{1}{\Delta x_j} \frac{1}{\Delta x} \left\{ \gamma_x^+ c^{cst} c^{sea} - c^{cst} (-1 + \gamma_x^- c^{sea}) \right\} \equiv a_1(j,k), \quad (24)$$

$$F_{j,k-1} : \frac{f_0^2}{\Delta z_k} \frac{1}{\Delta z} \left\{ \frac{c^{top}}{N_{k-1/2}^2} (1 + \gamma_z^- c^{bot}) - \frac{c^{bot}}{N_{k+1/2}^2} \gamma_z^+ c^{top} \right\} \equiv a_2(j,k), \quad (25)$$

$$F_{j,k+1} : \frac{f_0^2}{\Delta z_k} \frac{1}{\Delta_z^+} \left\{ \frac{c^{top}}{N_{k-1/2}^2} \gamma_z^- c^{bot} - \frac{c^{bot}}{N_{k+1/2}^2} (-1 + \gamma_z^+ c^{top}) \right\} \equiv a_4(j, k), \quad (26)$$

$$F_{j+1,k} : \frac{1}{\Delta x_j} \frac{1}{\Delta_x^+} \{ c^{sea} (1 + \gamma_x^+ c^{cst}) - \gamma_x^- c^{cst} c^{sea} \} \equiv a_5(j, k), \quad (27)$$

$$F_{j,k} : a_3 - \eta_{j,k} \cdot \frac{1}{c}, \quad (28)$$

where

$$\begin{aligned} a_3(j, k) = & \frac{1}{\Delta x_j} \left\{ c^{sea} \cdot \left[-\frac{1}{\Delta_x^+} + \gamma_x^+ c^{cst} \left(-\frac{1}{\Delta_x^+} - \frac{1}{\Delta_x^-} \right) \right] \right. \\ & \left. - c^{cst} \cdot \left[\frac{1}{\Delta_x^-} + \gamma_x^- c^{sea} \left(-\frac{1}{\Delta_x^+} - \frac{1}{\Delta_x^-} \right) \right] \right\} \\ & + \frac{f^2}{\Delta z_k} \left\{ \frac{c^{top}}{N_{k-1/2}^2} \cdot \left[\frac{1}{\Delta_z^-} + \gamma_z^- c^{bot} \left(-\frac{1}{\Delta_z^-} - \frac{1}{\Delta_z^+} \right) \right] \right. \\ & \left. - \frac{c^{bot}}{N_{k+1/2}^2} \cdot \left[\frac{1}{\Delta_z^+} + \gamma_z^+ c^{top} \left(-\frac{1}{\Delta_z^-} - \frac{1}{\Delta_z^+} \right) \right] \right\}, \end{aligned}$$

and

$$\eta_{j,k} = \frac{1}{\Delta x_j} \delta^{cst} f. \quad (29)$$

We would like to make (24)–(28) into a matrix with eigen value $\frac{1}{c}$. But here the problem is unusual, since $\frac{1}{c}$ take values only on boundaries [see the η in (28)], reflecting the fact that the inner product is defined along boundaries. To make it valid throughout the domain, let ε be some small number reflecting the machine precision, say, 10^{-7} , and define a new η such that

$$\eta_{j,k} = \varepsilon \cdot \max_{l=1}^5 \{ |a_l| \} \quad \text{if } \eta_{j,k} = 0.$$

Now, the equation with the new η should be the same as the old one up to the machine precision. Write

$$\tilde{a}_l = \frac{a_l}{\eta}, \quad l = 1, 2, \dots, 5. \quad (30)$$

The discretized equation is then

$$\tilde{a}_5 F_{j+1,k} + \tilde{a}_4 F_{j,k+1} + \left(\tilde{a}_3 - \frac{1}{c} \right) F_{j,k} + \tilde{a}_2 F_{j,k-1} + \tilde{a}_1 F_{j-1,k} = 0. \quad (31)$$

And the whole problem is now translated into finding the eigenvalue $\frac{1}{c}$ for a pentadiagonal matrix A , with entries along the five diagonal being \tilde{a}_i , $i = 1, 2, 3, 4, 5$.

Author details

X. San Liang

Address all correspondence to: x.san.liang@gmail.com

Center for Ocean-Atmosphere Dynamical Studies, Nanjing Institute of Meteorology, Nanjing, P. R. China

References

- [1] Huthnance JM. Circulation, exchange and water masses at the ocean margin: The role of physical processes at the shelf edge. *Progress in Oceanography*. 1995;**35**:353-431
- [2] Hamon BV. The spectra of mean sea level at Sydney Coff's harbour and Lord Howe Island. *Journal of Geophysical Research*. 1962;**67**:5147-5155
- [3] Robinson AR. Continental shelf waves and the response of sea level to weather systems. *Journal of Geophysical Research*. 1964;**69**:367-368
- [4] Mysak LA. On the theory of continental shelf waves. *Journal of Marine Research*. 1967;**25**: 205-227
- [5] Brink KH. The coastal Robinson. *Dynamics of Atmospheres and Oceans*. 2011;**52**(1-2):4
- [6] Allen JS. Coastal trapped waves in a stratified ocean. *Journal of Physical Oceanography*. 1975;**5**:300-325
- [7] Wang D-P, Mooers CNK. Coastal-trapped waves in a continuously stratified ocean. *Journal of Physical Oceanography*. 1976;**6**:853-863
- [8] Clarke AJ. Observational and numerical evidence for wind-forced coastal trapped long waves. *Journal of Physical Oceanography*. 1977;**7**:231-247
- [9] Huthnance JM. On coastal trapped waves: Analysis and numerical calculation by inverse iteration. *Journal of Physical Oceanography*. 1978;**8**:74-92
- [10] Chapman DC. Application of wind-forced, long, coastal-trapped wave theory along the California coast. *Journal of Geophysical Research*. 1987;**92**:1798-1816

- [11] Yin L, Qiao F, Zheng Q. Coastal-trapped waves in the East China Sea observed by a mooring array in winter 2006. *Journal of Physical Oceanography*. 2014;**44**:576-590
- [12] Feng S. A model of dissipative trapped-waves on a uniformly sloping shelf of finite width (in Chinese). *Chinese Journal of Oceanology and Limnology*. 1981;**12**:1-8
- [13] Liu Q, Qin Z. Instability of barotropic coastal trapped waves (in Chinese). *Chinese Journal of Oceanology and Limnology*. 1990;**21**:301-310
- [14] Kong X, Yin X, Li F. Continental shelf waves in the East China Sea and its impact to Kuroshio (in Chinese). *Acta Oceanologica Sinica*. 1992;**14**:8-14
- [15] Chen D, Su J. Continental shelf waves study along China coast (in Chinese). *Acta Oceanologica Sinica*. 1987;**9**:1-15
- [16] Zheng Q, Zhu B, Li J, Sun Z, Xu Y, Hu J. Growth and dissipation of typhoon-forced solitary continental shelf waves in the northern South China Sea. *Climate Dynamics*. 2014;**45**:853-865
- [17] Wang J, Yuan Y, Pan Z. Numerical studies and analysis about continental shelf waves (in Chinese). *Acta Oceanologica Sinica*. 1988;**10**:666-677
- [18] Hsueh Y, Pang I-C. Coastally trapped long waves in the Yellow Sea. *Journal of Physical Oceanography*. 1989;**19**:612-625
- [19] Brink KH. A comparison of long coastal trapped wave theory with observations off Peru. *Journal of Physical Oceanography*. 1982;**12**:897-913
- [20] Clarke A, van Gorder S. A method for estimating wind-driven frictional, time-dependent, and stratified shelf and slope water flow. *Journal of Physical Oceanography*. 1986;**16**:1013-1028
- [21] Brink. Coastal-trapped waves and wind-driven currents over the continental shelf. *Annual Review of Fluid Mechanics*. 1991;**23**:389-412
- [22] Battisiti DS, Hickey BM. Application of remote wind-forced coastal trapped wave theory to the Oregon and Washington coasts. *Journal of Physical Oceanography*. 1984;**14**:887-903
- [23] Wilkin JL, Chapman DC. Scattering of continental shelf waves at a discontinuity in shelf width. *Journal of Physical Oceanography*. 1987;**17**:713-724
- [24] Mysak LA. Recent advances in shelf wave dynamics. *Reviews of Geophysics*. 1980;**18**:211-241
- [25] Clarke AJ, Brink KH. The response of stratified, frictional flow of shelf and slope waters to fluctuating large-scale low-frequency wind forcing. *Journal of Physical Oceanography*. 1985;**15**:439-453
- [26] Liang XS, Anderson DGM. Multiscale window transform. *SIAM Journal of Multiscale Modeling and Simulation*. 2007;**6**:437-467
- [27] Liang XS, Robinson AR. Multiscale processes and nonlinear dynamics of the circulation and upwelling events off Monterey Bay. *Journal of Physical Oceanography*. 2009;**39**:290-313

- [28] Brink KH. Energy conservation in coastal-trapped wave calculations. *Journal of Physical Oceanography*. 1989;**19**:1011-1016
- [29] Chapman DC, Lentz SJ, Brink KH. A comparison of empirical and dynamical hindcasts of low-frequency, wind-driven motions over a continental shelf. *Journal of Geophysical Research*. 1988;**93**:12409-12422
- [30] Liang XS. A Solver for Coastal-Trapped Waves. Cambridge, MA: Technical Report, Harvard Ocean Group, Harvard University; 2004. p. 14

Meteorology and Atmospheric Physics (Precipitation, Soil Moisture, Typhoon)

Analysis for Soil Moisture in Jiangsu Province, China, Using GLDAS Data

Jingze Cai, Yuanzhi Zhang, Yu Li, Tingchen Jiang,
X. San Liang, Xia Lu and Jin Yeu Tsou

Additional information is available at the end of the chapter

<http://dx.doi.org/10.5772/intechopen.80736>

Abstract

In this chapter, we present the analysis for the evolution characteristics of temperature, precipitation, and soil moisture. We choose a newly developed method that is based on the information flow (IF) concept to research the causality between annual mean temperature, precipitation, and soil moisture in Jiangsu province, China, from 1961 to 2011 by using the Global Land Data Assimilation System (GLDAS). The correlation and the causality of air temperature and precipitation on soil moisture were compared and discussed. The causality value of 0–10 cm layer is significantly different from zero, while the deeper, in comparison to the surface layer, is negligible. This result unambiguously shows the causality in the sense that the precipitation increase and the temperature decrease are causing the shallow soil moisture to increase. Temperature and all layers of soil moisture have a negative correlation, but precipitation inverses. Precipitation strongly has the greatest effects on soil moisture in the surface layer, though the rest layers are not obvious.

Keywords: soil moisture, GLDAS, evolution, information flow, Jiangsu province

1. Introduction

Nowadays, the global temperature is warming, so the weather changes became a hot topic today. Soil moisture plays a very key role in the process of climate evolution. It not only carries the responsibilities of energy and water exchange between land and atmosphere, but also takes part in charge of land-atmosphere interaction. Soil moisture and climate changes are connected, soil albedo, soil heat capacity, the transfer of heat into the atmosphere, and so on are affected by the change of soil moisture and thus indirectly affect climate change, but

climate change will also re-act on the soil, and change its moisture content. For example, the heat capacity of the soil is small but the surface albedo is large, the transfer of heat into the atmosphere is not obvious in the area of small soil moisture; in different soil moisture area, the form of interaction is not the same [1, 2]. Because of the deep soil vertical direction, for the precipitation, soil moisture lags about 1–2 months. So, climate change is also restricted because of the soil moisture in the future [3]. In the same area, the evolution of soil moisture is mainly affected by the properties of soil, the strength of the light, the moisture of the air, the size of the wind speed, and so on. Particularly, the evolution of soil moisture is easy to be affected by temperature and precipitation [4]. Since the soil moisture plays a critical impact on the evolution of climate, soil moisture becomes the first consideration [5–8].

Affected by the length of the observation data and the influence of the area, the research of the climate evolution of the soil moisture in the area and the length of time is still very limited [4]. The numerical simulation is mature, and the study area and time scale are expanded. However, the correctness of numerical simulation is dependent on correct initial conditions [9]. Global Land Data Assimilation System (GLDAS) in order to overcome the scale difficulties and built up a global high-resolution land surface assimilation system, compared with other simulation products, GLDAS-driven data are more accurate and the simulation results are more reasonable. Currently, GLDAS supports a lot of research work with its unique advantages [10].

Currently, the applicability of GLDAS products has yet to be verified by the measured data [11, 12], but its distinct characteristics make many different works to be solved [13–15]. Some scholars reported that soil moisture change is active in the eastern China, the land-atmosphere interaction is very active, and the climate change is affected by the soil moisture greatly [16]. Coupled experiments have found strong coupling regions of soil moisture and precipitation: soil moisture in these regions is highly sensitive to precipitation [16]. Adding the soil moisture data assimilation not only improves the spatial distribution of rainfall and temperature in eastern China, but also makes the earth's surface temperature and rainfall simulation value be close to the observations [17]. Based on the observed data of soil moisture, some scholars studied the vertical evolution characteristics of soil moisture, and the relationship with precipitation [18], and the other scholars studied the relationship between soil moisture and climatic variation [19].

In this chapter, we used the data of GLDAS to analyze the evolution characteristics of soil moisture, focusing on the evolution characteristics of soil moisture and assessing the effects and differences between temperature and precipitation in different seasons from 1961 to 2011 in Jiangsu province, China. As soil moisture is an important reference of climate change, the evaluation of dry and wet climate conditions is significant not only to meteorology, but also to the natural environment, farming cultivation, and so on.

2. Materials and methods

The study area is located in the central part of China's east coast, the lower reaches of the Yangtze River and the Huaie River in Jiangsu province, China (30–35°N and 116–121°E). The east of Jiangsu is Yellow Sea. The annual runoff is between 150 and 400 mm in Jiangsu province, while there is more precipitation in the south than in the north. The average temperature was

between 12 and 16°C in Jiangsu province, China, rising from northeast to southwest. Jiangsu belongs to the transitional climate of the temperate zone to the subtropics, with mild climate, moderate rainfall, four distinct seasons. The Huaihe River and irrigation canal in north Jiangsu are considered as the boundary, always belongs to the humid warm temperate zone, north subhumid monsoon climate, the south of a subtropical humid monsoon climate.

GLDAS currently offers two versions of the dataset, namely GLDAS-1 and GLDAS-2; the former version provides CLM, Noah, MOS and 1 × 1° resolution land surface air pressure, air temperature, wind speed, rainfall, evaporation rate, snow rate, and soil moisture data since 1979 generated by VIC model as well as the resolution of the global 0.25 × 0.25° datasets since 2000 generated by Noah model [20]; GLDAS-2 provides datasets from 1948 to 2010 generated by Noah, in which resolution is 0.25 × 0.25° and 1 × 1° [21]. The time resolution of GLDAS-1 and GLDAS-2 both producing meteorological elements is 3 h, which is the basis for composing monthly scale data. In this chapter, we choose four layers' soil moisture data from GLDAS-2.0 and observed data of temperature and precipitation. The flow chart is shown in **Figure 1**.

In the chapter, we use information flow (IF) and Mann-Kendall test to investigate the change in soil moisture.

We choose a newly proven mathematical method [22–24], which is able to evaluate variable causal relation between time series, to distinguish quantitatively the causality between the driving and feedback factor. This new mathematical method is based on the information flow. The new formula is inferred from first principles, rather than an empirical formula, so the property of causality is guaranteed. It also clearly shows the differences between correlation and causality. In the linear limit, the maximum likelihood estimator of the causality from X2 to X1, (units: nats per unit time) is:

$$T_{2-1} = \frac{C_{11}C_{12}C_{2,d1} - c_{12}^2C_{1,d1}}{c_{11}^2c_{22} - c_{11}c_{12}^2} \quad (1)$$

where C_{ij} is the sample covariance between X_i and X_j ($i, j = 1, 2$), and $C_{i,dj}$ is the covariance between X_i and $[X_j(t + k\Delta t) - X_j(t)]/(k\Delta t)$, with Δt being the time step and $k \geq 1$ some integer. Ideally, when $T_2 \rightarrow 1$ is nonzero, then X_2 is causal to X_1 and vice versa. In practice, it usually cannot be precisely zero, and a statistical significance test should be performed [22]; in the present study, the computed causality is significant at the 95% level. A corollary of the above formula is that causation implies correlation, but correlation does not imply causation. For

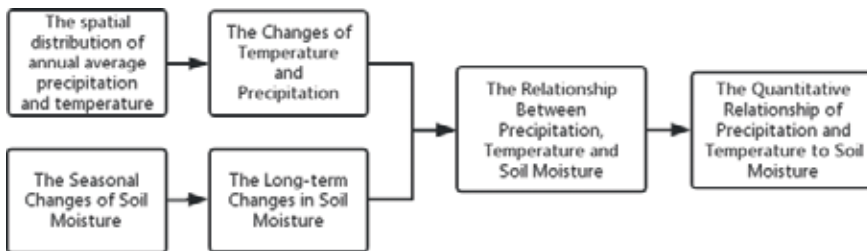


Figure 1. The flow chart of the analysis for the evolution characteristics of temperature, precipitation, and soil moisture in Jiangsu province.

details about the derivation and applications (in climate science and financial economics), see Liang [23–25] among others.

Mann-Kendall (MK) method is a nonparametric statistical test method. Nonparametric test method is also called distribution test, which not only do not need a sample to follow a certain distribution, but also is not affected by the interference of a few outliers [26–27].

The formula is expressed as:

$$Z_c = \begin{cases} \frac{S-1}{\sqrt{\text{var}(S)}}, & S > 0 \\ 0, & S = 0 \\ \frac{S+1}{\sqrt{\text{var}(S)}}, & S < 0 \end{cases} \quad (2)$$

If the Z_c value is greater than zero, this means an increasing trend, the reverse is the tendency to decrease.

$$S = \sum_{i=1}^{n-1} \sum_{k=i+1}^n \text{sgn}(x_k - x_i) \quad (3)$$

where x_k and x_i are the annual values in years k and i , and $k > i$, respectively.

$$\text{sgn}(\theta) = \begin{cases} 1, & \theta > 0 \\ 0, & \theta = 0 \\ -1, & \theta < 0 \end{cases} \quad (4)$$

$$\text{var}[S] = \left[n(n-1)(2n+5) - \sum_t t(t-1)(2t+5) \right] / 18 \quad (5)$$

in which t_i denotes the number of ties to extent i . The summation term in the numerator is used only if the data series contains tied values.

$$\beta = \text{Median} \left(\frac{x_i - x_j}{i - j} \right), \quad \forall j < i \quad (6)$$

$1 < j < i < n$, beta denotes slope; if beta is greater than zero, this represents rise, the reverse is decrease, the numerical value indicates the significance of the trend.

3. Results and discussion

3.1. Characteristics of climate change in Jiangsu province, China

3.1.1. The changes of temperature and precipitation

The Jiangsu province area roughly tends to warming and dry from 1961 to 2011, as shown in **Table 1**. Analyzing the observation data of rainfall and temperature evolution trend in Jiangsu

area, we can know that temperature in Jiangsu is warming, because of the large trend coefficient and passing the confidence level of 99%, while the precipitation presents the decreasing trend, in which trend coefficient is small, and fails to pass the confidence test. These results show that in recent years, Jiangsu province became warming and slightly drier.

The annual average precipitation in the south of the Yangtze river is more than in north of the Yangtze river, the value gets 10.8%. During 1961–2011, the precipitation in the south of the Yangtze river is increasing but in the north of the Yangtze river is not exactly the same. From 1985 to 1995, precipitation is reduced in the south of the Yangtze river. From microcosmic view, increase or decrease amplitude is significant in the south of the Yangtze river. The precipitation is relatively stable in the north of the Yangtze river. Interannual variability is quite different from 1971 to 2000 but gradually close in recent years.

From the perspective of the interannual relationship of extremely warm days, the threshold below (above) some station in Jiangsu has an extreme low temperature (high temperature) day, then counting extreme low temperature (high temperature) days from year to year. According to the statistical results, increasing amplitude of warm day is less than the decreasing amplitude of cold day; increasing amplitude of warm night is less than the decreasing amplitude of cold night. The phenomenon of warm days and warm nights is obvious. Overall, under the background of global warming, temperature is increasing in Jiangsu province and extreme low temperature events are reducing, but extreme high temperature events are rising.

The annual average precipitation in the south of the Yangtze river is more than in north of the Yangtze river, the value gets 10.8%. During 1961–2011, the precipitation in the south of the Yangtze river is increasing but in the north of the Yangtze river is not exactly the same. From 1985 to 1995, precipitation is reduced in the south of the Yangtze river. In general, the trends are the same. From microcosmic view, amplitude is significant in the south of the Yangtze river with significant increase or decrease. The precipitation is relatively stable in the north of the Yangtze river. Interannual variability is quite different from 1971 to 2000 but gradually close in recent years.

3.1.2. The long-term changes in soil moisture

Characteristics of the soil moisture anomaly in Jiangsu are consistent; the biggest soil moisture change rate is located in Jiangsu, which means Jiangsu is a soil moisture-sensitive area. This area is located in China’s north and south climate transition zone, the climate change rate is large, land-atmosphere interaction is very active, so soil moisture anomalies are relatively prominent. Shallow soil moisture in Jiangsu has obvious interannual variability features and

Category	Value Z_c	Slope
Precipitation	-1.01	-0.03
Temperature	5.48***	0.03

Note: *** represents passed 99% significance testing.

Table 1. Mann-Kendall test of temperature and precipitation change trends.

unobvious trend to dry, but there is an obvious trend to dry in the deep soil moisture since 1988. Although the interannual features of deep and shallow soil moisture have some differences in individual years, such as deep and shallow soil moisture anomalies are a reverse phase in 1989. Soil moisture in Jiangsu does not have an obvious trend for a long time, soil moisture has a 2–4 years cycle change before 1985, but the later cycle change is 6–8 years.

3.2. The relationship between precipitation, temperature, and soil moisture

Soil moisture plays a leading role on seasonal time scale of land-atmosphere interaction, partial wet soil can lead to more precipitation. The soil moisture as an important physical parameter of land surface process accumulates the surface hydrological processes, which is also the main process of solid earth, material life, biochemistry cycle, and so on. Through affecting the surface albedo, heat capacity, land surface vegetation growth status, sensible heat flux, latent heat flux, radiation flux and momentum flux, soil moisture can cause climate change.

Temperature and precipitation are key factors that result in the change of soil moisture, precipitation change is the main factor that affects soil moisture change, but the rise of the temperature will result in higher vapor pressure and evaporation, which increases evapotranspiration and decreases soil moisture. Using the theory of information flow in the time series of precipitation, temperature, and soil moisture in Jiangsu province found that there is a positive correlation between soil moisture and precipitation, and a negative correlation between soil moisture and temperature, but in different depth layer, the relationship is significant difference. However, previous researches about the impact of precipitation and temperature to soil moisture are mostly using the observation data in the local scale and short time scale, and just using simple mathematical correlation analysis. Under the background of global soil moisture significant changes, it is necessary to analyze long-term change trend of the impact of temperature and precipitation to soil moisture by using quantitative analysis. Therefore, the theory of information flow is used in this chapter to analyze the relationship between temperature, precipitation, and soil moisture, which can deepen our understanding of soil moisture change in the long time series and the mechanisms between temperature, precipitation, and soil moisture, take effective ways to inhibit the deterioration of soil moisture, improve soil condition, reasonably utilize climate resources, adjust the agricultural ecological layout, and provide a scientific reference actively respond to climate change.

Comparing the correlation and causality between temperature, precipitation, and soil moisture in Jiangsu province, it is obvious that every layer of soil moisture and precipitation has a positive correlation but temperature has negative correlation. The correlation between increasing precipitation or rising temperature and changing soil moisture alone is not necessarily to prove that the changing soil moisture is caused by the increasing precipitation or rising temperature. So we use information flow (IF) to analyze the precipitation, temperature, and soil moisture covering the period from 1961 to 2011 (51 years). We calculate the information flow (IF) in nat (natural unit of information) per unit time [nat/ut] from the 51 annual time series of precipitation and temperature to soil moisture.

The correlation of precipitation and soil moisture shows a declining with the rising of soil depth from 0.563 in the surface layer to 0.242 in the 100–200 cm layer. This result unambiguously shows precipitation has the greatest effects in the surface layer, though the rest layers are not obvious. The main reason of these results is that water in 0–10 cm layer comes from atmosphere, whereas the water in deep layer is from hydrosphere, like osmosis. Each soil (0–10 cm, 10–40 cm, 40–100 cm, and 100–200 cm), the correlation coefficient of soil moisture and temperature is 0.112, 0.458, 0.433, and 0.591, respectively. This shows that, in addition to 0–10 cm layer, the rest layers' temperature has a larger impact the deeper the soil layer.

We calculate the information flow (IF) in nat (natural unit of information) per unit time (nat/ut) from the 51 years' annual time series of temperature and precipitation to soil moisture. The values in **Tables 2** and **3** clearly confirm that the temperature, precipitation, and soil moisture have a causal relationship. Specifically, the variation of precipitation and temperature is the main driver of the 0–10 cm soil. Obviously, the value of 0–10 cm layer is significantly different from zero, while the deeper, in comparison to the 0–10 cm layer, is negligible. This result unambiguously shows the causality in the sense that the precipitation increase and the temperature decrease are causing the 0–10 cm soil moisture increase significantly. Jiangsu is located in the subtropical and warm temperate transition zone with mild climate, four distinct seasons, significant monsoon and other typical climate characteristics. **Table 4** indicates that when the temperature stabilizes more than 10°C, the correlation is positive with soil moisture in each layer and the temperature stabilizes less than 10°C, the correlation is negative. When the temperature stabilizes between 22 and 10°C, the temperature and precipitation with soil moisture in each layer has a strong correlation, and when the temperature stabilizes more than 22°C, only the shallow soil with temperature and precipitation has a strong positive correlation but a minimum correlation in 40–100 cm layer. When the temperature stabilizes less than 10°C, precipitation with soil moisture has a strong negative correlation and a weak correlation between soil moisture and temperature.

3.3. Discussion

To study the effects of climate change or predict the climate changes, soil moisture is worth to be considered, but the lack of soil moisture observation data, the various soil moisture

Soil layer	Correlation and causality		
	Correlation	Temperature→Soil moisture	Soil moisture→Temperature
0–10 cm	–0.112	0.513 ± 0.019	–0.479 ± 0.021
10–40 cm	–0.458	0.299 ± 0.019	–0.276 ± 0.017
40–100 cm	–0.433	0.179 ± 0.010	–0.177 ± 0.009
100–200 cm	–0.591	0.197 ± 0.010	–0.196 ± 0.010

The chosen unit time step is ut = 1 year.

Table 2. Correlation and causality between temperature and soil moisture in Jiangsu province.

Correlation and causality			
Soil layer	Correlation	Precipitation→Soil moisture	Soil moisture→Precipitation
0–10 cm	0.563	0.853 ± 0.138	-0.499 ± 0.029
10–40 cm	0.400	0.366 ± 0.068	-0.357 ± 0.019
40–100 cm	0.341	0.199 ± 0.052	-0.194 ± 0.011
100–200 cm	0.242	0.219 ± 0.025	-0.209 ± 0.012

The chosen unit time step is $\Delta t = 1$ year.

Table 3. Correlation and causality between precipitation and soil moisture in Jiangsu province.

Category	Regression coefficient	0–10 cm	10–40 cm	40–100 cm	100–200 cm
Spring	Temperature	0.99	0.79	0.99	0.95
	Precipitation	0.99	0.68	0.98	0.98
Summer	Temperature	0.74	0.62	0.29	0.40
	Precipitation	0.66	0.54	0.19	0.31
Autumn	Temperature	0.99	0.99	0.99	0.99
	Precipitation	0.99	0.99	0.99	0.98
Winter	Temperature	-0.13	0.06	-0.07	-0.14
	Precipitation	-0.91	-0.81	-0.88	-0.91

Table 4. Regression coefficients of temperature, precipitation, and soil depth in different seasons.

simulation data and uncertain output limit the pace of research. Combining the observation data and simulated data can make up the shortfall of them. With the evolution of pattern, the development of simulation data will infinite close to the observation data. In the following research, we will continue to explore GLDAS data accuracy and the scope of application.

4. Conclusions

By analyzing the evolution of soil moisture in Jiangsu province, China, a few conclusions have been summarized.

There are some differences in the decadal variability of average temperature on both sides of the Yangtze river, the average temperature in the south of the Yangtze river is higher than in the north of the Yangtze river, but the temperature is rising in whole Jiangsu. The temperature rose slightly in the early period but increased obviously in the later period. The average annual precipitation is generally more in the south of the Yangtze river than in the north of the

Yangtze River, the gap between the two is bigger from 1971 to 2000. In recent years, the gap is gradually close.

By using information flow, we can know that the causality value of shallow layer is significantly different from zero, while the deeper, in comparison to the shallow layer, is negligible. This result unambiguously shows the causality in the sense that the precipitation increase and the temperature decrease are causing the shallow soil moisture increase. Soil moisture in the surface layer is more affected by precipitation in four seasons from 1961 to 2011, but precipitation has a same regularity. The variation of precipitation lags soil moisture (10–40 cm, 40–100 cm, and 100–200 cm) about 1–3 months. Deeper soil has a certain memory function for climatic evolutionary process, which can accumulate lots of data about the surface hydrological processes. In line with the data analysis, soil moisture indicates a falling trend from 1961 to 2011, while interannual change is obviously different, which shows that Jiangsu province may have future drought conditions.

Temperature and precipitation have some relationships between different layers of soil moisture. When the temperature stabilizes between 22 and 10°C, the temperature and precipitation with soil moisture in each layer have a strong correlation. Once when temperature rose, only the shallow soil has a strong positive correlation with temperature and precipitation, the minimum correlation is in 40–100 cm layer. When the temperature dropped, precipitation with soil moisture has a strong negative correlation and a weak correlation between soil moisture and temperature.

Acknowledgments

The SST data and the local governmental data are highly appreciated. This research is jointly supported by the “2015 Jiangsu Shuangchuang Program of China”, the “National Key Research and Development Program of China (Project Ref. No. 2016YFC1402003)”, and the National Foundation of Natural Science of China (No. 41506106).

Conflicts of interest

The authors declare no conflict of interest.

Author contributions

Jingze Cai and Yuanzhi Zhang conceived and designed the experiments, performed the experiments, analyzed the data, and wrote the chapter; Yu Li and Xia Lu improved the data analysis; Tingchen Jiang, X. San Liang, and Jinyeu Tsou contributed reagents/materials/analysis tools.

Author details

Jingze Cai¹, Yuanzhi Zhang^{1,2*}, Yu Li³, Tingchen Jiang⁴, X. San Liang¹, Xia Lu⁴ and Jin Yeu Tsou²

*Address all correspondence to: yuanzhizhang@cuhk.edu.hk

1 School of Marine Sciences, Nanjing University of Information Science and Technology, Nanjing, China

2 Center for Housing Innovations, Chinese University of Hong Kong, Shatin, Hong Kong

3 Faculty of Information Science, Beijing University of Technology, Beijing, China

4 Faculty of Surveying and Mapping, Huaihai Institute of Technology, Lianyungang, China

References

- [1] Zhang Q, Wang S, Wei G. A study on parameterization of local land-surface physical processes on the GOBI of Northwest China. *Chinese Journal of Geophysics*. 2003;**46**: 616-623
- [2] Guan XD, Huang JP, Guo N. Variability of soil moisture and its relationship with surface albedo and soil thermal parameters over the Loess Plateau. *Advances in Atmospheric Sciences*. 2009;**26**:692-700
- [3] Zhu Q, Lan H, Shen T. Numerical study of the influence of soil moisture and surface albedo on climate of north part of China. *Acta Meteorologica Sinica*. 1996;**54**:493-500
- [4] Cai J, Zhang Y, Li Y, Liang XS, Jiang T. Analyzing the characteristics of soil moisture using GLDAS data: A case study in eastern China. *Applied Sciences*. 2017;**7**(6):566
- [5] Ma Z, Wei H, Fu C. Progress in the research on the relationship between soil moisture and climate change. *Advances in Earth Science*. 1999;**14**:300-303
- [6] Li B, Wen X, Wang L, Yan P. Tendency of soil moisture in spring of Heilongjiang province in recent 30 years. *Journal of Arid Meteorology*. 2011;**29**:289-296
- [7] Wang L, Wen J, Wei Z, Hu Z. Soil moisture over the west of Northwest China and its response to climate. *Plateau Meteorology*. 2008;**27**:1257-1266
- [8] Chen S, Guo Y, Zheng Y, Wang J. Impact of precipitation on soil moisture in Gansu arid agricultural regions. *Journal of Desert Research*. 2012;**32**:155-162
- [9] Liu S, Lin H, Hu F, Liang F, Wang J, Liu H. Numerical simulation of evapotranspiration mechanism over soil-vegetation-atmosphere system. *Journal of Arid Meteorology*. 2004;**22**:1-10

- [10] Tapley B, Bettadpur S, Ries J. GRACE measurements of mass variability in the earth system. *Science*. 2004;**305**:503-505
- [11] Long D, Scanlon B, Longuevergne L, Sun A, Fernando D, Save H. GRACE satellite monitoring of large depletion in water storage in response to the 2011 drought in Texas. *Geophysical Research Letters*. 2013;**40**:3395-3401
- [12] Long D, Shen Y, Sun A, Hong Y, Longuevergne L, Yang Y, et al. Drought and flood monitoring for a large karst plateau in Southwest China using extended GRACE data. *Remote Sensing of Environment*. 2014;**155**:145-160
- [13] Reichle R, Koster R, Liu P, Mahanama S, Njoku E, Owe M. Comparison and assimilation of global soil moisture retrievals from the advanced microwave scanning radiometer (AMSR) for the earth observing system (AMSR-E) and the scanning multichannel micro-wave radiometer (SMMR). *Journal of Geophysical Research-Atmospheres*. 2007;**112**:D09108. DOI: 10.1029/2006JD008033
- [14] Niu G, Yang Z, Dickinson R. Development of a simple groundwater model for use in climate models and evaluation with gravity recovery and climate experiment data. *Journal of Geophysical Research-Atmospheres*. 2007;**112**:277-287
- [15] Quintana P, Moigne P, Durand Y. Analysis of near-surface atmospheric variables: Validation of the SAFRAN analysis over France. *Journal of Applied Meteorology and Climatology*. 2008;**47**:92-107
- [16] Koster D, Dirmeyer P, Guo Z. Regions of strong coupling between soil moisture and precipitation. *Science*. 2004;**305**:1138-1140
- [17] Hu M, Ding H, Liao F. An improvement on summer regional climate simulation over East China: Importance of data assimilation of soil moisture. *Chinese Science Bulletin*. 2009;**54**: 2388-2394
- [18] Zhang X, Wu X, He J. Vertical character of soil moisture in China. *Acta Geographica Sinica*. 2004;**62**:60
- [19] Ma Z, Wei H, Fu C. Relationship between regional soil moisture variation and climatic variability over East China. *Acta Geographica Sinica*. 2000;**58**:284-286
- [20] Rui H. Readme Document for Global Land Data Assimilation System Version 1 (GLDAS-1) [EB/OL]. 2014. <http://disc.Sci.gsfc.nasa.gov/services/grads-gds/gldas>
- [21] Rui H. Readme Document for Global Land Data Assimilation System Version 2 (GLDAS-2) products [EB/OL]. 2014. <http://disc.Sci.gsfc.nasa.gov/services/grads-gds/gldas>
- [22] Vaid BH, Liang XS. An abrupt change in tropospheric temperature gradient and moisture transport over East Asia in the late 1990s. *Atmosphere-Ocean*. 2018;**1**:1-9
- [23] Liang XS. Unraveling the cause-effect relation between time series. *Physical Review E*. 2014;**90**:052150

- [24] Liang XS. Normalizing the causality between time series. *Physical Review E*. 2015;**92**:022126
- [25] Liang XS. Information flow and causality as rigorous notions ab initio. *Physical Review E*. 2016;**94**:052201
- [26] Mann B. Non-parametric tests against trend. *Econometrica*. 1945;**13**:163-171
- [27] Kendall G. Rank Correlation Methods. 4th ed. Vol. 4. London, UK: Charles Griffin; 1975. p. 202

Analysis for the Effect of Sea Surface Temperature (SST) on the Coastal Environments of Jiangsu Province, China

Chenxu Ji, Yuanzhi Zhang, Kapo Wong, Yu Li,
Tingchen Jiang, Xiangsan Liang and Xia Lu

Additional information is available at the end of the chapter

<http://dx.doi.org/10.5772/intechopen.80737>

Abstract

In this chapter, we present the analysis for the effect of summertime SST on the coastal environments of Jiangsu province, China. We analyze the relationship between the SST and the Jiangsu precipitation in summer based on GPCP's precipitation data and NOAA's SST data from 1979 to 2011, using approaches that include correlation analysis, regression analysis, and lead-lag analysis. The results show that certain strong oceanic signals affect summer Jiangsu precipitation, showing that SST of some oceanic areas significantly affect the precipitation of Jiangsu in summer. By the lead-lag analysis, it is found that the spring SST plays an important role in the summer precipitation in the coastal areas of Jiangsu, China.

Keywords: Jiangsu province, precipitation, sea surface temperature, Pacific Ocean, summer

1. Introduction

As one of the world's most densely populated regions, Jiangsu province, is dominated by the well-known East Asian monsoon. The economy and society are quite vulnerable to the variability in the summer precipitation [1]. Being located in the downstream of the Yangtze River, droughts and floods occur in Jiangsu province in summer.

According to the previous studies, many events occurring in the ocean could affect the precipitation of Jiangsu, such as ENSO and IOD.

The first studies about ENSO influence on precipitation events worldwide are dating back to the early 1920s [2]. More recent works are from the 1980s [3, 4].

Influenced by the continental and oceanic processes, Southeast China is affected by the precipitation related large-scale atmospheric circulation patterns. Over the Southeast China, some patterns have been demonstrated to be influential for the interannual variability of precipitation, such as East Asian Winter Monsoon, ENSO, the strength and position of the East Asian trough, Siberian High, and sea surface temperature (SST) of South China Sea [5–7].

The relationship between the SST anomalies over tropical Pacific and the climate of South China has changed after the late 1970s [8, 9], which is partially associated with the tropical SST patterns shifting from “conventional” ENSO SST to ENSO Modoki-like conditions in recent three decades [10, 11].

Previous work has shown that positive IOD events induce a stronger South Asian High, with an eastward-extending position and a strengthened Western Pacific subtropical high and with a westward-extending position [12], which leads to precipitation anomalies in East China and causes extremely hot and dry summers in South China by generating a Rossby wave train [13].

Tibetan Plateau underwent interdecadal warming around 2002, which led to the interdecadal shift northward of the West Pacific Subtropical High, and consequently, the interdecadal increase of summer precipitation over the Huaihe River valley during 2002–2010 in comparison to 1979–2001 [14].

Li and Leung found that there has been a tendency for enhanced summer precipitation over the Yangtze River valley and South China, but drought over North and northeastern China after the end of the 1970s [15]. It is claimed that the transformation is related to the Arctic spring warming. And some research found that compared with the above factors, the SST has played the greatest extent role on the decadal variability of precipitation in China [16]. Yang and Lau demonstrated that the upward trend of spring precipitation over southeastern China and downward trend of summer precipitation over northern China are attributable to the warming trend of the ENSO-like mode [17].

By reviewing the previous studies, although much research has examined the correlation between SST and precipitation, only a few have considered SSTs' influence on the precipitation of Jiangsu province. This study analyzes the relationship between the SST and the summer precipitation of Jiangsu province and discusses the lead-lag relationship between them.

2. Data and methods

2.1. Data

2.1.1. NOAA data

National Oceanic and Atmospheric Administration (NOAA) monthly mean SST data from 1979 to 2011, with a horizontal resolution of $2.5^\circ \times 2.5^\circ$ and 180×89 grid points.

2.1.2. GPCP version 2.3 combined precipitation data set

Monthly precipitation dataset are provided by Global Precipitation Climatology Project (GPCP) from 1979 to 2011 combines observations and satellite precipitation data into 2.5° × 2.5° global grids.

2.2. Methods

2.2.1. Calculation of standardization index

Z-SCORE standard method is used to measure the relationship between a value and the mean in a group of values [18]:

$$K_i = \frac{X_i - \bar{X}}{S} \quad i = 1, 2, 3, \dots, n \tag{1}$$

where X_i is the sample value, \bar{X} represents the mean of the sample, and S is the standard deviation of the sample.

A positive value indicating the score is above the mean and a negative score indicating it is below the mean. If the absolute value of K_i is greater than 1, we take it as abnormal.

2.2.2. Correlation analysis

In this chapter, to measure whether there is a linear relationship between the selected variables, we perform Pearson correlation test on the data. The formula is [19]:

$$r = \frac{1}{n-1} \sum_{i=1}^n \left(\frac{X_i - \bar{X}}{s_X} \right) \left(\frac{Y_i - \bar{Y}}{s_Y} \right) \tag{2}$$

where n is the sample size, r lies between -1 and 1 . When the value is above 0 , it indicates that the two variables are positively correlated. When it is less than 0 , the two variables are negatively correlated, and a T-test should be carried out to judge the relevant level.

2.2.3. Mann-Kendall test

Mann-Kendall trend test is a nonparametric test used to identify a trend in a series, even if there is a seasonal component in the series. We assume that the observations are independent before our computations [20, 21].

The formula is expressed as [20, 21]:

$$Z_c = \begin{cases} \frac{S-1}{\sqrt{\text{var}(S)}}, & S > 0 \\ 0, & S = 0 \\ \frac{S+1}{\sqrt{\text{var}(S)}}, & S < 0 \end{cases} \tag{3}$$

The test statistic Z_c is used as a measure of the significance of a trend.

$$S = \sum_{i=1}^{n-1} \sum_{k=i+1}^n \text{sgn}(x_k - x_i) \tag{4}$$

where x_k and x_i are the annual values in years k and i and $k > i$, respectively.

$$\text{var}[S] = \left[n(n-1)(2n+5) - \sum_t t(t-1)(2t+5) \right] / 18 \tag{5}$$

where t is the observations' number.

$$\beta = \text{Median} \left(\frac{x_i - x_j}{i - j} \right), \forall j < i \tag{6}$$

$1 < j < i < n$, β represents the slope; the positive value rises, and negative value declines.

2.3. Technology flowchart

See Figure 1.

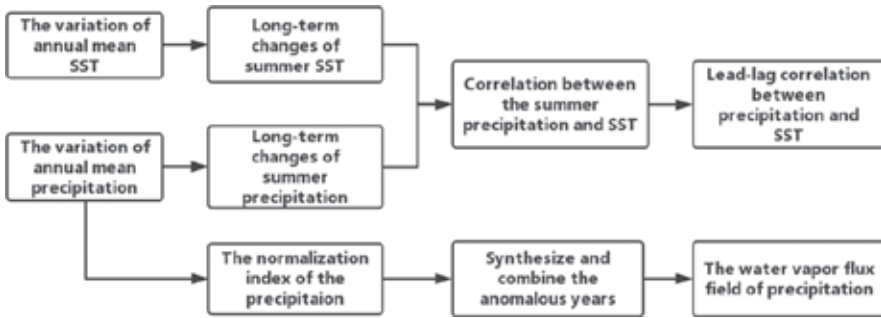


Figure 1. Flowchart of the study.

3. Results and discussion

3.1. Long-term variation of SST

The variations of SST in summer are studied first, as well as annual average from 1979 to 2011. During this period, according to the result, SSTs have fluctuated along an upward trend. Both trends for two SSTs pass the M-K test of 99% confidence with values of 5.3146 and 5.0667—thus the upward trend is significant. Specifically, the annual average SST has increased from 13.8 to 14°C, and the summer SST has increased from 13.9 to 14.2°C. Our results are consistent with those in [22, 23].

3.2. Long-term variation of the precipitation of Jiangsu province

Using the Global Precipitation Climatology Project (GPCP) monthly precipitation dataset, the precipitation of Jiangsu province is calculated. We selected the area of 116°–121.5°E and 30.5°–35.5°S as Jiangsu province. The results show an overall upward trend of summer-time precipitation, in which the values of 2002–2006 slightly drop but then rise later, much as described in [24]. And this trend passes the M-K test, with a value of 1.6269 and is significant.

Using Eq. 1, the normalization index of the precipitation during the period from 1979 to 2011 in Jiangsu province is calculated and analyzed.

Certain inter-annual variations of the precipitation are obvious. Taking $K_i = 1$ as the threshold, the high (low) value of the precipitation is immediately apparent. According to the result, abnormally high years were 1980, 1991, 1993, 2008, and 2011 and abnormally low years were 1981, 1985, 1988, 1992, 1994, 2002, and 2004.

3.3. SST signals affecting the precipitation of Jiangsu province

Figure 2 shows the correlation coefficient distribution of the precipitation in Jiangsu province for summer and contemporary SSTs during the period 1979–2011. Colored areas represent high correlation between SST field and precipitation, with correlation coefficients passing the t-test, with a confidence level of 95%. **Table 1** gives the correlation coefficient for each mainly correlated area (**Figure 2a**).

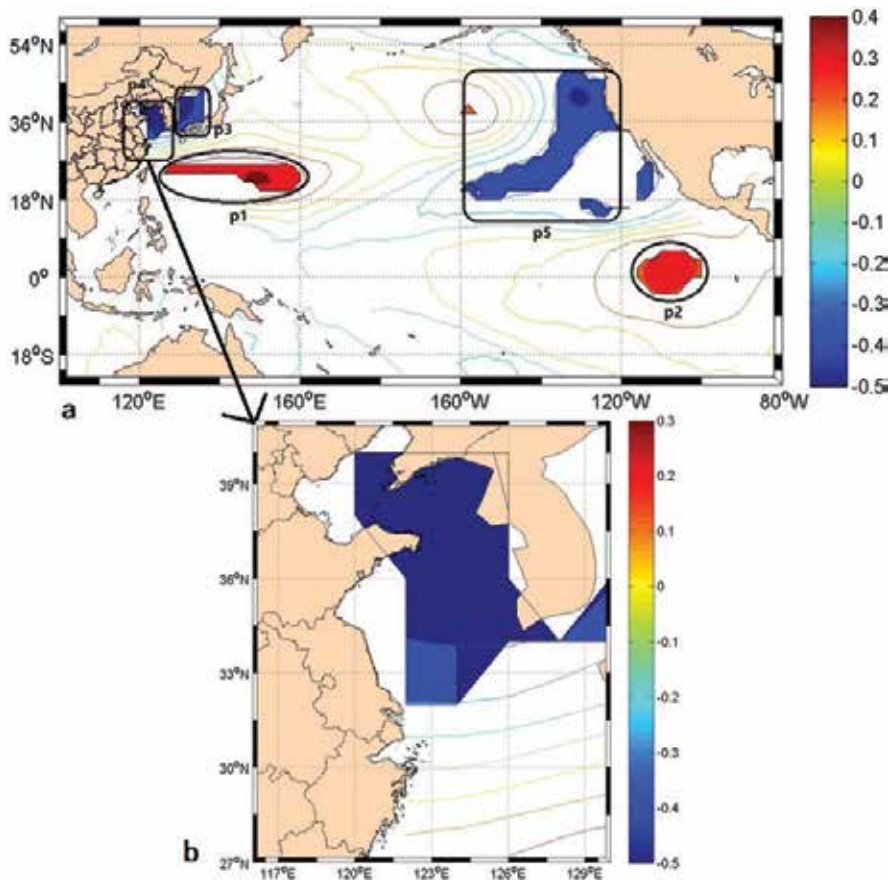


Figure 2. (a) Correlation between the summer precipitation and SST for the period of 1979–2011 and (b) the area p4 in **Figure 2a** (the areas passing 95% significance test are colored); before the correlation analysis on the SSTs time series, the data were detrended.

Area	p1	p2	p3	p4	p5
Coefficient	0.36	0.3	-0.4	-0.33	-0.33

Note: All color areas passed 95% significance testing. The p1, p2, p3, p4, and p5 are the areas of correlation marked in **Figure 2a**.

Table 1. The correlation coefficient of each color area.

As presented in **Figure 2a**, for the Pacific Ocean, two positive and three negative correlation areas are shown in **Figure 2**. The positive areas are situated in the West Pacific Ocean (125°–155°E and 25°N, marked as area p1) and the Equatorial Eastern Pacific Ocean (centered at about 110°W and 0°, marked as area p2). The Bohai Sea and Yellow Sea (marked as p4), Northeast Pacific Ocean (160°–130°W and 20°–45°S, marked as area p5), and Sea of Japan (marked as area p3) are three negative correlation areas.

Further, focusing on the area of p4 (**Figure 2b**), we could find that the SSTs of the Bohai Sea and Yellow Sea are highly correlated with the precipitation of Jiangsu province. And they present a negative correlation, that means when the SST is abnormally low (high), the precipitation of Jiangsu will be high (low). So, we could forecast the precipitation of Jiangsu by monitoring the SST of the Bohai Sea and Yellow Sea.

Moreover, the regression of summer time SST into the precipitation of Jiangsu province also shows statistically significant correlations between SST and precipitation. And the results in **Figure 2a** are similar to the area of correlation seen in regression analysis, which further illustrates the summer SSTs' effect on the precipitation of Jiangsu province.

To further analyze the effects of SST on the persistence of the precipitation over different periods, the precipitation in June, July, and August are selected to calculate the correlation coefficient with previous SST. Accordingly, it is found that the correlation field is more significant in June.

Figure 3 displays the distribution of the correlation coefficient between the precipitation of June and the previous SSTs of February, March, April, and May, respectively. The areas passed 95% significance test are colored. Focusing on the Pacific Ocean, we find that correlation areas are varying from time to time. **Table 2** is the correlation coefficient of each correlated month and area. **Table 3** gives the proportion of them (unit: %).

Here, we focus on the Pacific Ocean, and the areas of correlation vary from month to month. The North Pacific Ocean are positive (centered at about 180°W and 20°N, marked as area 1) correlation areas, and it becomes larger month by month. For the Equatorial Pacific Ocean, the average of negative correlation area (centered at about 150°W and 0°, marked as area 2) increases gradually. A positive correlation area is lying in the southwest of the Pacific Ocean (centered at about 180°W and 20°S, marked as area 4). Besides, a negative correlation region, presented in **Figure 3b–d**, lies in the West Coast of the United States (marked as area 3), becomes larger in May.

The years of anomalous precipitation have been selected above. When these anomalous precipitation years are synthesized and combined, all layers of the water vapor flux field are

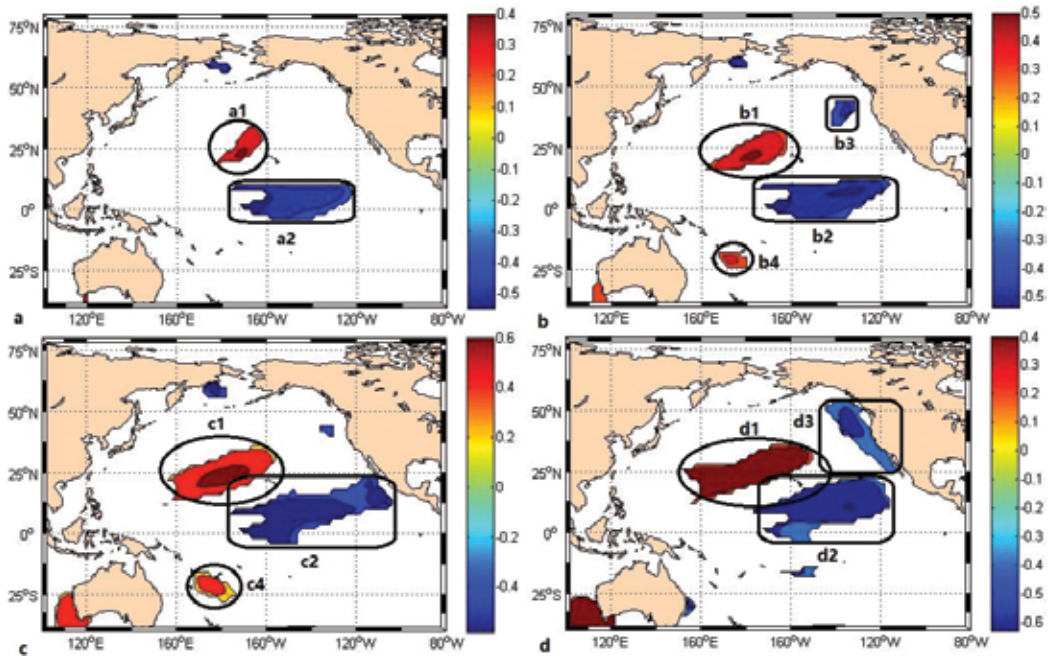


Figure 3. Correlation between precipitation in June and the SST in previous months ((a) February, (b) March, (c) April, and (d) May from 1979 to 2011) (the areas passing 95% significance test are colored).

Area	1	2	3	4
February (a)	0.38	-0.43		
March (b)	0.43	-0.44	-0.37	0.38
April (c)	0.46	-0.43		0.39
May (d)	0.5	-0.45	-0.38	

Note: All areas passed 95% significance testing. 1, 2, 3, and 4 are the areas of correlation marked in **Figure 3**.

Table 2. The correlation coefficient of each color area.

Area	1	2	3	4
February (a)	2.87	10.5		
March (b)	6.18	11.6	2.1	1.4
April (c)	8.86	16.3		2.8
May (d)	8.18	16.9	5.9	

Note: All areas passed 95% significance testing. 1, 2, 3, and 4 are the areas of correlation marked in **Figure 3**.

Table 3. The proportion of each correlated area (unit: %).

obtained. And we get the water vapor flux field of precipitation anomaly years. By analyzing it, we can see that water vapor is transported northeast over the Equatorial Northeastern Pacific Ocean. For the South East Pacific Ocean, it moves northeastward, which may enhance the convection and precipitation anomalies. Besides, for the Yellow Sea and the East China Sea, the water vapor propagates northward.

4. Conclusions

In this chapter, GPCP precipitation data and SST data from the NOAA have been used to analyze the strong signals of SSTs. We have discussed the relationship between summer SST and precipitation in Jiangsu province. The chapter shows that the precipitation of Jiangsu province in summer presents an upward trend during the period of 1979–2011. By analyzing the correlation coefficient distribution of the precipitation in Jiangsu province for summer and contemporary SSTs, finding that there are several high correlation areas in the Pacific Ocean that have significant effect on the precipitation in Jiangsu province. The results show that the precipitation in June is highly correlated to SSTs from the previous 1–4 months. This suggests that SSTs in February, March, April, and May might exert a significant influence on the precipitation of Jiangsu province, and their correlated areas and degrees are varying monthly. In the Pacific Ocean, the correlation is significant, with the area of correlation is bigger in May than other months.

According to the whole layer of water vapor flux field of precipitation anomaly years, it is transported northeast over the Equatorial Northeastern Pacific Ocean. And it moves northeastward in the South East Pacific Ocean, which may enhance the convection and precipitation anomalies. Besides, for the Yellow Sea and the East China Sea, the water vapor propagates northward.

Acknowledgements

The SST data and the local governmental data are highly appreciated. This research is jointly supported by the “2015 Jiangsu Shuangchuang Program of China,” the “National Key Research and Development Program of China (Project Ref. No. 2016YFC1402003),” and the National Foundation of Natural Science of China (No. 41506106).

Conflicts of interest

The authors declare no conflict of interest.

Author contributions

Chenxu Ji and Yuanzhi Zhang conceived and designed the experiments, performed the experiments, analyzed the data, and wrote the chapter; Kapo Wong, Yu Li, and Xia Lu

improved the data analysis; Tingchen Jiang and X. San Liang contributed reagents/materials/analysis tools.

Author details

Chenxu Ji¹, Yuanzhi Zhang^{1,2*}, Kapo Wong², Yu Li³, Tingchen Jiang⁴, Xiangsan Liang¹ and Xia Lu⁴

*Address all correspondence to: yuanzhizhang@cuhk.edu.hk

1 School of Marine Sciences, Nanjing University of Information Science and Technology, Nanjing, China

2 Center for Housing Innovations, Chinese University of Hong Kong, Shatin, Hong Kong

3 Faculty of Information Science, Beijing University of Technology, Beijing, China

4 Faculty of Surveying and Mapping, Huaihai Institute of Technology, Lianyungang, China

References

- [1] Zhu Y, Wang H, Zhou W, Ma J. Recent changes in the summer precipitation pattern in East China and the background circulation. *Climate Dynamics*. 2011;**36**:1463-1473
- [2] Walker GT. Correlation in seasonal variations of weather. Part VIII: A preliminary study of world weather. *Memoirs of the India Meteorological Department*. 1923;**24**:75-131
- [3] Rasmusson EM, Wallace JM. Meteorological aspects of El Nino/southern oscillation. *Science*. 1983;**222**:1195-1202
- [4] Shukla J, Paolino DA. The southern oscillation and long range forecasting of the summer monsoon rainfall over India. *Monthly Weather Review*. 1983;**111**:1830-1837
- [5] Zhou LT, Tam CY, Zhou W, et al. Influence of South China Sea SST and the ENSO on winter rainfall over South China. *Advances in Atmospheric Sciences*. 2010;**27**:832-844
- [6] Zhou LT, Wu RG. Respective impacts of the East Asian winter monsoon and ENSO on winter rainfall in China. *Journal of Geophysical Research*. 2010;**115**:D02107
- [7] Zhang L, Fraedrich K, Zhu XH, Sielmann F, Zhi XF. Interannual variability of winter precipitation in Southeast China. *Theoretical and Applied Climatology*. 2014;**119**:229-238
- [8] Ding RQ, Ha K, Li JP. Interdecadal shift in the relationship between the East Asian summer monsoon and the tropical Indian Ocean. *Climate Dynamics*. 2010;**34**:1059-1071
- [9] Li JP et al. Can global warming strengthen the East Asian summer monsoon? *Journal of Climate*. 2010;**23**:6696-6705
- [10] Feng J, Li J. Influence of El Nino Modoki on spring rainfall over South China. *Journal of Geophysical Research*. 2011;**116**:D13102

- [11] Zhang XB, Alexander L, Hegerl GC, Jones P, Tank AK, Peterson TC, et al. Indices for monitoring changes in extremes based on daily temperature and precipitation data. *WIREs Climate Change*. 2011;**2**:851-870
- [12] Xie SP, Hu K, Hafner J, et al. Indian Ocean capacitor effect on Indo-Western Pacific climate during the summer following El Nino. *Journal of Climate*. 2009;**22**:730-747
- [13] Guan Z, Yamagata T. The unusual summer of 1994 in East Asia: IOD teleconnections. *Geophysical Research Letters*. 2003;**30**:1544-1547
- [14] Zhu Y, Liu H, Ding Y, Zhang F, Li W. Interdecadal variation of spring snow depth over the Tibetan Plateau and its influence on summer rainfall over East China in the recent 30 years. *International Journal of Climatology*. 2015;**35**:3654-3660
- [15] Li Y, Leung LR. Potential impacts of the Arctic on interannual and interdecadal summer precipitation over China. *Journal of Climate*. 2013;**26**:899-917
- [16] Li H, Dai A, Zhou T, Lu J. Responses of East Asian summer monsoon to historical SST and atmospheric forcing during 1950-2000. *Climate Dynamics*. 2010;**34**:501-514
- [17] Yang F, Lau KM. Trend and variability of China precipitation in spring and summer: Linkage to sea-surface temperatures. *International Journal of Climatology*. 2004;**24**:1625-1644
- [18] Kreyszig E. *Advanced Engineering Mathematics*. 10th ed. New York: Wiley; 2010. p. 1280
- [19] Pearson K. Notes on regression and inheritance in the case of two parents. *Proceedings of the Royal Society of London*. 1895;**58**:240-242
- [20] Mann B. Non-parametric tests against trend. *Journal of Econometrics*. 1945;**13**:163-171
- [21] Kendall G. *Rank Correlation Methods*. 4th ed. Vol. 4. London, UK: Charles Griffin; 1975. p. 202
- [22] Cai Y, Wang ZG, Qiao FL. The simulation of Pacific Ocean temperature with the global warming during 1960-1999. *Acta Geographica Sinica*. 2008;**30**(5):9-16
- [23] Ji C, Zhang Y, Cheng Q, et al. On the relationship between the early spring Indian Ocean's sea surface temperature (SST) and the Tibetan Plateau atmospheric heat source in summer. *Global and Planetary Change*. 2018;**164**:1-10
- [24] Zhuang Y, Sun ZB. Characters of summer precipitation in Jiangsu Province and its correlations with Pacific SSTA. *Journal of Nanjing Institute of Meteorology*. 2007;**30**(6):835-840

The Cyclogenesis and Decay of Typhoon Damrey

X. San Liang and Lan Wang

Additional information is available at the end of the chapter

<http://dx.doi.org/10.5772/intechopen.80018>

Abstract

The cyclogenesis of typhoons has been a continuing challenge in dynamic meteorology. In this study, we use a recently developed methodology, namely, multiscale window transform (MWT), together with the MWT-based localized multiscale energy and vorticity analysis and the theory of canonical transfer, to investigate the formation, maintenance, and decay of the typhoon Damrey, a rarely seen tropical storm of higher-latitude origin. The atmospheric fields are first reconstructed onto three scale subspaces or scale windows: large-scale window, tropical cyclone-scale window, and cumulus convection-scale window. On the cyclone-scale window, Damrey is found right along the edge of the subtropical high. It is generated due to a strong barotropic instability in the lower troposphere, but its subsequent rapid amplification is, however, related to a baroclinic instability in the upper troposphere. Damrey begins to decay before landfall, right over East China Sea at the mouth of Yangtze River, where a strong inverse cascade center resides and transfers the cyclone-scale energy backward to the large-scale window.

Keywords: typhoon Damrey, twin typhoon, multiscale window transform, multiscale energetics, barotropic/baroclinic instability, canonical transfer

1. Introduction

A typhoon is a tropical cyclone that develops in the Northwestern Pacific basin and has wind speed of at least 64 knots (118 km/h). It is among the major meteorological phenomena that bring about natural hazards to coastal regions. For the densely populated coastal province Jiangsu, China, it has been recorded that since 1950, there have been landed 14 tropical cyclones (tropical storm level or higher). The typhoon Damrey that landed in Xiangshui, Jiangsu, on August 2, 2012, in particular, has inflicted a heavy damage to the region and its surrounding Chinese provinces such as Fujian, Zhejiang, and Shandong and has severely

affected 1.7 million residents, leaving 932,000 homeless. In this study, we present an analysis of the cyclogenesis and decay of Damrey.

Damrey is unique in that it does not originate between 20°N and 20°S , just like most of tropical cyclones [1]; rather, it is born at a relatively high latitude (a rare event). Moreover, it is actually a part of a twin typhoon. The other part, Saola, which appeared on the same day (July 28) as Damrey over the Western Pacific Ocean, also landed on China, but only several hours earlier. Shown in **Figure 1** are the paths of them. From it, Saola forms over the ocean east of the Philippines, while Damrey forms at a latitude as high as 24.8°N . On August 2, Damrey landed directly on Jiangsu, making the most powerful typhoon that has ever landed on China from north of Yangtze River. As it moves westward, Damrey becomes weakened, but its twin, Saola, becomes stronger. After landing, it turns northward, and then decays rapidly until it completely disappears.

This important meteorological phenomenon, however, has not caught enough attention from dynamic meteorologists. So far, the only report is by Wang and Liang [2], which we will be introduced henceforth.

Cyclogenesis is closely related to multiscale interactions. It has been reported (e.g., [3], and the references therein) that tropical cyclogenesis may be triggered by mesoscale processes under

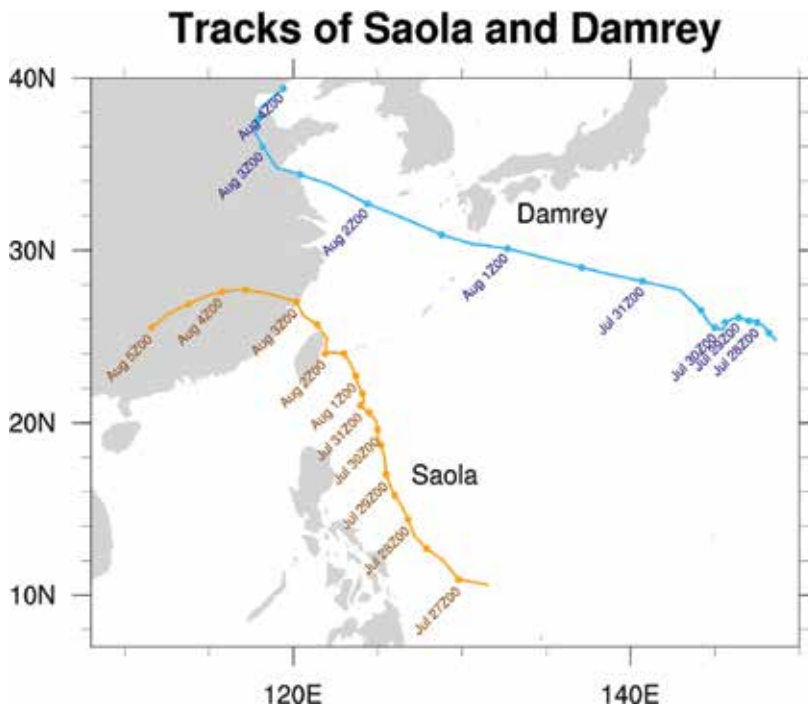


Figure 1. The paths of the twin typhoon Damrey and Saola (data courtesy of China Meteorological Administration).

the control of large-scale systems. Examples include the easterly waves in the Atlantic [4, 5], the monsoon troughs in the Pacific [1, 6–10], Madden-Julian oscillation (MJO) [11–14], tropical upper tropospheric troughs [15–17], and so forth. However, tropical cyclogenesis has seldom been investigated through multiscale energetics diagnosis, a natural approach to multiscale interactions, except a few studies such as Ooyama [18], Papin [19], Duan and Wu [20], etc. A reason is the lack of an appropriate methodology; a particularly critical issue here is: the traditional formalisms of the energy transfers between different scales cannot have the multiscale interaction faithfully represented. Recently, Wang and Liang [2] presented a study from this angle, using a newly developed functional analysis tool, multiscale window transform (MWT), and the MWT-based localized multiscale energy and vorticity analysis (MS-EVA). This chapter provides an exposition of what they have obtained, with some parts expanded as needed. The following is a brief introduction of the new methodology, and a theory of canonical transfer. We first apply it to reconstruct the two cyclones (Section 5), and then analyze the underlying dynamical processes (Section 6). Section 7 is a summary of the results; also in the same section, we make a brief comparison of some observations with the existing theories.

2. Multiscale window transform (MWT), canonical transfer, and localized multiscale energy and vorticity analysis (MS-EVA)

2.1. Multiscale window transform

As is well known, multiscale energetics formulated with time mean do not have information in time, and those formulated with zonal mean lose information in longitude, etc. Obviously, such formalisms cannot be used to study the energy burst processes such as cyclogenesis, which are in nature localized in space and time. During the past decades, a common practice is simply to remove the time mean in a Reynolds decomposition-based formalism. This is, unfortunately, conceptually wrong; we will soon see why below. A “more sophisticated” and widely adopted practice is to use filtering to replace the time averaging in the above formalism. For example, a field $u(t)$ (the spatial dependence is suppressed for clarity) can be decomposed with a filter into a slowly varying part \bar{u} and a fast varying eddy part u' . Now both of these parts have time information reserved, and this is precisely why filtering has been widely used. While mathematically this technique is indeed advantageous, however, a very basic physical question arises: What are the energies with respect to the resulting filtered fields? Particularly, we know for a time invariant \bar{u} in the decomposition $u(t) = \bar{u} + u'(t)$, the eddy energy is $\overline{[u'(t)]^2}$; now if \bar{u} is time variable, what is the eddy energy then?

During the past 2–3 decades, a common practice in the literature is simply to take it as $[u'(t)]^2$. However, the result is by no means this trivial; in fact, this is a very fundamental problem.

To illustrate, suppose we have a simple Fourier expansion

$$u(t) = \bar{u}(t) + u'(t) = [a_0 \cos t + b_0 \sin t] + [a_1 \cos 100t + b_1 \sin 100t] \quad (1)$$

where the subscripts 0 and 1 represent the slow- and fast-scale processes, respectively. Now what are the energies for these processes? By the common practice they are simply taken as

$$[\bar{u}(t)]^2 = [a_0 \cos t + b_0 \sin t]^2 \text{ and } [u'(t)]^2 = [a_1 \cos 100t + b_1 \sin 100t]^2. \quad (2)$$

Unfortunately, this is conceptually wrong! We know here the results should be, respectively,

$$a_0^2 + b_0^2 \text{ and } a_1^2 + b_1^2, \quad (3)$$

which are functions of the Fourier coefficients in phase space, not the reconstructions or filtered parts in physical space!

So, multiscale energy is a concept in phase space, which is related to its physical space counterpart through the Parseval relation in functional analysis. It is actually the square of the norm of a field variable, or, physically, it is the Fourier transform of an autocorrelation function (e.g., [21]). In the above example, when \bar{u} is time invariant, one can easily prove $a_1^2 + b_1^2 = \overline{[u'(t)]^2}$, just as that with the Reynolds decomposition. From this, one also sees why the time averaging in the classical energetic formalism cannot be removed to retain the time variability; otherwise, the resulting energetics does not make sense in physics.

It is, therefore, a rather complex and profound problem to have the local energy of a time-dependent filtered field faithfully represented. This even has been an impossible task until filter banks and wavelets are connected [22], and has just been systematically addressed by Liang and Anderson [23] in the development of multiscale window transform (MWT).

MWT is an apparatus that helps to decompose a function space into a direct sum of orthogonal subspaces, each with an exclusive range of scales (represented by wavelet scale levels). Such a subspace is termed a *scale window*, or simply a window. MWT is originally developed for representing the energies on the resulting multiple scale windows, in order to make multiscale energetics analysis possible. Liang and Anderson [23] find that, for some specially constructed orthogonal filters, there exists a transfer-reconstruction pair, just as the Fourier transform and inverse Fourier transform (Note here, *orthogonality* is crucial; otherwise, energy cannot even be defined.) This pair is the very MWT and its peer, namely, multiscale window reconstruction (MWR). Loosely speaking, the MWR of a series $S(t)$ results in a filtered series, while the corresponding MWT coefficients can give the energy of that filtered series. This is in contrast to the traditional filters; their outputs are fields in physical space, and, as argued above, cannot be used to represent multiscale energy, which is a concept in phase space.

In MWT, a scale window is demarcated on the wavelet spectrum by two scale levels, or window bounds. For a time series with a duration τ , a scale level j corresponds to a period $2^{-j}\tau$.

Obviously, the number of time steps need to be a power of 2. In this study, we will need three scale windows, which are bounded above by three scale levels: j_0 , j_1 , and j_2 . Alternatively, $2^{-j_0}\tau$, $2^{-j_1}\tau$, and $2^{-j_2}\tau$ are the time scale bounds. For convenience, we will, henceforth, refer to them as **large-scale window**, **tropical cyclone-scale window (or simply cyclone window)**, and **cumulus convection-scale window (or convection window)**, and will denote them by $\varpi = 0, 1, 2$ respectively.

Given a time series $\{S(t)\}$, application of MWT yields the transform coefficient, written $\widehat{S}_n^{\sim\varpi}$ [$\widehat{(\cdot)}_n^{\sim\varpi}$ denotes MWT on window ϖ at time step n]; likewise, application of MWR results in a reconstruction on window ϖ , written $S^{\sim\varpi}(t)$. Here, the tilde in the superscript indicates that the MWT is for a range of scales, rather than for a specific scale as in the other transforms (such as wavelet transform). It is also used to avoid confusion with notations that do not carry meaning of transform and/or reconstruction (We will see such notations later in the energetics.) It has been shown that the energy on window ϖ is proportional to $(\widehat{S}_n^{\sim\varpi})^2$ (Note it is by no means as trivial as $[S^{\sim\varpi}(t)]^2$, i.e., the square of the filtered field!). For a dry atmosphere, the multiscale kinetic energy (KE) and available potential energy (APE) are then, up to some proportionality, $\widehat{\mathbf{v}}_h^{\sim\varpi} \cdot \widehat{\mathbf{v}}_h^{\sim\varpi}$ and $(\widehat{T}^{\sim\varpi})^2$, respectively, where \mathbf{v} is velocity, T is temperature, and the subscript h indicates horizontal component. In the following, we will see more details.

2.2. Multiscale energetics and Lorenz cycle

Following Liang [24], we consider the primitive equations in an isobaric coordinate frame:

$$\frac{\partial \mathbf{v}_h}{\partial t} + \mathbf{v}_h \cdot \nabla_h \mathbf{v}_h + \omega \frac{\partial \mathbf{v}_h}{\partial p} + f \mathbf{k} \times \mathbf{v}_h = -\nabla_h \Phi + \mathbf{F}_{m,p} + \mathbf{F}_{m,h}, \quad (4)$$

$$\frac{\partial \Phi}{\partial p} = -\alpha, \quad (5)$$

$$\nabla_h \cdot \mathbf{v}_h + \frac{\partial \omega}{\partial p} = 0, \quad (6)$$

$$\frac{\partial T}{\partial t} + \mathbf{v}_h \cdot \nabla_h T + \omega \frac{\partial T}{\partial p} + \omega \bar{\alpha} \frac{L - L_d}{g} + \omega \alpha \frac{L - L_d}{g} = \frac{\dot{q}_{net}}{c_p}, \quad (7)$$

$$\alpha = \frac{R}{p} T \quad (8)$$

where L is the lapse rate and L_d the lapse rate for dry air, and the overbar stands for mean over time and over the horizontal isobaric plane. The other notations are conventional. Note here Φ (geopotential) and α (specific volume) are anomalies; their time averages have been presubtracted. From Eqs. (4)–(8), Liang [24] shows that the multiscale KE and APE equations are, for windows ϖ ($= 0, 1, 2$),

$$\frac{\partial K^\sigma}{\partial t} + \nabla \cdot \mathbf{Q}_K^\sigma = \Gamma_K^\sigma - \nabla \cdot \mathbf{Q}_P^\sigma - b^\sigma + F_{K,p}^\sigma + F_{K,h}^\sigma \quad (9)$$

$$\frac{\partial A^\sigma}{\partial t} + \nabla \cdot \mathbf{Q}_A^\sigma = \Gamma_A^\sigma + b^\sigma + S_A^\sigma + F_A^\sigma \quad (10)$$

The explanations and expressions for these terms are listed in **Table 1**. Note here the time step n has been suppressed for simplicity. Among these terms, the Γ terms represent transfers between different scale windows; they are very different from those in classical formalisms. Particularly, there is an interesting property, i.e.,

$$\sum_\sigma \left(\sum_n \Gamma_n^\sigma \right) = 0 \quad (11)$$

(now n is supplied) as first shown in Liang and Robinson [25] and later on rigorously proved (see [24]). Physically, this means that the energy transfer is a mere redistribution of energy among the scale windows, without generating or destroying energy as a whole. This property, though simply stated, does not hold in previous time decomposition-based or Lorenz-type energetics formalisms (see below). To distinguish, such as transfer is termed “*canonical transfer*.” A canonical transfer has a Lie bracket form that satisfies the Jacobian identity, reminiscent of the Poisson bracket in Hamiltonian mechanics; see Liang [24] for details (Note it is not the detailed balance relation in the Saltzman-type or space decomposition-based energetics formalisms, which results from the interaction analysis to be shown below).

To see how a canonical transfer differs from the energy transfer in classical energetics formalisms, we consider a passive tracer T (may be any scalar field; need not be temperature) in an incompressible flow, and neglect all other processes but for advection:

Symbol	Expression	Physical meaning
K^σ	$\frac{1}{2} \widehat{\mathbf{v}}_h \cdot \widehat{\mathbf{v}}_h$	KE on scale window σ
\mathbf{Q}_K^σ	$\frac{1}{2} (\widehat{\mathbf{v}\mathbf{v}}_h) \cdot \widehat{\mathbf{v}}_h$	Flux of KE on window σ
Γ_K^σ	$\frac{1}{2} [(\widehat{\mathbf{v}\mathbf{v}}_h) : \nabla \widehat{\mathbf{v}}_h - \nabla \cdot (\widehat{\mathbf{v}\mathbf{v}}_h) \cdot \widehat{\mathbf{v}}_h]$	Canonical transfer of KE to window σ
\mathbf{Q}_P^σ	$\widehat{\mathbf{v}} \cdot \widehat{\Phi}$	Pressure flux
b^σ	$\widehat{\omega} \widehat{\alpha}$	Buoyancy conversion
A^σ	$\frac{1}{2} c (\widehat{T})^2, c = \frac{g}{\bar{T}(g/C_p - L)}$	APE on scale window σ
\mathbf{Q}_A^σ	$\frac{1}{2} c \widehat{T} (\widehat{\mathbf{v}\mathbf{T}})$	Flux of APE on window σ
Γ_A^σ	$\frac{c}{2} [(\widehat{\mathbf{v}\mathbf{T}}) \cdot \nabla \widehat{T} - \widehat{T} \nabla \cdot (\widehat{\mathbf{v}\mathbf{T}})]$	Canonical transfer of APE to window σ
S_A^σ	$\frac{1}{2} \widehat{T} (\widehat{\omega T}) \frac{\partial c}{\partial p} + \frac{1}{T} \widehat{\omega} \widehat{\alpha}$	Apparent source/sink (usually negligible)

If total energetics (in W) are to be computed, the resulting integrals with respect to (x, y, p) should be divided by g . Besides, all terms are to be multiplied by $2^{1/2}$, which is omitted for notational simplicity.

Table 1. The energetic terms in Eqs. (9) and (10).

$$\frac{\partial T}{\partial t} + \nabla \cdot (\mathbf{v}T) = 0 \tag{12}$$

In a traditional Reynolds decomposition $\bar{\mathbf{v}}\bar{T}^2$ framework, its decomposed equations are

$$\frac{\partial \bar{T}}{\partial t} + \nabla \cdot (\bar{\mathbf{v}}\bar{T} + \overline{\mathbf{v}'T'}) = 0, \tag{13}$$

$$\frac{\partial T'}{\partial t} + \nabla \cdot (\mathbf{v}'\bar{T} + \bar{\mathbf{v}}T' + \mathbf{v}'T' - \overline{\mathbf{v}'T'}) = 0, \tag{14}$$

Multiplying (13) by \bar{T} and (14) by T' , followed by an averaging, one arrives at the evolutions of the mean energy and eddy energy (variance) (e.g., [26])

$$\frac{\partial \bar{T}^2/2}{\partial t} + \nabla \cdot \left(\frac{\bar{\mathbf{v}}\bar{T}^2}{2} \right) = -\bar{T}\nabla \cdot (\overline{\mathbf{v}'T'}), \tag{15}$$

$$\frac{\partial \overline{T'^2}/2}{\partial t} + \nabla \cdot \left(\frac{\overline{\mathbf{v}'T'^2}}{2} \right) = -\overline{\mathbf{v}'T'} \cdot \nabla \bar{T} \tag{16}$$

The terms in divergence form are generally understood as the transports of the mean and eddy energies, and those on the right-hand side as the respective energy transfers during the mean-eddy interaction. Particularly, when T is a velocity component, the right side of (16), $R = -\overline{\mathbf{v}'T'} \cdot \nabla \bar{T}$, has been interpreted as the rate of energy extracted by Reynolds stress against the mean profile; in the context of turbulence research, it is also referred to as the “rate of the turbulence production” [26]. It has been extensively utilized in geophysical fluid dynamics for the explanation of the phenomena such as cyclogenesis, eddy shedding, etc. However, Holopainen [27] and Plumb [28] have argued that the transport-transfer separation is ambiguous, and hence the resulting transfer is physically not robust. Moreover, Eqs. (15) and (16) do not, in general, sum to zero on the right-hand side. This is not what one would expect of an energy transfer, which by physical intuition should be a redistribution of energy among scale/scale windows and should not generate nor destroy energy as a whole.

With the MS-EVA formalism, the above are not issues any more. In this special case, the energy equations (9) and (10) are reduced to (see [24]),

$$\frac{\partial \bar{T}^2/2}{\partial t} + \nabla \cdot \left(\frac{1}{2}\bar{\mathbf{v}}\bar{T}^2 + \frac{1}{2}\bar{T}\overline{\mathbf{v}'T'} \right) = -\Gamma, \tag{17}$$

$$\frac{\partial \overline{T'^2}/2}{\partial t} + \nabla \cdot \left(\frac{1}{2}\overline{\mathbf{v}'T'^2} + \frac{1}{2}\bar{T}\overline{\mathbf{v}'T'} \right) = \Gamma, \tag{18}$$

where $\Gamma = \frac{1}{2} \left\{ \bar{T}\nabla \cdot (\overline{\mathbf{v}'T'}) - (\overline{\mathbf{v}'T'}) \cdot \nabla \bar{T} \right\}$. Now, one can see that the right-hand side is balanced, in contrast to Eqs. (15) and (16). We hence call this Γ a “canonical transfer.” As shown

by Liang [24], it has a Lie bracket form. Previously, Liang and Robinson [29] illustrate that, for a benchmark hydrodynamic instability model whose instability structure is analytically known, the traditional Reynolds stress extraction $R = -\overline{\mathbf{v}'T'} \cdot \nabla \overline{T}$ does not give the correct source of instability, while Γ does.

The MS-EVA equations (9) and (10) are thus fundamentally different from the classical ones. By collecting the energetic terms, one sees that a local Lorenz cycle is composed of four types of processes: transport (divergence of energy flux), canonical transfer, buoyancy conversion, and dissipation/diffusion. Obviously, the first three are conservative: a transport vanishes if integrated over a closed domain, a canonical transfer vanishes if summarized over windows and locations, while a buoyancy conversion disappears if the total mechanical energy, i.e., KE + APE, is considered. In **Figure 2**, these processes are schematized with a three-window decomposition.

Note that a canonical transfer to a window ϖ may involve contributions from different windows; we need to differentiate them to trace the dynamical source. As an example, we consider the cyclone window ($\varpi = 1$). The energy transferred to it can be from window 0, 2, and even itself $\varpi = 1$. Observe that both Γ_K^1 and Γ_A^1 (cf. **Table 1**) can be expressed as a linear combination of terms in the following triple product form:

$$\Gamma_n^1 = \widehat{\mathcal{R}}_n^{-1}(\widehat{pq})_n^{-1} \tag{19}$$

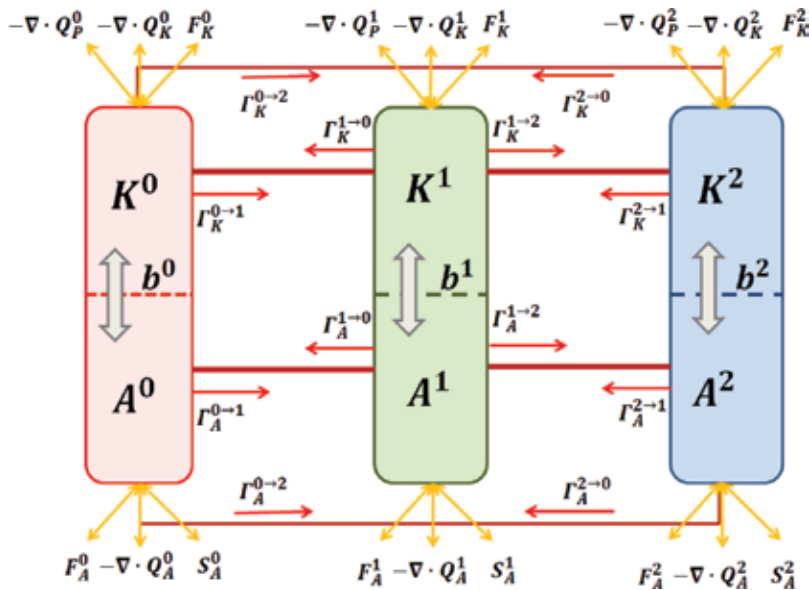


Figure 2. Multiscale energy pathway for a three-window decomposition (the scale windows are denoted in the superscripts as 0, 1, and 2, respectively).

It then suffices to consider Γ_n^1 only. As established in Liang [24], it can be decomposed as

$$\begin{aligned} \Gamma_n^1 = & \widehat{\mathcal{R}}_n^{-1} \left[(\widehat{p^{-0}q^{-0}})_n^{\sim 1} + (\widehat{p^{-0}q^{-1}})_n^{\sim 1} + (\widehat{p^{-1}q^{-0}})_n^{\sim 1} \right] \\ & + \widehat{\mathcal{R}}_n^{-1} \left[(\widehat{p^{-1}q^{-2}})_n^{\sim 1} + (\widehat{p^{-2}q^{-1}})_n^{\sim 1} + (\widehat{p^{-2}q^{-2}})_n^{\sim 1} \right] \\ & + \widehat{\mathcal{R}}_n^{-1} \left[(\widehat{p^{-0}q^{-2}})_n^{\sim 1} + (\widehat{p^{-2}q^{-0}})_n^{\sim 1} \right] \\ & + \widehat{\mathcal{R}}_n^{-1} (\widehat{p^{-1}q^{-1}})_n^{\sim 1} . \end{aligned} \tag{20}$$

where the first row on the right-hand side, $\widehat{\mathcal{R}}_n^{-1} \left[(\widehat{p^{-0}q^{-0}})_n^{\sim 1} + (\widehat{p^{-0}q^{-1}})_n^{\sim 1} + (\widehat{p^{-1}q^{-0}})_n^{\sim 1} \right] \equiv \Gamma^{0 \rightarrow 1}$ is the canonical energy transfer from window 0 to window 1. The second row, denoted by $\Gamma^{2 \rightarrow 1}$, is the canonical energy transfer from window 2 to window 1. The other two are usually very small. (For details, see [24]). It has been proved that $\Gamma^{0 \rightarrow 1}$ is related to the instability in geophysical fluid dynamics [29]. Particularly, $\Gamma_A^{0 \rightarrow 1}$ provides a quantitative measure of the baroclinic instability of the mean flow, while $\Gamma_K^{0 \rightarrow 1}$ provides a barotropic instability measure. For convenience, in the following, we will write them as BC and BT, and may refer to them as baroclinic transfer and barotropic transfer, respectively. We hence have the following criterion:

If what we are considering are windows 0 and 1, then:

1. a flow is locally unstable if $BT + BC > 0$, and vice versa;
2. for an unstable system, if $BT > 0$ and $BC \leq 0$, the instability the system undergoes is barotropic;
3. for an unstable system, if $BC > 0$ and $BT \leq 0$, then the instability is baroclinic; and
4. if both BC and BT are positive, the system must be undergoing a mixed instability.

If the windows in question are 1 and 2, the above criterion still works, but now the instability is with respect to the cyclone, which we will refer to as a secondary baroclinic/barotropic instability.

3. Data

The ERA-interim data with a horizontal resolution of $0.125^\circ \times 0.125^\circ$, including temperature, geopotential, and wind (u, v, ω), will be used in this study to handle the dynamical processes involved in the cyclones. This reanalysis product is supplied by the European Centre for Medium-Range Weather Forecasts (ECMWF); vertically, it has 37 levels (from 1000 to 1 hPa) and the time resolution is 6 h. We choose a time span from July 1 to September 2, 2012, which covers the whole process of the typhoon Damrey and gives a time series of 256 steps, or 2^8

steps, as required by the analysis (We have seen in the preceding section that the number of steps should be a power of 2.)

4. MS-EVA setup

To set up the MS-EVA analysis, we first need to determine the window bounds j_0 , j_1 , and j_2 . As shown above, the series has 2^8 steps, so $j_2 = 8$. To determine the other two scale levels, notice that although the duration of a tropical cyclone is generally 5–10 days, its life cycle from tropical turbulence at the cumulus convection scale to final decay may last more than 10 days. We have tried two lower bounds for the time scale levels—3 (corresponding to 16 days) and 2 (32 days). Through experiments, we find that $j_0 = 2$ gives a better cyclone separation, and hence will use this parameter for this study. The upper bound j_1 is chosen to be 7. That is to say, processes on time scales less than a day are regarded as cumulus convective disturbances. A summary of all other parameters is listed in **Table 2**.

Parameter	Value
Window bounds (j_0, j_1, j_2)	2, 7, 8 (corresponding to 32 days, 1 days, 6 h)
Horizontal grid	801×561
Spatial resolution	0.125°
Vertical levels	975, 950, 925, 900, 875, 850, 825, 800, 750, 700, 650, 600, 550, 500, 450, 400, 350, 300, 250, 225, 200, 175, 150, 125, 100, 70, 50, 30, 20, 10 hPa

Table 2. MS-EVA parameters.

5. Multiscale reconstructions

First we look at the reconstructions of the fields onto the three scale windows, i.e., the large-scale window, the cyclone window, and the convection window. Five pressure levels, 975, 850, 700, 500, and 300 hPa are selected for the illustration. They represent the boundary layer, the top of the boundary layer, lower, middle, and upper troposphere, respectively.

5.1. Large-scale flow

Figure 3 shows the original geopotential anomaly (left panel) and its large-scale reconstruction (right panel). Previously, it has been shown that, from late July to early August, in lower latitudes, the subtropical high lies further northward; in middle and high latitudes, the atmosphere at 500 hPa over East Asia is controlled by the Westerly in the south of a broad low with some short-wave troughs, while a ridge occupies aloft over the Seas of Okhotsk and Japan [30, 31]. **Figure 3** reconfirms this observation. On the 975 hPa level, the geopotential is characterized by low(s) in the west and high(s) in the east. The high pressure over the ocean is the

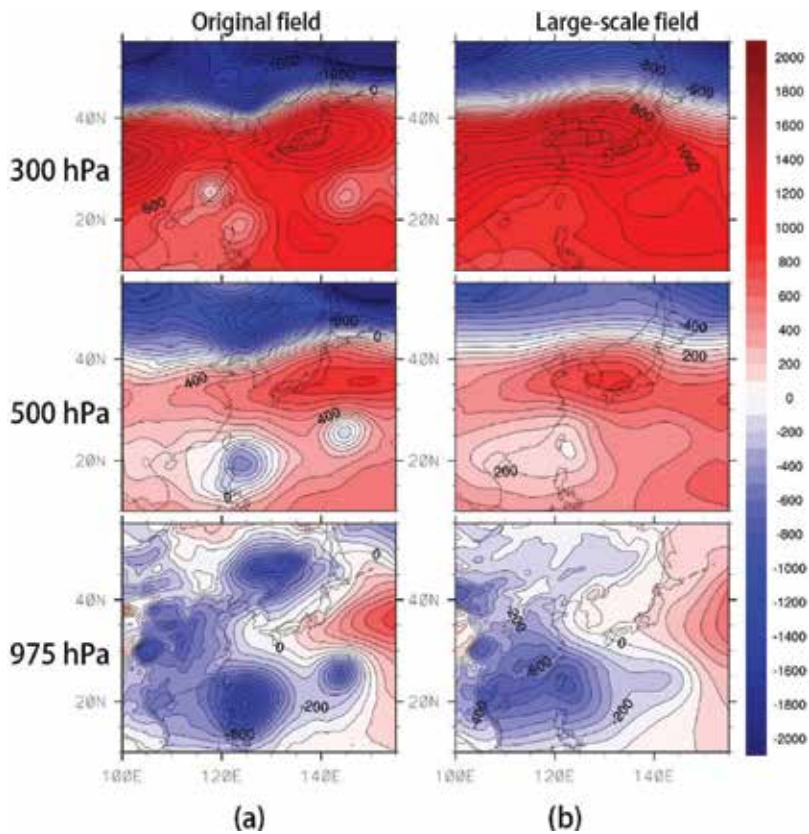


Figure 3. (a) The original geopotential ($m^2 \cdot s^{-2}$) and (b) its reconstruction on the large-scale window ($m^2 \cdot s^{-2}$) on July 30, 2012, at 975, 500, and 300 hPa.

subtropical high; around $30^\circ N$, there is a northwestern ridge. The low pressure covers the land, with intensity decreasing with height. The cyclones of the twin typhoon, Damrey and Saola, are clearly seen at all the levels shown. Damrey forms at the edge of the subtropical high; it then moves westward along the southern boundary. Saola has a different origin; it forms east of the Philippines, far from the subtropical high. It then moves northwestward and meets Damrey.

On the large-scale window (right panel in **Figure 3**), the low level (975 hPa) geopotential generally follows the original field, with a low in the west and a high in the east, but, differently, in middle and high latitudes, the interface separating the high and low is more along the land boundary, indicating the influence of the land. Over the West Pacific Warm Pool (WPWP), a low pressure sticks out eastward (centered around the island of Taiwan), and above the ocean at $30\text{--}37^\circ N$, east of $150^\circ E$, there is a high pressure center. In the lower troposphere, over the Sea of Japan is a low, but in the upper troposphere, a high center takes over the southern part of the Sea. North of $40^\circ N$, the region is mostly covered by low pressure. Generally, in the middle and upper troposphere, the large-scale geopotential is characterized by a high-pressure band between 25 and $35^\circ N$. That is to say, the subtropical high is narrow,

with a deep zonal easterly as its southern boundary; it lies farther in the north from bottom to the upper troposphere. This flow pattern provides the environment for Damrey's westward movement in higher latitudes.

A noteworthy feature on the large-scale geopotential anomaly map is the vertical dependence of the high- and low-pressure centers. From **Figure 3b**, the low weakens from 975 to 850 hPa, while the high strengthens from 500 to 300 hPa. The weakening of the low with height is due to the decreasing influence from the surface. We know a warm surface tends to cause a shallow warm low. In summer, both the warm land and the WPWP form warm surfaces, impacting together the form of the pressure field. For the subtropical high, it is more influenced by the downdraft branch of the Hadley cell, so there is a trend of strengthening with height. This results in a pattern above 700 hPa with a low in the north and a high in the south. Besides, the

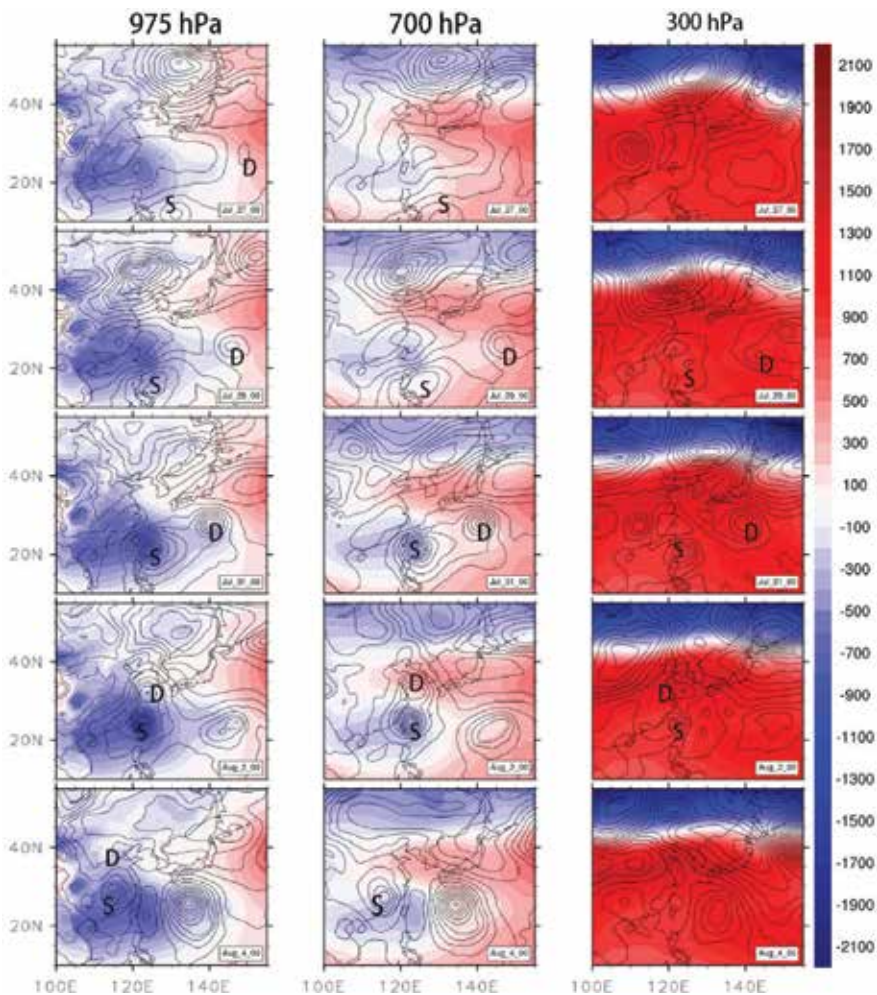


Figure 4. Geopotential anomaly ($m^2 \cdot s^{-2}$) on the cyclone window (contours) from July 27 to August 4, 2012, at 975, 700, and 300 hPa. The shaded background is the large-scale field.

South Asia high is clearly seen at 150 hPa (not shown), moving from the ocean to the Tibetan Plateau.

We remark that the large-scale field looks more like the climate state of the atmosphere. Many structures, the above vertical structure in particular, are largely disguised in the original field.

5.2. Cyclone-scale circulation

The cyclonic structures are reconstructed on the cyclonic window. Shown in **Figure 4** is the cyclone-scale geopotential anomaly (black solid line); for interpretation, also shown in the figure is the large-scale field (shaded). It is easy to see that both Damrey and Saola form at the interface between the low- and high-pressure regions, but in the original field, Saola is born far from the subtropical high. Initially, Damrey is weaker than Saola. After formation, the former moves westward along the interface, while latter moves northwestward to the low over Taiwan. They eventually hit the mainland of China in the north and south. The stronger Saola is then found to be weakened quickly, turning southwestward along the edge of the interface (This cannot be seen in the original field, either.)

For convenience, we define the birth time of a tropical cyclone as the time when the closed isopleths appear. By the criterion, both Damrey and Saola are first born in the lower troposphere: Damrey is born on July 27 at 0:00 at 975 and 850 hPa, while Saola is born before July 26. In the middle troposphere (700–500 hPa), Damrey appears slightly later (around 6:00, July 27). At 300 hPa and above, the scenario is quite different; a broad low occupies over the formation region.

By observation, the two cyclones last more than a week. At 975 hPa, the closed isopleths of Damrey completely disappear on August 4 at 12:00. At upper levels (e.g., 850, 700, and 500 hPa), Damrey dies on August 3 at 12:00 or earlier. In other words, Damrey not only appears more pronounced, but also lasts longer in the lower troposphere.

6. Canonical transfers and multiscale energetics

Among the multiscale energetics, the canonical transfers are pivotal to understanding the dynamics underlying the cyclogenesis of tropical cyclones. Different from the traditional transfer, which is a globally averaged quantity, it is a local notion, and hence can follow the cyclone's movement and trace its dynamical origin continuously. It has been validated with benchmark instability processes [29] and has been successfully applied to the study of many real atmosphere-ocean problems and engineering fluid problems. We will, henceforth, focus on these transfers and their evolutions. For convenience, the life cycle of Damrey is divided into three stages, namely, the stages of formation, maintenance, and decay.

6.1. Formation

The period between 0:00, July 27, and 0:00, July 31, is taken as the formation stage of Damrey. In this stage, the cyclone evolves from a tropical depression in the beginning, to a tropical storm at 0:00 July 28, and, eventually, to a strong tropical storm on July 31.

Figure 5 shows the canonical KE transfer, or barotropic transfer (BT) as called, between the large-scale window and cyclone window; a positive value indicates a transfer of energy from the basic flow to the cyclone, and the basic flow is hence unstable. Clearly, below 300 hPa, both cyclones have positive BT in the formation regions ($BT > 0$). By what is demonstrated in Section 2, the system is locally barotropically unstable. At 300 hPa, however, BT is quite differently distributed; in Damrey's birth place, BT is locally negative, i.e., the system is locally stable.

For the canonical KE transfer between the convection and cyclone windows, the scenario is different. As shown in **Figure 6**, it has not become significant until July 30. Around the typhoon Damrey, it gains KE from the convective processes ($-\Gamma_K^{1-2} > 0$) in the middle

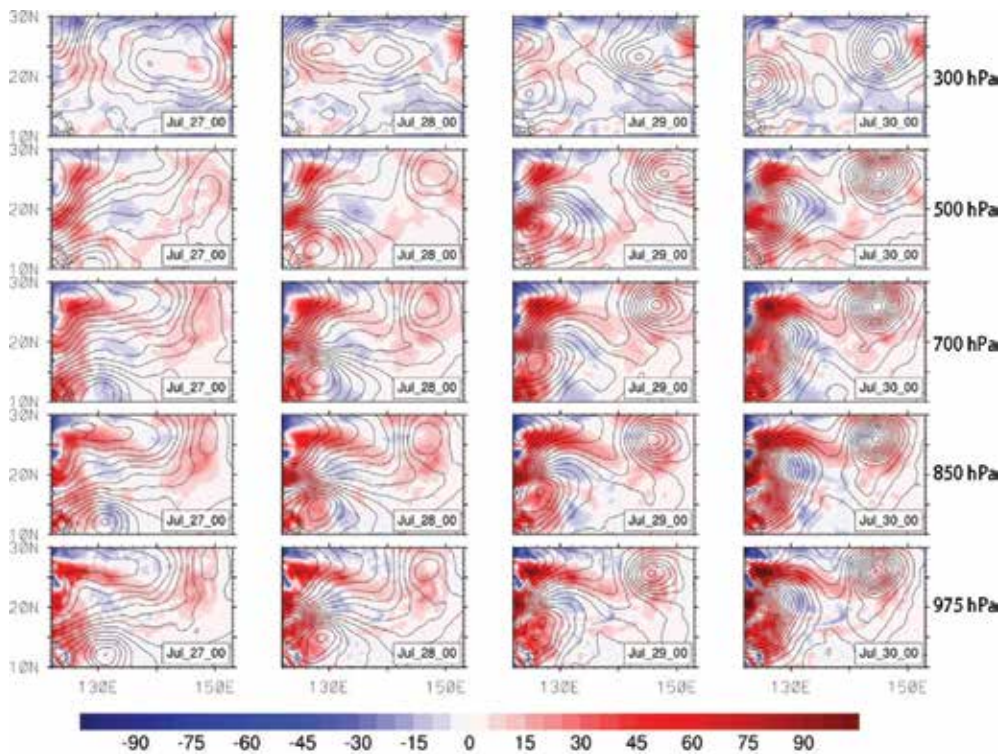


Figure 5. Canonical kinetic energy (KE) transfer ($10^{-5} \cdot \text{m}^2 \cdot \text{s}^{-3}$) between the large-scale and cyclone-scale windows from July 27 to July 30, 2012, at 975, 850, 700, 500, and 300 hPa. Shaded are the KE transfers between large-scale and cyclone-scale windows. (A positive value stands for a KE transfer from large-scale window to cyclone-scale window.) The red contour lines are the geopotential on the cyclone window; also superimposed are the cyclone-scale geopotential at 975 hPa (in black).

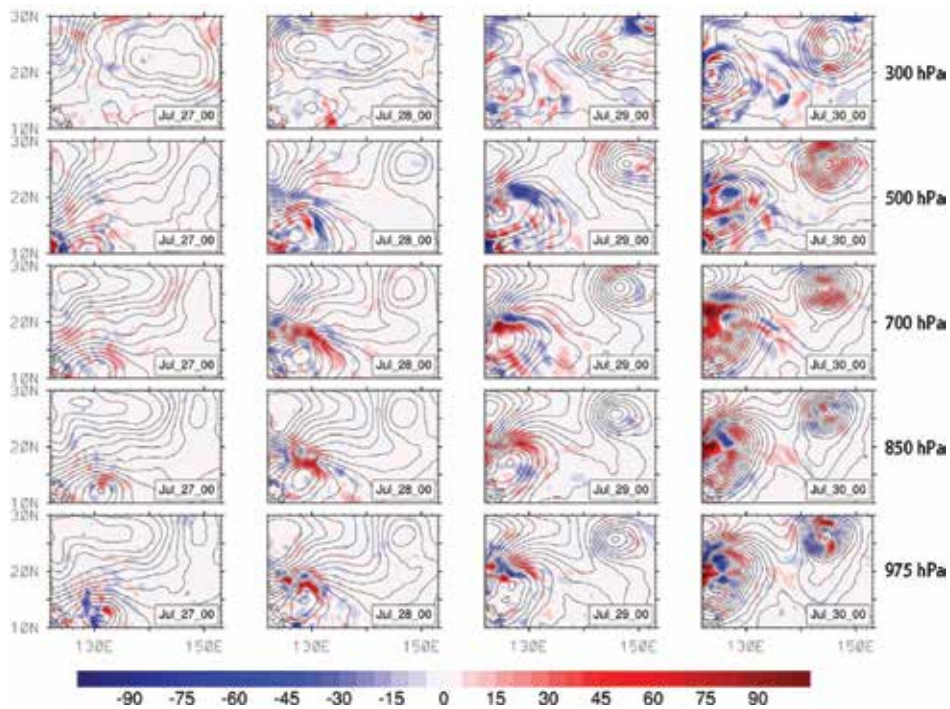


Figure 6. Same as **Figure 5**, but for canonical KE transfer ($10^{-5} \cdot m^2 \cdot s^{-3}$) between the convection and cyclone windows.

troposphere and loses KE ($-\Gamma_K^{1 \rightarrow 2} < 0$) in the upper troposphere, though the gain and loss are both insignificant, in comparison with those between the basic flow and the cyclonic-scale window. Somehow, the cyclone provides a mechanism that takes the impact of the convective cumulus to the upper troposphere.

In contrast to its barotropic counterpart, the baroclinic transfer, or canonical APE transfer between the large-scale and cyclone windows, is insignificant in the lower troposphere (975–700 hPa). (The values over Taiwan are invalid because the highest altitude there is 3997 m.) Above 500 hPa (**Figure 7**), clear transfers can be seen in the formation region. Positive transfers ($BC > 0$), and hence baroclinic instabilities, exist over Taiwan and the Philippines. Particularly, to the east BC takes its maximum, while this is precisely where Saola will rapidly develop later. At 300 hPa, a baroclinic instability band lies between 15 and 25°N. But, this band does not cover the path that Damrey takes, except a protuberance at 147°E, 25°N, and hence does not contribute much to the cyclogenesis.

The ambient dynamical environments for the two tropical cyclones are similar. Upon generating, the local system around Saola is baroclinically unstable at 500 hPa and stable at 300 hPa. As it moves northwestward, it enters a baroclinic instability area aloft, which fuels its growth, with closed contour appearing on the geopotential field. It then slows down and intensifies rapidly in the region where BC attains its maximum, as shown above.

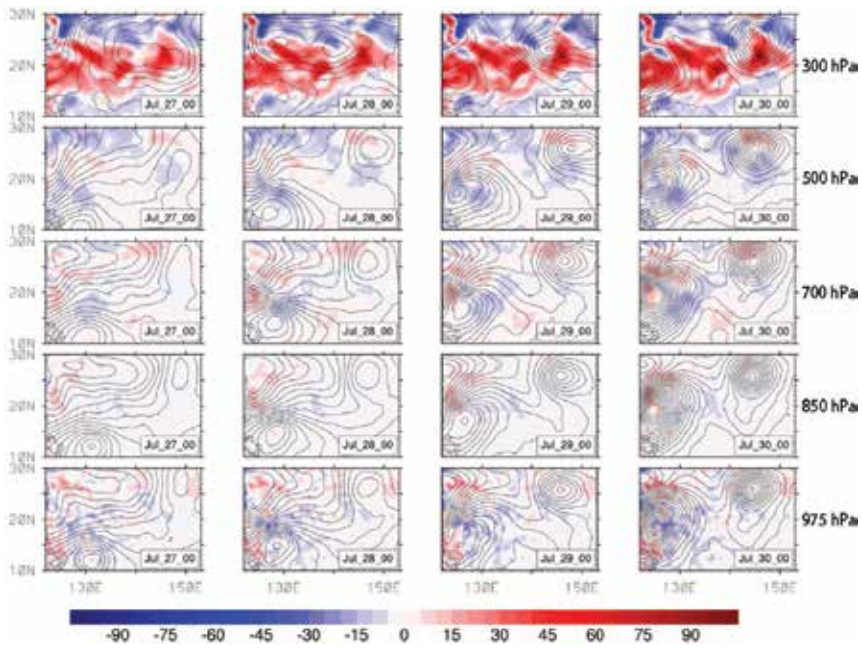


Figure 7. Same as Figure 5, but for canonical APE transfer ($10^{-5} \cdot m^2 \cdot s^{-3}$) at 500 and 300 hPa.

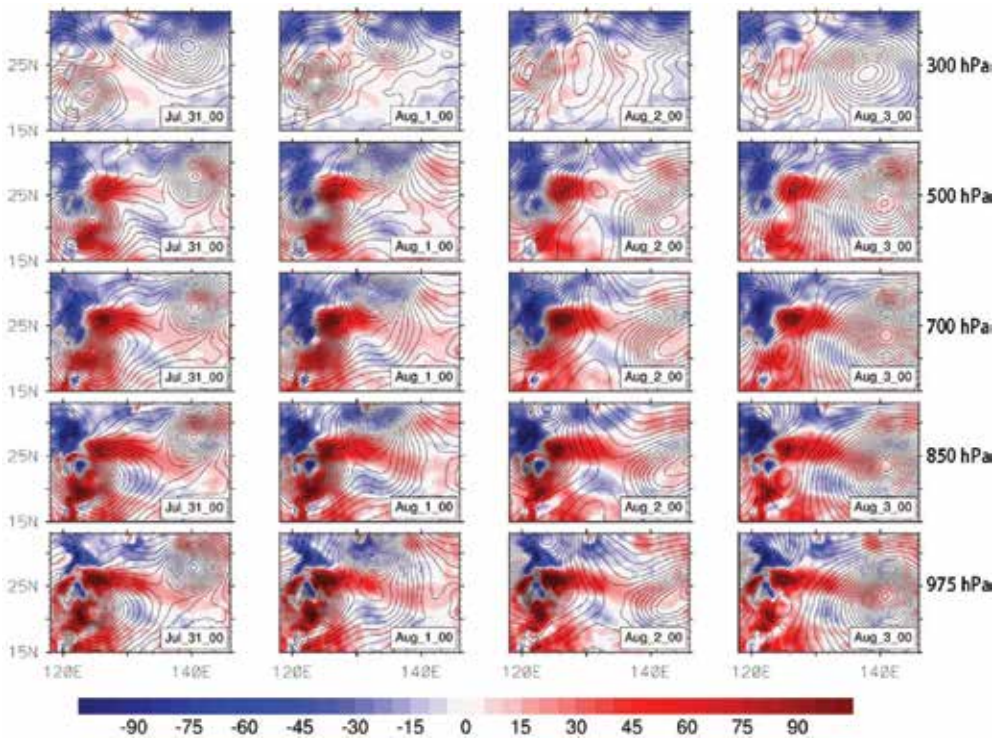


Figure 8. Same as Figure 5 but from July 31 to August 3, 2012.

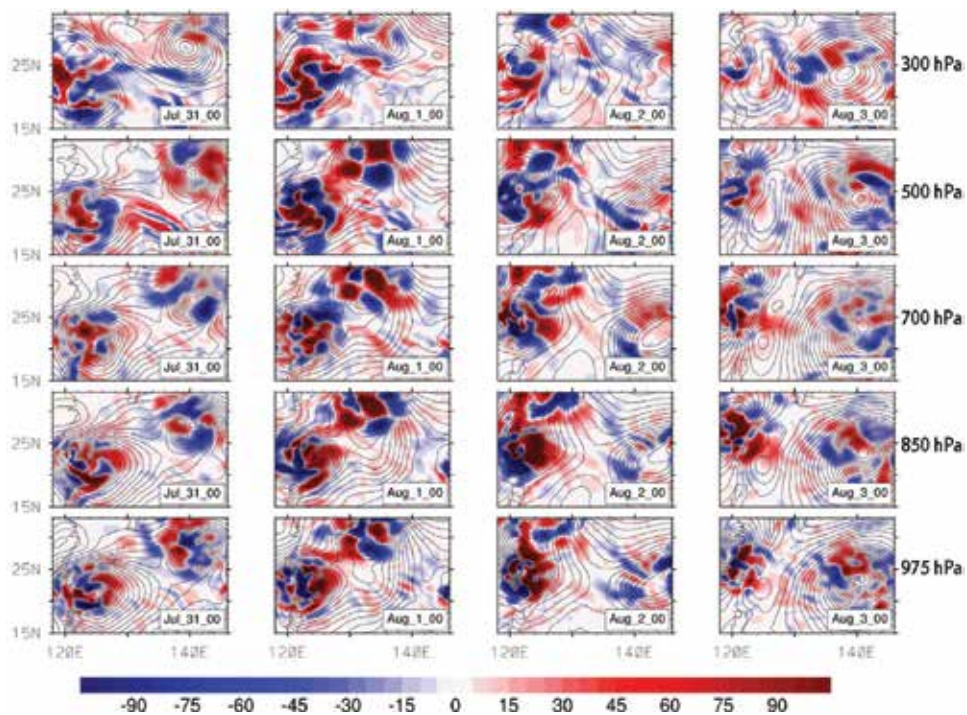


Figure 9. Same as **Figure 6** but from July 30 to August 3, 2012.

Damrey has gone through similar dynamical processes. In the beginning, it forms in a region, which is baroclinically unstable at 500 hPa and stable at 300 hPa. It moves westward and becomes strengthened at lower levels beneath that protuberance of the baroclinically unstable band (formed since July 28). The canonical APE transfer between the cyclone and convection windows is rather weak and does not make significant contribution.

6.2. Maintenance and rapid development

After the formation, Damrey actually experiences another intensification (since July 31), which eventually makes it a strong tropical storm. After August 1 at 12:00, it goes into a stage of rapid development until August 2 at 6:00.

As shown in **Figure 8**, after the cyclones are formed, the canonical KE transfer between the large-scale and cyclonic-scale windows takes a pattern of inverse cascade ($BT < 0$) in the north and barotropic instability ($BT > 0$) in the south. From 975 to 500 hPa, the inverse cascade region spreads southward and westward. At 300 hPa, a wide region of negative BT appears north of 30°N. During this period along the track of Damrey, the troposphere is barotropically stable ($BT < 0$).

For the canonical KE transfers between convection and cyclone windows (**Figure 9**), they mainly show up around the cyclones, with intensity positively related to the strength of the cyclones. From the figure, secondary instabilities and stabilities lie alternatively. By their

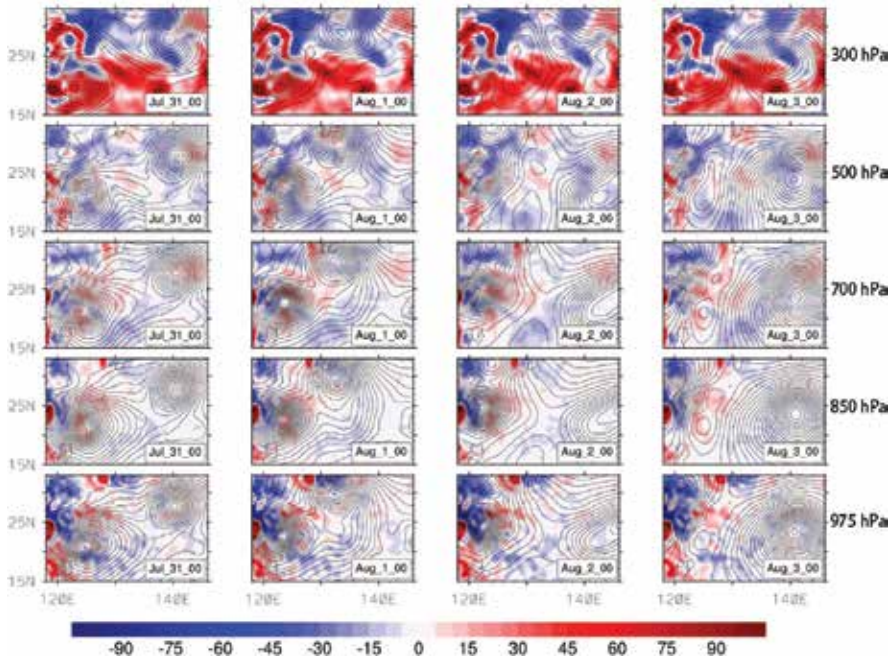


Figure 10. Same as Figure 7, but at 975, 850, 700, 500, and 300 hPa from July 31 to August 3, 2012.

magnitudes and distribution pattern, the convection-scale processes may not serve as energy sources or sinks to the cyclone.

The canonical APE transfers in the stage of maintenance are displayed in Figure 10. Obviously, at 850 hPa, the atmosphere east of the China mainland is baroclinically stable ($BC < 0$), but in the coastal region north of $25^{\circ}N$, there exist baroclinic instabilities. Below 500 hPa, the canonical transfer rate decreases with height. In the upper troposphere (300 hPa), the atmosphere is baroclinically unstable ($BC > 0$) over the mainland north of $25^{\circ}N$. But BC is still negative over the sea, to the east of Yangtze River’s estuary, and to the south of Japan. That is to say, the baroclinic canonical transfer is rather unfavorable for Damrey. This situation makes a slight difference for Saola. The positive baroclinic transfer over the sea above 500 hPa tends to facilitate Saola.

The canonical APE transfer between the convection and cyclone windows is rather weak below 500 hPa. But at 300 hPa, there exists a center of positive transfer to the convective window, indicating a secondary instability of the cyclonic-scale process.

6.3. Decay

On August 2 at 6:00, Damrey starts to decay, though it has not landed yet. Although it is argued that the dissipative/diffusive processes cause a perturbed atmosphere to resume to its original state, here, the decay of Damrey has its dynamical origin from within the atmosphere

itself. Generally, barotropic transfer seems to be unfavorable to its maintenance. A conspicuous feature of **Figure 5** is the existence of an inverse cascade region near the mouth of Yangtze River (outside Shanghai). Upon entering the region on August 2 at 6:00, Damrey stops growing and decays rapidly after it lands onto Jiangsu. Similarly, a local inverse baroclinic cascade over Fujian and Taiwan may cause the decay of Saola after its landing.

Note that when Damrey and Saola land, they are close to each other. As argued in Guinn and Schuber [32], two vortices will interact when getting together, with the strong one annihilating the weak one. The final decay of Damrey could be related to this kind of interaction mechanism; a discussion of it, however, is beyond the scope of this study.

7. Concluding remarks

In late July-early August 2012, a devastating typhoon, Damrey, landed on Jiangsu, the populous coastal province of China, causing severe flooding and other disasters in East China. Damrey is special in that it is of higher latitude origin, and, besides, it forms a part of a twin typhoon (another part is Saola). In this study, we investigated the multiscale dynamical processes that lead to the formation, maintenance, and decay of the phenomenon, using a newly developed functional analysis tool, multiscale window transfer (MWT), and the MWT-based localized multiscale energy and vorticity analysis (MS-EVA).

We first reconstructed the atmospheric fields onto three orthogonal subspaces, namely, the large-scale window, tropical cyclone-scale window, and cumulus convection-scale window, and then diagnosed the local Lorenz cycles among them. Based on the results, the two cyclones form in the lower troposphere due to some barotropic instabilities. To be specific, we have identified a pronounced area of barotropic instability in the region of 145–150°E, 20–25°N, and, remarkably, it corresponds to the birthplace of the tropical depression—the Damrey in its infant stage. The initial disturbance receives kinetic energy (KE) from the large-scale basic flow in lower troposphere and develops upward. This agrees with Duan and Wu [20], who found that barotropic transfers make significant contribution to the tropical cyclones generated at the confluence region of and inside the monsoon trough. It also agrees with Maloney [12] who concluded that during the formation stage of a tropical cyclone, eddy kinetic energy mainly comes from the large-scale circulation. In other words, the initial formation has little relation to baroclinic processes. In fact, Damrey receives available potential energy (APE) from the large-scale window in middle levels (700–500 hPa), and returns it to the same window at 300 hPa. But on the whole, the net canonical APE transfer between the large-scale and cyclone windows is insignificant, suggesting that Damrey's birth is not caused by accumulating of APE.

But the further developments of Damrey and its peer Saola are indeed related to baroclinic processes and, particularly, baroclinic instabilities in the upper troposphere. Their rapid intensifications after formation both happen at the strong baroclinic instability areas in the middle and upper troposphere. Nonetheless, the canonical transfers after formation are, in general, rather unfavorable to the maintenance of Damrey, especially the negative transfer over the East China Sea outside Shanghai (at the mouth of Yangtze River). The intense barotropic and

baroclinic inverse cascades are responsible for the rapid decay of Damrey before landing. But since at this time, its twin counterpart is just nearby, the final decay of Damrey is likely to be related to the interaction with Saola, a mechanism we leave to future studies.

It merits mentioning that the energetic scenario during the cyclogenesis of Damrey has a distinct vertical structure. We have seen from the analysis above that Damrey gets KE from the large-scale flow in the lower troposphere (below 500 hPa) and loses KE to the large-scale window and the convection window above. This explains why Damrey forms from lower to higher levels. Also, this is in accordance with Zhang and Bao [33], who proposed a "bottom-up hypothesis": deep convection will develop from bottom to top under the organization of mesoscale convective vortices (MCV) and lead to the formation of tropical cyclones.

The cumulus convection has been said to play a role in tropical cyclogenesis (e.g., [3]). In this study, however, the transfer between the convection and cyclone windows is always weak, implying that cumulus convections do not serve as an energy source, agreeing with air-sea interaction theory by Emanuel [34, 35], who argues that cumulus convections only function to transport energy rather than provide energy source in tropical cyclone formation. However, his hypothesis that the energy source be moisture entropy (estimated with equivalent potential temperature in his papers) from the underlying ocean is yet to be verified. In this special case, as we have seen before, Damrey forms as energy is extracted through a barotropic instability from the background flow. That is to say, the background flow provides the needed energy source. We hope to verify the existing theories of cyclogenesis in more case diagnoses with the new methodology.

Acknowledgements

Thanks are due to ECMWF for the ERA-interim data and to CMA for the track data. This study was partially supported by the Jiangsu Provincial Government through the 2015 Jiangsu Program for Entrepreneurship and Innovation Group and the Jiangsu Chair Professorship, by the National Science Foundation of China (NSFC) under Grant 41276032 and by the State Oceanic Administration through the National Program on Global Change and Air-Sea Interaction (GASI-IPOVAI-06).

Author details

X. San Liang^{1,2*} and Lan Wang¹

*Address all correspondence to: x.san.liang@gmail.com

1 School of Atmospheric Sciences, Nanjing University of Information Science and Technology, Nanjing, China

2 School of Marine Sciences, Nanjing University of Information Science and Technology, Nanjing, China

References

- [1] Gray WM. Global view of the origin of tropical disturbances and storms. *Monthly Weather Review*. 1968;**96**:87
- [2] Wang L, Liang XS. A diagnosis of some dynamical processes underlying a higher-latitude typhoon using the multiscale window transform. *Atmosphere*. 2017;**8**:118. DOI: 10.3390/atmos8070118
- [3] Cheung KKW. Large-scale environmental parameters associated with tropical cyclone formations in the western north pacific. *Journal of Climate*. 2010;**17**:466-484
- [4] Landsea CW. A climatology of intense (or major) atlantic hurricanes. *Monthly Weather Review*. 1993;**121**:1703
- [5] Molinari J, Vollaro D, Skubis S, Dickinson M. Origins and mechanisms of eastern pacific tropical cyclogenesis: A case study. *Monthly Weather Review*. 2000;**128**:2010
- [6] Li XY, Wu LG, Zong HJ. Analysis of influence of monsoon gyres on tropical cyclogenesis over the western North Pacific. *Transactions of Atmospheric Sciences*. 2014;**37**:653-664. (in Chinese)
- [7] Qiu WY, Wu LG. Influence of north-west Pacific monsoon depression on tropical cyclogenesis. *Chinese Journal of Atmospheric Sciences*. 2015;**35**:237-247. (in Chinese)
- [8] Ritchie EA, Holland GJ. Large-scale patterns associated with tropical cyclogenesis in the western Pacific. *Monthly Weather Review*. 1999;**127**:2027-2043
- [9] Zhang WL, Zhang DL, Wang AS, Cui XP. An investigation of the genesis of typhoon Durian (2001) from a monsoon trough. *Acta Meteorologica Sinica*. 2008;**67**(5):811-827. (in Chinese)
- [10] Zong HJ, Wu LG. Re-examination of tropical cyclone formation in monsoon troughs over the western North Pacific. *Advances in Atmospheric Sciences*. 2015;**32**:924-934
- [11] Maloney ED, Hartmann DL. Modulation of hurricane activity in the gulf of Mexico by the Madden-Julian oscillation. *Science*. 2000;**287**:2002-2004
- [12] Maloney ED, Hartmann DL. The Madden-Julian oscillation, barotropic dynamics, and North Pacific tropical cyclone formation. Part I: Observations. *Journal of the Atmospheric Sciences*. 2001;**58**:2545-2558
- [13] Sun Z, Mao JY, Wu GX. Influences of intraseasonal oscillations on the clustering of tropical cyclone activities over the western North Pacific during boreal summer. *Chinese Journal of Atmospheric Sciences*. 2009;**33**:950-958. (in Chinese)
- [14] Zhu CW, Nakazawa T, Li JP. Modulation of tropical depression/cyclone over the Indian-Western Pacific oceans by Madden-Julian oscillation. *Chinese Journal of Atmospheric Sciences*. 2004;**62**:42-50. (in Chinese)

- [15] McBride JL, Keenan TD. Climatology of tropical cyclone genesis in the Australian region. *International Journal of Climatology*. 1982;**2**:13-33
- [16] Montgomery MT, Farrell BF. Tropical cyclone formation. *Journal of the Atmospheric Sciences*. 1993;**50**:285-308
- [17] Sadler JC. A role of the tropical upper tropospheric trough in early season typhoon development. *Monthly Weather Review*. 1974;**104**:57
- [18] Ooyama KV. Conceptual evolution of the theory and modeling of the tropical cyclone. *Journal of the Meteorological Society of Japan*. Ser. II. 1982;**60**:369-380
- [19] Papin P. Using the Rossby radius of deformation as a forecasting tool for tropical cyclogenesis. In: *Proceedings of the National Conference on Undergraduate Research*; 31 March-2 April 2011; Ithaca, NY, USA
- [20] Duan JJ, Wu LG. Kinetic energy budget analysis of tropical cyclogenesis precursors in the monsoon trough. *Chinese Journal of Atmospheric Sciences*. 2016;**36**:141-148. (in Chinese)
- [21] Batchelor GK. *The Theory of Homogeneous Turbulence*. Cambridge: Cambridge University Press; 1953
- [22] Strang G, Nguyen T. *Wavelets and Filter Banks*. Wellesley: Wellesley-Cambridge Press; 1996
- [23] Liang XS, Anderson DGM. Multiscale window transform. *SIAM Journal on Multiscale Modeling & Simulation*. 2007;**6**:437-467
- [24] Liang XS. Canonical transfer and multiscale energetics for primitive and quasi-geostrophic atmospheres. *Journal of the Atmospheric Sciences*. 2016;**73**:4439-4468. DOI: 10.1175/JAS-D-16-0131.1
- [25] Liang XS, Robinson AR. Localized multiscale energy and vorticity analysis: I. Fundamentals. *Dynamics of Atmospheres and Oceans*. 2005;**38**(3):195-230
- [26] Pope SB. *Turbulent Flows*. Cambridge: Cambridge University Press; 2004. p. 771
- [27] Holopainen EO. A diagnostic study on the kinetic energy balance of the long-term mean flow and the associated transient fluctuations in the atmosphere. *Geophysica*. 1978;**15**:125-145
- [28] Plumb RA. A new look at the energy cycle. *Journal of the Atmospheric Sciences*. 1983;**40**:1669-1688. 1669: ANLATE.2.0.CO;2. DOI: 10.1175/1520-0469(1983)040
- [29] Liang XS, Robinson AR. Localized multi-scale energy and vorticity analysis: II. Finite-amplitude instability theory and validation. *Dynamics of Atmospheres and Oceans*. 2007;**44**:51-76
- [30] Tao YW. Analysis of the August 2012 atmospheric circulation and weather. *Meteorological Monographs*. 2012;**28**(11):1429-1435. (in Chinese)
- [31] Zhou NF. Analysis of the July 2012 atmospheric circulation and weather. *Meteorological Monographs*. 2012;**38**(10):1307-1312. (in Chinese)

- [32] Guinn TA, Schubert WH. Hurricane spiral bands. *Journal of the Atmospheric Sciences*. 1993;**50**:3380
- [33] Zhang DL, Bao N. Oceanic cyclogenesis as induced by a mesoscale convective system moving offshore. Part II: Genesis and thermodynamic transformation. *Monthly Weather Review*. 1996;**124**:2206
- [34] Emanuel KA. An air-sea interaction theory for tropical cyclones. Part I: Steady-state maintenance. *Journal of the Atmospheric Sciences*. 1986;**43**:585-605
- [35] Emanuel KA. The theory of hurricanes. *Annual Review of Fluid Mechanics*. 2003;**23**:179-196

Urbanization and Its Impacts

Analysis of Urban Impervious Surface in Coastal Cities: A Case Study in Lianyungang, China

Tingchen Jiang, Yuxi Liu, Kapo Wong,
Yuanzhi Zhang, Yu Li and X. San Liang

Additional information is available at the end of the chapter

<http://dx.doi.org/10.5772/intechopen.80019>

Abstract

Impervious surface is an important indicator of the level of urbanization. It is of great significance to study the impervious surface to promote the sustainable development of the city. In the process of urban development, the increase of impervious surface cities is bound to be accompanied by a reduction of one or more types of land use in the city. This paper, taking Lianyungang as an example, introduces the methods of extracting urban impervious surface based on VIS model, NDVI (normalized vegetation index), MNDWI (modified normalized water body index), and unsupervised classification, analyzes the changes of impervious surface in Lianyungang from 1987 to 2014, and on this basis, analyzes the trend and driving forces of land use types in Lianyungang city in depth. The results show that the impervious surface of Lianyungang increased by a total of 29.70% between 1987 and 2014. While the impervious surface continues to increase, the area of cultivated land and coastal areas (including salt works and tidal flats) has been greatly reduced, and the types of land use have undergone significant changes.

Keywords: impervious surface, urbanization, land use, driving factor

1. Introduction

Impervious surface refers to the natural or artificial surface that can prevent vertical runoff (surface water penetrates directly into the soil), mainly including asphalt pavement, square and roof of buildings [1]. As a typical component of surface coverage, the impervious surface can be used as a basis for measuring the difference of urbanization level in different areas,

and it is one of the important indexes to measure the urban ecological environment [2]. It is of great importance to study the impervious surface of the city in terms of more effective solutions to urban problems and the promotion of sustainable urban development.

Remote sensing is the most important and effective technology of monitoring impervious surface. The methods of remote sensing for monitoring impervious surfaces are usually classified into three types [3, 4]: interpretation and classification, model simulation and spectral analysis method, which mainly includes CART [5–7], Multiple Regression [5], Image Classification [5], Sub Pixel Classification [1, 8], and ANN [6].

As one of the first open coastal cities in China, Lianyungang has now developed into an international port city and one of China's top 10 seaports. Lianyungang is still the East Bridgehead of the New Eurasian Continental Bridge, the East Bridgehead of the Silk Road Economic Belt, the pilot city of the national innovation, and the central city for the development of the coastal areas of Jiangsu. In addition, Lianyungang is an important population concentration area and a center for political, economic, and cultural activities. It has obvious locational advantages and valuable resources, and it has great advancement and leading role in the development of the national economy. Studying the dynamic changes of impervious surface in Lianyungang city can help us understand the development history of Lianyungang city and promote the sustainable development of the city and the scientific development of the economy. Although the definition of impervious surface in cities has attracted widespread attention among relevant scholars and researchers, there are few research data on the impervious surface of coastal cities represented by Lianyungang city. Since the reform and opening up, the rapid development of Lianyungang has caused a lot of urban problems. Based on the theoretical model of V-I-S, this study uses the NDVI index, MNDWI index, and unsupervised classification technology to extract and analyze the impervious surface of Lianyungang city.

2. Study area and data used

2.1. Study area

Lianyungang city is located on the eastern coast of mainland China and is located in the northeast of Jiangsu province (**Figure 1**). The geographical range is between latitude 33°59'–35°07'N and longitude 118°24'–119°48'E. The total land area is 7499.9 km², the water area is 1759.4 km², and the urban built-up area is 120 km². Since the reform and opening up, the level of urbanization in Lianyungang city has been developing rapidly. Its most obvious manifestation is the continuous increase in impervious surface. With the development of globalization and information technology, the urbanization process of Lianyungang city will continue to deepen.

2.2. Data used

The data used in this study were downloaded from the USGS. A total of four images were recorded in 1987, 1996, 2005, and 2014. All images are from the US Land Exploration Satellite System. The auxiliary data are the administrative boundary vector data of Lianyungang city. Specific image data information is shown in **Table 1**.

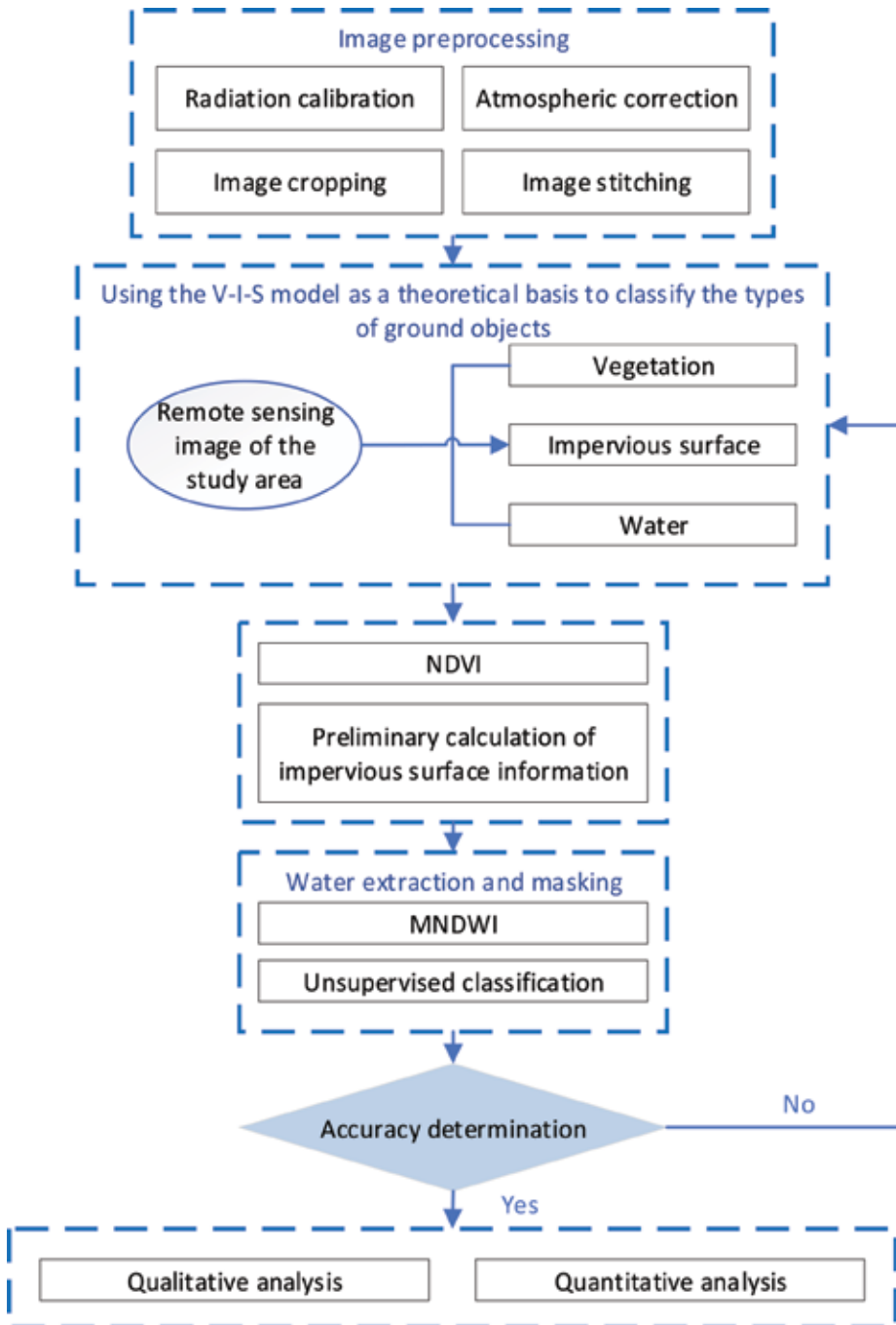


Figure 2. Flowchart of the technical route.

3.2. V-I-S model

In 1995, by analyzing the type of urban land cover, Ridd puts forward the model of surface property composition of urban ecological system and builds the V-I-S model (Vegetation-Impervious Surface-Soil) [10] of urban surface coverage. He supposes that the ground surface of the city is composed of vegetation, water, and soil with different proportions [11]. He suggested that V-I-S model provide the basis for describing biophysical composition of the urban environment and become the basis of further analysis of the urban environment [12, 13]. In this model, if the water surface is ignored, urban coverage can be modeled by soil, impervious surfaces, and the fraction of vegetation. This study is based on the V-I-S model. At the same time, in actual remote sensing images, the surface cover of Lianyungang city is divided into three types: water body, vegetation, and impervious surface, because the bare soil surface is small and negligible. This can be concluded that, with the exception of water, there is a negative correlation between vegetation and water impervious surface in Lianyungang city.

The NDVI (Normalized Difference Vegetation Index) [14–19], also known as biomass index change, makes vegetation to be separated from water and soil. According to the negative correlation between vegetation coverage and impervious surface, this study used vegetation coverage calculation based on NDVI index to extract impervious surface information in Lianyungang city.

The vegetation coverage calculated for the study is based on the standard vegetation index, and its expression is as follows:

$$NDVI = \frac{NIR - Red}{NIR + Red} \quad (1)$$

According to the NDVI, an information map reflecting the vegetation coverage on the ground can be calculated, and the expression of vegetation coverage is as follows:

$$V_c = \frac{NDVI - NDVI_{soil}}{NDVI_{veg} - NDVI_{soil}} \quad (2)$$

The region can be approximated as $NDVI_{veg} = NDVI_{max}$, $NDVI_{soil} = NDVI_{min}$, so the formula in the above can be changed to:

$$V_c = \frac{NDVI - NDVI_{min}}{NDVI_{max} - NDVI_{min}} \quad (3)$$

Based on the negative correlation between impervious surface and vegetation, impervious surface can be calculated by the following formula:

$$IS = 1 - V_c \quad (4)$$

3.3. Improved normalized differential water index (MNDWI) and unsupervised classification

The most common water index is the differential water index (NDWI) [20, 21]. NDWI uses the green belt and near infrared to calculate the difference. This method effectively eliminates vegetation information to highlight moisture but neglects the impact of buildings [22]. Considering the larger urban area in the study area, we chose the improved normalized differential water index (MNDWI). This method utilizes the difference of objects in different bands and highlights the information of the water body through proportional calculations. The formula is as follows:

$$MNDWI = \frac{Green - MIR}{Green + MIR} \quad (5)$$

Unsupervised classification technique, also known as clustering or point group analysis, is defined as the process of searching for similar spectral cluster groups in multispectral remote sensing images and classifying them [23, 24]. According to the distribution of the spectral features of the remote sensing imagery, unsupervised classification technology can distinguish the different types of land features in remote sensing images. At present, the most widely used method in the unsupervised classification is the dynamic clustering method, which mainly includes the K-means mean value algorithm, the heuristic method based on the nearest neighbor rule, and the iterative self-organized data analysis method (ISODATA).

This study combines MNDWI with unsupervised classification algorithms. The water body information image of Lianyungang city was calculated using the MNDWI index, and then, the unsupervised classification algorithm was used to extract the water body vector image and mask processing.

4. Result and discussion

4.1. Accuracy verification

In this study, some reference sample points were randomly selected from the original image. The classification accuracy was evaluated using RMS error. Root mean square error is the deviation between the measured observation and the actual value, and the result must be less than 0.02. In order to quantitatively evaluate the accuracy of the model, the accuracy of the root mean square (RMS) error of the impervious surface gray scale in Lianyungang was tested. The RMSE results for 1987, 1996, 2005, and 2014 are 0.007532, 0.004238, 0.006820, and 0.001956, respectively. All four results are less than 0.02, so the results of this study meet the accuracy requirements.

4.2. Preliminary extraction of impervious surface based on V-I-S model and NDVI index

The main function of NDVI index is to distinguish vegetation from water and soil, and according to the negative correlation between vegetation coverage and impervious surface,

impervious surface information image can be calculated. Through the calculation of remote sensing images of Lianyungang city in 1987, 1996, 2005, and 2014, the vegetation coverage maps of Lianyungang city can be separately obtained.

4.3. Water extraction and mask based on MNDWI index and unsupervised classification

Using the MNDWI index and unsupervised classification algorithm to extract water from remote sensing images in Lianyungang city. First, the center point is randomly selected in the initial image, and the distance from the pixel to the center is calculated. According to the minimum distance rule, it is divided into corresponding category groups. In this study, the maximum number of iterations was set to 15 and the cluster components were divided into 5 categories. Compared with the original remote sensing image, the water group can be clearly identified and the black and white mask image can be extracted. The water obtained through unsupervised classification is shown in **Figure 3**.

4.4. Quantitative estimation of impervious surface

After masking the water body, the final water-impermeable surface map can be obtained. The impervious surface image after the water mask is shown in **Figure 4**. The impervious surface area can be calculated by selecting the appropriate threshold. In this study, the selected thresholds were further tested and evaluated by Google Earth satellite images. In addition, due to the selection of sufficient reference data, a suitable random sampling method was applied. Specific results are presented in **Table 2**.

4.5. Spatial analysis of land use types in Lianyungang city

4.5.1. Analysis on the changing trend of land use types in Lianyungang city

Comparing the impervious surface image with the original image, from the general trend of changes in land use structure, while the impervious surface continues to increase, the area of cultivated land and coastal areas (beach and salt fields) has decreased significantly. From 1987 to 1996, the increased impervious surface was mainly transformed from arable land. From 1996 to 2005, while the continuous decrease of cultivated land, the impervious surface in the coastal area has increased significantly. From 2005 to 2014, the impervious surface in the coastal areas increased more significantly, and the increased impervious surface was mainly composed of coastal beaches and salt fields.

4.5.2. Analysis on driving factors of land use type change in Lianyungang city

4.5.2.1. Natural drivers

From 1987 to 1996, the economic development of Lianyungang city was relatively backward, and the topography was the main factor affecting human agglomeration. During this period, human activities were mainly in the flat terrain. Changes in land use types were mainly caused by the conversion of cultivated land to impervious surface.

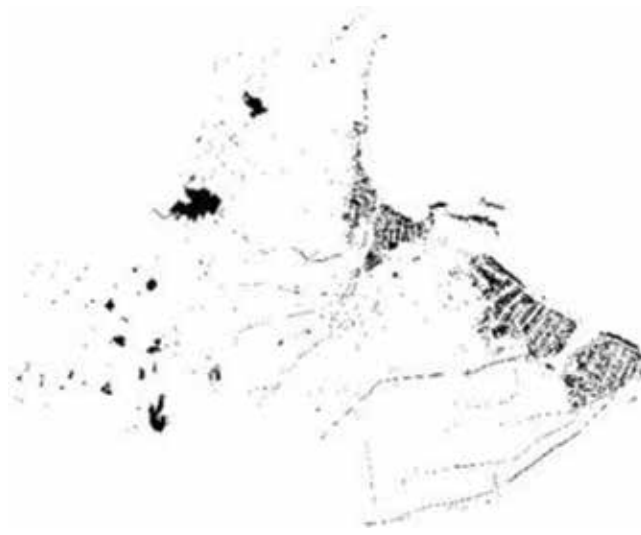


Figure 3. Water image.



Figure 4. Impervious surface image.

4.5.2.2. Social and economic drivers

The socio-economic impacts on land use types mainly include population and industry. The increase of the social population is one of the major factors affecting the changes in land use types. The population of Lianyungang increased from 3.2 million in 1987 to 5.3 million in 2014. The large increase in population directly contributed to the increase in impervious surface. In addition, from 1987 to 1996, land use types were mainly concentrated in the first industrial land, and impervious surface changes were mainly concentrated in inland areas. From 1996 to 2005, Lianyungang continued to develop the aquaculture industry while developing the

Years	1987	1996 年	2005 年	2014 年
Percentage (%)	3.17	9.24	23.93	32.87
Area (km ²)	181.95	530.38	1373.58	1886.74

Table 2. Dynamic changes information of impervious surface in Lianyungang.

traditional salt industry. Therefore, during the period when Lianyungang’s inland impervious surface growth occurred, the impervious surface of the coastal areas also showed more significant changes. From 2005 to 2014, the primary industry in Lianyungang quickly moved to the second and third industries. Under the strategic conditions of “Revitalize the city with the harbor,” the tourism industry and the port transportation industry were vigorously developed to realize the integration of the port city and the coastal area.

4.5.2.3. Policy drivers

Since 1984, China has implemented a coastal open policy. Lianyungang city is located in a key strategic development area in China. However, from 1987 to 2005, Lianyungang was unable to give full play to the unique advantages of the port city and did not make full use of characteristic resources. This directly led to the slower economic development of Lianyungang city during this period, and the Land use has outstanding inlandization characteristics. Since 2005, under the conditions of the new national development strategy, Lianyungang has focused on the development and construction of coastal areas, and the type of land use in the coastal areas has undergone major changes.

5. Conclusion

This study used the VIS model, NDVI normalized vegetation index, MNDWI index, and unsupervised classification methods to extract the impervious surface of Lianyungang city. Based on the feature types of Lianyungang city, the image was divided into impervious surface, water body, and vegetation coverage area. Based on this analysis, the changing trend and driving factors of land use types in Lianyungang from 1987 to 2014 were analyzed. The research data show that from 1987 to 2014, the impervious surface of Lianyungang city has increased by 29.7%, and the type of land use has undergone major changes with obvious stage characteristics. The general trend is that the cultivated land and the area along the beach have been greatly reduced, and the impervious area has continued to rise.

Acknowledgements

The data from the website of USGS and from the local government are highly appreciated. This research was jointly supported by the “2015 Jiangsu Shuangchuang Program” and the “National Key Research and Development Program of China (Project Ref. No. 2016YFC1402003).”

Author details

Tingchen Jiang¹, Yuxi Liu¹, Kapo Wong², Yuanzhi Zhang^{2,3*}, Yu Li⁴ and X. San Liang³

*Address all correspondence to: yuanzhizhang@cuhk.edu.hk

1 Faculty of Surveying and Mapping, Huaihai Institute of Technology, Lianyungang, China

2 Center for Housing Innovations, Chinese University of Hong Kong, Shatin, Hong Kong

3 School of Marine Sciences, Nanjing University of Information Science and Technology, Nanjing, China

4 Faculty of Information Science, Beijing University of Technology, Beijing, China

References

- [1] Lu D, Weng Q. Use of impervious surface in urban land-use classification. *Remote Sensing of Environment*. 2006;**102**(1):146-160
- [2] Arnold CL Jr, Gibbons CJ. Impervious surface: The emergence of a key urban environmental indicator. *Journal of the American Planning Association*. 1996;**62**(2):243-258
- [3] Herold ND. Mapping impervious surfaces and forest canopy using classification and regression tree (CART) analysis. In: *Proceedings ASPRS Annual Convention*. 2003
- [4] Weng Q, Lu D. A sub-pixel analysis of urbanization effect on land surface temperature and its interplay with impervious surface and vegetation coverage in Indianapolis, United States. *International Journal of Applied Earth Observations & Geoinformation*. 2008;**10**(1):68-83
- [5] Yang L, Jiang L, Lin H, et al. Quantifying sub-pixel urban impervious surface through fusion of optical and InSAR imagery. *Giscience & Remote Sensing*. 2009;**46**(2):161-171
- [6] Bernat K. Two-stage subpixel impervious surface coverage estimation: Comparing classification and regression trees and artificial neural networks. In: *Proceedings of SPIE Remote Sensing*. International Society for Optics and Photonics; 2014
- [7] Patel N, Mukherjee R. Extraction of impervious features from spectral indices using artificial neural network. *Arabian Journal of Geosciences*. 2015;**8**(6):3729-3741
- [8] Lu D, Li G, Kuang W, et al. Methods to extract impervious surface areas from satellite images. *International Journal of Digital Earth*. 2014;**7**(2):93-112
- [9] Civco D, Chabaeva A, Hurd J. A comparison of approaches to impervious surface characterization. In: *IEEE International Symposium on Geoscience and Remote Sensing*. IEEE; 2006. pp. 1398-1402
- [10] RIDD MK. Exploring a V-I-S (vegetation-impervious surface-soil) model for urban ecosystem analysis through remote sensing: Comparative anatomy for cities. *International Journal of Remote Sensing*. 1995;**16**(12):2165-2185

- [11] Perdana AP. Analysis of urban land cover change through V-I-S (vegetation-impervious surface-soil) model using multitemporal Landsat data in watersheds across DKI Jakarta. Thesis, Universitas Gadjah Mada. 2012;(1320-H-2012):91 p
- [12] Townshend JRG, Justice CO. Spatial variability of images and the monitoring of changes in the normalized difference vegetation index. *International Journal of Remote Sensing*. 1995;**16**(12):2187-2195
- [13] Hu X, Weng Q. Estimating impervious surfaces from medium spatial resolution imagery: A comparison between fuzzy classification and LSMA. *International Journal of Remote Sensing*. 2011;**32**(20):5645-5663
- [14] Yang F, Matsushita B, Fukushima T, et al. Temporal mixture analysis for estimating impervious surface area from multi-temporal MODIS NDVI data in Japan. *Isprs Journal of Photogrammetry & Remote Sensing*. 2012;**72**(3):90-98
- [15] Guo W, Lu D, Wu Y, et al. Mapping impervious surface distribution with integration of SNNP VIIRS-DNB and MODIS NDVI data. *Remote Sensing*. 2015;**7**(9):12459-12477
- [16] Dhivya B, Niranjana SS, Sarup J, Dharavath K. Mapping of impervious surface using spectral angle mapper (SAM) and NDVI techniques, case study: Bhopal City. *Indian Journal of Science & Technology*. October 2015;**8**(28). DOI: 10.17485/ijst/2015/v8i28/87121
- [17] Wu X, Cheng Q. Coupling relationship of land surface temperature, impervious surface area and normalized difference vegetation index for urban heat island using remote sensing. In: *Remote Sensing*. International Society for Optics and Photonics; 2007
- [18] Yuan F, Bauer ME. Comparison of impervious surface area and normalized difference vegetation index as indicators of surface urban heat island effects in Landsat imagery. *Remote Sensing of Environment*. 2007;**106**(3):375-386
- [19] Knight J, Voth M. Mapping impervious cover using multi-temporal MODIS NDVI data. *IEEE Journal of Selected Topics in Applied Earth Observations & Remote Sensing*. 2011;**4**(2):303-309
- [20] Gao BC. NDWI—A normalized difference water index for remote sensing of vegetation liquid water from space. *Remote Sensing of Environment*. 1996;**58**(3):257-266
- [21] Mcfeeters SK. The use of the normalized difference water index (NDWI) in the delineation of open water features. *International Journal of Remote Sensing*. 1996;**17**(7):1425-1432
- [22] Powell SL, Cohen WB, Yang Z, et al. Quantification of impervious surface in the snowmelt water resources inventory area of western Washington from 1972-2006. *Remote Sensing of Environment*. 2008;**112**(4):1895-1908
- [23] Lizarazo I. Fuzzy image regions for estimation of impervious surface areas. *Remote Sensing Letters*. 2010;**1**(1):19-27
- [24] Bezdek JC. A physical interpretation of fuzzy ISODATA. *IEEE Transactions on Systems Man & Cybernetics*. 2007;**6**(5):387-389

Evaluating Urban Heat Island Effects in Rapidly Developing Coastal Cities

Siqiang Wang, Meng Xiang, Yanan He, JinYeu Tsou,
Yuanzhi Zhang, X. San Liang and Xia Lu

Additional information is available at the end of the chapter

<http://dx.doi.org/10.5772/intechopen.80020>

Abstract

In this chapter, we present the analysis of urban heat island (UHI) effects on coastal urban areas using satellite images as a case study in Hangzhou, China. With the sustainable development of coastal areas, land use and land cover have been dramatically changed. Such changes make the phenomenon of urban heat island (UHI) becoming serious, which has brought some negative influences on human activities or public health issues in coastal regions. This study takes Hangzhou as an example of coastal cities and uses the Landsat TM, ETM+ and OLI images to retrieve the urban land surface temperature (LST). We also mapped and compared the intensity of UHI effects in different years of 2003, 2008 and 2013. The result shows that the intensity of UHI effect in 2013 was more serious than previous years, which is increasing year by year. The study also analyzed the relationship between UHI, NDVI, and NDBI and provided some useful suggestions to mitigate the UHI effects on coastal cities such as Hangzhou in China.

Keywords: urban heat island, land surface temperature, normalized difference vegetation index, normalized difference build-up index

1. Introduction

Urban heat island (UHI), which means the temperature in urban and suburban area are higher than the surrounding rural area, has become the most significant phenomenon of climate change [1]. One important reason is that the urban land space once was moist and permeable that changed to dry and impervious surface after human activities [2]. With the continuous development and expansion of the city, this phenomenon gradually becomes more common,

especially in summer. The extreme temperature increases the energy consumption of city and causes respiratory diseases and other difficulties [3]. A fast and available monitoring of UHI effect has become particularly necessary. Remote sensing technology provides a continuous monitoring of urban heat island in a vast scope. The land surface temperature can be easily retrieved by using the thermal infrared wave band [4].

There has been a lot of research on remote sensing temperature retrieval. Senanayake et al. used the thermal band (band 6) images of a serious Landsat satellite to map the distribution of the land surface temperature of Colombo City [5]. Huang et al. carried out three different methods (one radiative transfer equation (RTE) method, two mono-window algorithm methods) to retrieve the land surface temperature and demonstrated that the accuracy of the temperature results retrieved by remote sensing data is acceptable compared with the actual temperature data [6]. Rinner and Hussain used Toronto as an example to explore the relationship between land use and urban environment; the vector data analysis (zonal statistics) and descriptive statistics along with an analysis of variance (ANOVA) were applied [7]. Chen et al. combined the statistic of population and economic to build a model, argued the correlation between the investigation of urbanization and urban heat island in Beijing [8]. They also used zonal statistics (raster grid analysis and regional analysis) and geostatistical tool in ArcGIS to compare the 2 years' data and found that there was a close relationship between the remote UHI and urbanization. Some studies focus on the urban heat island of big cities in China, such as Hong Kong [9], Wuhan [10], Shanghai [11], and so on. The research objectives in this chapter have been formulated as follows: (1) to compare the change of UHI intensity on the temporal and spatial level, (2) to define the relationship among UHI, vegetation and buildings.

Hangzhou, which is in Zhejiang province, China (30°15'0"N, 120°10'0"E), was selected as the study area in this research. In recent decades, the economic development in Hangzhou is very fast, which led to urban construction activities, once the rural land has now become an urban area. Besides, the weather is wet and extremely hot in summer, so it is necessarily to mitigate the urban heat island effect. The major city area is selected in this study, which contains eight districts, such as Gongshu, Shangcheng, Xiacheng, Jianggan, Xihu, Bingjiang, Yuhang, and Xiaoshan.

2. Methodology

2.1. Data collection

The Landsat TM, ETM+ and OLI data are used in this study. The historical meteorological data are also collected. Landsat Program is the most widely used and most effective remote sensing source, which is available on the USGS website [9]. In order to have a better image quality, there are some difficulties. First, good weather condition (mainly affected by cloud cover) is a must. Second, there is little data of each month, for the repeat interval of Landsat satellite is 16 days, which means only two image data per month at the same location. In addition, the Landsat 7 data after May 31, 2003 have not been used because the scan line corrector (SLC) has failed and made some data lost. Therefore, the data that can be used are very

limited, so the chosen data are not on the same month. In that way, **Figure 1** illustrates the image data information (display in true color): March 26, 2003, ETM+; May 2, 2008, TM; April 14, 2013, OLI. All data are with little cloud cover to avoid interference.

2.2. Image preparation

Because of some inevitable interference, the data need to be processed before the analysis. First is to do radiometric calibration to correct the sensitivity of the remote sensor, topography, Sun angle, atmospheric scattering and absorption. Next is to do the geometric correction to make the image's projection precisely matches a specific projection surface or shape (here unified the projection of WGS_1984). Another important step is to do atmospheric correction to eliminate the error caused by atmospheric scattering, absorption and reflection, and the FLAASH is used in our study. Finally, it also needs to resample the image data because the resolution of the thermal band is different to other bands. The resolution of the thermal band of Landsat 5 (band 6) is 120 m, Landsat 7 (band 6) is 60 m, and Landsat 8 (bands 10 and 11) is 100 m, and the resolution of the rest other bands is 30 m. The result of the treatment is shown in **Figure 2**.



Figure 1. The original image data of study area.

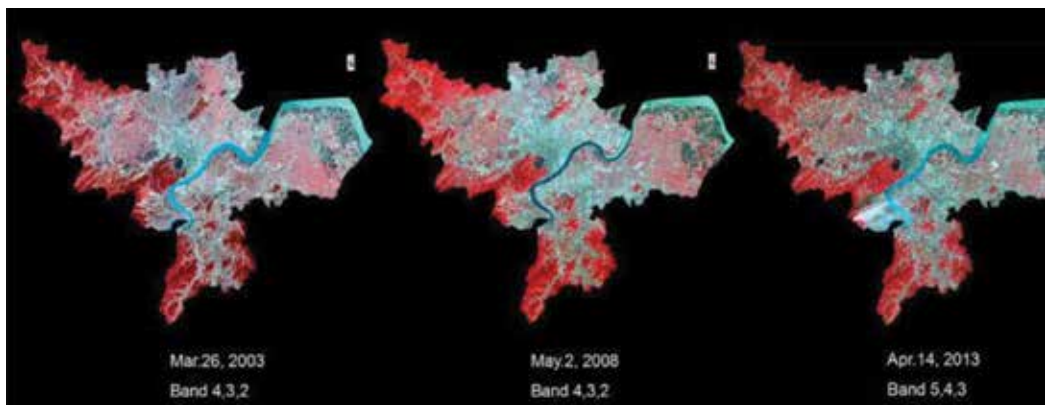


Figure 2. Prepared map combined with different band.

2.3. Method selecting

The most common ways to retrieve land surface temperature (LST) via remote sensing approaches can be summarized into four methods: (1) image-based method (IBM); (2) radiative transfer equation (RTE) also are called atmospheric correction method; (3) Qin et al.'s mono-window algorithm (MWA) [12] and (4) Jiménez-Muñoz and Sobrino single-channel algorithm (SCA) [13].

According to the literature review, it can be found that, using IBM to retrieve LST has less dependent on external factors in real times, and it only takes the impact of land surface emissivity (LSE) into account while ignoring that of atmospheric radiance (AR). When it comes to the RTE and MWA, although they both consider the influence of LSE and AR, excessive external factors which are needed in the equations may decrease the accuracy of the result. In terms of the RTE, those factors include atmospheric sounding database (τ - total atmospheric transmission; L_{\uparrow} -atmospheric upwelling radiance; L_{\downarrow} -atmospheric downwelling radiance). In terms of the MWA, those are atmospheric water vapor content and near-surface temperature.

After an overall consideration, SCA was finally chosen by our research team as the major method to conduct our study, since it only needs water vapor content as the absolute external factor, when both considering the impact of LSE and RTE.

3. The single-channel algorithm

3.1. General equations of SCA

In the SCA, LST could be expressed by the general Eq. (1) [13]:

$$T_s = \gamma \left[\frac{1}{\varepsilon} (\psi_1 L_{sen} + \psi_2) + \psi_3 \right] + \delta \quad (1)$$

In this equation, T_s is the land surface temperature in K and γ is parameter according to the Planck function (2) and (3) [13].

$$\gamma = \left\{ \frac{c^2 L_{sen}}{T_{sen}^2} \left[\frac{\lambda^4}{c_1} L_{sen} + \lambda^{-1} \right] \right\}^{-1} \quad (2)$$

$$\delta = -\gamma L_{sen} + L_{sen} \quad (3)$$

where $c_1 = 1.09104 \times 10^8 \text{ W } \mu\text{m}^4 \text{ m}^{-2} \text{ sr}^{-1}$, $c^2 = 1438.77 \text{ } \mu\text{mK}$, λ refers to the effective wavelength in μm .

Other elements needed in the general equation are ε (the surface emissivity); the at-sensor radiance in $\text{W}/(\text{m}^2 \cdot \text{sr})$; T_{sen} (the at-sensor brightness temperature in K); and the atmospheric parameters ψ_1 , ψ_2 , and ψ_3 .

3.2. Land surface emissivity

Land surface emissivity (ε) can be calculated by the value of the normalized difference vegetation index (NDVI). This index is usually used to detect the growth and coverage of vegetation. NDVI can be expressed by Eq. (4) [14]:

$$NDVI = \frac{NIR - R}{R + NIR} \tag{4}$$

Based on the study of Zhang in 2006, value of NDVI can be divided into four ranges, and each of the range corresponds to a certain value of land surface emissivity as shown in **Table 1** [14].

3.3. At-sensor radiance

L_{sen} (at-sensor radiance in $W/(m^2 \cdot sr)$) can be achieved by applying radiometric calibration in the data processing software of remote sensing (ENVI 5.1 was used in this research). The equation that used in the software is written as Eq. (5) [15]:

$$L_i = L_{min} + (L_{max} - L_{min}) Q_{dn} / Q_{max} \tag{5}$$

where L_i stands for the at-sensor spectral radiance in $MW \cdot cm^{-2} \cdot sr^{-1} \cdot \mu m^{-1}$; L_{max} and L_{min} refer to the maximum and the minimum at-sensor spectral radiance, respectively; Q_{dn} and Q_{max} are the DN value and the maximum of it in pixel.

3.4. At-sensor brightness temperature

T_{sen} (at-sensor brightness temperature in K) can be transformed from the radiance values of thermal band by Eq. (6) [15].

$$T_{sen} = \frac{K_2}{\ln\left(\frac{K_1}{L_{sen}} + 1\right)} \tag{6}$$

where K_1 and K_2 are the thermal calibration constants supplied by the Landsat Project Science Office, which are presented in **Table 2**.

3.5. Atmospheric parameters

ψ_1 , ψ_2 , and ψ_3 are three different atmospheric parameters and can be obtained in equations of atmospheric water vapor content. For TM/ETM +6 data [13], $\psi_1 = 0.14714w^2 - 0.15538w + 1.1234$, $\psi_2 = -1.1836w^2 - 0.37607w - 0.52894$, and $\psi_3 = 0.00918w^2 + 1.36072w - 0.27514$. For TIRs data [16], $\psi_1 = 0.04019w^2 + 0.02916w + 1.01523$, $\psi_2 = -0.38333w^2 - 1.50294w - 0.20324$, and $\psi_3 = 0.00918w^2 + 1.36072w - 0.27514$.

Based on the study of Jiménez-Muñoz and Sobrino [13], when the value of w is greater than $3 \text{ g} \cdot \text{cm}^{-2}$, it will have impacts on the accuracy of the result. In this situation, the original Eq. (7) has been suggested to use to obtain different atmospheric parameters ψ_1 , ψ_2 , and ψ_3 .

NDVI ranges	Main ground covers	Corresponding emissivity
<0.185	Water	0.99
0.185–0.157	Urban used land	0.956
0.157–0.727	Natural ground	$1.0094 + 0.047\ln(\text{NDVI})$
>0.727	High density vegetation	0.985

Table 1. NDVI ranges and corresponding emissivity values.

Sensor	K_1	K_2
Landsat 5 TM band6	607.76	1260.56
Landsat 7 ETM+ band6	666.09	1282.71
Landsat 8 TIRs band10	774.89	1321.80
Landsat 8 TIRs band 11	480.89	1201.14

Table 2. Thermal calibration constants.

$$\psi_1 = \frac{1}{\tau} \psi_2 = -L^\downarrow - \frac{L^\downarrow}{\tau} \psi_3 = L^\downarrow \tag{7}$$

where w is the water vapor content, which can be acquired from Eq. (8).

$$w = w(0)/R_w(0) \tag{8}$$

where $w(0)$ is the water vapor content at 2 m above the ground in the study area. It can be found in the meteorological data recorded in the local observatory. $R_w(0)$ refers to the ratio of near-surface water vapor content of air in the total water vapor content of atmosphere. According to the research by Qin et al. in [17], when the real data are hard to achieve, it can be replaced by standardized atmospheric ratio that is demonstrated in **Table 3**.

HIGHT/km	USA 1976 (Mean)	Tropical	Mid-latitude (summer)	Mid-latitude (winter)	Mean $R_w(z)$
0	0.402058	0.425043	0.438446	0.400124	0.416418
1	0.256234	0.261032	0.262100	0.254210	0.258394
2	0.158323	0.168400	0.148943	0.161873	0.159385
3	0.087495	0.075999	0.074471	0.095528	0.083373
4	0.047497	0.031878	0.038364	0.046510	0.041062
5	0.024512	0.019381	0.017925	0.023711	0.021382
6	0.012846	0.009771	0.009736	0.011514	0.010967
7	0.006250	0.004782	0.005223	0.004092	0.005087
8	0.003132	0.002257	0.002611	0.001471	0.002368
9	0.001049	0.000954	0.001315	0.000587	0.000976
10	0.000358	0.000349	0.000616	0.000238	0.000390
11	0.000142	0.000104	0.000185	0.000060	0.000123
12	0.000055	0.000032	0.000044	0.000026	0.000039
13	0.000023	0.000008	0.000009	0.000016	0.000014
14	0.000009	0.000004	0.000004	0.000011	0.000007
15	0.000006	0.000002	0.000002	0.000008	0.000004

Table 3. Water vapor content distribution by height of atmosphere.

4. Results and discussion

4.1. Land surface temperature distribution in Hangzhou

Based on **Figures 3** and **4**, it can be found that LST of Hangzhou has changed dramatically during the research period (in 2003, 2008, and 2013). In 2003, the mean temperature concentrated in the temperature ranging between 15 and 25°C. Higher temperature (over 20°C) appeared more in the central and west area, such as Yuhang district, Xihu district, the central three districts (i.e., Gongshu district, Jianggan district, and Shangcheng district), and the most part of south-western Xiaoshan district.

When it comes to 2008, compared to 2003, the mean temperature generally increased 5°C in this year, and the higher temperature moved slightly toward east area. The LST increased severely in 2013. Area of temperature in the range of 25–30°C expanded significantly. Higher temperature almost covered the whole Hangzhou city and extreme high temperature demonstrated in the central area aside by the Qiantang River evidently. However, it should be noted that the northwest corner of Xihu district had covered by cloud in that day, so the result of that area is inaccurate (**Table 4**).

4.2. Calculation of urban thermal field variance index

The urban thermal field variance index (UTFVI) is commonly used to express the urban heat island effect. It can be calculated by Eq. (9) [18]:

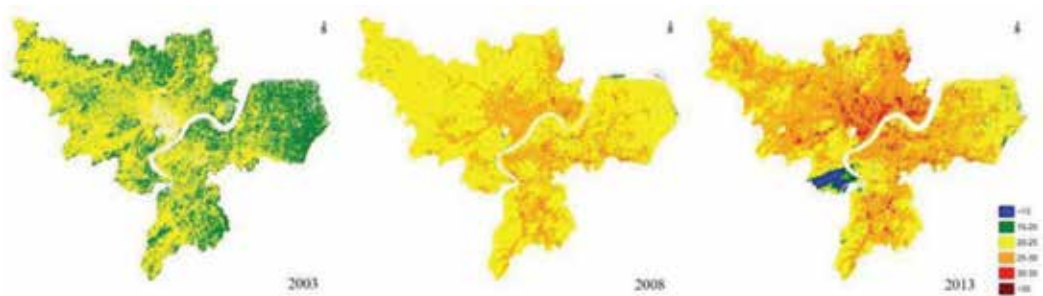


Figure 3. Land surface temperature of Hangzhou in 2003, 2008, and 2013 (°C).

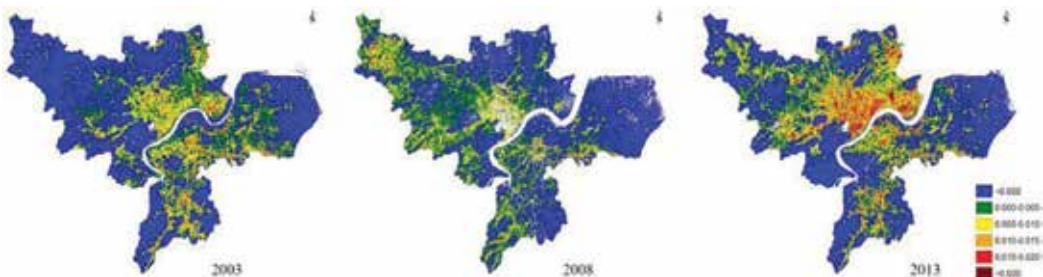


Figure 4. UTFVI of Hangzhou in 2003, 2008 and 2013.

Year	LST (Min)	LST (Max)	LST (Mean)	Stdev
2003	273.541595	309.538513	293.388575	1.683309
2008	285.579773	314.425720	297.305008	1.852384
2013	271.901184	316.897858	298.611333	3.077064

Table 4. Land surface temperature of Hangzhou in 2003, 2008, and 2013 (°C).

$$\text{UTFVI} = \frac{T_s - T_{mean}}{T_s} \quad (9)$$

where T_s is the LST in certain point of the map and T_{mean} is the corresponding mean temperature of the whole area.

In order to illustrate the level of urban heat island effect more clearly, the result of UTFVI can be divided into six categories as shown in **Table 5**, and each category is corresponded to a fixed ecological evaluation index (EEI) [18]. The result of UTFVI is shown in **Figure 4**. It can be seen that, UTFVI shows a same pattern of variation as the LST during the given period in Hangzhou city. The urban heat island phenomenon was shown more evidently in 2013, with large area in the central city present extreme high value of UTFVI (over 0.010). Correspondingly, the ecological evaluation index also got worse in this year.

4.3. Change of urban heat island intensity

Urban heat island intensity is defined by Iain D. Stewart as a simultaneous “urban-rural” temperature difference, with “rural” understood as the open countryside and “urban” as the built-up environment of the city [19], which is an index to measure the urban heat island effect.

Some calculation methods have been used in urban heat island study. One is using the difference between typical temperature of rural area and typical highest temperature of urban area [20], which is not easily used because it is difficult to find a meteorological station in rural area in natural situation that has not been impacted by cities. Another is to define the difference of several average temperatures between urban and rural area [21]. This method is widely used

Urban thermal field variance index	Urban heat island phenomenon	Ecological evaluation index
<0	None	Excellent
0.000–0.005	Weak	Good
0.005–0.010	Middle	Normal
0.010–0.015	Strong	Bad
0.015–0.020	Stronger	Worse
>0.020	Strongest	Worst

Table 5. UTFVI and its corresponding EEI.

because it is easy to calculate, however, it cannot reflect the highest rising temperature as it uses the average temperature as measure index. These methods are not easy to measure and compare because they are limited by materials and measure conditions. To avoid these disadvantages, two concepts have been introduced in this research to measure urban heat island intensity.

4.3.1. *The highest urban heat rising temperature*

The highest UHI rising temperature is the difference between the highest temperature of city center and average temperature of rural area. Eq. (10) [22] can be written as:

$$\max \Delta T_{ij} = T_{ij} - \hat{T}_R \tag{10}$$

where ΔT_{ij} is the UHI intensity of position ij, T_{ij} is the surface temperature of position ij, and \hat{T}_R is the average temperature of 32 positions in rural area in eight directions.

The results of the highest UHI rising temperature are shown in **Table 6** and **Figure 5**, which reflect the trend that the highest UHI rising temperature is increasing year by year. In the first 5 years, the change is not so apparent and from the period 2008 to 2013, there is a rapid growth and the temperature increased by approximately 2.7°C.

4.3.2. *The total amount of urban heat island rising temperature*

Another index is the total amount of UHI rising temperature, which reflects the total rising amount of temperature that UHI effects on cities in certain spatial resolution. In order to calculate the total amount of UHI rising temperature, Eq. (11) [22] can be used as:

$$T = \frac{a \times \sum_{j=1}^m \sum_{i=1}^n x_{ij}}{10000} \tag{11}$$

where T is Total amount of UHI rising temperature (°C·ha), x_{ij} is UHI intensity of position ij, and a is the area of each grid, which is 900 m² in this research.

Table 7 and **Figure 6** indicate the calculation result and change of the total amount of UHI rising temperature from 2003 to 2013. It is significant that overall the total amount of UHI rising temperature grows annually from 168681.2°C·ha in 2003 to 447284.8°C·ha in 2013, which is more than doubled. Another change trend is that from 2003 to 2008, the temperature showed a sharp increase, and in the last 5 years, the increasing speed was slowed down, which is opposite to the change of the highest UHI rising temperature. Compared with the change of two concepts,

	2003	2008	2013
Average temperature of rural area (°C)	17.41	26.77	25.4
Highest temperature of city center (°C)	28.67	38.06	39.39
Highest UHI rising temperature (°C)	11.24	11.29	13.99

Table 6. Result of the highest UHI rising temperature.

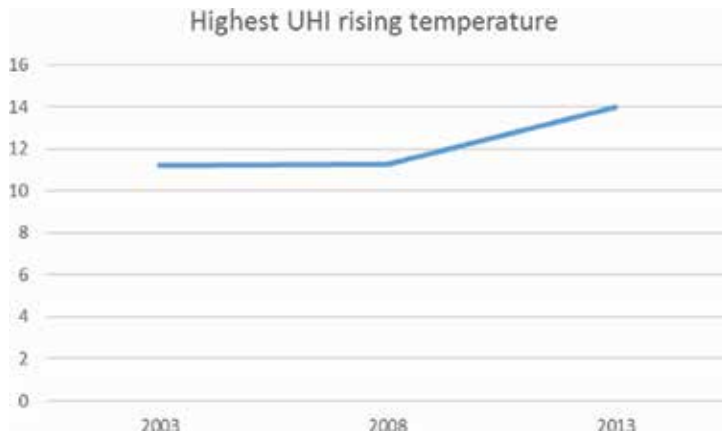


Figure 5. Change of the highest UHI rising temperature.

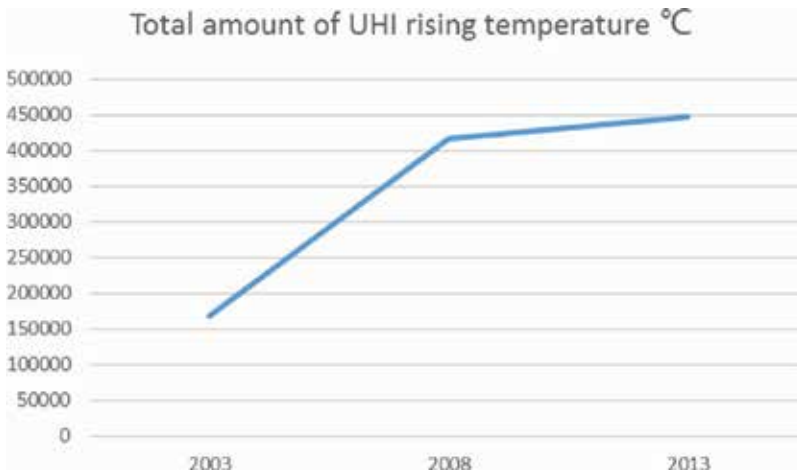


Figure 6. Change of the total amount of UHI rising temperature.

	2003	2008	2013
Sum of UHI intensity (°C)	1874235.59	4634287.11	4969830.97
Total amount of UHI rising temperature °C·ha	168681.2	417085.8	447284.8

Table 7. Result of the total amount of UHI rising temperature.

it can be found that in the first 5 years, the total amount of UHI rising temperature rose in high speed although the highest UHI rising temperature did not change a lot. In the rest years from 2008 to 2013, the change of the total amount of UHI rising temperature had been controlled and the growing speed was slowed down; in contrast, the highest rising temperature increased rapidly, which demonstrates that the temperature difference had been further expanded.

4.3.3. The urban heat island intensity

To define the differences of urban heat island intensity between 3 years, the difference between the temperature of each grid and the average temperature of rural area, which is chosen in eight directions, is used as the measurement. **Figure 7** and **Table 8** demonstrate the change of urban heat island intensity from 2003 to 2013. It can be found in figures and table that the most obvious change happened in the first 5 years as the max temperature difference increased from 11.25 to 21.09°C, and the average temperature difference increased nearly three times from 0.5 to 1.24°C.

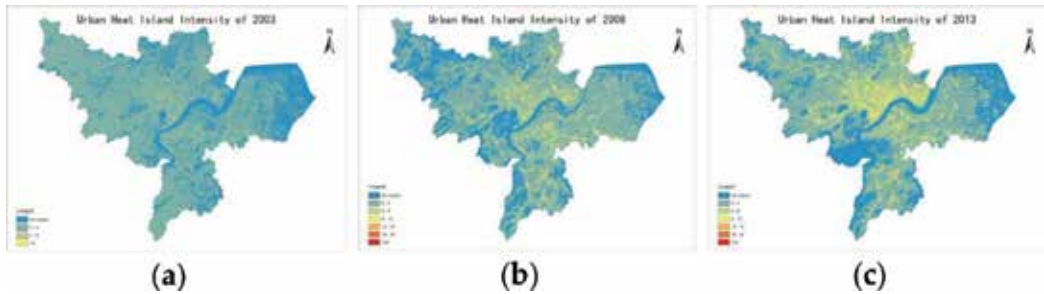


Figure 7. (a) Urban heat island intensity of Hangzhou in 2003; (b) urban heat island intensity of Hangzhou in 2008; and (c) urban heat island intensity of Hangzhou in 2013.

	2003	2008	2013
Max temperature (°C)	11.25	21.09	22.13
Average temperature (°C)	0.5	1.24	1.33

Table 8. Change of urban heat island intensity of Hangzhou from 2003 to 2013.

		UHI intensity	NDVI	NDBI
UHI intensity	Pearson correlation	1	-0.872 **	0.682**
	Sig. (two-tailed)		0.000	0.000
	N	300	300	300
NDVI	Pearson correlation	-0.872**	1	-0.799**
	Sig. (two-tailed)	0.000		0.000
	N	300	300	300
NDBI	Pearson correlation	0.682**	-0.799**	1
	Sig. (two-tailed)	0.000	0.000	
	N	300	300	300

**Correlation is significant at the 0.01 level (two-tailed).

Table 9. Correlations between UHI intensity and NDVI and NDBI index.

4.4. Response mechanism of urban heat island

The normalized difference vegetation index (NDVI) is a graphical indicator that usually be used to examine whether the object being observed contains live green vegetation or not through remote sensing measurements [23]. The normalized difference build-up index (NDBI) “highlights urban areas where there is characteristically a higher reflectance in the shortwave-infrared (SWIR) region, compared to the near-infrared (NIR) region [24].” Based on the previous research, urban heat island effect is impacted by plants and urban build-up area [24–28], so in this research, NDVI and NDBI have been selected to investigate the response mechanism of urban heat island effect.

In order to calculate the correlations between UHI intensity and NDVI and NDBI index, 300 sampling points had been chosen from high-temperature area, mid-temperature area and low-temperature area of data of 2008. The analysis of correlation is shown in **Table 9**.

Based on the study, it is significant that the urban heat island effect is impacted by NDVI and NDBI, and the NDVI has negative correlation with UHI intensity, while NDBI has positive correlation. This finding of response mechanism of UHI could provide guide to urban planners about how to control the urban heat island effect through planning and design tools.

5. Conclusion and limitation

It is significant that the area in Hangzhou which is impacted by urban heat island effect is expanded annually, and another point that should be mentioned is that the highest UHI rising temperature and total amount of UHI rising temperature show a rapid growth in past 10 years from 2003 to 2013. These changes indicate that Hangzhou is facing a big challenge caused by climate change and urban heat island effect which would have negative impact on people’s lives and economic growth.

Based on the liner regression analysis, the NDVI is negative correlated to UHI intensity, and in contrast, NDBI has the positive correlation with UHI intensity. As the UHI intensity has such close correlation with NDVI and NDBI index, two suggestions have been supposed to decrease the urban heat island effect. The first one is greenery design which means that government should encourage developers to design green roof, green pavement, and so on. Another strategy is to optimize the urban morphology, such as mix the green land with building area. These two strategies can decline the UHI intensity by spread NDVI index or drop down the NDBI index.

Nevertheless, we only measure the 3 years’ UHI intensity due to the limited time and resources, it is almost certain that more years’ data can reflect the change clearer. Another limitation is that only NDVI and NDBI have been taken into assessment. Urban heat island is a thematic effect that is caused by a various kind of factors. Further elements can be added in future study that may reflect the response mechanism better.

Acknowledgements

The data from the website of USGS and from the local government of Hangzhou are highly appreciated. This research was jointly supported by the “2015 Jiangsu Shuangchuang Program,” the “National Key Research and Development Program of China (Project Ref. No. 2016YFC1402003),” and the National Foundation of Natural Science of China (No. 41506106).

Conflicts of interest

The authors declare no conflict of interest.

Author contributions

Siqiang Wang and Yuanzhi Zhang conceived and designed the experiments, analyzed the data and wrote the chapter; Meng Xiang and Yanan He performed the experiments; Xia Lu improved the data analysis; and Jin Yeu Tsou and X. San Liang contributed to reagents/materials/analysis tools.

Author details

Siqiang Wang¹, Meng Xiang¹, Yanan He¹, JinYeu Tsou¹, Yuanzhi Zhang^{1,2*}, X. San Liang² and Xia Lu³

*Address all correspondence to: yuanzhizhang@cuhk.edu.hk

1 Center for Housing Innovations, The Chinese University of Hong Kong, Shatin, New Territories, Hong Kong

2 School of Marine Sciences, Nanjing University of Information Science and Technology, Nanjing, Jiangsu Province, China

3 Faculty of Surveying and Mapping, Huaihai Institute of Technology, Lianyungang, China

References

- [1] Santamouris M. *Energy and Climate in the Urban Built Environment*. Oxford, UK: Routledge, Taylor & Francis Group; 2013. 410p
- [2] Oke TR, Johnson GT, Steyn DG, Watson ID. Simulation of surface urban heat islands under “ideal” conditions at night part 2: Diagnosis of causation. *Boundary-Layer Meteorology*. 1991;**56**:339-358

- [3] Kolokotroni M, Ren X, Davies M, Mavrogianni A. London's urban heat island: Impact on current and future energy consumption in office buildings. *Energy and Buildings*. 2012;**47**:302-311
- [4] Adams MP, Smith PL. A systematic approach to model the influence of the type and density of vegetation cover on urban heat using remote sensing. *Landscape and Urban Planning*. 2014;**132**:47-54
- [5] Senanayake IP, Welivitiya WDDP, Nadeeka PM. Remote sensing based analysis of urban heat islands with vegetation cover in Colombo city, Sri Lanka using Landsat-7 ETM+ data. *Urban Climate*. 2013;**5**:19-35
- [6] Huang MF, Xing X, Wang PJ, Wang C. Comparison between three different methods of retrieving surface temperature from Landsat TM thermal infrared band. *Arid Land Geography*. 2006;**29**:132-137
- [7] Rinner C, Hussain M. Toronto's urban heat island—Exploring the relationship between land use and surface temperature. *Remote Sens*. 2011;**3**(6):1251-1265
- [8] Chen W, Zhang Y, Gao W, Zhou D. The investigation of urbanization and urban heat island in Beijing based on remote sensing. *Procedia - Social and Behavioral Sciences*. 2016;**216**:141-150
- [9] Liu L, Zhang Y. Urban heat island analysis using the Landsat TM data and ASTER data: A case study in Hong Kong. *Remote Sensing*. 2011;**3**:1535-1552
- [10] Shen H, Huang L, Zhang L, Wu P, Zeng C. Long-term and fine-scale satellite monitoring of the urban heat island effect by the fusion of multi-temporal and multi-sensor remote sensed data: A 26-year case study of the city of Wuhan in China. *Remote Sensing of Environment*. 2016;**172**:109-125
- [11] Li J, Wang X, Wang X, Ma W, Zhang H. Remote sensing evaluation of urban heat island and its spatial pattern of the Shanghai metropolitan area, China. *Ecological Complexity*. 2009;**6**:413-420
- [12] Qin Z, Karnieli A, Berliner P. A mono-window algorithm for retrieving land surface temperature from Landsat TM data and its application to the Israel-Egypt border region. *International Journal of Remote Sensing*. 2001;**22**:3719-3746
- [13] Jiménez-Muñoz JC, Sobrino JA. A generalized single-channel method for retrieving land surface temperature from remote sensing data. *Journal of Geophysical Research-Atmospheres*. 2003;**108**
- [14] Zhang J, Wang Y, Li Y. A C++ program for retrieving land surface temperature from the data of Landsat TM/ETM+ band6. *Computers & Geosciences*. 2006;**32**:1796-1805
- [15] Zhi Q, Ming Z, Karnieli A, Berliner P. Mono-window algorithm for retrieving land surface temperature from Landsat TM6 data. *Acta Geographica Sinica*. 2001;**56**(4):456-466
- [16] Han-Qiu X. Retrieval of the reflectance and land surface temperature of the newly-launched Landsat 8 satellite. *Chinese Journal of Geophysics-Chinese Edition*. 2015;**58**:741-747

- [17] Qin Z, Li W, Zhang M, Karnieli A, Berliner P. Estimating of the essential atmospheric parameters of mono-window algorithm for land surface temperature retrieval from Landsat TM6. *Remote Sensing for Land & Resources*. 2003;**2**:37-43
- [18] Zhang Y, Yu T, Gu X, Zhang Y, Chen L, Yu S, Zhang W, Li X. Land surface temperature retrieval from CBERS-02 IRMSS thermal infrared data and its applications in quantitative analysis of urban heat island effect. *Journal of Remote Sensing-Beijing*. 2006;**10**:789
- [19] Stewart ID. Measuring the Urban Heat Island Intensity: Challenges with “Urban-Rural” Differentiation and the East Asian City. Available online: http://www.lsgi.polyu.edu.hk/RSRG/resources/News/2nd_ws/abstract/stewart.pdf [Accessed: April 10, 2016]
- [20] Lowry WP. Empirical estimation of urban effects on climate: A problem analysis. *Journal of Applied Meteorology*. 1977;**16**:129-135
- [21] LIN X, YU S. Interdecadal changes of temperature in the Beijing region and its heat island effect. *Chinese Journal of Geophysics*. 2005;**48**:47-54
- [22] Huang H, Yun Y, Zhao R. Key parameters in urban form layout for weakening urban heat island intensity and its response mechanism. *Tumu Jianzhu Yu Huanjing Gongcheng/ Journal of Civil Architectural & Environmental Engineering*. 2014;**36**:95-102
- [23] Normalized Difference Vegetation Index. Wikipedia 2016. Available online: https://en.wikipedia.org/w/index.php?title=Normalized_Difference_Vegetation_Index&oldid=710783256 [Accessed: March 19, 2016]
- [24] Zha Y, Gao J, Ni S. Use of normalized difference built-up index in automatically mapping urban areas from TM imagery. *International Journal of Remote Sensing*. 2003;**24**:583-594
- [25] Kumar D, Shekhar S. Statistical analysis of land surface temperature–vegetation indexes relationship through thermal remote sensing. *Ecotoxicology and Environmental Safety*. 2015;**121**:39-44
- [26] Li X, Li W, Middel A, Harlan S, Brazel A, Turner B. Remote sensing of the surface urban heat island and land architecture in Phoenix, Arizona: Combined effects of land composition and configuration and cadastral–demographic–economic factors. *Remote Sensing of Environment*. 2016;**174**:233-243
- [27] Tian P, Tian G, Wang F, Wang Y. Urban heat island effect and vegetation cover index relation using Landsat TM image. *Bulletin of Science and Technology*. 2006;**5**:28
- [28] Li Y, Zhang J, Gu R. Research on the relationship between urban greening and the effect of urban heat island. *Journal of Chinese Landscape Architecture*. 2004;**1**:72-75

Methodology Development

Evaluation of Ocean Forecasting in the East China Sea

Xiaochun Wang, Yingjun Zou and Xianqiang He

Additional information is available at the end of the chapter

<http://dx.doi.org/10.5772/intechopen.80319>

Abstract

The accuracy of the initial condition of a global ocean forecasting system and its prediction skill was evaluated against in situ temperature, salinity and satellite salinity observations during the winter of 2015 and the summer of 2016 for the East China Sea. The ocean forecasting system demonstrates better skill for the Yangtze River estuary and the East China Sea during winter time than during summer time. During winter time, the root-mean-square error (RMSE) of the initial fields of the system for salinity is 1.90 psu, and the correlation is 0.56. The model has a salty bias of 0.29 psu. The salinity RMSE reduces with increasing distance from the coast. In contrast, the RMSE for temperature is 0.76°C, and the correlation is as high as 0.95. There is no bias between model temperature and observation. During summer time, the accuracy and forecast skill of the global ocean forecasting system are very poor. The RMSE for salinity is 3.14 psu, and the correlation is 0.28. The model has a salty bias of 0.95 psu. The RMSE for temperature is 7.22°C, and the model has a warm bias as high as 5.52°C.

Keywords: HYCOM, East China Sea, Yangtze River discharge

1. Introduction

Recent two decades have seen a rapid development in ocean forecasting systems for various regions of the world ocean due to the development in ocean observing systems, ocean models, data assimilation algorithms and computing hardware and software. Currently, numerous institutions provide ocean forecasting operationally (e.g., [1–6]). The skill of these forecasting systems may differ for various regions of the ocean because of the model bathymetry, atmospheric forcing fields, and availability of data that can be used in data assimilation process. Given the potential application of these forecasting systems, the evaluation of the forecasting skill of these forecasting systems is a necessary step.

The East China Sea, especially the region of Yangtze River estuary and the coastal region of Jiangsu and Zhejiang provinces, is a region of great economic interest since the region has the largest harbor of the world besides many other economic activities. This region is also influenced heavily by freshwater runoff from the Yangtze River, which has an annual averaged discharge around 30,000–40,000 m³/s and is the fourth largest river of the world. Given the economic and scientific interest of the region, we evaluated the accuracy of the initial fields of a global ocean forecasting system in the region against in situ temperature, salinity measurements, and satellite sea surface salinity measurements.

The global ocean forecasting system is the one used operationally by U.S. Navy. The system is configured from the HYbrid Coordinate Ocean Model (HYCOM, e.g., [5, 7–9]). Besides many other applications, HYCOM was also used in the Chinese coastal oceans, for example, the South China Sea (e.g., [10–12]), the Yellow Sea [13], the Yellow Sea and the Kuroshio region [14], and the East China Sea [15, 16]. Based on the comparison between monthly SST with output from a circulation model configured from the HYCOM, Lu et al. [10] identified the spatial difference in the quality of simulation. In general, the model performs well in the deep sea region and tends to have large errors in the shallow regions because of the error in heat flux. The conclusion from Lu et al. [10] is further verified in [11], which indicates that the root mean square error in SST simulation in the South China Sea is generally less than 1°C and less than 0.5°C in the middle of the ocean basin of the South China Sea. However, the root mean square error in the coastal region is larger than 1°C. Comparison of ocean models based on HYCOM, POM, and ROMS in the South China Sea region does indicate better performance of HYCOM in the thermocline and in the regions of steep bathymetry. There is a large difference in the simulation of temperature and salinity field in the Yellow Sea [13]. For temperature field, the accuracy of HYCOM reanalysis is greatly improved after using observations in data assimilation. For salinity field, there is not much improvement between the reanalysis and analysis field.

The global ocean forecasting system used in the study has a horizontal resolution of 0.08° and 32 hybrid vertical coordinate surfaces. The data assimilation algorithm can assimilate various types of data, sea surface height, sea surface temperature from satellites, in situ data from CTD, XBT, Argo floats and gliders, and many other types of data [17]. The atmospheric forcing fields are from the NAVy Global Environmental Model (NAVGEN), with 3-h temporal interval. The river discharge includes climate discharge of 986 rivers in various regions of the world [5]. The forecasting fields are available to the public with a delay less than 24 h and can be used for societal application, such as oil platform operation, ship routing planning, and so on. However, there is not much work to evaluate the performance of the global ocean forecasting system in the Chinese coastal ocean. The present research evaluates the performance of the global ocean forecasting system in the East China Sea region using in situ observation and satellite sea surface salinity observation. The in situ CTD measurements used to evaluate the global forecasting system are from two field campaigns: one in the winter of 2015 and one in the summer of 2016. Thus, our comparison also focuses on these two periods.

This chapter is organized as follows. After Section 1, the details of the global forecasting system are presented in Section 2, so are the in situ campaigns, data and processing details. Section 3 evaluates the initial fields and forecast skill of the global ocean forecasting system for the winter of 2015 and the summer of 2016. Our findings are summarized in Section 4.

2. HYCOM global ocean forecasting system and observations

2.1. HYCOM global ocean forecasting system

The HYbrid Coordinate Ocean Model is based on a density coordinate ocean model developed at University of Miami [7]. The vertical coordinate of HYCOM can be switched between Z coordinate, density coordinate and σ coordinate. The Z-coordinate can be used in the upper ocean mixed layer where stratification is weak or even unstable. The σ -coordinate can be used for shallow coastal regions and regions where bathymetry varies significantly. The density coordinate can be used in the open ocean where stratification is strong. Compared to the ocean modeling systems that only use single vertical coordinate, HYCOM provides the flexibility to handle different situations [8, 9, 18]. For instance, it was also demonstrated that HYCOM performs better to simulate variability of thermocline in the South China Sea compared with POM and ROMS [12].

Based on HYCOM, the U.S. Navy has developed a global ocean forecasting system, with horizontal resolution of 0.08° . The system is nearly global, with a domain of 78.64°S - 66°N , 180°W - 180°E , and provides ocean forecasting for 1 week. The atmospheric forcing fields are from NAVy Global Environmental Model (NAVgEM), with 3-h temporal interval. The river discharge is included through climate river discharge of 986 rivers [5].

Using a 3D multivariate variational data assimilation scheme, the system can assimilate various ocean observations, such as sea surface height, sea surface temperature, sea surface salinity from satellite missions, in situ temperature and salinity from CTD, XBT, Argo floats and gliders, and vector current observations [17].

In our research, we compared the initial fields of the system at 0 GMT and its forecasting fields for 7 days also at 0 GMT. The output of the global forecasting system is already interpolated to Z coordinate. We evaluated the initial fields and forecasting at the following 19 levels when measurements and model fields are available, 0, 2, 4, 8, 10, 12, 15, 20, 25, 30, 35, 40, 45, 50, 60, 70, 80, 90 m.

2.2. Observations

The temperature and salinity measurements are from ship "Rongjiang No1". The field campaigns include a winter one from December 20 to 30, 2015, and a summer one from August 3 to 13, 2016. The sea-bird SBE plus CTD was used for all the station measurements. For each

station, the CTD instrument was put in the water for 3–5 min, and descends with speed of 1 m/s. The procedure was repeated 1–2 times to get measurements. In our analysis, we found there are some spurious measurements and our quality control procedure includes two steps. The first step is to remove all the data that have pressure less than 0. The second step is to remove all data that are outside the 3 standard deviation of the mean. The CTD data were interpolated to 19 model levels for comparison. The initial and forecasting fields were interpolated to the location of CTD stations.

The sea surface salinity observations from NASA Soil Moisture Active and Passive Mission (SMAP, [19]) are also used to evaluate the global ocean forecasting system in the East China Sea. A level-3 gridded product with resolution of 0.25° is used in our evaluation. These data are downloaded from PODAAC of Jet Propulsion Laboratory of NASA (podaac-ftp.jpl.nasa.gov).

3. Evaluating ocean forecasting fields

3.1. Initial condition

3.1.1. Winter time

For the estuary region, salinity plays a major role in determining the density. **Figure 1a** shows the root-mean-square error (RMSE) for all the CTD stations in the 2015 winter campaign. The RMSE is computed for all the available observations for entire water column at a particular station. There are large salinity RMSE regions at the Yangtze River estuary and coastal regions. The maximum salinity RMSE can reach 3.94 psu. The salinity RMSE reduces with increasing distance from the coast. For the sea surface salinity difference (**Figure 1b**), observations minus model output, most of the stations are negative, indicating model tends to overestimate sea surface salinity. However, right at the Yangtze River estuary, the salinity difference is positive. Thus, the error of the global ocean forecasting system has complex spatial distributions.

The RMSE for temperatures is generally less than 1°C except a few stations with RMSE greater than 1°C . The maximum temperature RMSE is greater than 1.7°C (**Figure 1c**). The sea surface temperature difference, observation minus model, is generally positive. The temperature difference at the Yangtze River estuary is negative, different from the situations in other regions.

The gridded SMAP data are also used to evaluate the initial condition of the global ocean forecasting system. **Figure 2** presents sea surface salinity from SMAP (**Figure 2a**), CTD stations (**Figure 2b**), and global ocean forecasting system (**Figure 2c**). During winter time, freshwater from the Yangtze River estuary tends to spread southward, hugging the coastal line (**Figure 2b**). The SMAP gridded product does not have spatial resolution to resolve this feature. The global ocean forecasting system seems to have issues to spread freshwater southward, which may explain the CTD and sea surface salinity difference is positive at Yangtze River estuary and negative in other places, because the freshwater from the Yangtze River is not spread efficiently.

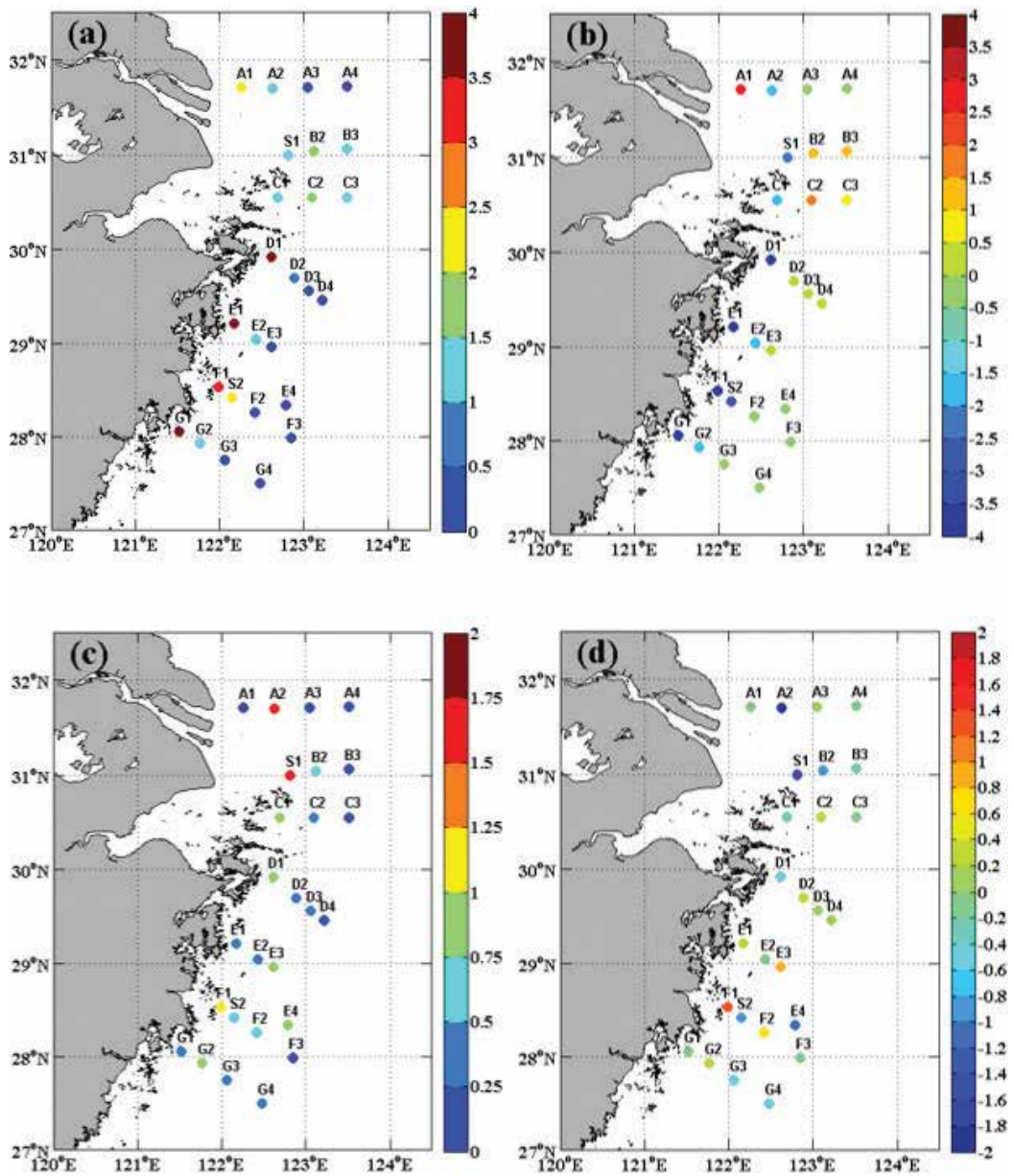


Figure 1. Comparison of temperature and salinity from a global ocean forecasting system configured from HYCOM and CTD observations conducted from December 20 to 30 in the winter of 2015, (a) root-mean-square error of salinity, (b) salinity difference (observation—model) at the surface, (c) root-mean-square error of temperature, and (d) temperature difference (observation—model) at the surface. The unit for salinity is psu and the unit for temperature is °C.

Figure 3 compares the initial condition of global forecasting system more qualitatively in terms of scattering plot and T-S plot. Overall, during the winter of 2015, the global ocean forecasting system agrees better with CTD observation in terms of temperature field (**Figure 3a**).

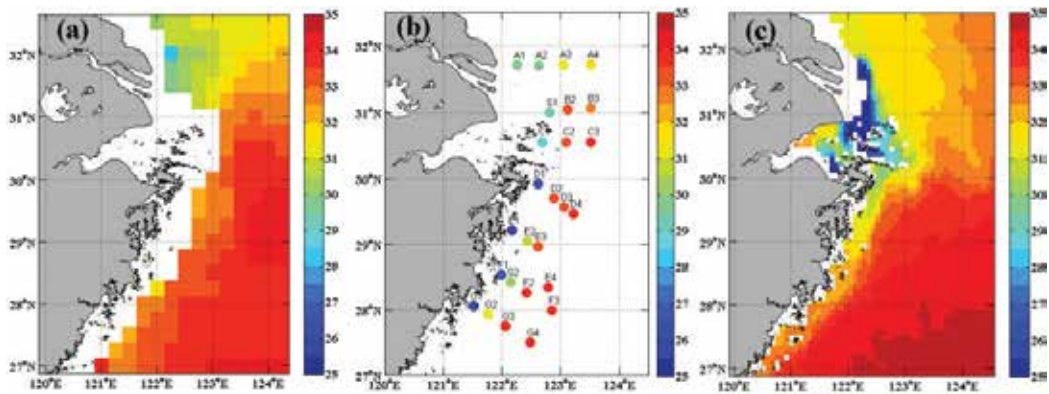


Figure 2. Comparison of sea surface salinity from (a) SMAP, (b) CTD observation, and (c) a global ocean forecasting system. The unit for salinity is psu and the unit for temperature is $^{\circ}\text{C}$.

The RMSE of temperature is 0.76°C , with a bias close to 0°C (-0.04°C). The correlation coefficient of temperature is 0.95. However, the RMSE of salinity is 1.9 psu, with a bias of -0.29 psu. The global forecasting ocean system tends to overestimate salinity at this estuary region. The correlation coefficient between salinity from the global forecasting system and CTD station is only 0.56.

The RMSE of both temperature and salinity decreases with depth (**Figure 3c, d**). For water depth shallower than 35 m, the RMSE of temperature is generally around $0.7\text{--}0.8^{\circ}\text{C}$, and reduces to less than 0.6°C when the water depth is deeper than 35 m. The RMSE of salinity decreases greatly from 2.5 psu at the surface to around 0.2 psu, when the depth is deeper than 80 m (**Figure 3d**). The water mass T-S property differs greatly between the global forecasting system and CTD observations (**Figure 3e**). In reality, the surface temperature cools significantly during winter. This cool water mass is associated with salinity around 25–28 psu with temperature around $12\text{--}14^{\circ}\text{C}$. In the global ocean forecasting system, this water mass is under-represented.

From the average temperature, salinity, and density change with depth, the above feature is more clearly shown (**Figure 4**). The surface temperature is cooler than temperature at depth during wintertime. The fresh and cool water mass stays on top of the warm and salty water. The global forecasting system cannot represent this feature and maintain a uniform temperature and salinity structure for the entire water column.

3.1.2. Summer time

Based on historical observations, the path of discharged freshwater from the Yangtze River has distinct seasonal variability. During summer time, the freshwater spreads toward northeast direction. The field campaign in the summer of 2016 made observations along this direction. Compared to the situation of the winter of 2015, the salinity RMSE has much larger values. The maximum RMSE reaches 7.8 psu. The sea surface salinity difference also has a large value, mostly negative, indicating that the global ocean forecasting system overestimates the sea surface salinity by 3–4 psu (**Figure 5a, b**).

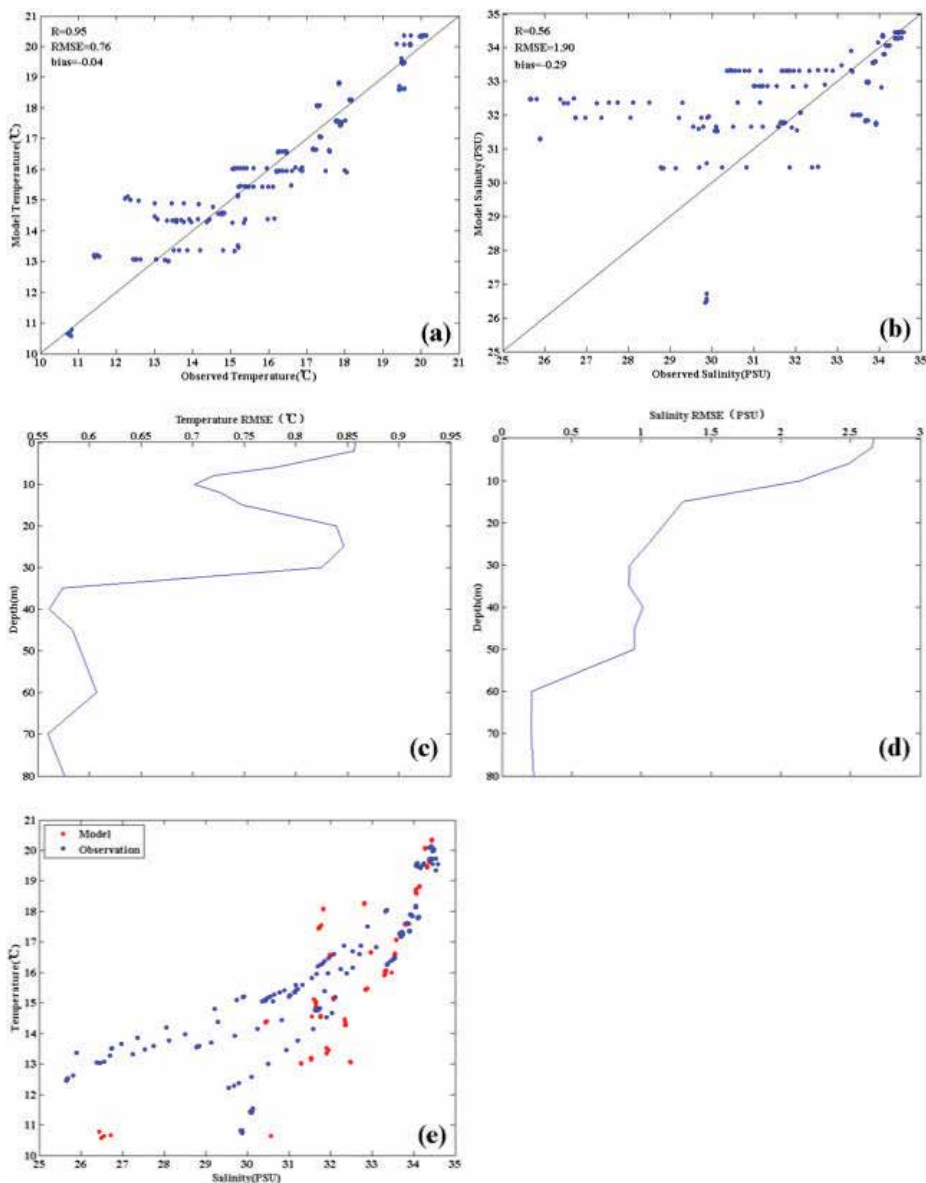


Figure 3. The scattering plot for (a) temperature, (b) salinity; distribution of root-mean-square error with depth for (c) temperature and (d) salinity, (e) the T-S relationship for observation (red dot) and model (blue dot). All the comparisons are for the observation made from December 20 to 30 in the winter of 2015. The unit for salinity is psu and the unit for temperature is °C.

The RMSE of temperature also has large values, with higher RMSE with increasing distance from the coastal region. The sea surface temperature difference is generally between -1° and 1° indicating large temperature difference toward deeper depth (Figure 5c, d).

From the two-dimensional sea surface salinity distribution of SMAP (Figure 6a) and CTD stations (Figure 6b), it is clear that the freshwater from the Yangtze River tends to form a low

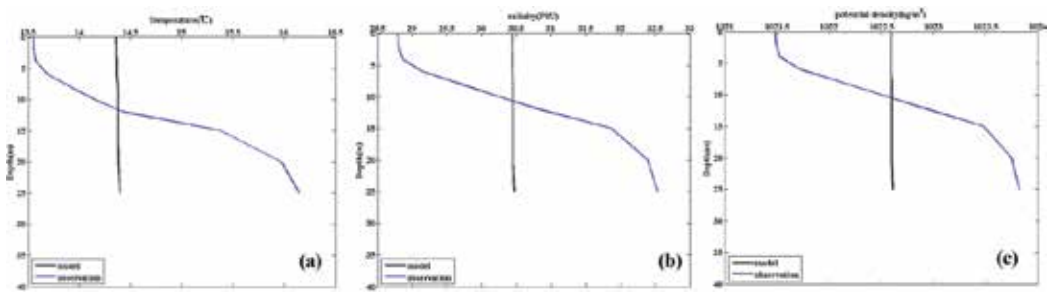


Figure 4. Averaged distribution of (a) temperature, (b) salinity and (c) density for the observation and global ocean forecasting system output from December 20 to 30 in the winter of 2015. The unit for salinity is psu and the unit for temperature is °C.

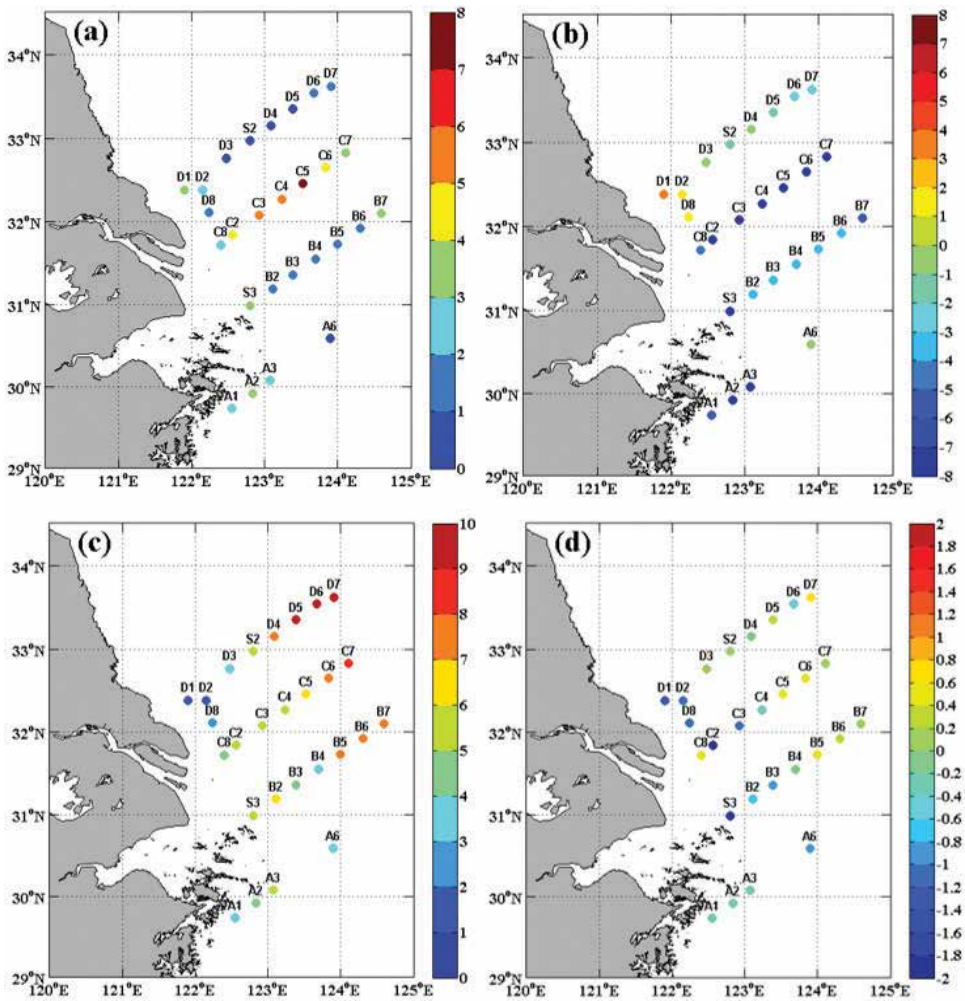


Figure 5. Comparison of temperature and salinity from a global ocean forecasting system configured from HYCOM and CTD observations conducted from August 3 to 13 in the summer of 2016, (a) root-mean-square error of salinity, (b) salinity difference (observation—model) at the surface, (c) root-mean-square error of temperature, and (d) temperature difference (observation—model) at the surface. The unit for salinity is psu and the unit for temperature is °C.

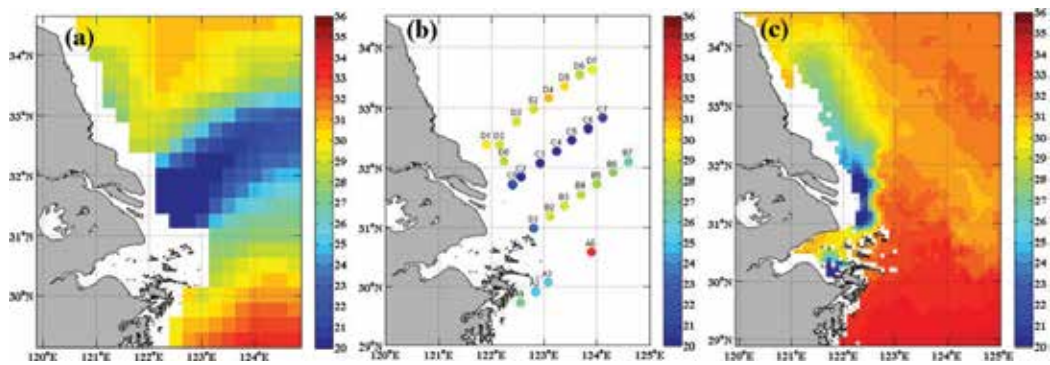


Figure 6. Comparison of sea surface salinity from (a) SMAP, (b) CTD observation, and (c) a global ocean forecasting system from August 3 to 13, 2016. The unit for salinity is psu and the unit for temperature is °C.

salinity region extending northeastward from the Yangtze River estuary. However, the initial field from the global ocean forecasting system misses the features (**Figure 6c**).

The root-mean-square difference of sea surface salinity between SMAP and CTD is 3.02 psu. The RMSE of sea surface salinity between CTD and the global ocean forecasting system is 6.76 psu, indicating that the SMAP data could provide valuable information around this coastal region.

More quantitative comparisons between temperature from the global ocean forecasting system and CTD observations indicate the difficulty to represent stratification structure during summer time. The RMSE of temperature is 7.22 °C, with the global ocean forecasting system having a warm bias of 5.52 °C. The correlation coefficient between the temperature from the global forecasting system and CTD observation is 0.28 (**Figure 7a**). For salinity, the RMSE is 3.4 psu; the global forecasting system has a salty bias of 0.95 psu and correlation coefficient for salinity is 0.28 (**Figure 7b**).

Contrary to the situation in wintertime, the temperature RMSE actually increases with depth, and can reach 14 °C at 60 m depth, indicating the difficulty to represent summer stratification of the region. The RMSE of salinity decreases from 6 to 7 psu at the surface to less than 1 psu at the depth of 60 m, with large RMSE in top 10 m. The observed T-S relationship indicates a wide spread of warm-fresh and cool-salty characteristic. The global ocean forecasting system, however, has a narrow T-S relationship centered at 24–30 °C and 26–34 psu.

The stratification structure from the global ocean forecasting system is also very different from that shown in CTD observations. During summer time, the water column here is stratified with a shallow warm and fresh layer at the top and cool and salty water at the bottom. However, the water column in the global forecasting system is mixed well with uniform temperature and salinity from the surface to the bottom of the ocean (**Figure 8**).

3.2. Evaluation of forecasting skill

3.2.1. Winter time

The forecasting skill of the global ocean forecasting system is also evaluated using CTD observations. The CTD observations are matched with temperature and salinity prediction with

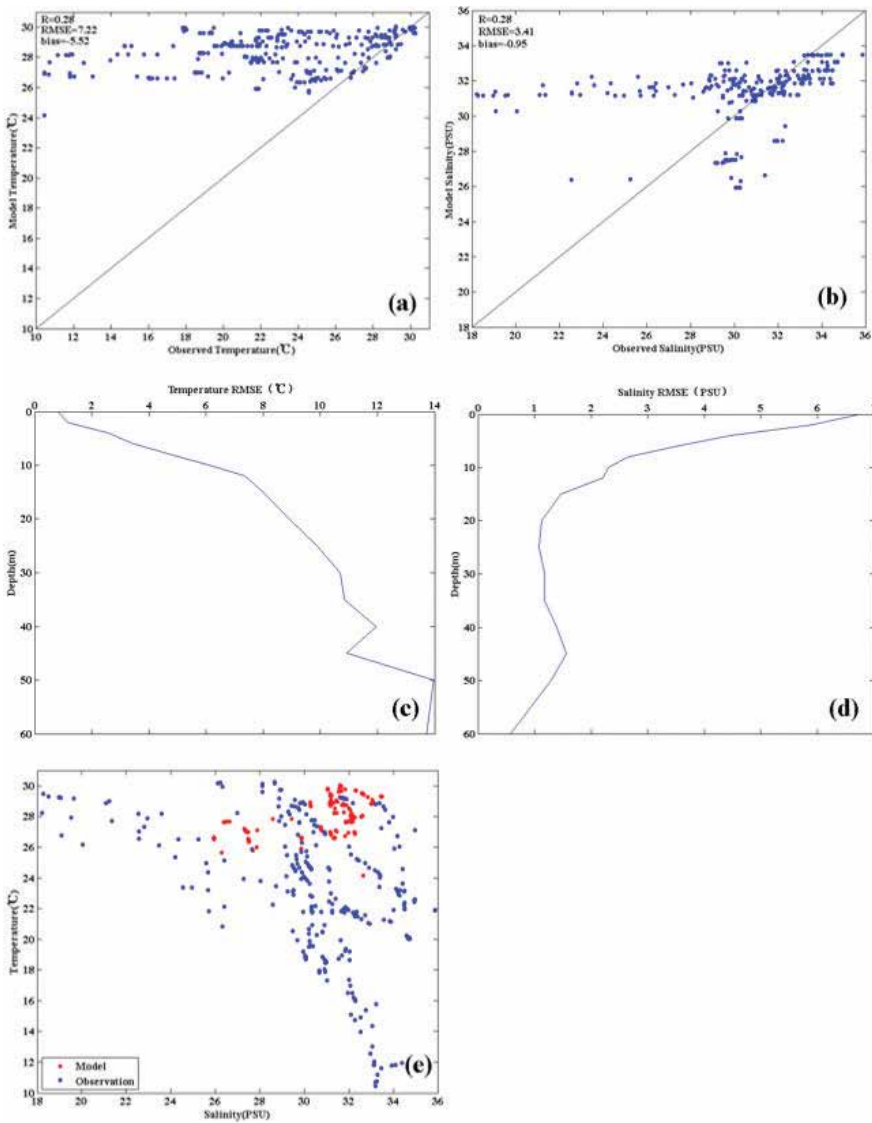


Figure 7. The scattering plot for (a) temperature, (b) salinity; distribution of root-mean-square error with depth for (c) temperature and (d) salinity, (e) the T-S relationship for observation (red dot) and model (blue dot). All the comparisons are for the observations made from August 3 to 13 in the summer of 2015.

leading time from 1 to 7 days. The forecasting skill is measured by correlation coefficient and root-mean-square error of temperature and salinity (**Figure 9**). For temperature prediction during winter time, the correlation coefficient decreases from around 0.95 to around 0.85, and the RMSE increases from less than 0.8–1.3 °C when the leading time increases from 1 to 7 days.

Overall, the situation reflects the general tendency that when the leading time increases, the prediction skill decreases. For the prediction of salinity, neither RMSE nor correlation coefficient changes significantly with the increase of leading time (**Figure 9b**) indicating that the forecasting skill for salinity in this region is limited.

3.2.2. Summer time

During the summer of 2016, the RMSE of temperature prediction varies from 7.2 to 8 °C and the correlation coefficient varies from 0.26 to 0.29 when the leading time increases from 1 to 7 days. The RMSE of salinity prediction varies from 3.1 to 3.2 psu and the correlation

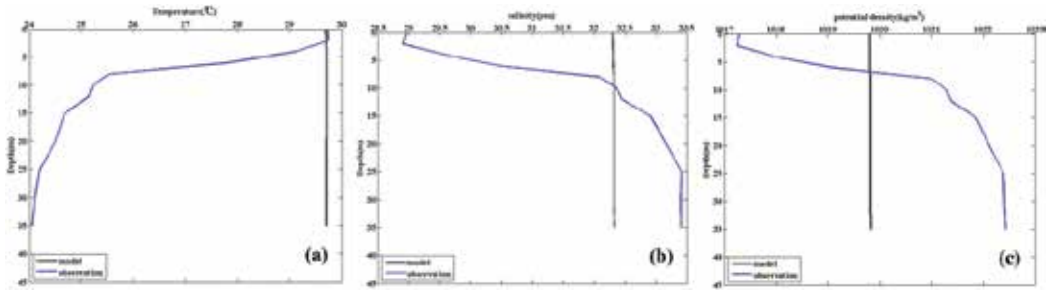


Figure 8. Averaged distribution of (a) temperature, (b) salinity and (c) density for the observation and global ocean forecasting system output from August 3 to 13 in the summer of 2015.

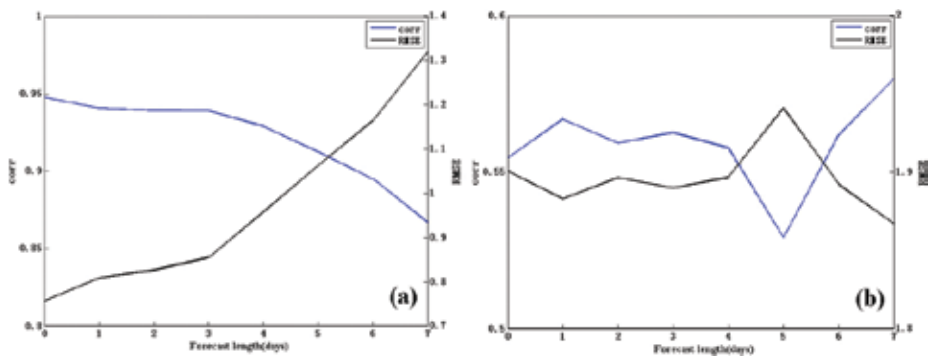


Figure 9. The root-mean-square error and correlation coefficient for (a) temperature and (b) salinity between CTD observation and the global ocean forecasting system configured from HYCOM with leading time increasing from 1 to 7 days. The comparison is for December 20 to 30 in the winter of 2015.

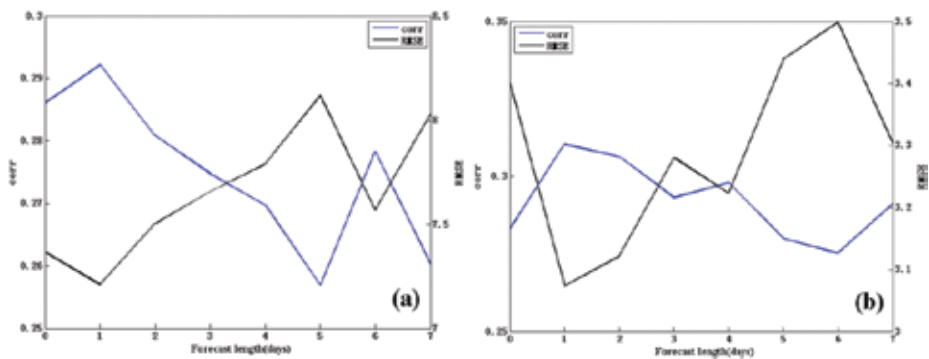


Figure 10. The root-mean-square error and correlation coefficient for (a) temperature and (b) salinity between CTD observation and the global ocean forecasting system configured from HYCOM with leading time increasing from 1 to 7 days. The comparison is from August 3 to 10 in the summer of 2016.

coefficient varies around 0.3, when the leading time increases from 1 to 7 days (**Figure 10**). The comparison indicates relatively poor prediction skill for the region during summer time for both temperature and salinity.

4. Summary

Using CTD and SMAP observations, our research evaluates the initial condition and forecasting skill of a global ocean forecasting system configured from HYCOM during the winter of 2015 and the summer of 2016 for the East China Sea. During winter time, the temperature of the global ocean forecasting system agrees with observation reasonably well. During summer time, the temperature field from the global ocean forecasting system has large errors and the error tends to increase with depth. For salinity field, the salinity field agrees better with observation during winter time than that during summer time. The global forecasting system seems to have issues to represent the northeastward spreading of the freshwater discharged from the Yangtze River.

In terms of forecasting skill, the global ocean forecasting system shows some skill in predicting temperature during winter time with a lead time of 7 days, with RMSE increasing from 0.8 to 1.3 °C. For salinity prediction, the RMSE is around 1.9 psu during winter time. The RMSE of temperature prediction increases from 7 to 8 °C, and the RMSE for salinity increases from 1.9 psu to 3–3.5 psu during summer. Overall, there is a large space for improvement in terms of temperature and salinity prediction in the East China Sea around the Yangtze River estuary. Evaluation of the ocean forecasting system will be useful for its applications in the East China Sea region and provides guidelines for the development of future ocean forecasting systems.

Acknowledgements

The work is supported by 2015 Program for Innovation Research and Entrepreneurship Team in Jiangsu Province, the Ocean Public Welfare Scientific Research Project, State Oceanic Administration of the People's Republic of China (201505003-05), the National Key Research and Development Program of China (2016YFC1401600) and the Priority Academic Program Development of Jiangsu Higher Education Institutions (PAPD).

Author details

Xiaochun Wang^{1,2*}, Yingjun Zou^{1,2} and Xianqiang He³

*Address all correspondence to: xcwang@nuist.edu.cn

1 School of Marine Sciences, Nanjing University of Information Science and Technology, Nanjing, Jiangsu, China

2 JIFRESSE, University of California at Los Angeles, Los Angeles, USA

3 Second Institute of State Ocean Administration, Hangzhou, Zhejiang, China

References

- [1] Chassignet EP, Smith LT, Halliwell GR, Bleck R. North Atlantic simulations with the Hybrid Coordinate Ocean Model (HYCOM): Impact of the vertical coordinate choice, reference pressure, and thermobaricity. *Journal of Physical Oceanography*. 2003;**33**(12):2504-2526
- [2] Zheng P. Introduction to some common OGCMs. *Marine Forecasts*. 2008;**25**:108-120
- [3] Zhan L, Wei Z, Wang L, Fang G, Wang X. Overview of numerical studies on the China adjacent seas. *Advance of Marine Sciences*. 2009;**2**:250-265
- [4] Fang C, Zhang X, Yin J. Development status and trends of ocean forecasting system in the 21st century. *Marine Forecasts*. 2013;**4**:93-102
- [5] Metzger EJ, Smedstad OM, Thoppil PG, Hurlburt HE, Cummings JA, Wallcraft AJ. US Navy operational global ocean and Arctic ice prediction systems. *Oceanography*. 2014;**27**(3):32-43
- [6] Ma Y. Overview of marine observation and forecast system for China. *Marine Forecasts*. 2008;**1**:31-40
- [7] Bleck R. An oceanic general circulation model framed in hybrid isopycnic-Cartesian coordinates. *Ocean Modelling*. 2002;**4**(1):55-88
- [8] Halliwell GR. Evaluation of vertical coordinate and vertical mixing algorithms in the HYbrid-Coordinate Ocean Model (HYCOM). *Ocean Modelling*. 2004;**7**(3):285-322
- [9] Winther NG, Evensen G. A hybrid coordinate ocean model for shelf sea simulation. *Ocean Modelling*. 2006;**13**(3):221-237
- [10] Lu ZM, Shan XD, Chen GY. Simulation of South China Sea circulation forced by COADS using Hybrid Coordinate Ocean Model. *Journal of Tropical Oceanography*. 2008;**27**(4):23-31
- [11] Yu Q, Wang H, Wan L. Numerical simulation of the temporal and spatial variability of sea surface temperature over South China Sea. *Marine Forecasts*. 2010;**27**:59-66
- [12] Wu L. *Ocean Model Adaptability Comparison and Improvement in the South China Sea*. Wuhan, Wuhan University of Technology; 2013
- [13] Dai Z. *Seasonal Variability of Thermohaline Structure and its Influence on Suspended Sediment Distribution*. Qingdao, Ocean University of China; 2015
- [14] Bai ZP, Gao S, Wang HT. A HYbrid Coordinate Ocean Model (HYCOM) for simulating the climatological Kuroshio in the East China Sea. *Marine Science Bulletin*. 2010;**29**(2):121-129
- [15] Chen M, Hou Y, Zhao B. Numerical simulation of the circulation and the mesoscale eddies in the East China Seas in winter. *Marine Sciences*. 2003;**27**:53-60
- [16] Chen X, Zhou L, Chen X, Zheng C, Wu Y. A comparative study of HYCOM vertical coordinate in the East China Sea. *Marine Sciences*. 2015;**7**:60-68

- [17] Cummings JA, Smedstad OM. Variational data assimilation for the global ocean: Data Assimilation for Atmospheric, Oceanic and Hydrologic Applications (Vol II). Springer-Verlag Berlin Heidelberg 2013. pp. 303-343
- [18] Renaudie C, Baraille R, Morel Y, Hello G, Giordani H. Adaptation of the vertical resolution in the mixed layer for HYCOM. *Ocean Modelling*. 2009;**30**(2):178-189
- [19] Fore A, Yueh S, Tang W, Hayashi A. SMAP Salinity and Wind Speed Data User's Guide. Pasadena, Jet Propulsion Laboratory, California Institute of Technology, Available from: <ftp:podaac-ftp.jpl.nasa.gov>; 2016

Validation and Application of SMAP SSS Observation in Chinese Coastal Seas

Qiong Wu, Xiaochun Wang, Xianqiang He and
Wenhao Liang

Additional information is available at the end of the chapter

<http://dx.doi.org/10.5772/intechopen.80318>

Abstract

Using sea surface salinity (SSS) from the Soil Moisture Active Passive (SMAP) mission from September 2015 to August 2016, the spatial distribution and seasonal variation in SSS in the Chinese coastal seas were investigated. First, in situ salinity observation over Chinese East Sea was used to validate SMAP observation. Then, the SSS signature of the Yangtze River fresh water was analyzed using SMAP data and the river discharge data. The SSS around the Yangtze River estuary in the Chinese East Sea, the Bohai Sea and the Yellow Sea is significantly lower than that of the open ocean. The SSS of Chinese coastal seas shows significant seasonal variation, and the seasonal variation in the adjacent waters of the Yangtze River estuary is the most obvious, followed by that of the Pearl River estuary. The minimum value of SSS appears in summer while maximum in winter. The root-mean-squared difference of daily SSS between SMAP observation and in situ observation is around 3 psu in both summer and winter, which is much lower than the annual range of SSS variation. The path of fresh water from SMAP and in situ observation is consistent during summer time.

Keywords: SMAP, CTD (conductance, temperature and depth), SSS (sea surface salinity), Yangtze River estuary

1. Introduction

Sea surface salinity (SSS) is one of the most important variables in describing the basic state of the ocean and can also be considered a proxy for the impact of the hydrologic cycle or the flux of freshwater across the air-sea interface [1]. The areas of low SSS tend to be regions where

precipitation is a dominant process with a net transport of freshwater from the atmosphere to the ocean [2]. The observation of SSS can enhance the understanding of the global water cycle. SSS is also an important tracer of the water mass.

Field observation and satellite remote sensing are two main methods to obtain SSS data (e.g., [3–4]). Field observation is extensively used in scientific research and operational monitoring of the ocean. Subrahmanyam et al. [5] used temperature and salinity profile data from Argo floats to investigate the seasonal and inter annual variations of SSS over the equatorial east India Ocean. Liu et al. [6] analyzed the influence of the wind on the extension of the Yangtze River freshwater plume northeast by using the salinity data from two zonal sections near Jeju Island. Although salinity data can be obtained from in situ observations, it cannot describe the changes of salinity at fine spatial scales due to the sparse distribution of in situ measurements. The maturity of the SSS satellite observation method provides a new way for the study of SSS. In recent years, several satellites have been launched, such as SMOS, AQUARIUS and SMAP for observing salinity. SMOS is the first SSS satellite mission launched by the European Space Agency in 2009 (e.g., [7–8]). AQUARIUS is a passive/active L band microwave instrument jointly launched by NASA and Argentina Space Agency in 2011 to observe the SSS (e.g., [9–11]). The Soil Moisture Active Passive (SMAP) satellite is the first satellite of the United States Space Agency (NASA) to detect soil moisture, which was launched on 31 January, 2015. The L band radar and radiometer on the SMAP satellite can also observe SSS. In order to achieve larger coverage on the ground and ocean, the antenna of SMAP rotates at a speed of 14.6 cycles per minute. The orbit of the SMAP is combined with the rotation of the antenna, forming a 1000 km wide observation stripe. This large area coverage makes SMAP complete the measurement of the Earth surface every 2–3 days (e.g., [12–15]). The SSS from SMAP can also show the freshwater plume of many large rivers, such as the Amazon River, Niger River, Ganges River, Nujiang and the Mississippi River [15]. In addition, the validation of SMAP observation was conducted for various regions. For example, Fournier et al. [16] showed a general agreement of SMAP SSS with in situ SSS over the Gulf of Mexico.

SSS satellite missions provide new opportunity to study SSS variation and their potential applications in terms of ocean monitoring and forecasting need to be explored, especially in coastal regions where the riverine freshwater discharge plays a significant role in oceanic processes and in situ salinity observation is often sparse in space. In present research, the SSS observation from SMAP mission is used to study SSS variation in Chinese coastal seas. Section 2 presents the data we used. Section 3 validates SMAP observation using in situ observation and analyzes SSS variability on seasonal and sub-seasonal time scales. Section 4 summarizes our results.

2. Data and methodology

The SSS product is obtained from NASA SMAP mission. A gridded product by blending original observation from 7 days is used in our analysis, which has a spatial resolution of 0.25 and a temporal resolution of 1 day. We used the gridded product from September 1, 2015 to August 31, 2016.

The in situ salinity measurements are from “Rongjiang No.1” research vessel. The field campaigns include a winter one from December 20 to 30, 2015 and a summer one from August 3 to 13, 2016. The sea-bird SBE conductivity, temperature, and depth (CTD) was used for all measurements. For each station, the CTD instrument was put in the water for 3–5 min and descends with a speed of 1 m/s. The procedure was repeated 1–2 times to get measurements. In our analysis, we found there are some spurious measurements and our quality control procedure includes two steps. The first step is to remove all the data that have pressure less than 0. The second step is to remove all data that are outside the three standard deviations of the mean.

The Yangtze River Datong hydrological station is located in the Meilong town of Chizhou, Anhui province. The station was built in the early twentieth century and is the upper boundary of the ocean tidal influence. This station has long-term observation data in the lower reaches of the Yangtze River basin. For the discharge data, we also selected data from September 2015 to August 2016.

3. Results

3.1. Validation

The daily gridded SSS observation from SMAP was first validated against in situ observation from two field campaigns around Yangtze River estuary. **Figure 1** shows the comparison of daily SSS from SMAP mission and in situ CTD observation for the winter of 2015 (**Figure 1a**), and summer of 2016 (**Figure 1b**). During the winter of 2015, the bias between in situ SSS and SMAP SSS observation is -1.36 psu, with SMAP mission overestimating SSS. The root mean square difference (RMSD) of the in situ and SMAP SSS observation is 3.15 psu. During the summer of 2016, the RMSD of in situ and SMAP SSS observation is 3.02 psu, with a bias of 0.47 psu. It is interesting to note that SMAP mission tends to overestimate SSS around Yangtze River estuary.

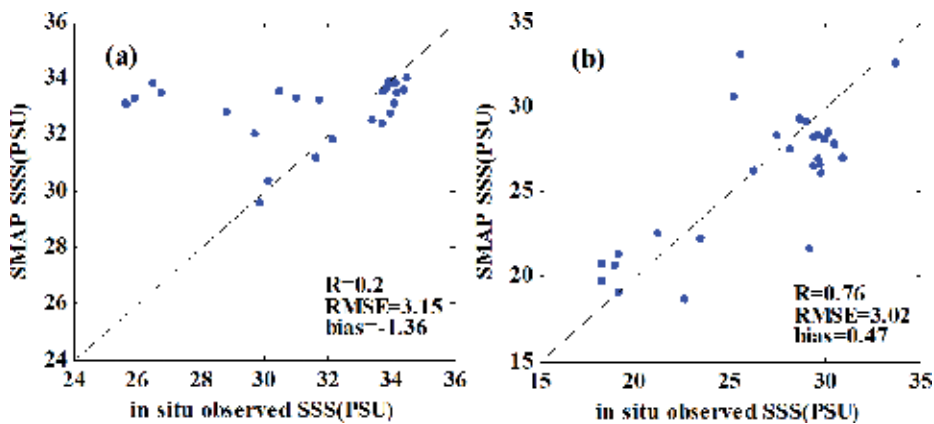


Figure 1. Comparison of daily SSS from SMAP mission and in situ CTD observation for (a) the winter of 2015 and (b) the summer of 2016. The unit for SSS is psu.

Though there is large bias of SMAP SSS observation during the winter of 2015, it is encouraging to note the similarity between SSS spatial distribution from SMAP (**Figure 2a**) and in situ measurement (**Figure 2b**). For instance, gradual increase of SSS from around 29–31 psu along 32°N is visible in both SMAP and in situ SSS observation. **Figure 2c** and **d** presents the distribution of SMAP and in situ CTD observation for the summer of 2016. The major feature in both SMAP and in situ SSS observation is the northeastward extension of Yangtze River freshwater plume, similar to the observations of Kim et al. [17] and Xuan et al. [18].

Though the errors in SMAP SSS observation are as large as 3 psu, it is encouraging to note that the SMAP SSS observation has great potential to monitor the spreading of freshwater plume from the Yangtze River.

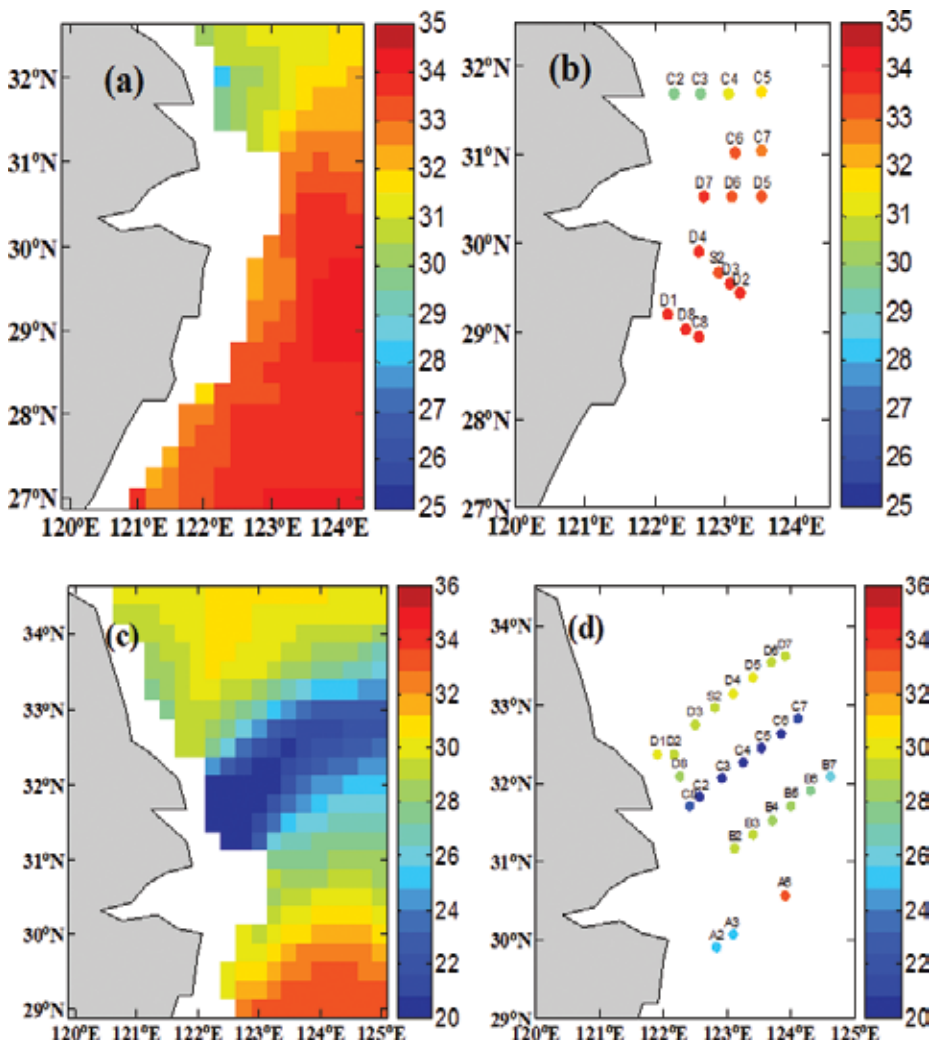


Figure 2. (a) SSS of SMAP from December 20 to 30, 2015; (b) SSS of in situ CTD observation from December 20 to 30, 2015; (c) SSS of SMAP from August 3 to 13, 2016 and (d) SSS of in situ CTD observation from August 3 to 13, 2016. The unit for SSS is psu.

3.2. Mean and range of SSS

Because of the sparseness of in situ observations, the fine spatial structure of SSS is poorly known over most coastal areas of China. However, the SMAP data (**Figure 3a**) show the spatial distribution of annual averaged SSS in different coastal areas of China. Due to the influence of discharge, the annual averaged SSS over Bohai Sea, Yellow Sea, and Yangtze River estuary are lower than other regions. The minimum value of SSS is about 25 psu around the Yangtze River estuary. The averaged SSS over South China Sea (SCS) is 33–34 psu, significantly higher than that of the Yellow Sea, Bohai Sea and Yangtze River estuary. However, the SSS over the SCS is lower than that of the Pacific Ocean. As seen from **Figure 3a**, the SSS gradient is large between the west and east side of the Luzon strait. Another feature is that the SSS is significantly decreased from the near coastal region to the outer sea.

In order to further illustrate the variability of SSS over the Chinese coastal regions, we calculated the differences of the maximum and the minimum values of SSS at each grid point (**Figure 3b**). The range of SSS changes is about 16 psu during 1 year. The Yangtze River estuary is associated with the large values while the amplitude of SSS decreases from the estuary to the outer sea. The influence of the Yangtze River is obvious in the spatial distribution of SSS range, with a belt of large SSS range extending northeastward from the Yangtze River estuary to Jeju Island.

3.3. Seasonal variation

The SSS of Chinese coastal seas experiences large seasonal variability. In **Figure 4a–d**, the low value SSS region over the Chinese coastal seas gradually retreats to the Bohai Sea from September 2015 to December 2015 and gradually invades the coastal regions from January 2016 to July 2016 (**Figure 4e–k**). The SSS reaches the minimum in July 2016 (**Figure 4k**), mainly due to the increasing precipitation over the Yangtze River basin from winter to summer. The Pearl River, which is the largest river in South China, also causes large SSS variability in coastal region. The SSS varies from 32 to 33 psu over Pearl River estuary from September 2015 to October 2015 (**Figure 4a, b**), and the SSS value decreases gradually from April 2016 to July 2016 (**Figure 4h–k**).

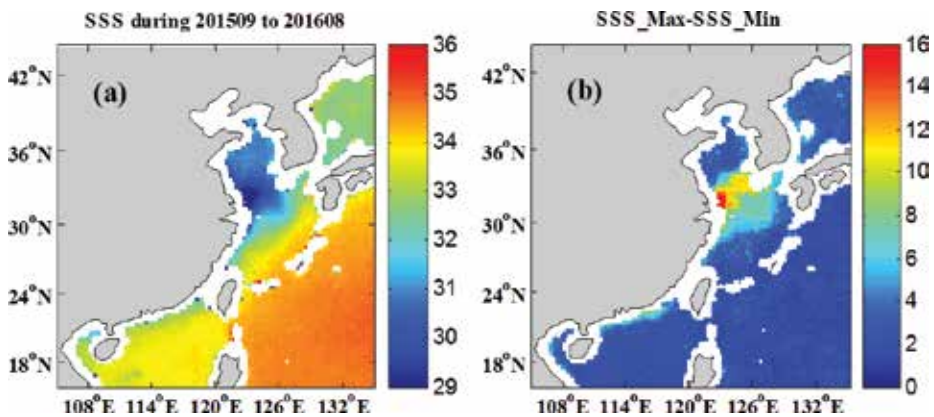


Figure 3. (a) Mean SMAP SSS from September 2015 to August 2016 in Chinese coastal seas. (b) The difference of maximum and minimum SSS. The unit for SSS is psu.

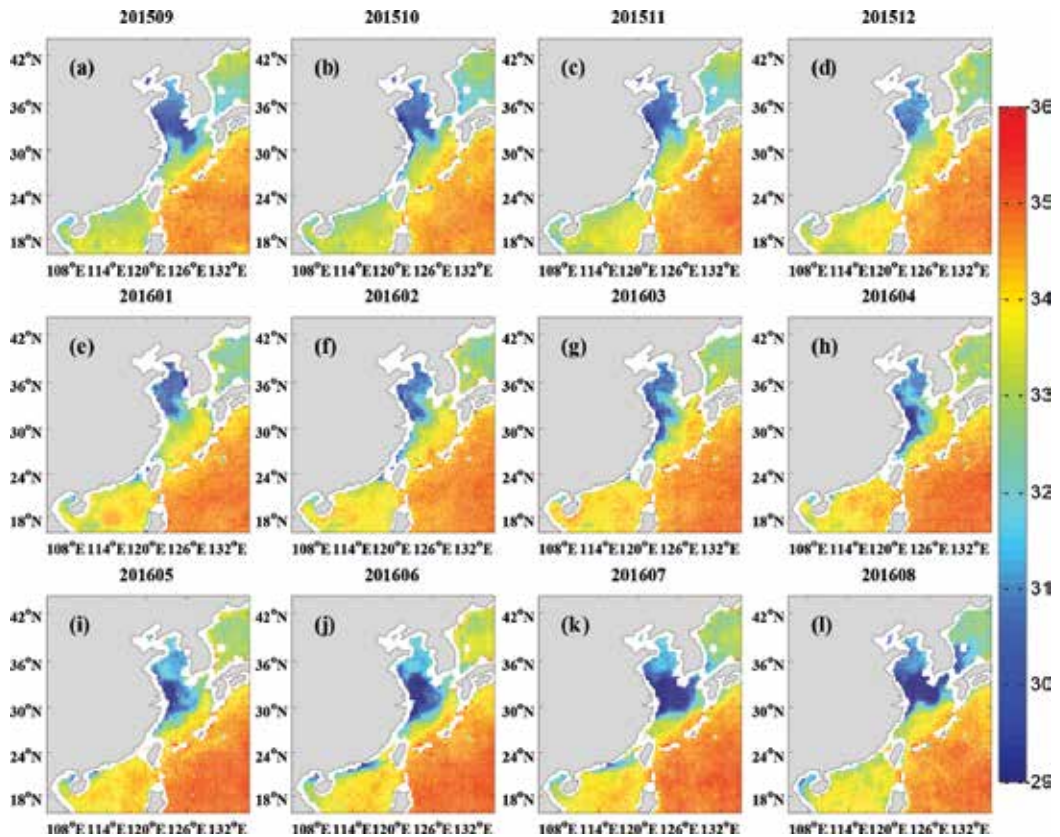


Figure 4. (a-l) Monthly SSS from September 2015 to August 2016 of Chinese coastal seas. The month is shown at the top part of each figure. The unit for SSS is psu.

Generally, the SSS of the Yangtze River estuary and the Pearl River estuary are relatively higher in winter and lower in summer, which reflects that the SSS variation in Chinese coastal seas is influenced by the precipitation and freshwater discharge.

To analyze the relationship of SSS change and hydrological cycle, the mean SSS from 32°N to 33°N, 122°E to 124°E is used as an index to represent SSS in the Yangtze River estuary. **Figure 5** presents the time evolution of SSS in the Yangtze River estuary and the Yangtze River discharge at Datong hydrological station.

The SSS of the Yangtze River estuary is around 31 psu from September 2015 to February 2016. At this time, the value of discharge is maintained from 2×10^4 to 3×10^4 m³/s. When the discharge increased gradually from February 2016 to July 2016, reaching a peak value of 7×10^4 m³/s in July of 2016, the SSS of the Yangtze River estuary fluctuated downward and the SSS value reached the minimum value of 24 psu in July of 2016. After July of 2016, the SSS increased rapidly following the decreasing of the discharge.

Overall, the time evolution of the mean SSS and discharge in Yangtze River estuary is opposite. Large discharge value corresponds to the low salinity, and the small discharge corresponds to

the high salinity. The correlation coefficient between them is -0.91 , which is significant at 99% confidence level. The above mentioned analysis indicates the potential of using SSS observation to infer the change of discharge for remote areas where the discharge observation is not available.

From **Figure 4a–l**, we can see that besides the Yangtze River estuary, SSS also shows a clear seasonal variation in the Pearl River estuary, but its variation is smaller than that in the Yangtze River estuary.

Rainy season usually appears in South China from April to May every year and ends around October. **Figure 6a** shows the time series of discharge from the Pearl River [19]. The discharge of the Pearl River is high in spring and in summer. The amount of discharge of Pearl River from April to September accounted for 79% of the total discharge of entire year while it is relatively small in winter, resulting in the seasonal variation of SSS. **Figure 6b–g** shows the evolution of SSS every 2 months from September 2015 to July 2016 over Pearl River estuary. It is obvious that the SSS over Pearl River estuary reaches the maximum in winter and the minimum in summer. The SSS in the coastal areas is lower than that of the outer sea.

3.4. Path of Yangtze River freshwater

Because of its high spatial and temporal resolution, SMAP observation can depict the diffusion and advection path of freshwater plume in the Yangtze River estuary very well. We can see that the Yangtze River plume spreads from near coastal region to the outer sea. The most obvious feature is that there is a clear trend of spreading to the northeast from May to July in 2016. By August, the trend of spreading to the northeast has weakened (**Figure 4**). In order to analyze the spreading of Yangtze River freshwater in summer, we showed the SSS distribution map of 15th and 30th of May, June, July in 2016 (**Figure 7a–f**). It can be seen that since May, the areas affected by Yangtze River freshwater become larger increasingly and the area of low salinity extends northeastward gradually. During the winter, there is a completely different diffusion path for the Yangtze River

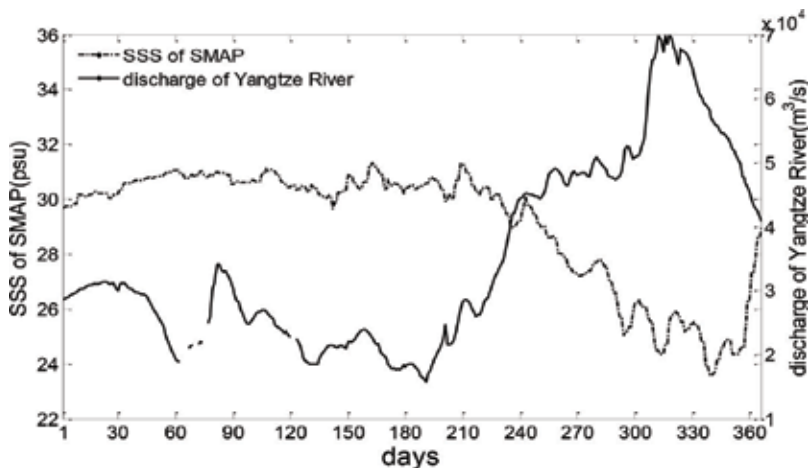


Figure 5. Mean SSS for the region of 32°N to 33°N , 122°E to 124°E from September 2015 to August 2016, representing Yangtze River estuary and discharge of the Yangtze River from the Datong hydrological station during the same period. The unit of salinity is psu. The unit for discharge is m^3/s .

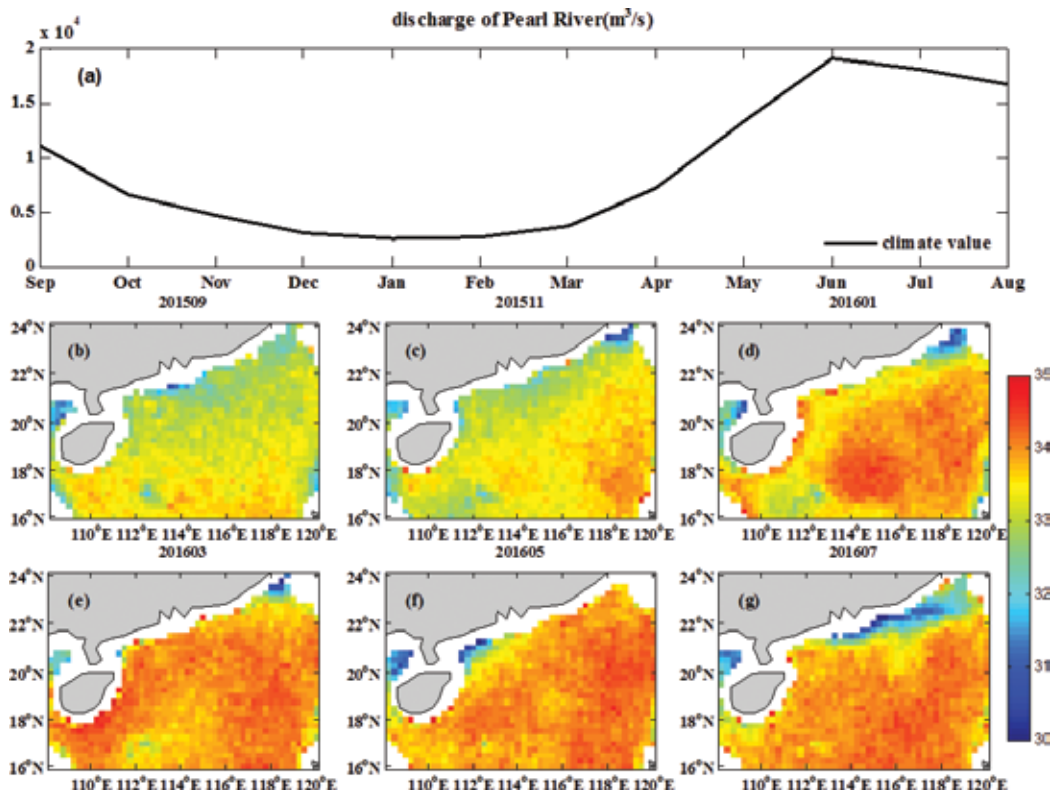


Figure 6. (a) The climate discharge of Pearl River. The distribution monthly SSS from September 2015 to August 2016 over the Pearl River estuary (b)–(g). The unit for SSS is psu. The unit for discharge is m³/s.

freshwater. **Figure 7g–i** shows the distribution of SSS for every 15 days from December of 2015 to February of 2016. We found that the southward diffusion of freshwater plume is weak, the SSS decreasing from 30°N to the South China coastal area and reaching the minimum value. The diffusion is presumably associated with the north wind in winter. Compared with the summer, the scope of the Yangtze River freshwater diffusion is much weaker during winter time.

In addition, **Figure 7g–i** shows that the SSS in the near coastal area 20–34°N, 112–126°E is high at north and south part while low over the Yangtze River estuary. The Yangtze River has a small discharge in winter (**Figure 5**). It flows out of the Yangtze River mouth and spreads to the south near the coastal area and it does not exceed 70 km in the range of 27–31°N. Due to the increasing measurement error of satellite in the near coastal region, the chance of missing data is increased. The diffusion of the Yangtze River freshwater to the south is not as clear as its diffusion to the north. But the phenomenon can be seen from the SMAP data. For example, a low salinity belt can be observed along the coastal area near 30–24°N.

Comparing the diffusion of Yangtze River freshwater in summer and winter, it is obvious that the discharge of Yangtze River is larger in summer than that in winter. The range of diffusion to the northeast direction is far greater than that to the south direction. In addition to the influence of the discharge, the wind is also an important factor. Affected by the monsoon, southerly winds prevail in summer, the Yangtze River discharge flows to the north, while northerly winds reign in winter, and the Yangtze River discharge flows to the south.

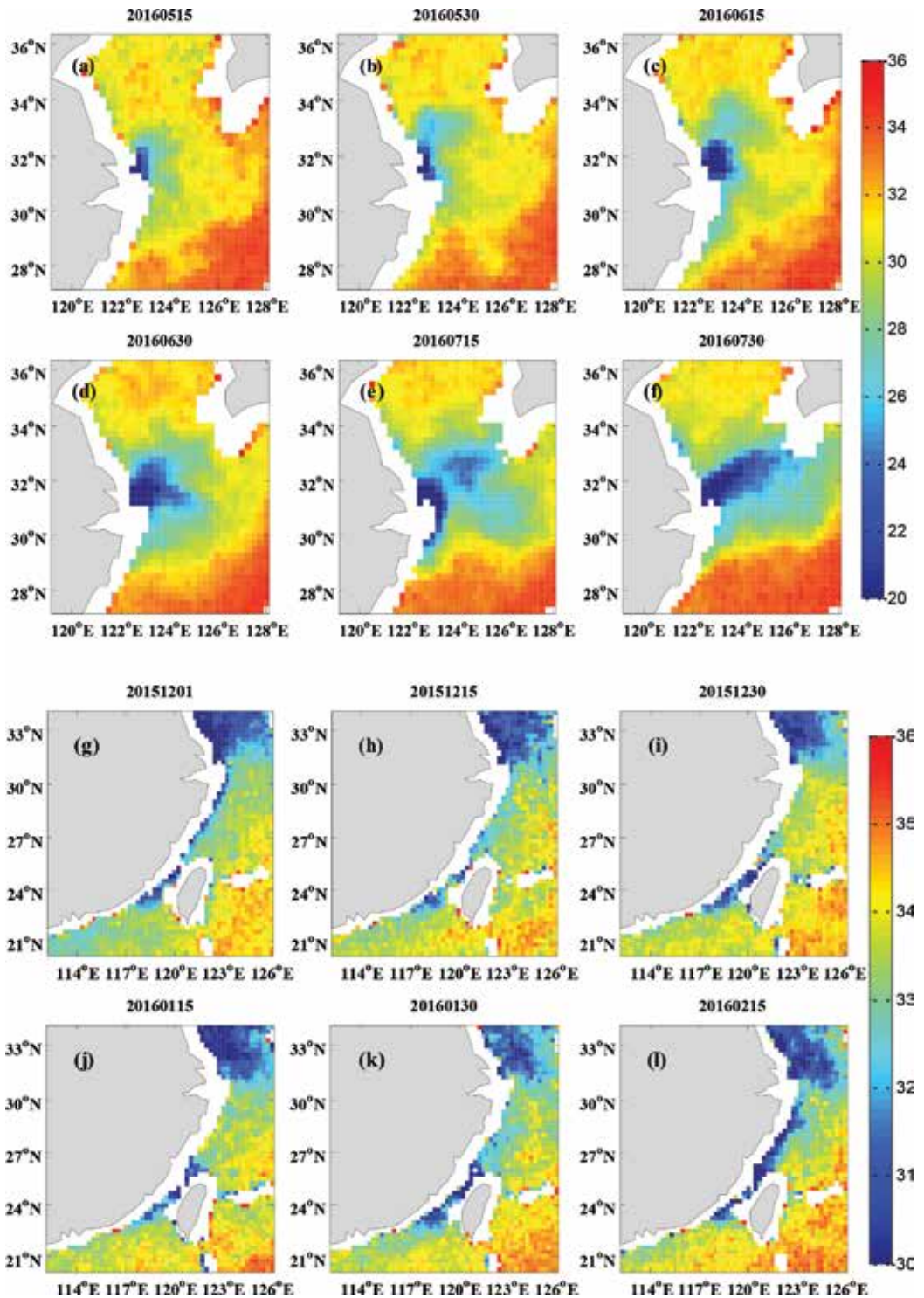


Figure 7. (a)–(f) Daily SSS from May 2016 to July 2016 for every 15 days for the Yangtze River estuary; (g)–(l) same as (a)–(f), but from December 2015 to February 2016. The exact date of the SSS observation is labeled in the top part of each figure. The unit for SSS is psu.

4. Summary

The spatial characteristics and temporal evolution of SSS over the Chinese coastal seas from SMAP data are analyzed in this paper. The results show that the SSS of Chinese coastal seas including the adjacent area of the Yangtze River and Bohai is lower than that of the outer sea. The SSS has obvious seasonal cycle, especially over the Yangtze River estuary. The annual amplitude of SSS change is more than 16 psu with the minimum appearing in summer and the maximum in winter. The SSS over the Pearl River estuary also shows seasonal changes although the change of SSS is relatively small due to the weaker discharge of the Pearl River than that of the Yangtze River. The comparison of SSS from SMAP against in situ observation indicates a RMSD between them is about 3 psu. However, it is encouraging to note that the SSS from SMAP mission can depict the spreading of freshwater plume from the Yangtze River, especially during summer time.

The SSS over Yangtze River estuary is negatively correlated with the discharge. Due to the influence of discharge, the SSS in the Pearl River estuary also shows similar results. However, the SSS difference between summer and winter is smaller than that of Yangtze River estuary. Salinity observation from satellites is an important supplement to in situ salinity observation. It can be used to monitor the diffusion of freshwater discharge in the coastal seas and the real-time prediction of the marine condition.

Acknowledgements

This study was supported by the 2015 Jiangsu Program of Entrepreneurship and Innovation Group, the Ocean Public Welfare Scientific Research Project, State Oceanic Administration of the People's Republic of China (201505003-05), the National Key China (Grant No. 2015g016), and the 2015 Jiangsu Program of Entrepreneurship and Innovation Group (Grant No. 2191061503801/002). Research and Development Program of China (2016YFC1401600) and the Priority Academic Program Development of Jiangsu Higher Education Institutions (PAPD).

Author details

Qiong Wu¹, Xiaochun Wang^{2,3*}, Xianqiang He⁴ and Wenhao Liang²

*Address all correspondence to: xcwang@nuist.edu.cn

1 School of Atmospheric Sciences, Nanjing University of Information Science and Technology, Nanjing, China

2 School of Marine Science/Jiangsu Engineering Technology Research Center for Marine Environment Detection, Nanjing University of Information Science and Technology, Nanjing, China

3 JIFRESSE, University of California at Los Angeles, Los Angeles, USA

4 Second Institute of State Ocean Administration, Hangzhou, China

References

- [1] Bingham FM, Foltz GR, McPhaden MJ. Characteristics of the seasonal cycle of surface layer salinity in the global ocean. *Ocean Science*. 2012;**8**:915-929
- [2] Durack PJ, Wijffels SE. Fifty-year trends in global ocean salinities and their relationship to broad-scale warming. *Journal of Climate*. 2010;**23**:4342-4362
- [3] Bai Y, Pan DL, Cai WJ, He XQ, Wang DF, Tao BY, Zhu QK. Remote sensing of salinity from satellite-derived CDOM in the Changjiang river dominated East China Sea: Satellite salinity of Changjiang plume. *Journal of Geophysical Research: Oceans*. 2013;**118**:227-243
- [4] Bai Y, He XQ, Pan DL, Chen C-TA, Yan K, Chen XY, Cai WJ. Summertime Changjiang river plume variation during 1998-2010. *Journal of Geophysical Research: Oceans*. 2014;**119**:6238-6257
- [5] Subrahmanyam B, Murty VSN, Heffner DM. Sea surface salinity variability in the tropical Indian Ocean. *Remote Sensing of Environment*. 2011;**115**:944-956
- [6] Liu B, Feng L. An observational analysis of the relationship between wind and the expansion of the Changjiang river diluted water during summer. *Atmospheric and Oceanic Science Letters*. 2012;**5**:384-388
- [7] Berger M, Camps A, Font J, Kerr Y, Miller J, Johannessen J, et al. Measuring ocean salinity with ESA's SMOS mission. *ESA Bulletin-European Space Agency*. 2002;**111**:113-121
- [8] Font J, Camps A, Borges A, Martín-Neira M, Boutin J, Reul N, Kerr YH, Hahne A, Mecklenburg S. SMOS: The challenging sea surface salinity measurement from space. *Proceedings of the IEEE*. 2010;**98**:649-665
- [9] Le Vine DM, Lagerloef GSE, Colomb FR, Yueh SH, Pellerano FA. Aquarius: An instrument to monitor sea surface salinity from space. *IEEE Transactions on Geoscience and Remote Sensing*. 2007;**45**:2040-2050
- [10] Lagerloef G, Colomb FR, Le Vine D, Wentz F, Yueh S, Ruf C, et al. The aquarius/SAC-D mission: Designed to meet the salinity remote-sensing challenge. *Oceanography*. 2008;**21**:68-81
- [11] Yueh S, Tang W, Fore A, Hayashi A, Song YT, Lagerloef G. Aquarius geophysical model function and combined active passive algorithm for ocean surface salinity and wind retrieval. *Journal of Geophysical Research: Oceans*. 2014;**119**:5360-5379
- [12] Entekhabi D, Njoku EG, O'Neill PE, Kellogg KH, Crow WT, Edelstein WN, et al. The soil moisture active passive (SMAP) mission. *Proceedings of the IEEE*. 2010;**98**:704-716
- [13] Entekhabi D, Das N, Yueh S, et al. SMAP Handbook Soil Moisture Active Passive: Mapping Soil Moisture and Freeze/Thaw From Space. Instrument Design and L1 Data Products. California, USA: National Aeronautics and Space Administration Jet Propulsion Laboratory, California Institute of Technology Pasadena; 2014. pp. 31-46
- [14] Das NN, Entekhabi D, Njoku EG. An algorithm for merging SMAP radiometer and radar data for high-resolution soil-moisture retrieval. *IEEE Transactions on Geoscience and Remote Sensing*. 2011;**49**:1504-1512

- [15] Yueh S, Fore A, Tang WQ, Hayashi A, Stiles B, Zhang FQ, Weng YH, Reul N. Applications of SMAP data to retrieval of ocean surface wind and salinity. *SPIE Remote Sensing*. 2016;**9999**:99990F
- [16] Fournier S, Reager JT, Lee T, Vazquez-Cuervo J, David CH, Gierach MM. SMAP observes flooding from land to sea: The Texas event of 2015: SMAP observes Texas flooding. *Geophysical Research Letters*. 2016;**43**:10338-10346
- [17] Kim K, Kim KR, Rhee TS, Rho HK, Limeburner R, Beardsley RC. Identification of water masses in the Yellow Sea and the East China Sea by cluster analysis. *Elsevier Oceanography Series*. 1991;**54**:253-267
- [18] Xuan JL, Huang DJ, Zhou F, Zhu XH, Fan XP. The role of wind on the detachment of low salinity water in the Changjiang Estuary in summer: Wind role on the LSW detachment. *Journal of Geophysical Research: Oceans*. 2012;**117**:C10004
- [19] Dai AG, Trenberth KE. Estimates of freshwater discharge from continents: Latitudinal and seasonal variations. *Journal of Hydrometeorology*. 2002;**3**:660-687

Edited by X. San Liang and Yuanzhi Zhang

The coastal environment is deteriorating at an alarming rate and is currently a great societal concern. This book provides a selected collection of papers on coastal environmental change, coastal disasters, and coastal infrastructure due to global warming, with a focus on the coasts of the rapidly developing country China. What makes the book distinctly different from others is its diversity, reflecting the interdisciplinary nature of coastal problems. With contributions from over 30 authors, the book is a comprehensive account of diverse topics, such as coastal upwelling, estuarine processes, coastal pollution, sea level rise, meteorological and atmospheric problems, urbanization and the heat island effect, and coastal infrastructure, to name just a few, from theoretical study and phenomenological description, to methodological development. This book is expected to serve as a relatively comprehensive reference for coastal researchers, graduate students, as well as policymakers and coastal resource managers.

Published in London, UK

© 2018 IntechOpen

© Andrzej Kryszpiniuk / unsplash

IntechOpen

ISBN 978-1-83881-841-8



9 781838 818418